



UNIVERSITY OF
BIRMINGHAM

Destruction of Diesel Soot Aggregates with the
Use of Fuel-borne Oxygen and the Application
of Hydrogen Assisted SCR Catalyst

By
Nahil Serhan

A thesis submitted to
the University of Birmingham
for the degree of
DOCTOR OF PHILOSOPHY

School of Mechanical Engineering
The University of Birmingham
May 2019

**UNIVERSITY OF
BIRMINGHAM**

University of Birmingham Research Archive

e-theses repository

This unpublished thesis/dissertation is copyright of the author and/or third parties. The intellectual property rights of the author or third parties in respect of this work are as defined by The Copyright Designs and Patents Act 1988 or as modified by any successor legislation.

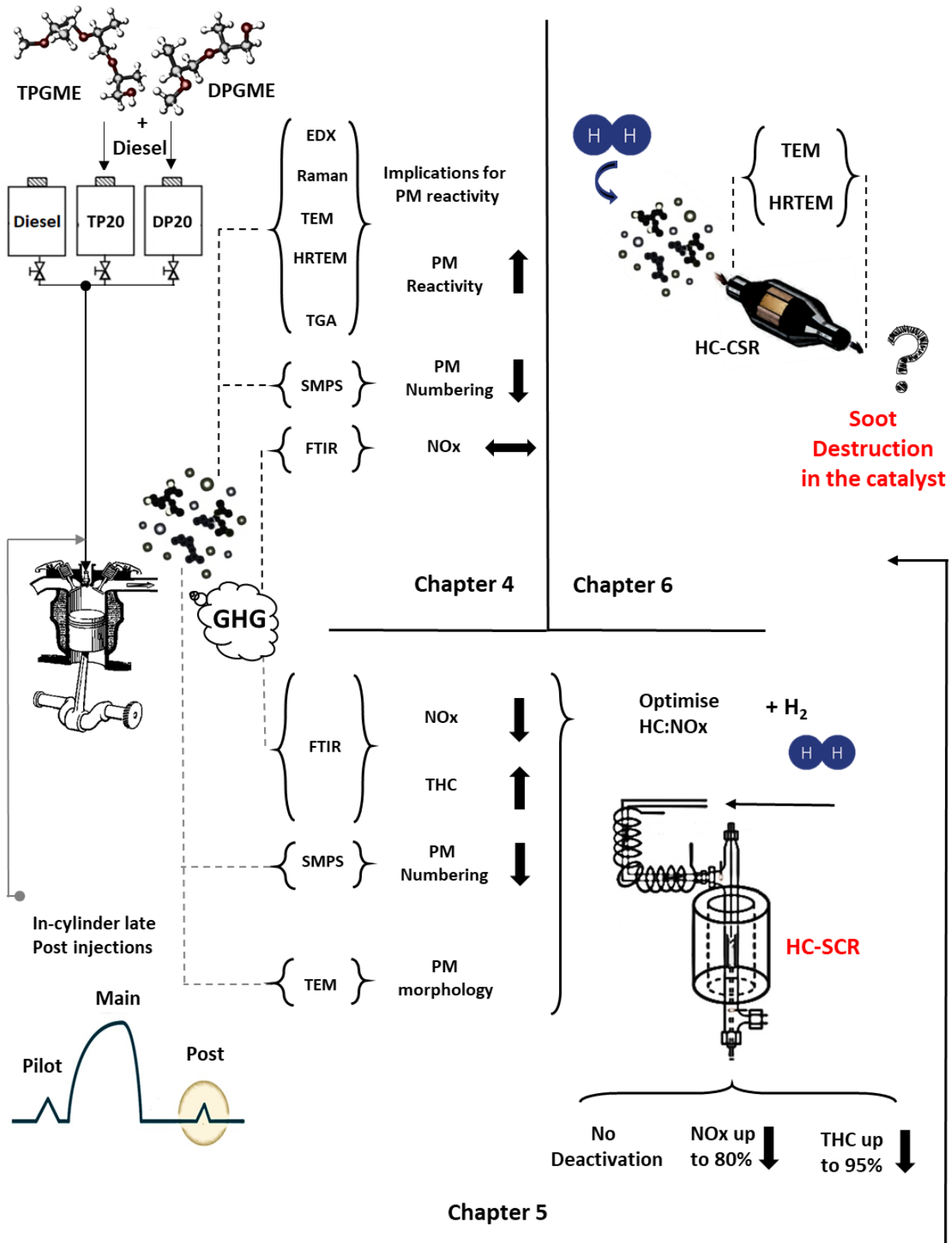
Any use made of information contained in this thesis/dissertation must be in accordance with that legislation and must be properly acknowledged. Further distribution or reproduction in any format is prohibited without the permission of the copyright holder.

ABSTRACT

The sustainability of diesel-powertrain technology in the light-duty vehicles' market is mainly dependant on the level to which the engine-out emissions, mainly particulate matter (PM) and nitrogen oxides (NOx), can be suppressed. The use of new-fuel generation, fuel injection calibration and advanced aftertreatment devices is the main state-of-the-art technology to control diesel emissions. To evaluate the impact of alternative fuels and in-cylinder post-fuel injection (PFI) on PM characteristics and a non-commercial silver alumina hydrocarbon selective catalytic reduction (HC-SCR) catalyst, glycol ether-diesel blends were studied at various steady-state engine operating conditions. The results indicate that glycol ethers permits a lower NOx/PM trade-off and produces more reactive PM compared to neat diesel without deterring the combustion stability. Introduction of PFI can adequately regulate the exhaust HC:NOx ratios to fully activate the HC-SCR when minute concentration (500 ppm) of Hydrogen (H_2) is fed to the flow. NOx reduction up to 80% with a fuel penalty of 2.8% was achieved in the low temperature region. Considering the effective de-NOx mechanism shown with this application, the soot destruction throughout the catalyst was also examined to reveal synergies that can assist in the development of the next generation of aftertreatment devices. Given the needed enhancers (H_2) and exhaust temperatures, HC-SCR can effectively breakdown and oxidise the soot aggregates throughout the catalyst channels. Soot oxidation

rate up to 17% was seen in the low temperature window (280 °C) despite of the limited catalyst/soot residence time.

GRAPHICAL ABSTRACT



ACKNOWLEDGMENTS

The following research work wouldn't be possible without the support, guidance and help of my lead supervisor, Professor Athanasios Tsolakis.

I would also like to thank Dr. Francisco Javier Martos Ramos and Dr. Jose Martin Herreros for their technical expertise and useful suggestions provided throughout the experimental work.

Special thanks to my colleagues for their moral and technical support throughout all the period of my studies.

Johnson Matthey Technology Centre is acknowledged for supplying of the catalysts used in this thesis. Engineering and Physical Sciences Research Council (ESPRC) is acknowledged for supporting and funding my latest research work (regarding the HC-SCR catalyst) to be published as an open access document in the Applied Catalysis B: Environmental journal.

Last, but not least, to my beloved family and to my partner, Chrysa, I'm grateful for all the support, motivation and encouragement you have made to get me through my Ph.D.

Nahil Serhan

May 2019

TABLE OF CONTENTS

CHAPTER 1.....	1
INTRODUCTION	1
1.1 Overview	1
1.2 Research objective and focus	3
1.3 Thesis outline.....	6
CHAPTER 2.....	9
LITERATURE REVIEW	9
2.1 Fuel Option	9
2.2 PM Formation Pathway	14
2.2.1 Pyrolysis	15
2.2.2 Nucleation.....	16
2.2.3 Mass growth	17
2.2.4 Coalescence, agglomeration and carbonisation.....	18
2.2.5 Oxidation	19
2.3 Soot Structural Configuration and Elemental Composition	20
2.4 Correlation between soot physio-chemical properties and the corresponding oxidative reactivity	23
2.4.1 Soot Oxidative reactivity dependence upon morphology	26
2.4.2 Soot Oxidative reactivity dependence upon elemental composition.....	27
2.4.3 Soot Oxidative reactivity dependence upon nanostructure and the uncertainties presented.....	29
2.4.4 Uncertainties in the impact of the parent fuel type on the soot oxidative reactivity	
36	
2.5 Lean-NOx Catalytic Reduction and Soot Destruction in the After-Treatment System	
38	
2.5.1 Hydrocarbon selective catalytic reduction	39
2.5.2 Silver alumina as a soot oxidation promoter	46
2.5.3 Variation in soot structure along the exhaust after-treatment system	48

2.6	In-cylinder Late Post Fuel Injections.....	54
2.6.1	Impact of PFI on the particulate matter emissions	56
2.6.2	Impact of PFI on the gaseous emissions.....	58
2.7	Summary.....	60
CHAPTER 3.....	63	
TEST FACILITY AND METHODS	63	
3.1	Engine test rig.....	63
3.2	Fuel specifications	65
3.3	HC-SCR testing setup.....	67
3.4	Gas and particulate emission Analysers	69
3.4.1	Fourier Transform Infrared Spectroscopy (FTIR).....	69
3.4.2	Gas chromatography with a thermal conductivity detector (GC-TCD)	70
3.4.3	Scanning mobility particulate sizer (SMPS)	71
3.5	Soot characterization analyzers	72
3.5.1	Thermo-gravimetric analysis (TGA)	72
3.5.2	Scanning/Transmission electron microscope with energy dispersive x-ray spectroscopy	76
3.5.3	TEM and HRTEM analysis	77
3.5.3.1	Morphology analysis	78
3.5.3.2	Nanostructure analysis.....	81
3.5.4	Raman spectroscopy (RS)	85
CHAPTER 4.....	87	
FUEL-BORNE OXYGEN IMPACT ON PM STRUCTURE AND REACTIVITY IN MODERN DIESEL ENGINE	87	
4.1	Combustion performance and gas emission analysis	89
4.2	Particulate Matter tendency	94
4.3	Particulate characterisation.....	96
4.3.1	Soot oxidative reactivity.....	96
4.3.2	PM Elemental Composition	100
4.3.3	Soot morphology	104

4.3.4	Soot nanostructure	108
4.3.5	Soot graphitisation order	113
4.4	Summary.....	116
CHAPTER 5.....		118
MANIPULATING DIESEL EXHAUST COMPOSITION THROUGH GLYCOL ETHER FUELLING AND POST INJECTION STRATEGIES FOR EFFICIENT HC- SCR PERFORMANCE.....		118
5.1	Post injection optimisation	120
5.1.1	Post injection impact on combustion performance and gaseous emissions	121
5.1.2	Post injection impact on PM emissions and morphology	131
5.2	HC-SCR de-NOx efficiency	135
5.2.1	2 bar IMEP testing.....	135
5.2.1.1	No-post mode	138
5.2.1.2	PFI mode	139
5.2.2	4 bar IMEP testing.....	141
5.2.2.1	No-post mode	144
5.2.2.2	PFI mode	144
5.3	Catalyst sulphur tolerance	148
5.4	Hydrocarbon activation in the HC-SCR.....	149
5.5	Summary.....	152
CHAPTER 6.....		155
CATALYTICAL BREAKDOWN OF THE EXHAUST SOOT PARTICULATES BY THE USE OF SILVER BASED HC-SCR CATALYST		155
6.1	Catalyst filtration efficiency	158
6.2	Catalyst impact on morphology at 2 bar IMEP	160
6.3	Catalyst impact on morphology at 4 bar IMEP	164
6.4	Catalyst impact on nanostructure	168
6.5	Summary.....	171
CHAPTER 7.....		174

CONCLUSIONS.....	174
7.1 Concluding Remarks	174
7.2 Future Work.....	178
REFERENCES	179

List of Tables

Table 3.1: Engine specification	63
Table 3.2: warm-up engine parameters and the optimal condition to start the experimental test	64
Table 3.3: Fuel physical properties of ULSD, TPGME, DPGME, TP20 and DP20.....	66
Table 3.4: FTIR lowest detection limit for the different gaseous species	69
Table 3.5: TGA heating program steps	74
Table 4.1: Correlation of the nanostructure with soot oxidative potential (theory versus tested results)	113
Table 6.1: Testing parameters for the HC-SCR impact on the particulates	157

List of Figures

Figure 1.1: Market share in light duty vehicle market	1
Figure 2.1: Required fossil oil displacement in EU road transport to meet the GHG emissions	9
Figure 2.2: Biodiesel production, glycerol production and glycerol price forecast to 2020	10
Figure 2.3: Manufacturing process of propylene glycol methyl ethers originated from bio-glycerol	12
Figure 2.4: Schematic of a diesel soot particulate magnified by TEM to 0.2 μm scale showing the different morphological parameters.....	21
Figure 2.5: Schematic representation of (a) The primary particulate nanostructure (binary picture), (b) Carbon atoms in the basal and edge plane of a platelet, (c) Crystallite arrangement and (d) Tortuous layer configuration.....	22
Figure 2.6: DPF filtration mechanism	24
Figure 2.7: Soot carbon, ash and oxygen content relationship with the assigned oxidative reactivity	33
Figure 2.8: Biodiesel soot nanostructure alteration during the oxidation process	35
Figure 2.9: Morphological transformation of silver particulates in presence of H ₂ and oxygen reduction into reactive species.....	41
Figure 2.10: The mechanism by which the reactive oxygen species reduce the NOx emissions	42
Figure 2.11: Soot-cake representation with regards to its Peclet number	50
Figure 2.12: Sampling collection positions for reference (Lee & Zhu, 2004, 2005)	54

Figure 2.13: HRR produced from a common-rail engine operating with a pilot, main, close coupled and late post fuel injection strategy	56
Figure 2.14: Expected soot level from different post injection strategies. The horizontal line present the equivalent soot FSN at no post condition	57
Figure 3.1: HC-SCR catalyst used in this thesis.....	67
Figure 3.2: HC-SCR testing setup	68
Figure 3.3: (a) GC-H ₂ chromatogram of the calibration bottle and (b) Chromatogram of the sampled gas along with the method of calculation for the H ₂ volumetric concentration	71
Figure 3.4: TGA used in the research work	72
Figure 3.5: Representation for the E _a calculation method.....	75
Figure 3.6: Representation for the soot ignition temperature calculation method	76
Figure 3.7: EDS micrograph showing the compositional element of the agglomerate	77
Figure 3.8: (a) Micrograph of an agglomerate, (b) Post processed micrograph: background removal and primary particulates fit by circular approximation using ImageJ, (c) Results.....	78
Figure 3.9: Calculation for the particulate fractal dimension	80
Figure 3.10: Image enhancement and post-processing methods implemented in the MATLAB coding	82
Figure 3.11: Calculation of L _a and T _f : (a) Carbon layer schematic in the continuous field, and (b) Binarized layer in the digitized field.....	84
Figure 3.12: Calculation of d002: (a) Carbon layer schematic in the continuous field, and (b) Binarized layer in the digitized field	85
Figure 3.13: Example of a corrected and de-convoluted Raman spectra with the corresponding de-convoluted peaks	86
Figure 4.1: Schematic representation of the filter holder setup and location	88

Figure 4.2: BSFC and BTE resulted from the combustion of diesel, DP20 and TP20	89
Figure 4.3: In-cylinder pressure and HRR resulted from the combustion of diesel, DP20 and TP20	91
Figure 4.4: Gaseous emissions and exhaust temperature resulted from the combustion of diesel, DP20 and TP20.....	92
Figure 4.5: GMD, TPNC and d_{smps} distribution for the particulates produced from the combustion of diesel, DP20 and TP20	95
Figure 4.6: The corresponding structure of (a) DPGME, and (b) TPGME.....	95
Figure 4.7: PM chemical distribution, elemental carbon and volatiles fraction.....	97
Figure 4.8: Soot weight loss and the corresponding rate of weight loss	98
Figure 4.9: (a) Soot activation energy calculated following the Arrhenius-type model and (b) Correlation of volatile fraction with the soot activation energy	99
Figure 4.10: EDS analysis of the different tested samples	101
Figure 4.11: Correlation of the O/C ratio with the soot activation energy	103
Figure 4.12: TEM micrographs for soot particulates produced from Diesel, DP20 and TP20. Background was removed for better understanding of the morphology	105
Figure 4.13: R_g , n_{p0} and D_f of the different particulates resulted from diesel, DP20 and TP20 combustion	107
Figure 4.14: Primary particulate size distribution for the soot resulted from the combustion of the different fuel tested	107
Figure 4.15: Post processed HRTEM micrograph showing the nanostructure of S_{diesel} , S_{DP20} and S_{TP20}	108
Figure 4.16: Normal distribution of the carbon layer's length in the primary particulates of diesel, DP20 and TP20 samples	109

Figure 4.17: Normal distribution of the interlayer spacing of the primary particulates resulted from the combustion of diesel, DP20 and TP20.....	110
Figure 4.18: Normal distribution of the curvature of the carbon layers in the primary particulates resulted from the combustion of diesel, DP20 and TP20	111
Figure 4.19: Raman spectra resulted from the analysis of the S_{diesel} , S_{DP20} and S_{TP20}	114
Figure 4.20: Intensity and area ratios results from the RS analysis for S_{Diesel} , S_{DP20} and S_{TP20}	116
Figure 5.1: Schematic diagram presenting the main idea of the chapter and the related questions that this section is aiming to cover	119
Figure 5.2: Schematic presentation of the pilot, main and post fuel injection pulses	120
Figure 5.3: Impact of different PFI strategies on the combustion of diesel fuel under (a) 2 bar IMEP and (b) 4 bar IMEP	122
Figure 5.4: BSFC, BTE and exhaust temperature resulted from the different PFI strategies for diesel and TP20 under 2 bar IMEP and 4 bar IMEP conditions.....	123
Figure 5.5: NO, NO ₂ , NOx, THC and the resultant HC:NOx ratio for the 2 bar IMEP testing	125
Figure 5.6: NO, NO ₂ , NOx, THC and the resultant HC:NOx ratio for the 4 bar IMEP testing	126
Figure 5.7: CO and H ₂ emissions resulted from the post application.....	129
Figure 5.8: HC speciation for the different fuelling and operating conditions that will be tested with the HC-SCR.....	131
Figure 5.9: TPNC and GMD for the particulates produced from the combustion of diesel and TP20 under 2 bar IMEP and 4 bar IMEP with the most optimal PFI timings	132

Figure 5.10: R_g , n_{p0} , D_f , and d_{p0} for diesel and TP20 combustion at 4 bar IMEP with and without 80 CAD ATDC PFI	135
Figure 5.11: NO, NO ₂ , NOx and THC emissions before and after the HC-SCR with/without H ₂ introduction at low-load testing for diesel combustion	136
Figure 5.12: NO, NO ₂ , NOx and THC emissions before and after the HC-SCR with/without H ₂ introduction at low-load testing for TP20 combustion	137
Figure 5.13: NO, NO ₂ , NOx and THC emissions upstream and downstream the catalyst with and without H ₂ introduction at 4 bar IMEP for diesel combustion	142
Figure 5.14: NO, NO ₂ , NOx and THC emissions upstream and downstream the catalyst with and without H ₂ introduction at 4 bar IMEP for TP20 combustion	143
Figure 5.15: Diesel and TP20 distillation curves, reproduced from (B. L. Smith et al., 2008)	145
Figure 5.16: 2000 and 4000 ppm H ₂ effect on the different gaseous emissions throughout the catalyst	146
Figure 5.17: SO ₂ concentrations before and after the catalyst with and without introduction of 500 ppm H ₂	148
Figure 5.18: Light HCs and unburned fuel portion activity within the catalyst with/without 500 ppm H ₂ addition	150
Figure 5.19: Summary of the HC-SCR findings with the application of post fuel injections and TP20 fuelling	154
Figure 6.1: Schematic diagram presenting the chapter aims and the questions that will be covered in this research work	156
Figure 6.2: HC-SCR soot filtration efficiency at 2 bar IMEP for diesel combustion with and without the presence of 500 ppm H ₂	158

Figure 6.3: HC-SCR soot filtration efficiency at 4 bar IMEP for diesel combustion with and without the presence of 500 ppm H ₂	159
Figure 6.4: R _g , n _{p0} and D _f before and after the HC-SCR catalyst with/without H ₂ addition at 2 bar IMEP condition	160
Figure 6.5: Primary particulate size distribution (d _{p0}) before and after the HC-SCR catalyst at 2 bar IMEP (a) Diesel, (b) T20.....	161
Figure 6.6: TEM micrograph for diesel and TP20 soot particulates before catalyst, after catalyst without H ₂ addition and after cat with 500 ppm H ₂ addition.....	161
Figure 6.7: R _g , n _{p0} and D _f , before and after the HC-SCR catalyst with/without H ₂ addition at 4 bar IMEP condition.	164
Figure 6.8: Primary particulate size distribution (d _{p0}) before and after the HC-SCR catalyst at 4 bar IMEP	165
Figure 6.9: TEM micrograph for diesel and T20 particulates before catalyst, after cat without H ₂ addition and after the catalyst with 500 ppm H ₂ addition	165
Figure 6.10: Nanostructure parameters ratios including L _a , T _f and d ₀₀₂	169
Figure 6.11: Soot burn-off rate for 2 bar IMEP and 4 bar IMEP conditions.....	170
Figure 6.12: Summary of the chapter 6 findings	173

List of Abbreviations

A/F	Air to fuel ratio
Ag/Al ₂ O ₃	Silver supported on alumina
Al ₂ O ₃	Alumina
ATDC	After top dead centre
BSFC	Brake specific fuel consumption
BTE	Brake thermal efficiency
CAD	Crank angle degrees
CCPFI	Close coupled Post Fuel injection
CH ₃ COO ⁻	Acetate
CH ₃ OH	Methanol
CH ₄	Methane
CN	Cyanide
CO	Carbon oxide
CO ₂	Carbon dioxides
d ₀₀₂	Interlayer spacing
Df	Fractal dimension
DOC	Diesel oxidation catalyst
d _{p0}	Primary particulate size
DPF	Diesel Particulate Filter
DPGME	Di-propylene glycol methyl ethers
d _{smps}	Electrical mobility particulate diameter
Ea	Soot activation energy
EDS	Energy dispersive X-ray spectroscopy
FTIR	Fourier Transform Infrared Spectroscopy
FWHM	Full width at half maximum

GC-TCD	Gas Chromatography –Thermal Conductivity Detector
GHSV	Gas hourly space velocity
GMD	Agglomerates geometric mean diameter
H ₂	Hydrogen
HACA	Hydrogen - abstraction / acetylene-addition
HCs	Hydrocarbons
HC:NOx	Hydrocarbons to NOx ratio
HC-SCR	Hydrocarbon selective catalytic reduction
HRR	Heat release rate
HRTEM	High-Resolution Transmission Electron Microscopy
HVO	Hydro-treated Vegetable Oil
IMEP	Indicated mean effective pressure
IR	Infrared
La	Fringe length
Lc	Carbon layers' thickness
LPFI	Late Post Fuel injection
MMD	Mass mean diameter
MO	n-butanol/biodiesel surrogate
MO	Methyl-octanoate, C ₉ H ₁₈ O ₂
N ₂	Nitrogen
NH ₃	Ammonia
nm	Nanometres
NO	Nitrogen oxide
NO ₂	Nitrogen dioxides
NOx	Nitrogen oxides
n _{p0}	Number of primary particulates within the aggregate
O ₂	Oxygen

O_2^-	Superoxide ions
OH	Hydroxyl radical
PAH	Polycyclic aromatic hydrocarbon
Pe	Peclet number
PFI	Post Fuel injection
PGMEs	Propylene glycol methyl ethers
PM	Particulate matter
Rg	Gyration radius
rpm	Revolution per minute
RS	Raman Spectroscopy
S_{diesel}	Soot resulted from diesel combustion
S_{DP20}	Soot resulted from DP20 combustion
SEM	Scanning Electron Microscopy
SMPS	Scanning mobility particulate sizer
SO_2	Sulphur dioxide
SOF	Soluble organic fraction
SSA	Specific surface area
S_{TP20}	Soot resulted from TP20 combustion
T_f	Fringe tortuosity
TGA	Thermo-Gravimetric Analyser
TPGME	Tri-propylene glycol methyl ethers
TPNC	Total particulate number concentration
ULSD	Ultra-low sulphur diesel fuel
VOF	Volatile organic fraction
XRD	X-ray diffraction

CHAPTER 1

INTRODUCTION

1.1 Overview

Given the good fuel economy, lower CO₂ emissions and higher efficiency of the diesel engines, light duty diesel market has been sharply increasing during the last decade, reaching around 50% of the total shares (The society of motor manufacturers and traders, 2018).

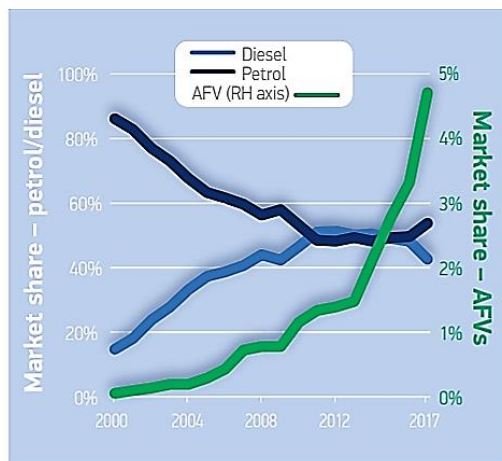


Figure 1.1: Market share in light duty vehicle market, reproduced from (The society of motor manufacturers and traders, 2018)

However, due to the nature of the diesel combustion process, the injected fuel has no sufficient period to homogeneously mix with air (fuel rich regions), and as a result, particulate matters (PMs) emissions are formed (Frenklach, 2002). Diesel exhaust particulates from modern engines are primarily fine particulates (PM_{2.5}); including a considerable component of ultrafine particulates (PM_{0.1}). PM_{2.5} penetrate deep into the lung and PM_{0.1} have been shown to cross from the airways into the blood, causing severe health effects such as asthma and

pulmonary inflations. In 2012, the International Agency for Research on Cancer classified diesel engine exhaust as “carcinogenic to humans” (The society of motor manufacturers and traders, 2018). In addition, due to the absence of throttling, fuel combustion occurs under lean burn condition, and as a result high level of Nitrogen Oxides (NOx) are emitted (Bosch, 2005). On the other hand, the increased thermal efficiency and expansion ratio lead to relatively low exhaust temperatures, which increases the challenges presented in the functionality of the aftertreatment catalysts, especially in reducing NOx (Herreros et al., 2014).

Consequently, the diesel shares in the light duty vehicle market starts to drop in the last few years and more stringent regulations have been imposed to limit these harmful emissions. The current Euro VI emission standard for diesel passenger cars limits the PM emissions to 0.005 g/km and 6.0×10^{11} particulates/km while NOx is forced to be reduced to 0.08 g/km instead of 0.18 g/km, as used to be with the Euro V standard (DieselNet, 2018).

To meet the latest legislations, vehicle manufacturers decided to introduce exhaust after-treatment units to purify the different types of unregulated emissions. During the last decade, diesel particulate filters (DPFs) has become the common technique used to trap the PMs. The imprisoned particulates should be oxidised as part of the regular DPF regeneration process to maintain its optimal functionality (CTS Corporation, 2019). The oxidative reactivity (i.e. ability to combust) of the soot, the solid part of the PM, directly depends on the environment under which it is incepted and the pathway undergone before being filtered (i.e. effect of after-treatment units) (Liati et al., 2013). There is a need to understand the correlation between fuel properties and aftertreatment units on the chemical and physical structure of the soot as well as its oxidative reactivity. Such kind of knowledge will allow more efficient DPF regenerations

and thereby prolong the filter lifetime span, avoid any unwanted backpressures in the exhaust, and most importantly, lower the fuel penalties associated with this strategy.

Concerning the NOx purification, selective catalytic reduction (SCR) by urea is considered as the most efficient deNOx technique used in lean environments and is currently available in the market. However, several limitations are still presented to this technology, mainly urea slip and catalyst poisoning by ammonium sulphates at low exhaust temperatures (Trichard, 2007). Therefore, a simpler alternative, which could potentially provide a comparable efficiency to the latter technology is the hydrocarbon-SCR (HC-SCR), and as such has been extensively studied for NOx abatement (Bethke & Kung, 1997; Houel et al., 2007a; K. I. Shimizu & Satsuma, 2006). The knowledge and the applicability of this catalyst in conjunction with new fuel generations (mainly oxygenated hydrocarbons) and modern diesel engines is still not mature enough. Further real-life testing is needed to evaluate this technology and ease its introduction to the market.

1.2 Research objective and focus

The use of new generation fuels, engine optimisation and after-treatment devices are currently the sole approach to control and regulate the diesel exhaust emissions. This thesis work can be divided into three main areas:

- (a) Glycol ether impact on the soot characteristics and oxidative reactivity
- (b) Manipulating exhaust gas composition through glycol ether fuelling and post injection strategies for efficient SCR performance
- (c) Soot destruction in the lean NOx SCR channels

Glycol ether impact on the soot characteristics and oxidative reactivity

It is commonly accepted that fuel-borne oxygen can effectively reduce the PM emissions and strongly modify their physical and chemical properties, and hence the oxidative reactivity (Barrientos, 2014; Bhardwaj et al., 2014; Boehman et al., 2005; Ess et al., 2016; Lapuerta et al., 2012; Liati et al., 2012; Man et al., 2015; Rodríguez-Fernández et al., 2016; Salamanca et al., 2012; Savic et al., 2016; A. Strzelec et al., 2010; R. L. Vander Wal & Mueller, 2006). The knowledge of the soot structure and oxidative behaviour is the key factor in designing effective DPF and exhaust aftertreatment technologies with low fuel penalties. Among the fuel-borne oxygen, Propylene Glycol Methyl Ethers (PGMEs) are characterised with a special molecular structure that can offer an effective reduction in soot emissions. However, their impact on the soot characteristics is not reported. The primary focus of the research in this part is to characterise the soot particulates from the combustion of Di and Tri-Propylene Glycol Methyl Ether (DPGME and TPGME, respectively)/diesel blends. Thermogravimetric Analysis (TGA), High-Resolution Transmission Electron Microscopy (HRTEM), Raman Spectroscopy (RS) and Energy Dispersive X-ray Spectroscopy (EDS) are used in the analysis of the soot physio-chemical properties.

These findings will help not only to assess the feasibility of these fuels but also to fill part of the gap presented in the literature regarding the impact of the initial soot characteristics on the resulting oxidative reactivity.

Manipulating exhaust gas composition through glycol ether fuelling and post injection strategies for efficient SCR performance

Hydrogen (H_2) assisted Ag/Al_2O_3 catalyst HC-SCR is considered as an effective deNOx catalyst which can provide similar NOx reduction to urea-based SCR under all engine operating

conditions. To date, most real-life testing was carried out using old engine technologies as a source for the exhaust gas, which is typically disadvantageous (i.e. high PM emissions) for its functionality. Therefore, high concentrations of H₂ were needed to compensate the negative impact of the particulates, which is not practical for vehicular applications, especially, if exhaust fuel reforming is used to supply the required H₂ (Houel et al., 2007b). However, modern engine systems and new generation fuels are extremely beneficial in terms of reducing the overall exhaust PM emissions, thus providing a new opportunity for the silver-based HC-SCR catalysts to operate more efficiently in real life applications. Furthermore, in modern common rail systems, the exhaust gas composition could be actively controlled and manipulated using in-cylinder fuel post injection strategies. Late post fuel injections could be a possible application to regulate the exhaust hydrocarbons to NOx ratio (HC:NOx) and composition (i.e. HC species, soot, H₂), however, extra fuel penalties remain a critical parameter to be evaluated. This application can simplify the complexity of the HC-SCR system since no additional fuel injector is needed to be installed in the exhaust and the reactive HC mixture is expected to be properly mixed once reaching the catalyst, which can also enhance the system performance compared to in-line injections.

Soot destruction in the lean NOx SCR channels

As for the soot destruction through the exhaust after-treatment system, all studies focus on the role of diesel oxidation catalyst (DOC) in modifying the soot characteristics, however, no study investigated the impact of the H₂-assisted HC-SCR on the soot particulates. It is proved that with the introduction of H₂, this catalyst can effectively oxidise the trapped soot aggregates at a low-temperature region (250 °C) seen in modern light duty diesel engines (Houel et al.,

2007b). Consequently, it is interesting to understand if any oxidation reactions are taking place on the soot passing throughout the catalyst beside to the oxidation of the trapped particulates.

1.3 Thesis outline

The thesis work presented here is divided into seven different chapters and a summary of their content follows below:

Chapter 2 – Literature Review

A brief review on the DPGME and TPGME combustion history and soot formation pathways is given. The soot structure and the current correlation between the different soot physio-chemical properties and the relative oxidative reactivity is detailed to spot the uncertainties presented till date. Description of the lean HC-SCR operation principles and the soot structural modification along the after-treatment system is also detailed with a small attention for the impact of in-cylinder post fuel injections on the exhaust emissions.

Chapter 3 – Experiment and Methods

A comprehensive description of the engine test rig, gas and PM analysers along with the catalyst specifications and testing methods is given in this part of the thesis.

Chapter 4 - Fuel-borne Oxygen Impact on PM Characteristics and Reactivity in Modern Diesel Engines

The effect of adding DPGME and TPGME oxygenates to diesel blend is studied in this chapter regarding their impact on the PM concentration, physio-chemical characteristics and oxidative reactivity. Special attention was addressed to identify the relation of each physical

and chemical parameter with the associated oxidative reactivity. The resultant gaseous emissions and combustion performance were also evaluated.

Chapter 5 - Manipulating Diesel Exhaust Composition Through Glycol Ether Fuelling and Post Injection Strategies for Efficient HC-SCR Performance

In this chapter, diesel and TPGME/diesel blend combustion studies were carried out. The research work can be divided into two main parts:

The first is to study the influence of the post injection strategies in terms of achieving the most optimal HC:NOx ratio in the exhaust without significantly deteriorating the fuel economy. Gaseous and PM emission analysis and soot characterisation (morphology) was also carried out.

The second part focuses on understanding the impact of the fuel type (using the most optimal injection strategies nominated in the first part) and H₂ concentrations on the HC-SCR activity under 2 bar IMEP and 4 bar IMEP (low and medium load respectively) engine running conditions for an efficient deNOx performance.

Chapter 6 - Catalytical Breakdown of the Exhaust Soot Particulates by the Use of Silver Based HC-SCR Catalyst

The soot/catalyst surface interactions were studied in this chapter with special attention given to the properties of the fuel used, operating catalyst temperature and the presence/absence of the H₂ in the flow. To carry the analysis, PM structure was evaluated on both macro (morphology) and micro-scale (nanostructure of primary particulates).

Chapter 7 - Conclusions

A summary of the core findings of the thesis are given with a series of recommendations for the future work that can be carried.

CHAPTER 2

LITERATURE REVIEW

2.1 Fuel Option

The international energy agency reported that by 2050 road travel is likely to be doubled compared to what it used to be in 2015, where passenger light-duty vehicles are expected to present the biggest growth in this sector (Dulac, 2012). The increased rate of CO₂ and other pollutants such as NOx and PM in the atmosphere are mainly triggered by the excessive use of fossil fuels (i.e. coal, gas and oil) in the different energy sectors, mainly in transportation (Curran et al., 2001; Kumar, 2007). To face the combustion-generated pollutants crisis, the European Union decided to follow the Paris Agreement and adopt a vision towards a 30% reduction in the greenhouse gas emissions resulting from the transport sector by 2030. To achieve this vision, two strategies have been proposed, a long-term plan consisting of the electrification of the transportation and an immediate action-plan aiming to increase the biofuel market share in liquid fuels (Figure 2.1).

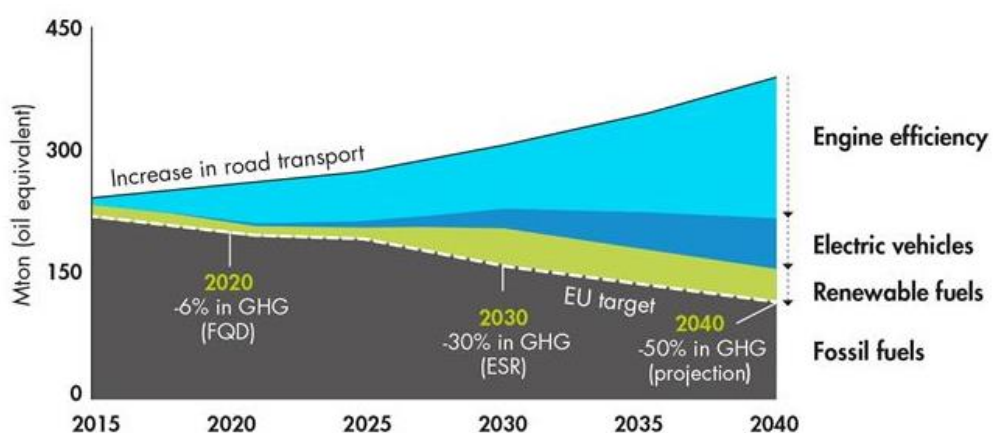


Figure 2.1: Required fossil oil displacement in EU road transport to meet the GHG emissions,
reproduced from (UPM Biofuels, 2019)

Biodiesel fuels consist of several long chain alkyl esters that hold similar physical and chemical properties as the diesel fuel (Ismail & Ali, 2016). They are usually manufactured from the transesterification of lipids (i.e. animal fat or vegetable oil) with short chain alcohols (i.e. ethanol or methanol) using a sodium (NaOH) or potassium hydroxide (KOH) based catalyst to chemically decompose the reactants into ethyl/methyl esters. It should also be noted that 16 to 18% of the lipids input yields glycerol as a by-product in a proportion of 10% from the esters produced (Santibáñez et al., 2011; Silva et al., 2009). Glycerol is also produced from the manufacturing process of bio-ethanol (Yazdani & Gonzalez, 2007). Therefore, with the increased demand on biofuels, the excess of glycerol volumes is likely to result in ecological hazards as it is contaminated and cannot be safely disposed in the environment (Silva et al., 2009). Given the high price of biofuels compared to fossil fuels, upgrading of glycerol by-products into added value products can achieve a secondary-income source and make the production of these new fuels generation economically sustainable in the long-term (Rodrigues et al., 2017).

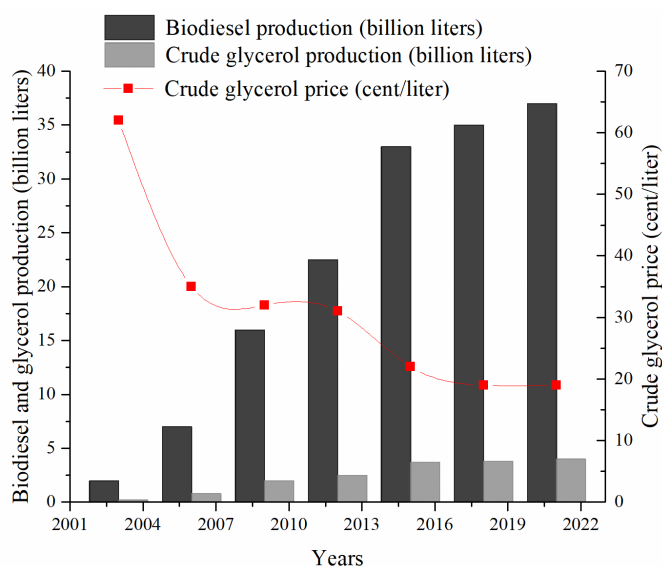


Figure 2.2: Biodiesel production, glycerol production and glycerol price forecast to 2020,
reproduced from (Nomanbhay et al., 2018)

Considering the reduction seen in the crude glycerol price (from 19-20 US cents/L in 2014 to 12-15 US cents/L in 2018-2020) based on the increased volume of biodiesel production, one applicable solution to benefit from these unwanted by-products could be to produce glycol ether from the resulting glycerol. Like biodiesel, glycol ether fuelling is also suitable for use in compression ignition (CI) engines with regards to price, safety, accessibility and miscibility with diesel fuel (Guo et al., 2016). In addition, glycol ethers' combustion is also considered more efficient in reducing particulate emissions compared to biodiesel fuelling (rapeseed methyl ester) when utilised in modern diesel engines (Zannis et al., 2004). Glycol ethers can be classified as Ethylene Glycol Methyl Ether (EGME, e-series) and Propylene Glycol Methyl Ethers (PGMEs; p-series) depending on whether they are derived from ethylene oxide or propylene oxide, respectively. PGMEs are generally considered as a safe substitute for EGMEs due to its negligible toxic level (Browning & Curry, 1994).

The PGME group includes three structurally related products known as, Propylene Glycol Methyl Ether ($C_4H_{10}O_2$; PGME), Di-PGME ($C_7H_{16}O_3$; DPGME) and Tri-PGME ($C_{10}H_{22}O_4$; TPGME). PGME's are manufactured in closed reactors having methanol (CH_3OH) and Propylene Oxide (C_3H_6O) as precursors (Burke et al., 2015; Gómez-Cuenca et al., 2013; Liang et al., 2011). As presented in Figure 2.3, the required propylene oxides can be easily derived from the unwanted bio-glycerol products using a 2-step reaction mechanism: (I) Glycerol is transformed to Propylene Glycol ($C_3H_8O_2$) through the traditional consecutive dehydration (- H_2O) hydrogenation (+ H_2) process. (II) The resulting propylene glycol are converted to propylene oxides using an alkali-loaded silica catalyst, a method that has been proposed and detailed by Yu et al. (2009).

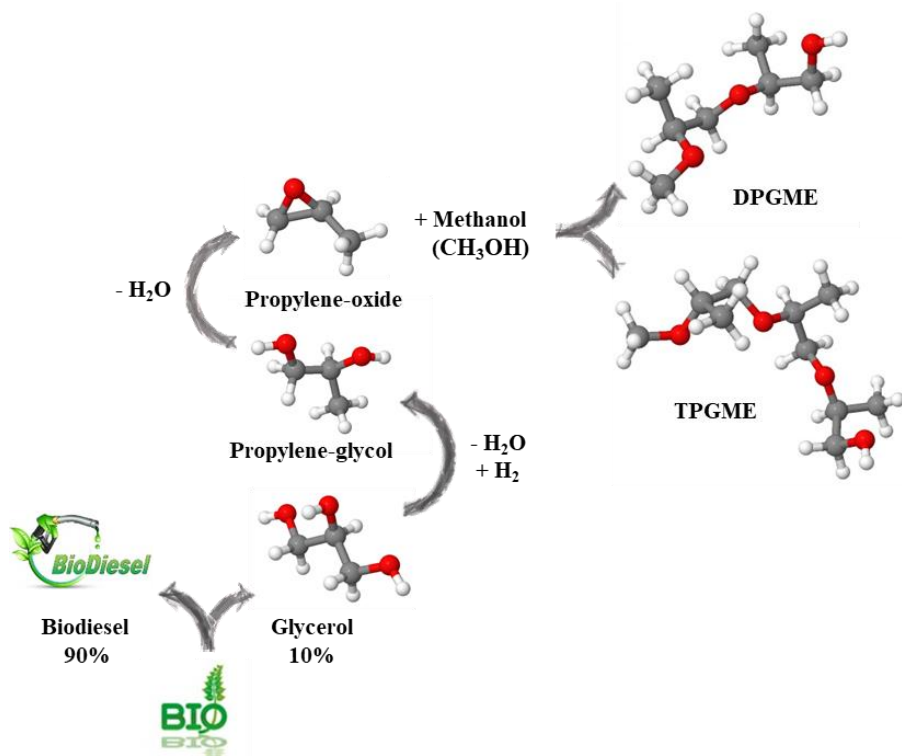


Figure 2.3: Manufacturing process of propylene glycol methyl ethers originated from bio-glycerol

Numerous studies in the literature proved the advantageous effect of PGMEs in reducing the engine-out PM emissions, particularly TPGME which was recognised for yielding near non-sooting combustion (Burke et al., 2015). The first study concerning these compounds started with Natarajan et al. (2001) who screened 71 potential oxygenates to test its suitability for blending with diesel in terms of exhaust emission reduction, mixture toxicity, lubricity and cetane number improvement. Following this experimental work, 8 candidates were selected for further testing including DPGME, TPGME and di-butyl maleate (DBM). Afterwards, Gonzalez et al. (2001) launched an experimental campaign to further investigate the selected nominees in ref. (Natarajan et al., 2001) and reported that TPGME and DBM offer the highest reduction in PM and in some of the gaseous emissions. Incorporating numerical simulations next to kinetic studies, Mueller et al. (2003) investigated the effect of both DBM and TPGME on the soot

formation process (high temperature model) and found that TPGME is more effective in reducing soot under all testing conditions. This was speculated to result from the highly branched structure of TPGME in which four evenly dispersed oxygen elements are comprised in a manner that three of the oxygen atoms are linked to two carbon atoms (ether group) and the fourth is linked to a single carbon atom (hydroxyl group). This effective configuration ensures that throughout the combustion process, the TPGME molecule is likely to be decomposed into carbon oxides (CO) instead of CO₂, hence eliminating the maximum portion of carbon elements from the pool of soot precursors (Burke et al., 2015). The soot formation process will be explained in the following section of the thesis. Burke et al. (2015) designed a chemical-kinetic model that includes both low and high-temperature reactions to simulate the ignition process of TPGME/diesel blend and illustrates its effectiveness in limiting the soot inception process. Dumitrescu et al. (2016) tested the impact of a TPGME/diesel blend (50% vol. blend, TP50) on the combustion behaviour (i.e. flame lift-off length and the corresponding ignition delay) and emissions level produced from a single-cylinder version of a heavy-duty diesel engine. It was concluded that with respect to diesel, TP50 can effectively limit the soot formation process (but not eliminate it) and/or increase the rate of soot oxidation throughout all the combustion stages (i.e. during the fuel injection process and onward in the cycle).

DPGME is also another candidate presenting a point of focus since it holds the same advantageous configuration as TPGME (Figure 2.3). However, no combustion model was designed for this candidate and the number of studies that have studied it was also limited. Gomez-Cuenca et al. (2013) studied several propylene glycol ethers and reported that blending DPGME with conventional diesel enhances the fuel cetane number and reduces the CO discharges; however, THC, NOx and PM did not show any significant variation. Hilden et al. (2001) reported that a mixture of 6.5 wt.% oxygen of DPGME/diesel and TPGME/diesel

displays a similar reduction in the PM emissions. However, other authors (González et al., 2001) reported that under the same oxygen content (7 wt.%), diesel blended with TPGME is significantly more capable in eliminating the PM emissions compared to DPGME/diesel blend.

2.2 PM Formation Pathway

Diesel smoke, so called PM, can be presented as a combination of carbonaceous material blended with several types of inorganic and organic substances, resulting in mutagenic and carcinogenic elements by nature (Silverman et al., 2012).

Soot inception is generally defined as a combination of different physical and chemical reactions that result in the transition of the fuel HCs from the vapour phase into a complex solid carbon structure (Dec, 1997, 1999; Frenklach & Wang, 1994; Haynes & Wagner, 1981; Omidvarborna, Kumar, & Kim, 2014; Shandilya & Kumar, 2013). This mechanism takes place within the fuel-rich regions presented in the diesel combustion process when enough temperature (1000-2800 K) and pressure conditions (50-100 Bars) are available (Dec, 1997, 1999; Frenklach & Wang, 1994; Haynes & Wagner, 1981; Omidvarborna, Kumar, & Kim, 2014; Shandilya & Kumar, 2013). The detailed mechanism by which the soot is produced is still under debate in the literature despite that a significant number of publications (Frenklach & Wang, 1994; Haynes & Wagner, 1981; Mansurov, 2005) have examined this process (Omidvarborna et al., 2015). However, there have been few agreements regarding that process and can be generally summarised by five different developments as it will be discussed in more detail in the following subsections.

2.2.1 Pyrolysis

In the absence of oxygen, the majority of the HCs involved in the combustion process thermally decompose (i.e. pyrolysis reactions) into various types of lighter HCs (C₄ group or lower), usually characterised with a lower molecular mass and saturation level compared to the parent fuel, such as methane (CH₄), acetylene (C₂H₂), ethylene (C₂H₄), propynyl (C₃H₃) and propene (C₃H₆) (Haynes & Wagner, 1981; Shah, 2011; O. I. Smith, 1981).

It is believed that the key step governing the soot inception process is the development of the first polycyclic aromatic hydrocarbon (PAH) ring, known as benzene (C₆H₆). The process by which this first ring is initiated is still under debate in the literature with several theories being proposed, as discussed in the work of Xi et al. (2006). However, till date, it is mostly accepted that the production of the first benzene/phenyl structure starts by the combination of two propynyl radicals (Miller & Kee, 1990; Miller & Melius, 1992; Xi & Zhong, 2006). Afterwards, the first ring grows into a more mature PAH structure via the addition of small chemical units, such as C₂ and C₃ groups, of which acetylene received the most attention (Glassman, 1989; Miller & Melius, 1992; Richter & Howard, 2000). This could possibly happen through (a) hydrogen - abstraction / acetylene-addition (HACA) mechanism: the first step of the reaction consists of abstracting hydrogen to activate the aromatic ring, then C₂H₂ is added to promote the development and cyclization of the rings into larger PAH structure (Richter & Howard, 2000; Xi & Zhong, 2006). (b) PAH-PAH radical combination, which occurs in the initial growth stages, where no sufficient level of C₂H₂ is presented to launch the HACA process (Xi & Zhong, 2006).

PAH with an average molecular mass of 500 to 1000 atomic mass unit (amu) is considered as the dominant soot precursor (i.e. building block for the soot formation) (Mansurov, 2005).

Furthermore, fuel pyrolysis is endothermic in nature, therefore the reaction kinetics are directly influenced by the in-cylinder thermal condition and the reactants level (O. I. Smith, 1981; Tree & Svensson, 2007). Besides, the precursors oxidation rate by hydroxyl radical (OH) is also temperature dependant, however, the rate of oxidation is considerably faster than that of the pyrolysis reactions (Tree & Svensson, 2007). As a result, most of the precursor species are not produced in the pre-mixed phase (oxygen is still not fully depleted from the reactions), but mostly inception in the mixing controlled burning process, where oxygen is already depleted from the fuel-rich zone where the pyrolysis reactions take place (Dec, 1997; Tree & Svensson, 2007).

2.2.2 Nucleation

During this phase, the first recognisable nascent soot particulates, so called “nuclei”, is produced into the chamber. It is commonly assumed that the aliphatic HC species, mainly acetylene, stick into the larger aromatic rings (i.e. radical addition) to result in larger PAH cluster that turns into a nuclei when large enough (Shah, 2011; H. Song, 2003; Tree & Svensson, 2007; Xi & Zhong, 2006). This process is likely to happen in a temperature level ranging between 1300-1600 K (Tree & Svensson, 2007). Bartok and Sarofim (1991) describe the nucleation products (i.e. nuclei) as small solid particulates shown in the luminous flame with a diameter ranging between 1.5 to 2 nm with an average molecular mass of 2000 amu (Haynes & Wagner, 1981). Furthermore, it is also suggested that the soot formation mechanism can even start with lower amu level of 300-700 (Frenklach, 2002). The soot inception paths are generally

influenced by the parent fuel-type along with the in-cylinder thermal environment. Otherwise stated, the development rate of the 1st and 2nd aromatic ring is the governing parameter dictating the final soot level. Thus, slower rates drop the precursor's concentration and as a result decreases the final soot mass. The later growth steps leading to soot nucleation are generally faster than that of the pyrolysis and independent of the fuel type (Tree & Svensson, 2007).

2.2.3 Mass growth

The reactive surface of the newly formed nascent particulates offers a proper constructive site for the gas-phase precursors (typically acetylene and PAH) to be adsorbed on, which significantly increases the soot mass, however, the nuclei's number remains the same. The fundamental process for the mass growth phase is not yet understood (Xi & Zhong, 2006). It is however suggested by Frenklach et al. (Frenklach & Wang, 1991; Frenklach & Warnatz, 1987) that the surface growth mechanism could be like the HACA mechanism described earlier for the PAH development reactions. Otherwise stated, it is predicted that the surface of the nuclei is identical to that of the PAH edge sites, surrounded by multiple C-H bonds. Abstracting the hydrogen atoms helps in activating the particulate's edge sites (generating radicals), which ease the bonding of the precursors onto the particulate's periphery and thus results in further development of the surface (Xi & Zhong, 2006). This mechanism yields in distinct growing spherules with distorted profile, usually seen as two distinct parts, an outer shell that includes a series of concentric carbon layers and an inner part (i.e. centre of the spherule) that presents a less ordered structure compared to the outer part (H. Song, 2003). Spatially, the mass evolution process remains beyond the primary sooting region, even if (a) the particulates moves into less reactive and cooler areas, (b) the HCs concentration is lower than that required for the soot

inception. Usually, soot nucleation and mass growth are considered as concurrent mechanisms.

The number of soot particulates is not affected during this process, only the soot mass increases.

2.2.4 Coalescence, agglomeration and carbonisation

Coalescence is favoured after soot formation directly, or in the case where particulates are still relatively small or young (Wagner, 1979). During nucleation/mass growth, particulate development occurs through the coalescence step (Xi & Zhong, 2006). Coalescence/coagulation occurs when the soot spherules merge together to form a single entity (i.e. primary particulates), causing a decrease in the overall particulate number without affecting their total mass. However, when the soot is mature enough, the different particulates start sticking together without coalescing (keep their original shape) to form larger group of particulates. This procedure is called agglomeration and the particulates resulted are reported to be arranged in a chain-like aggregate structure. So, the coagulation process is the fusion of small particulates together to produce one large molecule, while agglomeration is the collection of several particulates into each other. Simultaneously, carbonisation process also starts at this stage of the soot formation mechanism, resulting in a progressive change in the particulates structure from the initially distorted silhouette into more graphitic carbon material. Carbonisation mechanism was defined by Xi et al. (2006) as follows: “The polyaromatic material comprising the formed particulates undergoes functional group elimination, cyclization, ring condensation, and ring fusion accompanied by dehydrogenation and growth and alignment of polyaromatic layers”.

2.2.5 Oxidation

Oxidation mechanism can be simply described as the conversion of the soot carbon material (PAH and HCs) into CO and CO₂ products (i.e. combustion process). When soot is partially or fully oxidised, no more routes will be available for that carbon atom to participate in the soot formation, even in fuel-rich regions. This process is not limited to any specific level of the soot inception development, it may happen at any stage starting from the nucleation till the agglomeration. Glassman & Yetter (2008) reported that particulates oxidation happens when combustion temperatures are beyond 1300 K. Smith (1981) highlighted that the higher the soot graphitic order, the higher the needed in-cylinder temperatures to launch the oxidation reactions, and vice versa. This procedure can be divided into two stages, (a) absorption of the O₂ atom over the soot surface via chemical attachment (i.e. change its phase from gaseous reactant into a solid complex) and (b) the bonded O₂ and the involved carbon element are both desorbed from the soot surface as a combustion product (Glassman & Yetter, 2008; Marsh & Kuo, 1989). The main oxidizing elements are O, O₂, and OH. Bartok and Sarofim (1991) reported that in fuel-rich and stoichiometric environments, OH present the dominant oxidiser, while in lean environments, soot may be combusted by both O₂ and OH. It has been also seen that different compounds such as, CO₂, nitrogen oxides (NO), nitrogen dioxides (NO₂), nitrous oxides (N₂O) and water (H₂O) can also help in oxidising the soot particulates (Roth & Gersum, 1993; Stanmore B. R. et al., 2001). Wagner (1979) found that 10-20% of the total soot-OH collisions are effective in eliminating a carbon atom.

2.3 Soot Structural Configuration and Elemental Composition

Soot generally comprises carbon (C) as the main component and to a lesser extent some traces of hydrogen can be also detected, resulting in an overall density of $1.84 \pm 0.1 \text{ g/cm}^3$ (Choi et al., 1994). When the particulates are immature (during the initial stages of the soot inception process), hydrogen is considered one of the basic soot components (C/H ratio ~ 1). However, as the soot becomes more mature, the corresponding carbon portion increases while hydrogen's level drops (Omidvarborna et al., 2015). In addition, soot also contains a soluble organic fraction (SOF) that mainly originates from the fuel aromatic compounds and the different unburnt hydrocarbon species of the fuel (Daido et al., 2000; Tree & Svensson, 2007). Both oxygen, as strongly bonded oxygen functionalities, and sulphur, in the form of sulphates, can be found on the soot surface. Moreover, different types of metals such as zinc (Zn), iron (Fe), silicon (Si), calcium (Ca), chromium (Cr) and phosphorus (P) can be detected in the soot elemental composition (Omidvarborna, Kumar, & Kim, 2014; Omidvarborna, Kumar, & Kumar, 2014; Shandilya & Kumar, 2013; Xi & Zhong, 2006). These types of metals are generally referred to as the “ash” portion in the aggregate and mainly result from the engine wear, lubrication oil and the various inorganic compounds of the fuel (Mühlbauer et al., 2016). The combination of the soot particulates (the solid part) with SOF and ash is so called PM. Following the findings of Roessler et al. (1981), a representative diesel PM holds on weight basis 70% C, 20% O₂, 3% Sulphur (S), 1.5% H₂, <1% N₂, <1% trace metal.

Soot profile can be generally described as a fractal aggregate with an average size of 80-300 nanometres (nm). Each aggregate can include up to 4000 carbonized spherules, so called “primary soot particulates” (Wagner, 1979). In a typical diesel engine, the sum of primary particulates grouped in a single aggregate falls in the range of 22 to 100 (H. Song, 2003). This

number is influenced by the total in-cylinder air to fuel (A/F) ratio: the leaner the combustion, the lesser the agglomeration (Roessler et al., 1981; H. Song, 2003). The diameter of the spherules varies from 10 to 80 nm however, in normal diesel operation, the typical diameter range is 15 to 50 nm (Walker et al., 1966).

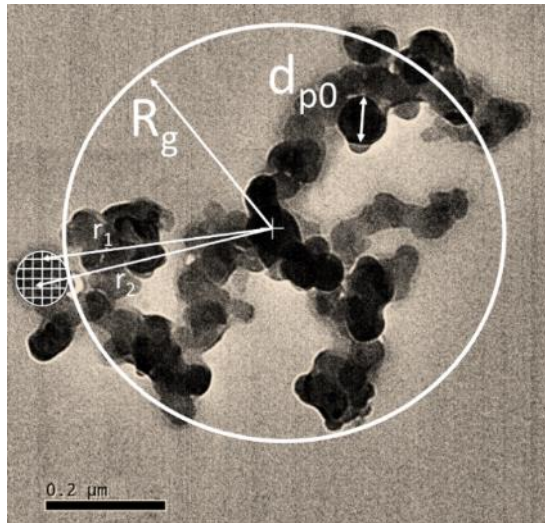


Figure 2.4: Schematic of a diesel soot particulate magnified by TEM to 0.2 μm scale showing the different morphological parameters

When it comes to the morphological analysis (i.e. assessing the agglomerate geometry), all the different variables discussed above should be analysed. Technically speaking, the fractal dimension (D_f), gyration radius (R_g), number of primary particulates within the aggregate (n_{p0}) and primary particulate size (d_{p0}) should be evaluated (Figure 2.4). D_f demonstrates what growth mechanism governs the production of the aggregate particulates through the combustion course (Meakin P, 1989). Larger magnitudes imply that the particulates are more likely to be spherical in shape and smaller magnitudes indicate a stretched chainlike structure (Meakin P, 1989). R_g is a representative of the average length that links the centroid of the aggregate with the centre of each spherule (D. Lee et al., 2013), highlighting the average size of the whole

aggregate. As for n_{p0} , as its name shows, this parameter is an indication of the number of spherules comprised in an aggregate. d_{p0} is the average size of these spherules. Further details regarding the method used to analyse the morphology parameters can be found in Section 3.5.3.1.

Apart from the morphology, it is also important to understand the nanoscale ordering of the primary particulates (nanostructure) as the soot formation process and the corresponding oxidative reactivity is partly reflected in the nanostructure (detailed information is presented later in Section 2.4.3)

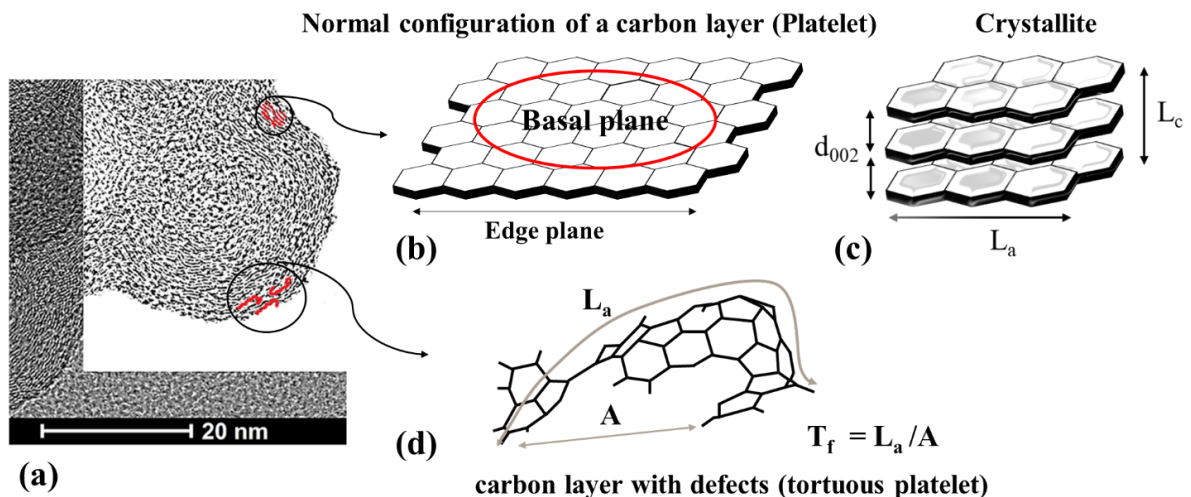


Figure 2.5: Schematic representation of (a) The primary particulate nanostructure (binary picture), (b) Carbon atoms in the basal and edge plane of a platelet, (c) Crystallite arrangement and (d) Tortuous layer configuration, reproduced from (Gaddam et al., 2016)

Each primary particulate includes around 10^5 - 10^6 carbon atoms in its structure (Walker et al., 1966). These atoms are chemically bonded with each other following a hexagonal fashion arrangement, usually referred to as “platelet” or “graphene layer” (Figure 2.5) (Glassman & Yetter, 2008). In general, the carbon atoms in each of these layers are positioned within a two-

dimensional plane, known as “basal plane” and “edge plane” (Figure 2.5). Typically, these platelets are placed parallel to each other and usually stack in a group of 2 to 5 (Xi & Zhong, 2006). This configuration is generally known as a “crystallite”. The interlayer spacing separating the graphene layers in the diesel soot, usually defined by d_{002} , is slightly larger than that of the graphite (0.335 nm) and falls in the range of 0.35-0.36 nm (Glassman & Yetter, 2008). Diesel spherules usually hold around 10^3 crystallites that have an approximate thickness (L_c) of 12 nm each (Xi & Zhong, 2006). These crystallites form the outer shell of the primary particulate and they are usually arranged parallel to each other and surround the particulate’s centre (Amann & Siegla, 1982). The inner core of the spherule ranges from 18 to 30 nm and incorporates several fine particulates characterised with an amorphous assembly. This configuration reveals that the central part is structurally and chemically less stable than the outer shell (Amann & Siegla, 1982). In addition to d_{002} and L_c , two different parameters should be also examined in the nanostructure analysis: the crystallite basal plane length, also known as “the fringe length” (L_a) (Gaddam et al., 2016; Yehliu et al., 2012), and the curvature of the carbon layer, also known as “the fringe tortuosity” (T_f) (Al-Qurashi & Boehman, 2008; Gaddam et al., 2016; Randy L. Vander Wal & Tomasek, 2004).

2.4 Correlation between soot physio-chemical properties and the corresponding oxidative reactivity

DPF is the common technique used in the market to trap the resulted PM from the exhaust. The most common filters are the cellular ceramic (Silicon carbide and cordierite) wall-flow monoliths with channels that are plugged at alternating ends (Figure 2.6). The plugged end forces the exhaust gases to flow through the porous walls of the filter. During this mechanism, the exhaust gases can pass through the channel’s wall, however, the solid particulates will be

trapped within the filter pores (deep bed filtration) or in the surface of the filter (i.e. formation of a soot cake layer), as shown in Figure 2.6 (CTS Corporation, 2019).

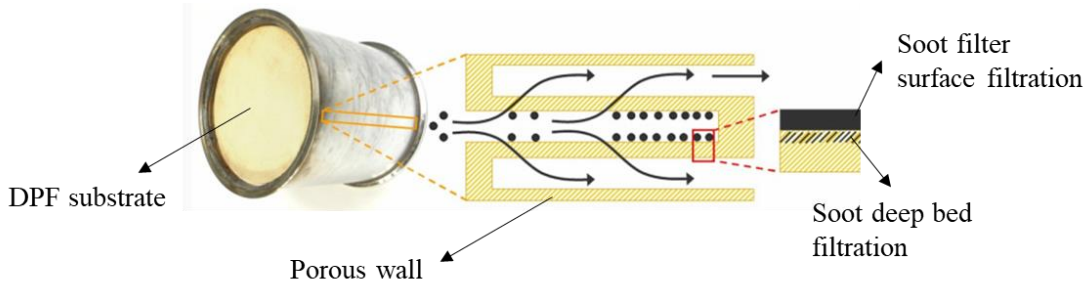


Figure 2.6: DPF filtration mechanism, reproduced from (CTS Corporation, 2019)

The trapped particulates should be oxidised regularly (the process is known as DPF regeneration) to avoid any unwanted backpressures in the exhaust which in turn can deteriorate the engine's thermal efficiency and increase the fuel consumption (2-3% fuel penalty) (CTS Corporation, 2019). Regeneration methods can be achieved following two different processes: passive or active regeneration. In the passive version, the particulates are regularly oxidised with NO₂ when the exhaust temperature varies from 200 to 450 °C. The needed NO₂ is usually delivered to the DPF by the help of the DOC which converts the engine-out NO into NO₂. However, in case the filter backpressure is above the normal range and the available NO₂ and exhaust temperature are not enough (i.e. urban and extra urban cycles), the regeneration is accomplished through the active method. With this technique, the oxygen presented in the exhaust is used to regenerate the filter however, exhaust temperatures of 550 °C or higher are required. To achieve that, fuel is injected in the exhaust pipe to be oxidised through the DOC (exothermic process) with a view to achieve the required temperature ($\Rightarrow 550$ °C) level to launch the PM oxidation reactions.

Soot oxidative reactivity is generally known as the ability of the PM to combust in an oxidising environment (i.e. usually air) (Al-Qurashi et al., 2011). In simple terms, it defines the needed time and temperature to fully oxidise a known mass of PM. This property is usually tested using a TGA that can function via two different programs, either isothermal or ramp-up. Further details will be provided in the Experiment and Method chapter (Section 3.5.1). The knowledge of the soot oxidation behaviour is the key factor in optimising the DPF design and the regeneration cycles.

It is widely accepted that different engine technologies, operating modes and fuel types result in particulates that strongly differ in their physical and chemical properties (Burtscher, 2005; Matti, 2007). This usually includes a variation in the particulate's elemental composition, morphology and carbon layer arrangement (i.e. nanostructure of the primary particulate). Several theories and assumptions have been proposed in the literature to correlate these physio-chemical parameters to the assigned particulate's reactivity (Mühlbauer et al., 2016); however, the relationship is still quite complex and no clear agreement showing the sensitivity of each property is reported till date (Leidenberger et al., 2012; Liati et al., 2013; Mühlbauer et al., 2016). Furthermore, fuel-borne oxygen such as alcohol, ether, ester, carbonate and acetate compounds blended with diesel can effectively enhance the PM oxidative reactivity (McCormick et al., 1997; Nord & Haupt, 2005; Raj, 2010; Ren et al., 2008; Sukjit et al., 2013; J. Wang et al., 2009; Zhang & Balasubramanian, 2014). However, as it will be explained in the literature (Section 2.4.4), this is not always the case and sometimes particulates with lower oxidative potential are resulted from the oxy-diesel combustion compared to neat diesel. To critically analyse the literature and further understand the influence of the fuel type and the different soot physio-chemical properties on the associated reactivity, the most reliable research

work achieved till date has been summarised in the sections below to highlight the different uncertainties that are still not clarified.

2.4.1 Soot Oxidative reactivity dependence upon morphology

Numerous researchers suggest that R_g and d_{p0} change according to the parent fuel type (Fayad et al., 2015; Fayad et al., 2017; Savic et al., 2016) and the engine operating conditions (Lapuerta et al., 2007; Leidenberger et al., 2012; Xua et al., 2014). Hence, many authors base their analysis on these physical parameters (R_g and d_{p0}) to explain the difference in the particulate's reactivity. Lapuerta et al. (2012) and Rodríguez-Fernandez et al. (2017) spotted a noticeable reduction in R_g and d_{p0} along with a significant improvement in the PM reactivity when operating the engine with synthetic fuel (Gas to Liquid – GTL), biodiesel blends (such as Hydro-treated Vegetable Oil (HVO) and conventional biodiesel originated from animal fat methyl ester). It was suggested that due to the reduction in d_{p0} or R_g , a larger specific surface area (SSA) was available for the oxidisers (i.e. O_2 , etc.) to react with, thus easing and enhancing the oxidation process. Both authors calculated the SSA assuming that the particulate shape is spherical. Rodríguez-Fernandez et al. (2017) also assumed that a higher level of D_f (i.e. more chain-like structure) can also increase the SSA, however did not took into account this parameter in the final analysis. On the contrary, other researchers reported that increasing the biodiesel portion in diesel fuel results in larger PM (Lin et al., 2008; Ye et al., 2014). However, the soot oxidation activity was better than that produced from the conventional diesel fuel (Ye et al., 2014). Lu et al. (2012) highlights that along the particulate's size range, various rates of oxidation can be presented. Leidenberger et al. (2012) reported that by increasing the fuel injection pressure, smaller PM size is produced and as a result better oxidative reactivity is achieved compared to lower injection pressures. In another study, Ye et al. (2014) reported that

as the fuel pressure increases, the soot reactivity increases accordingly yet, the size of the primary particulate remains constant, highlighting a negative correlation with the reactivity recorded.

Overall, primary particulate size and aggregate radius cannot solely predict the differences presented in the particulate's reactivity. Other factors, including the nanostructure of the primary particulates along with the aggregate elemental composition should be also examined for a better understanding.

2.4.2 Soot Oxidative reactivity dependence upon elemental composition

In addition to morphology, soot elemental composition, mainly the surface functional group, has been also recognised as a vital parameter governing the soot oxidation mechanism. Morjan et al. (2004) suggested that the presence of oxygen molecules in the reactive mixture can significantly alter the final soot structure. The electron affinity of this moiety can increase the surface chemical activity and therefore alter the soot physical configuration in a way that more curved layers are obtained. Furthermore, the chemisorbed oxygen can be easily bonded to the carbon edge sites due to the presence of unpaired sp^2 electrons. As a result, the reactivity of the edge plane is increased, thus enhancing the reactivity of the whole particulate (Barrientos, 2014; Radovic et al., 1983). Muller et al. (2006) reported that oxygenated functional groups including C-O-C, C-OH and C=O are likely to be very reactive agents that facilitate the soot oxidation. Smith and Chughtai (1995) found that the soot reactivity is influenced by the concentration of oxygen and hydrogen radicals linked to the non 6-membraned PAH rings in the soot surface. They reported that an increase in these elements will reduce the energy required to launch the soot oxidation process, in other words, the energy required to desorb the oxygen functionality from the surface as a combustion product (i.e. CO, CO₂) will be reduced.

Several other publications (Bueno-Lopez et al., 2005; Mendiara et al., 2007; Setiabudi et al., 2004; X. Wang et al., 2012) also studied the impact of the surface oxygen functional groups and depicted that these species significantly enhance the soot oxidation process.

Wang et al. (2013) examined the variation of the soot surface functional groups (i.e. aliphatic and oxygenated compounds) along with the corresponding oxidative reactivity throughout all the combustion stages, including premixed, diffusion, late combustion phase and the resulted exhaust soot. It was concluded that the soot apparent activation energy presents a positive linear relationship with the concentration of the aliphatic functional groups condensed on the particulate's surface however, the oxygen functional groups did not present any clear correlation. Soot reactivity has been also reported in several studies (Ahlstrom & Odenbrand, 1989; Kandas et al., 2005; Stanmore B. R. et al., 2001) to be influenced by the amount of volatile organic fraction (VOF) condensed onto the surface of the aggregates. It was seen that during the oxidation process, the adsorbed VOF devolatilises and as a result new micro-pores opening are generated onto the soot surface. These new available sites increase the inner soot surface area where the oxygen can diffuse and react, thus increasing the kinetics of the oxidation mechanism.

On the other hand, the inorganic elements (ash), especially the metal species, show to have a catalytic impact that can significantly enhance the particulate's oxidative reactivity (Hansen et al., 2013; Johnson, 2015; Jung et al., 2003; Liati et al., 2012). Hansen et al. (2013) studied the oxidative reactivity of different soot samples with and without the presence of different inorganic species that simulate the various ash components comprised in biodiesel fuel and engine oil. The author depicts that biodiesel ash components, such as sodium carbonate (Na_2CO_3), potassium carbonate (K_2CO_3) and tri-potassium phosphate (K_3PO_4) have a

positive impact on the oxidation reactions, while the oil-derived ash such as Calcium sulphate (CaSO_4) can negatively affect the soot oxidation kinetics (i.e. slower rates). In contrast, Jung et al. (2003) also studied the impact of the engine oil ash species (mainly Ca) and reported that metallic catalysed particulates (mainly Ca) present better oxidation rate compared to non-catalysed particulates.

In summary, the dependency of the oxygen functional group, aliphatic content, VOF and ash species on the soot oxidation reactivity is still not precisely clarified, with different approaches assessing what is the most critical parameter.

2.4.3 Soot Oxidative reactivity dependence upon nanostructure and the uncertainties presented

It is of importance to understand the reactivity of the carbon atoms upon their position within the graphene layer (basal and edge plane) to further understand the influence of the nanostructure parameters (d_{002} , L_a and T_f) towards the particulate's oxidation reactivity. To start with, the carbon atoms positioned in the edge sites hold a significantly higher reactivity (around 100-1000 times more reactive) compared to that located in the basal plane (Gogoi et al., 2015; Randy L. Vander Wal & Tomasek, 2003). This is mainly due to the presence of unpaired sp^2 electrons that allows the edge site atoms to easily bond with the upcoming oxygen molecules (Ma et al., 2014; Marsh & Kuo, 1989; Randy L. Vander Wal & Tomasek, 2003). However, this is not the case for the atoms placed within the basal plane as they can only share Π (pi) electrons forming chemical bonds (Ma et al., 2014; Marsh & Kuo, 1989; Randy L. Vander Wal & Tomasek, 2003). In addition, edge site atoms also present a greater accessibility for oxygen attack (Ma et al., 2014; Marsh & Kuo, 1989; Randy L. Vander Wal & Tomasek, 2003). In summary, the overall reactivity of the primary particulate, and as a subsequence of the whole

aggregate, can be predicted by evaluating the amount of carbon atoms situated in the basal plane with respect to these in the edge sites (Randy L. Vander Wal & Tomasek, 2003). This could be mainly concluded by analysing the crystallite basal plane length (i.e. L_a): shorter layers indicate the presence of higher amounts of carbon atoms in the edge sites and as a result better oxidative reactivity is expected (Ma et al., 2014; Marsh & Kuo, 1989; Andrea Strzelec et al., 2017; Randy L. Vander Wal & Tomasek, 2003). In addition, wavy layers (increasing T_f) usually indicate the existence of a non-6 membered ring (i.e. 5 and 7 membered rings) and/or indicate the presence of defects in the layer, as presented earlier in Figure 2.5 (Al-Qurashi & Boehman, 2008; Bogarra et al., 2017; Gaddam et al., 2016; Randy L. Vander Wal & Tomasek, 2004). This kind of structure is reported to reduce the electronic resonance stability of the C-C bonds positioned within the basal plane as their atomic orbitals (i.e. electron cloud) are overlapped. Consequently, the C-C bonds are weakened which in turn increases their reactivity and makes them more vulnerable towards oxidation (Andrea Strzelec et al., 2017; Randy L. Vander Wal & Tomasek, 2003). On the other hand, during the oxidation process, curvy layers can be more easily stripped out from the outer surface of the particulate compared to flat layers, hence improving the particulate's reactivity (Lapuerta et al., 2012). d_{002} is also considered as a critical parameter when evaluating the soot structure. Larger values of d_{002} indicate that the particulate ordering is less stable in a manner that eases the access of the oxygen moieties into the edge site position leading to more reactive particulates (R. L. Vander Wal & Mueller, 2006).

It is generally accepted that the combustion of oxygenated diesel blends results in more reactive soot particulates compared to conventional diesel fuelling (Barrientos, 2014; Bhardwaj et al., 2014; Boehman et al., 2005; Ess et al., 2016; Lapuerta et al., 2012; Liati et al., 2012; Man et al., 2015; Rodríguez-Fernández et al., 2016; Salamanca et al., 2012; Savic et al., 2016; A.

Strzelec et al., 2010; R. L. Vander Wal & Mueller, 2006). Numerous researchers (Barrientos, 2014; Man et al., 2015; Savic et al., 2016; R. L. Vander Wal & Mueller, 2006) proved that this ameliorated reactivity was mainly influenced by the initial arrangement of the graphene layers (soot nanostructure) which was seen to be structurally less ordered compared to that presented in a diesel soot particulate. The research work summarising this theory is presented below:

Vander Wal & Tomasek (2003) showed that the soot oxidative reactivity mainly depends on the initial carbon layer arrangement which in turn relies on the nature of the fuel combusted. Under similar testing conditions, they found that the particulates generated from benzene, acetylene and ethanol combustion present different oxidation rates mainly due to the difference shown in the nanoscale ordering of the primary particulates and not their size. In addition, it was also reported that the curvature of the carbon layers presents a more influential factor that dictates the particulate's oxidative reactivity when compared to the basal plane diameter. Yet, in another research work, Vander Wal & Tomasek (2004) highlighted that the oxidative reactivity and the nanostructure of the primary particulates is mainly determined by the synthesis conditions upon which the soot was incepted, such as temperature and residence time in the combustion chamber. It was found that at low temperature conditions (~ 1250 °C), the combustion yields amorphous particulates that comprise short and disconnected carbon layers (which is stacked in a non-uniform direction), regardless of the operating fuel type or the mixture flow rate. However, an increase in the combustion temperatures (~ 1650 °C) leads to particulates with different structural order according to the flow speed and the nature of the fuel incorporated. For example, indene, benzene and acetylene tend to produce highly ordered particulates (less reactive) at low flow rates (i.e. increasing the soot residence time), whereas soot with curved carbon layers (more reactive) are yielded at higher flows. As for ethanol,

irrespective of the flow rate, more reactive soot characterised with curved graphene layers was always emitted. In both studies, the authors confirmed the dependence of the soot reactivity upon its initial nanostructure ordering. Man et al. (2015) examined the effect of biodiesel fuel originated from waste cooking oil on the PM structure under different engine load and speed conditions. It was found that biodiesel fuelling results in more reactive PM mainly due to shorter L_a and higher T_f , while d_{002} did not show any conclusive trend. Vander Wal. et al. (2006) and Savic et al. (2016) also show that an increase in the oxygenate portion (i.e. biodiesel originated from various feedstocks and diethylene glycol diethyl ether) in diesel blends leads to particulates with greater oxidative reactivity mainly due to a more disordered structure (shorter and more curved layers with larger interlayer spacing) compared to the diesel reference.

Some other authors highlight that the portion of surface oxygen/aliphatic functional groups and ash components are sometimes more influential than the initial nanostructure in dictating the particulates reactivity. The research work summarising this theory is presented below:

Gogoi et al. (2015) analysed the impact of 2,5-dimethylfuran (DMF) diesel blends on the soot oxidative behaviour and reported that by increasing the oxygenate percentage (up to 15% by volume) the resulted soot becomes more prone to oxidation. In this research work, the increase of the DMF volume did not alter the interlayer spacing however, slight reduction was recorded along the fringe's length. The soot reactivity was more dependent on the PM chemical composition with higher level of oxygen and aliphatic surface functionalities detected when increasing the DMF volume. López Suárez et al. (2011) also checked the impact of biodiesel fuelling on the PM characteristics. The collected samples were analysed using TEM, Raman, DRIFTS and XRD. No significant structural variation was spotted between diesel and biodiesel

soot however, the TGA results confirmed that biodiesel tend to produce more reactive PM than diesel. This enhanced oxidative reactivity was linked to a higher portion of ash in the particulates, such as copper (Cu), Cr, Magnesium (Mg) and potassium (K), which serves as a catalytic active material in the soot. The same theory has been also asserted by Cordiner et al. (2013). Mühlbauer et al. (2016) tested the impact of a various range of boost and fuel injection pressures on the different soot properties using a modern common-rail diesel engine operating solely with diesel fuel. The experiments show a wide range of PM reactivity reaching around 162 °C difference between the different testing conditions. The analysis included a detailed inspection of the morphology, nanostructure and elemental composition of the PM to assess which parameter influences the soot oxidative behaviour the most when changing the engine settings. It was found that the primary particulate size and its corresponding nanostructure did not clearly correlate with the oxidation patterns. However, as shown in Figure 2.7, the soot composition, mainly the ash content, presented an adequate positive linear relation with the assigned soot reactivity.

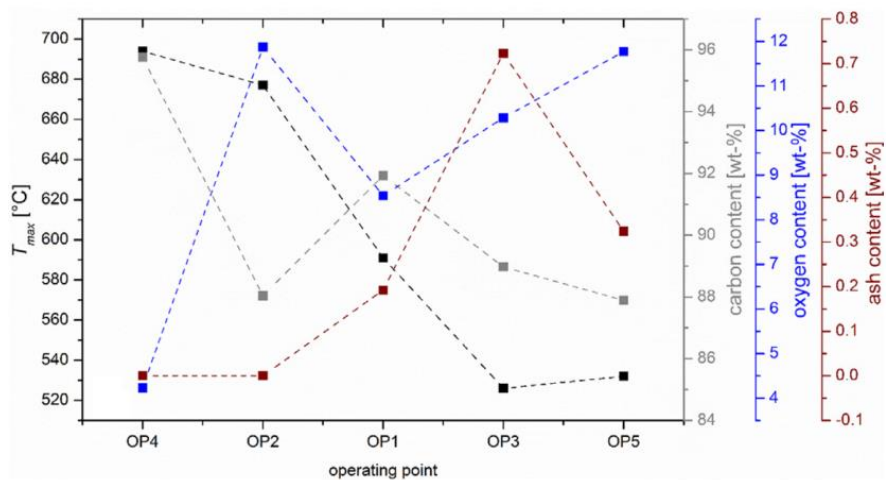


Figure 2.7: Soot carbon, ash and oxygen content relationship with the assigned oxidative reactivity, reproduced from (Mühlbauer et al., 2016)

Other research works (Lapuerta et al., 2012; J. Song et al., 2006; Soriano et al., 2017) also suggested that oxygenated fuel combustion can result in particulates with the same nanostructure ordering or even with more graphitic structure compared to diesel. However, despite that this structural configuration highlights that less reactive particulates should be produced, the obtained soot is still more reactive than that obtained from the diesel combustion. The research work summarising this theory is presented below:

Song et al. (2006) found that pure biodiesel (B100) combustion results in more graphitic particulates compared to diesel and FT combustion yet, it was still more reactive. It was reported that in case of B100, the increased portion of oxygen surface groups results in an unusual series of nanostructure alterations during the oxidation process (Figure 2.8), leading to better reactivity. Conventional soot oxidation (i.e. diesel and FT) is usually presented as a surface burning mechanism characterised with a slow burning rate. However, in case of B100, the soot is more likely to start its oxidation from the inside (i.e. internal burning) rather than the outside (i.e. surface burning). It was presumed that as soon as the oxidation starts, the devolatilization of the increased portion of oxygen functionalities condensed on the particulate's periphery helps in developing micro-pore openings that stretch inside the external shell and expose the internal core for oxidation. As a result, faster oxidation was reported at the early stages of the oxidation up to 75% burn off rate in case of B100 with respect to diesel and FT. However, the fast oxidation of the core releases a considerable amount of heat, which in turn helps to reorganise the remaining outer shell (thermal annealing mechanism) leading to slower burning rates at late stages of the burn off cycle (after 75%) (J. Song et al., 2006).

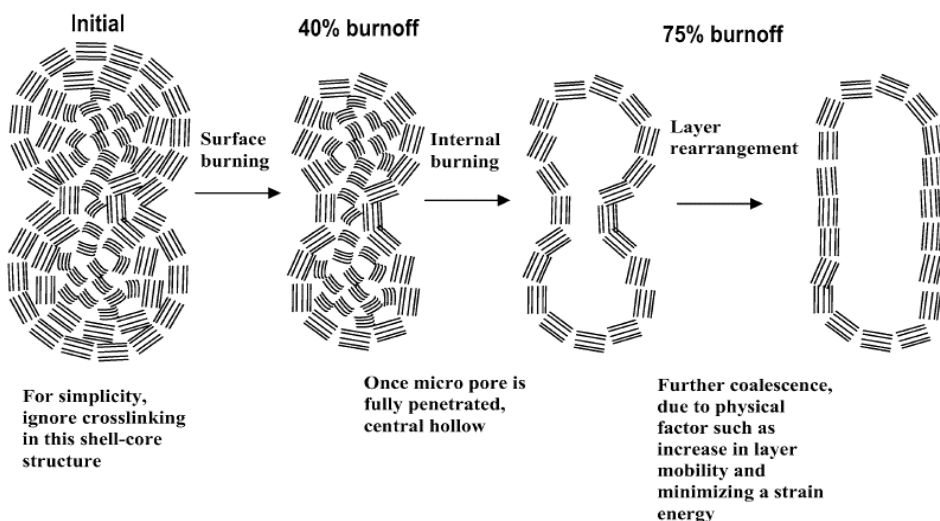


Figure 2.8: Biodiesel soot nanostructure alteration during the oxidation process, reproduced from (J. Song et al., 2006)

Soriano et al. (2017) reported that no clear structural differences supported by HRTEM, RS and XRD analysis were recorded between the different soot samples collected from the combustion of diesel, biodiesel, fossil paraffinic (GTL) and renewable paraffinic (Farnasane) fuels. Same reactivity was spotted between diesel and Farnasane samples however, biodiesel and GTL soot seemed to be more active towards oxidation (reactivity of biodiesel > GTL > diesel = Farnasane). Since no structural variation was detected, the author decided to investigate the soot surface functional group to understand if any positive correlation could be assorbed with the particulate's reactivity. Biodiesel soot presented the highest absorbance of oxygenated functionalities and aliphatic groups among all the tested samples and therefore it was the most reactive. Furthermore, despite that both Farnasane and GTL fuel share similar physical and chemical properties (i.e. paraffinic), GTL combustion produced soot with higher concentration of alkenes compared to Farnasane, which was the reason for the enhanced reactivity spotted. Lapuerta et al. (2012) tested the influence of the biodiesel fuelling on the regeneration tendency of a DPF. It was shown that the DPF break-even temperature was approximately 40 °C less

compared to that of the neat diesel combustion. These results were further confirmed through thermogravimetric analysis which also indicates that biodiesel particulates are significantly more reactive than the diesel counterpart. However, RS and XRD analysis revealed that biodiesel soot is characterised with more graphitic structure and less amorphous content. To explain their results, TEM analysis was also introduced to assess the primary particulate size, through which it was concluded that smaller spherules are presented in the biodiesel soot compared to diesel. Based on this observation, the author speculates that since the primary particulate size is smaller, the external surface of the spherule is more stretched and as a result carbon layers with a higher tortuosity should be comprised inside it (i.e. more reactive configuration). However, HRTEM analysis was not conducted to reveal this theory.

Summarising this section, it is clearly seen throughout the literature that the relationship between the particulate physio-chemical characteristics and the assigned reactivity is still complex, vague and under debate with several approaches proposed to answer this correlation. More extensive research should be made to fill the gaps presented, mainly to cover the competency of each individual nanostructure parameter and further approve the role of the elemental composition in altering the soot reactivity.

2.4.4 Uncertainties in the impact of the parent fuel type on the soot oxidative reactivity

In contrast to what have been stated above, newly published researches (Abboud et al., 2017; Abboud et al., 2018; Liu et al., 2018) suggested that the addition of oxygenated fuel compounds into conventional diesel fuel can also yield particulates that have a lower oxidative potential compared to that resulted from diesel combustion.

Abboud et al. (2017) studied the impact of adding various portion (3, 7, 15 and 30% in molar basis) of Methyl-decanoate (MD, C₁₁H₂₂O₂) to diesel surrogates named as “Aref” (30% α-methylnaphthalene and 70% n-decane) using a diffusion flame burner to test the impact of these oxygenated mixtures on the PM propensity, structure and reactivity. It has been reported that by increasing the oxygenate blending portion, soot was effectively reduced however, Raman analysis revealed that the particulate structure turned to be more graphite-like and TGA tests revealed a reduced oxidative reactivity compared to Aref soot. It was also reported that MD combustion reduced the soot SOF and oxygen content. This was speculated to result from the increased oxidation rate during the combustion process. The increased reactivity for the soot generated from the diesel surrogate was linked to its higher SOF and oxygen content along with more disordered structure. To further assess the results, this research work also included a real soot sample, so called “B7-BM-CA”, obtained from a real driving condition of an 8L diesel engine equipped with a euro VI after-treatment configuration (i.e. DOC, DPF and SCR). The fuel used was the standard EN590 blended with 7% vol. rapeseed methyl ester. Interestingly, B7-BM-CA soot presented more ordered structure and lower oxidative reactivity compared to diesel surrogate. In another study, Abboud et al. (2018) tested the impact of the ester chain length on the soot propensity along with its different physio-chemical properties including the chemical composition, structure and reactivity. For this aim, methyl-butanoate (MB, C₅H₁₀O₂), methyl-octanoate (MO, C₉H₁₈O₂) and MD were used as oxygenate candidates to be blended with the same “Aref” diesel surrogate used in the previous study (Abboud et al., 2017), with different blending portion ranging between 3-30 mole % replacement. No important variations were recorded along the particulate’s graphitic structure, independently from the operating fuel type or blending portion. However, all the blended fuels results in less reactive particulates compared to that produced from the Aref combustion. Furthermore, the alkyl chain length of a

methyl ester showed a significant influence on the soot characteristics: longer alkyl chains result in less reactive particulates with lower level of surface oxygen functionalities and SOF. This correlation was even more prevailed while increasing the amounts of methyl esters within the diesel surrogate.

Those new findings confirm the importance of testing the PM characteristics from different new-fuel generations to ensure that the advantageous role of those candidates in reducing the PM emissions is not negated by a worsened oxidative reactivity.

2.5 Lean-NOx Catalytic Reduction and Soot Destruction in the After-Treatment System

NOx emissions include NO and NO₂ as compounds, with the latter being a minor contributor in the overall NOx production from diesel engines (concentrations ranging from 5-30% maximum). Significant attention has been given towards reducing the NOx discharges due to its environmental impact which is associated with the development of photochemical smog and the threat of acid rain (Bosch, 2005). As for the health-risks, NO is dangerous when subjected to the human bloodstream where it can react with haemoglobin and transform it to meta-haemoglobin, which at elevated concentrations can be fatal. Concerning NO₂, it is an irritant reddish-brown gas that can severely damage the human lungs, causing asthma and other respiratory symptoms such as wheezing and coughing, along with potentially increasing the vulnerability of the respiratory system towards infections (United States Environmental Protection Agency, 2017). Both petrol and diesel engines produce significant levels of NOx emissions, yet, in petrol engines, a three-way catalytic converter (TWC) is used to effectively reduce these pollutants. The petrol deNOx mechanism consists of catalytic reactions of the NOx with CO under stoichiometric operating conditions to yield N₂ and CO₂ as biproducts. However,

this application is not suitable for the compression ignition (CI) engines since, under lean-burn conditions, the excess of oxygen in the exhaust helps in oxidising CO into CO₂ and prevent it from reacting with the NOx (Herreros et al., 2014). Several de-NOx after treatment devices have been proposed for diesel engines with the SCR catalyst being the most promising till this date (Valanidou et al., 2012).

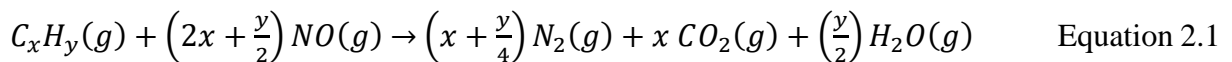
2.5.1 Hydrocarbon selective catalytic reduction

Among the SCR technologies, Urea-SCR mitigates the NOx emissions using an aqueous urea (CO(NH₂)₂) solution as a reducing agent. Some challenges in introducing this technology to light vehicles includes ammonia (NH₃) slip (should be maximum 10 ppm), catalyst corrosion and fouling by ammonium sulphate ((NH₄)₂SO₄) at temperatures below 250 °C (Sitshebo, 2010). Also, the complexity of the system is considered another drawback that limits its applicability since several devices should be introduced to ensure the functionality of the catalyst such as (Trichard, 2007):

- (a) On-board reservoir to store the reductant (urea)
- (b) Unit control to specify the amount of urea to be injected
- (c) Urea injector
- (d) NOx sensor to monitor the needed volume of reductant
- (e) Mixing device to ensure the homogeneity of the exhaust/NH₃ mixture in the catalyst
- (f) Hydrolysis catalyst to improve the conversion of urea into NH₃
- (g) Oxidation clean-up catalyst after the SCR to ensure that the NH₃ slip is kept below 10 ppm

Therefore, a simpler alternative, which can provide a similar efficiency to the latter technology is the HC-SCR, and as such has been extensively studied for NOx abatement. It is

one of the simplest techniques where a metal-based catalyst is used to convert NO_x to N₂ through reactions with a variety of hydrocarbon-based fuels as shown below:



Alumina (Al₂O₃) coating with a 2 wt. % silver (Ag) dispersion ratio is currently the most favourable wash coat for the HC-SCR catalyst. This is mainly due to its high selectivity to N₂, low activity for sulphur dioxide (SO₂) oxidation and its deNO_x efficiency can be maintained greater than 80% at temperatures higher than 350 °C (Bethke & Kung, 1997; Houel et al., 2007a; K. I. Shimizu & Satsuma, 2006). However, such temperatures are not seen very often in modern diesel engines and as a result poor catalytic activity is expected with real on-road vehicular applications. This is attributed to several factors, such as:

- (a) The existing HCs in the exhaust transform their nature from gas-phase to carbon-rich species that can cover the catalyst active sites and hinder their activity (Houel et al., 2007a; Houel et al., 2007b).
- (b) Exhaust soot particulates can also foul the silver catalyst by coking (i.e. deposition of carbon rich solids) when exhaust temperature are below 290 °C (Houel et al., 2007a).
- (c) Introducing NO₂ flow below 250 °C is also known for its ability to yield stable surface nitrates (AgNO₃) on the silver particulates which in turn self-poison the catalyst (Meunier et al., 1999; Ken Ichi Shimizu et al., 2001).

H₂ gas has been recognised as a promoter for the Ag/Al₂O₃ de-NO_x activity, especially in the low temperature regions when enough reductants are available (Breen et al., 2007; Theinnoi et al., 2008). The mechanism by which H₂ promotes the activity has been widely investigated in the literature and a summary of the work achieved till now is presented below.

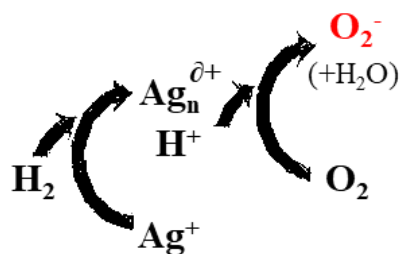


Figure 2.9: Morphological transformation of silver particulates in presence of H_2 and oxygen reduction into reactive species

Under reaction conditions, silver cations (Ag^+) are considered to prevail on the 2 wt. % $\text{Ag}/\text{Al}_2\text{O}_3$ surface (Bethke & Kung, 1997; Meunier et al., 1999). Once the H_2 is introduced to the catalyst, it dissociates on the Ag^+ sites and spillover as an acidic proton (H^+) on the alumina support (Gill, 2012; Ken Ichi Shimizu, Tsuzuki, Kato, et al., 2007). This is followed by an aggregation of the isolated Ag^+ ions to form reduced Ag clusters ($\text{Ag}_n^{\delta+}$) and metallic Ag (Ag^0). Afterwards, the resulted $\text{Ag}_n^{\delta+}$ and H^+ species help in reducing the existing molecular O_2 in the exhaust flow to superoxide ions (O_2^-) that are weakly chemisorbed on the silver species. These highly active oxygen species could be presented with a various range of compounds such as, Ag(OH)_2 , $\text{Ag}^+(\text{O}_2)^-$, Ag_2O_3 and AgO on the $\text{Ag}/\text{Al}_2\text{O}_3$ surface (Kim et al., 2013). Shimizu et al. (2007) reported that monomeric Ag^+ and Ag^0 are inactive particulates in the H_2 -assisted HC-SCR mechanism and only $\text{Ag}_n^{\delta+}$ is responsible for the reductive activation of O_2 , however, H^+ should be always presented.

The resulted active oxygen species activate the existing hydrocarbons in the exhaust and increase the rate of NOx absorption over the catalyst surface which in turn increases and enhances the overall deNOx mechanism (Breen et al., 2007; Theinnoi et al., 2008). A summary of the basic SCR reactions involved in this process is indicated in Figure 2.10.

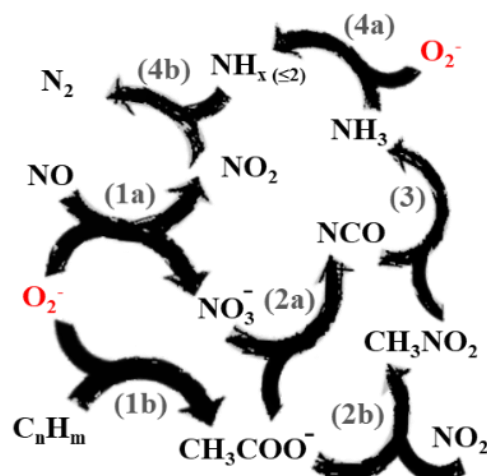


Figure 2.10: The mechanism by which the reactive oxygen species reduce the NOx emissions

- Summary of the main de-NOx SCR reactions:

- (1a)** O_2^- reacts with the exhaust NO emissions to yield NO_2 in the gaseous state and surface nitrates (NO_3^-) as adsorbed NO_2 on the catalyst surface (Breen et al., 2007).
- (1b)** In parallel, O_2^- also reacts with the exhaust HCs and activates their C-H bonds to yield active HC components such as enol and acetate (CH_3COO^-) (Breen et al., 2007).
- (2a)** The surface reactions between the bonded NO_3^- and the CH_3COO^- anions produces cyanide (CN) and isocyanate (NCO) species.
- (2b)** In parallel, the gas phase NO_2 reacts with the activated CH_3COO^- to yield nitromethane (CH_3NO_2).
- (3)** The resulted CH_3NO_2 reacts with the NCO species and convert into NH_3 and CO_x compounds.

(4a-b) The N-H bond in the resulted NH₃ molecules is then activated via the reactive O₂⁻ species to produce NH_x ($x \leq 2$), which in turn reacts with the NO₂ molecules to yield the desired N₂ (Ken Ichi Shimizu & Satsuma, 2007).

In addition, the increased concentration of NO₂ produced during this process (mechanism 1a) is also expected to enhance the oxidation of the carbonaceous species trapped in the catalyst. As a result, H₂ addition is reported to limit the coke deposition and sustain the SCR catalytic reactions at every stage of the low temperature region (200 °C to 350 °C) (Houel et al., 2007b). Brosius et al. (2005) also suggested that at low exhaust temperature (~ 200 °C), H₂ addition retard the nitrate poisoning by reducing the stability of the strongly adsorbed surface nitrates. This assumption is further clarified from the mechanism presented in point 2a.

Furthermore, the quality of the reductants also plays an important role in improving the de-NOx reactions. For instance, alcohol fuels, such as ethanol and butanol, significantly enhance the low-temperature NOx conversion (250 °C) and provide better performance in higher temperature windows compared to diesel compounds (Herreros et al., 2014; Thomas et al., 2005). This is mainly due to their higher reactivity (i.e. easily react with the O₂⁻ to yield nitrogen) along with being polar in nature (i.e. successfully competing with water to reach the catalyst active sites) (Herreros et al., 2014; Thomas et al., 2005). In addition, compared to diesel molecules, the shorter chain length, lower molecular mass and lower viscosity of alcohols offer the chance of being diffused more easily on the catalyst active sites (Herreros et al., 2014; Thomas et al., 2005). In contrast to alcohols, alkanes, such as dodecane, decane, octane and propane, require higher temperatures to achieve the desired SCR de-NOx reactions while alkenes are activated at an intermediate temperature between alcohols and alkanes (Houel et al., 2007a; Houel et al., 2007b). Long chain HCs (for alcohols, alkenes and alkanes) were shown

to improve the low temperature NOx conversion; however, the catalyst poisoning by carbon-rich species was reported to be higher and therefore the catalyst activity was not sustained (Theinnoi et al., 2008). On the contrary, low aromatic fuels (e.g. gas to liquid fuel) were proved to reduce the coke deposition, thus maintaining higher and stable NOx conversions compared to conventional diesel (Herreros et al., 2014; Houel et al., 2007a).

HC to NOx ratio (HC:NOx) also plays an important role in promoting and sustaining the catalyst activity. This ratio strongly depends on the exhaust temperature level: low ratios (~1:1 at 250 °C) are required for the low temperature region to avoid any catalyst deactivation by coking whereas, higher ratios (up to 5.5:1 at 500 °C) are required at higher temperatures since the reductants are more prone to be combusted rather than being transformed into reactive HC species (Houel et al., 2007a; Houel et al., 2007b).

So far, most of the real-life testing for the HC-SCR catalysts were carried out using old engine technologies as a source for the exhaust gas, which is typically disadvantageous due to high level of exhaust PM emissions (Houel et al., 2007a; Houel et al., 2007b; Sitshebo, 2010; Theinnoi et al., 2010) and only limited number has been reported for modern engines, mainly focusing on the heavy-duty area (Niemi et al., 2009; Viola, 2008).

For HC-SCR application, H₂ can be stored on-board the vehicle and be used on demand, however, this practice raises safety concerns in real vehicular application. Alternatively, H₂ can be produced on-board using a mini-reformer catalyst, Ruthenium (Ru), Rhodium (Rh) or Platinum (Pt) base, that can chemically/thermally crack the exhaust reactants (fuel-rich condition) to a H₂-rich gas on-demand, however, high temperatures are required. A potential application to overcome the low exhaust temperatures seen in diesel engines is the auto-thermal reforming. The process consists of injecting some fuel into the reactor, so that at low

temperatures, the reactants fully oxidise in the presence of oxygen thus increasing the catalyst thermal condition towards a sufficient state to start the reforming reactions (Theinnoi et al., 2008; Tsolakis et al., 2005; W. Wang et al., 2013). However, this will result in energy-penalty that needs to be kept as small as possible. Recent studies at University of Birmingham showed that under a low-load engine condition (~ 35%), a real exhaust mixture of 10 L/min (O₂, CO₂, CO, H₂O, heat) can reform a 60 ml/hr flow of diesel fuel to result in a total concentration of 2240 ppm H₂ at the inlet of the HC-SCR catalyst. This test was made using a full-scale engine exhaust configuration and a fuel penalty of 6% was recorded. However, the applicability of this method is still under debate as the fuel penalty should be ideally in the range of 1-3%. In this framework, research is still on-going in an effort to increase the process efficiency and minimize the energy penalty with the latest tests showing lower penalties limited to 2-3% (Sitshebo, 2010).

Modern clean engines and new fuel generations are extremely beneficial in terms of reducing the overall exhaust PM emissions, thus providing a new opportunity for the silver-based catalysts to operate more efficiently in real life applications. Along with reducing the PM level, oxygen borne fuels can also provide more reactive HC compounds to the exhaust, factors which are critical for the HC-SCR de-NOx activation. This is expected to reduce the needed amount of H₂ to fully activate the catalyst, which is also considered a critical parameter in case exhaust fuel reforming is used as a source for this gas. In this framework, it should be noted that on-board H₂ production is not in the scope of this thesis, instead, HC-SCR applicability with modern engines and cleaner fuels is assessed to evaluate the deNOx efficiency in term of maximum reduction versus fuel penalties.

2.5.2 Silver alumina as a soot oxidation promoter

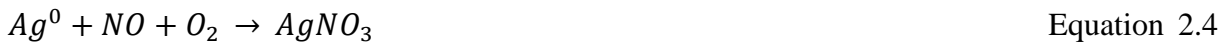
Along with its known role as an efficient de-NOx selective catalyst, silver coating was also recognised as a promising catalyser that can promote the soot oxidation kinetics in a lean operating environment (Aneggi et al., 2009; Corro et al., 2013; Gao et al., 2017; Ken Ichi Shimizu et al., 2010; Villani et al., 2005). Ag/Al₂O₃ and Pt/Al₂O₃ were recently recognised as an active soot oxidation promoter in the presence of a simulated diesel exhaust gas containing 10% O₂, 1000 ppm NO and 5% H₂O (Villani et al., 2005). The coating activity was evaluated with regards to the onset temperatures at which the soot starts to oxidise. The results were classified as follows: nitrated Ag/Al₂O₃ (400 °C) < Pt/Al₂O₃ (430 °C) < oxidized Ag/Al₂O₃ (~500 °C) < soot reference (~500 °C) ≤ nitrated Al₂O₃ (~500 °C). The higher activity of nitrated Ag/Al₂O₃ was mainly resulted from the reduction of silver nitrates (i.e. AgNO₃) into finely dispersed metallic silver (i.e. Ag⁰) and silver oxide (i.e. Ag₂O) species as soon as the exhaust temperature reaches 400 °C. It should be noted that this transition is mainly triggered by the available NO emissions in the feed flow as shown in the reactions below



The yielding of Ag⁰ particulates was selected in this research work and several other publications (Bethke & Kung, 1997; Meunier et al., 1999) as an effective element that helps in oxidising NO into NO₂ emissions, thus favouring the low-temperature soot oxidation reactions since NO₂ is known for being a more active oxidiser compared to O₂ (Ehrburger et al., 2002). Nitrated Al₂O₃ shows similar kinetics as the soot reference sample confirming that the ameliorated reactivity of the nitrated Ag/Al₂O₃ correlates with the existence of the silver

particulates and not the nitrates. On the other hand, the ineffectiveness of oxidised Ag/Al₂O₃ confirms the role of the NO₂ emissions in yielding the soot oxidation reactions since oxidised silver (in the state of Ag⁺) cannot trigger the NO/NO₂ conversion pathway (Bethke & Kung, 1997; Bogdanchikova et al., 2002). In addition, the author suggests that the nitrated Ag/Al₂O₃ can conserve the same soot initial activation activity when the catalyst is cooled down using the same simulated diesel exhaust flow. This was mainly attributed to the nature of the Ag⁰ particulates that can shift their state back to AgNO₃ when cooled down in the presence of NO.

The representing mechanism is shown in the reaction below:



Aneggi et al. (2009) also tested the applicability of silver based catalyst in promoting the soot oxidation kinetics using oxygen as the sole reactant. Different catalyst supports were incorporated in this test, which are alumina (Al₂O₃), ceria (CeO₂) and zirconia (ZrO₂). The study focuses on evaluating the chemistry of the different Ag species and distinguish their synergies with the support's material. The soot oxidation kinetics were monitored during the catalyst regeneration (i.e. monitoring the released CO₂ levels) when subjected to a controlled air flow (80% vol. of N₂ and 20% vol. of O₂). Ag/Al₂O₃ and Ag/ZrO₂ were reported as the most effective oxidisers in this experiment, for both, fresh and aged state. It was concluded that the majority of the Ag particulates presented on the Al₂O₃ and ZrO₂ supports are in the metallic state (i.e. Ag⁰). The author relates the presence of Ag⁰ with the better reactivity recorded. The main advantage of Ag⁰ in this research was not related to any NO₂ formation as the feed flow is NO free (only O₂ as a reactant). However, it was reported that the Ag⁰ particulates can act as an oxidation catalytic agent since this element can form numerous suboxide species in the presence of an oxygen-rich atmosphere. The author also reports that Ag⁰ can activate the oxygen

molecules into superoxide ions (O_2^-) that can further promote the soot oxidation process. However, in case of Ag/CeO₂, the Ag particulates were stabilised in an oxide state (i.e. Ag⁺) and thus limited improvement was achieved compared to the non-coated CeO₂ catalyst. This is possibly attributed to the ability of CeO₂ in storing oxygen which can stabilises the Ag in an oxidised state.

The catalytic impact of silver on silicon dioxide (Ag/SiO₂), copper on SiO₂ (Cu/SiO₂) and gold on SiO₂ (Au/SiO₂) has been recently reviewed for the diesel soot oxidation process (Corro et al., 2013). In this work, soot was produced by the help of a diesel burner and collected inside a coated DPF mounted in a reactor. Afterwards, the DPF was subjected to a temperature-controlled oxidation program using air flow as an oxidising environment. The results obtained highlight that Ag/SiO₂ is the most favourable catalytic agent between the tested samples. The soot oxidation reactions started at 150 °C and the highest rate of oxidation was achieved at ~ 200 °C. It was found that the presence of Ag⁰ particulates on the SiO₂ surface is the sole reason in promoting the soot oxidation reactions. This was related to the ability of these particulates to promote the formation of atomic oxygen species on the catalyst surface, as discussed before in ref. (Aneggi et al., 2009). In addition, it was also speculated that these active oxygen species can also improve the soot/oxidisers contact and may also create electronic interaction between the surface of the catalyst and the soot particulates.

2.5.3 Variation in soot structure along the exhaust after-treatment system

Soot structural modifications (i.e. morphology) do not only impact the oxidative/mutagenic properties of the soot but also influence the motion and contact (i.e. convective or diffusive flow) between the particulates which in turn impacts the magnitude of the Peclet number (Pe) accordingly. Pe is a dimensionless factor whose magnitude strongly

depends on the soot morphological aspects, mainly, d_{p0} and to a lesser extent, R_g (Konstandopoulos et al., 2002). The lower the Pe (<1) the more open and porous the soot-cake is (i.e. layer of soot deposited in the DPF channels) and the higher the Pe ($1 < Pe < 5$) the more compact it is. In general, an increase in d_{p0} will yield a higher Pe number and vice versa (Konstandopoulos et al., 2002). Factors as the soot cake permeability, packing density, porosity, pressure-drop in the channels and DPF thermal behaviour during regeneration (also influenced by the oxidative behaviour of the particulates discussed in chapter 2.3) can be calculated (i.e. simulated) once obtaining the Pe number. In general, a porous soot cake ($Pe < 1$) looks like the first left illustration in Figure 2.11. Such kind of structure highlights that the soot is dispersed in a way that can induce lower backpressure than that presented in the other two illustrations which are representative for higher Peclet number configuration. The reader is referred to (Chiatti et al., 2009; Konstandopoulos & Kostoglou, 2004; Konstandopoulos et al., 2002) for a more detailed interpretation of the incorporated formulas that link the Pe number with the soot cake characteristics. As a matter of fact, recognising the filtration efficiency of a DPF is important, however, predicting the exact dimensioning of the system to optimise the resulted backpressure is even more critical, especially in the norm of the severe legislations and economic viability of diesel-powered vehicles.

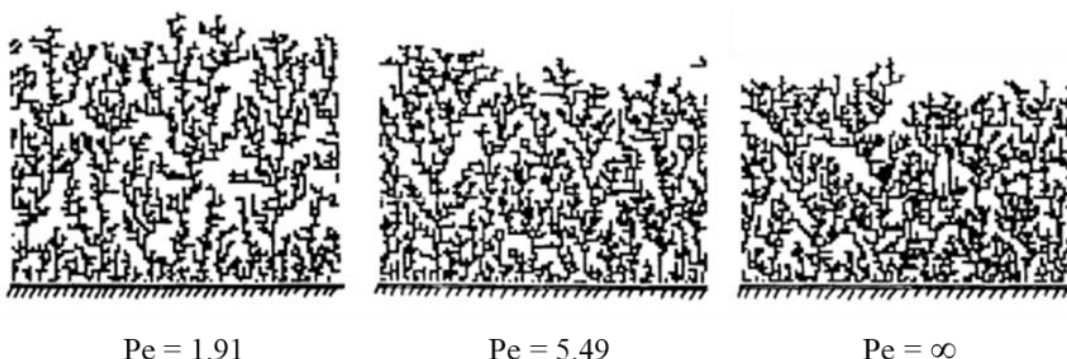


Figure 2.11: Soot-cake representation with regards to its Peclet number, reproduced from
(Tassopoulos et al., 1989)

After recognising the importance of the particulates' structure on the DPF performance, it becomes a subject of interest to understand if the exhaust particulates will face any modifications within the after-treatment units, e.g. diesel oxidation catalyst (DOC), SCR, etc., before being trapped in the DPF. While the dependency of the soot structure on its fuelling source and engine technology is a well-researched topic, to our knowledge, limited work (Fayad et al., 2015; Lapuerta et al., 2007; Lee & Zhu, 2005; Liati et al., 2013; Ma et al., 2014) has been carried out regarding the impact of the after-treatment system on the structure of the exhaust PM (i.e. morphology and nanostructure).

Lapuerta et al. (2007) studied the impact of changing the soot sampling point in the exhaust line to check if d_{p0} will be altered by the thermal or fluid-dynamic conditions along the line. However, the study did not involve any after-treatment unit. It was seen that d_{p0} remains constant throughout all the tested positions since as reported, the exhaust temperature level (110 to 324 °C) was not enough to launch any chemical reactions with the soot surface. Fayad et al. (2015) investigated the influence of the DOC with regards to the oxidation/reduction mechanism of the soot particulates produced from the combustion of diesel, rapeseed methyl

ester (RME) and butanol/RME/diesel blend. It was seen that DOC can help in reducing the small-scale particulates (<20 nm) by diffusion mechanism (trapping) and can also result on average with larger soot particulates because of an enhanced collision phenomenon in the catalyst channels. This theory was further verified by morphologically analysing the particulates, upstream and downstream the catalyst. From the analysis it was reported that after passing the DOC, the collected soot tended to present a greater n_{p0} and a larger R_g compared to these tested upstream the catalyst. However, DOC did not modify neither the particulates' d_{p0} nor the carbon layers arrangements, highlighting that a longer soot/catalyst residence time was required to perform those alterations (soot oxidation). Liati et al. (2013) studied the morphological and nanostructure aspects of soot particulates upstream and downstream the DOC in an effort to understand the impact of this catalyst on the particulate's oxidative reactivity. Concerning the morphological alterations, slight reduction was noted along d_{p0} when the particulates flow throughout the catalyst. This was attributed to the devolatilization of the soluble organic fraction from the particulates surface however, the author did not link these changes with the existence of any possible carbon oxidation phenomenon. As for the graphitisation order, slightly more ordered structure was presented downstream the DOC and therefore, to some extent, the particulates were considered less reactive towards oxidation. Close edge X-ray absorption fine structure analysis (NEXAFS) was also employed to understand the difference in the particulate's surface functional compounds upstream and downstream the catalyst. It was shown that marginal changes took place downstream the DOC and more specifically, most of the carboxyl functionalities had disappeared and the soot seemed to be more homogeneous in its chemical structure.

Ma et al. (2014) studied the impact of the DOC on the particulate's carbon layer arrangement and its corresponding oxidative reactivity. The analysis showed that DOC can alter the primary particulate's inner structure in a way that makes it more ordered towards graphitisation (longer L_a and remarkably shorter d_{002}). As for the oxidative behaviour, the post-catalyst soot seemed to be more reactive, yet a different oxidation mode was recorded compared to that in the pre-catalyst case. To be more specific, the soot mass loss was extremely faster than that of the pre-catalyst test at the early stages of the oxidation (before 50% soot mass loss) however, at later stages (after 50 %), the oxidation rate turned to be slower and the residual ash mass significantly higher. Concerning the residuals, they were mainly influenced by the sample collection method and not by any direct soot interactions with the DOC. The author reported that a longer period was needed to collect the soot downstream the catalyst since the increased concentrations of NO_2 (resulted from the NO oxidation in the DOC) continuously oxidised the soot placed on the filter. However, during the collection time, the ash deposition remained intact and did not oxidise, thus increasing the ash percentage of the sample placed after the DOC. The soot nanostructure variations were also recorded throughout the different stages of the temperature-controlled oxidation to further investigate the oxidation mechanism of the soot samples (pre and post catalyst). It was concluded that the soot collected upstream the DOC undergoes a surface burning process, in other words, it keeps a shell-core structure along all the oxidation period. As for the post-catalyst particulates, the same oxidation mode as that of the "biodiesel oxidation" (J. Song et al., 2006) was seen for this testing case. In summary, despite the more graphitic initial structure, the HRTEM analysis revealed that the soot undergoes an internal-burning process at the early stages of the oxidation which leads to a capsule-like structure. The significant energy released during this phase helps to thermally restructure the soot silhouette and transform it to a closed outer shell profile. The highly stable configuration

of the latter is the main reason for the slower oxidation rates recorded after the first 50% of the soot weight loss. It was speculated that the DOC contributed to the devolatilization of the surface volatile compounds, which in turn generated this unique mode of oxidation. (For further clarification refer to Section 2.4.3, as this oxidation mode is similar to the biodiesel oxidation mode).

Lee & Zhu (Lee & Zhu, 2004, 2005) studied the evolution of the soot morphological parameters along the different positions of the exhaust system (that includes two DOCs) as a function of engine speed and load condition. The different soot sampling positions are presented in Figure 2.12. The analysis showed that independently from the engine operating settings, the first DOC helped to reduce the particulates R_g and d_{p0} and increased their circularity (higher D_f). The reduction in d_{p0} was related to the existence of a soot catalytic oxidation, which was also confirmed through qualitative inspection for the TEM micrographs. It was shown that upstream the catalyst, the particulates presented the standard graphitic configuration of a diesel soot where the primary particulates are mostly spherical and quite distinct from the other spherules. However, downstream the catalyst, the primary particulates appear to have no definite borders and seem to be fused in each other, indicating the presence of a catalytic oxidation, as speculated by the author. The second DOC (Position P4) also reduces d_{p0} , however the particulates R_g tend to slightly increase and their geometrical configuration highlights a more chain-like structure (lower D_f). It was expected that the resulted particulates undergo an enhanced aerodynamic mixing after going out of the catalyst (after 200 cm), which in turn favours their aggregation together to yield larger particulates with a more complex geometry. Overall, it was seen that d_{p0} and R_g decrease progressively throughout the catalysts with R_g presenting a bigger drop compared to d_{p0} . It was speculated that this further reduction in R_g

could possibly arise from the breakdown of the particulates throughout the catalyst channels along with reduction in the interstitial distances among the spherules. However, the average number of the primary particulates in the aggregates (n_{p0}) was not evaluated in this study, keeping those findings (i.e. breakdown and reduction in interstitial spacing) as theoretical approaches and not proved by analysis.

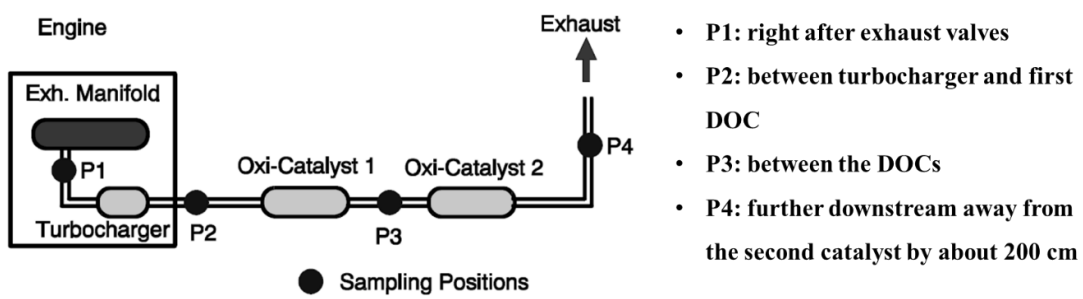


Figure 2.12: Sampling collection positions for reference (Lee & Zhu, 2004, 2005)

In summary, the literature presents two trends regarding the DOC mechanism, some authors suggest that there is no enough residence time to launch the soot oxidation reactions while others stated and confirmed that the oxidation can really happen in such kind of flow-through substrates. As for the H₂-assisted HC-SCR soot interaction mechanism, to the author knowledge, no work has been carried out. However, for the reasons stated in Section 2.5.2, recognising the impact of that aftertreatment unit becomes a necessity to understand if such technique can combine both, de-NOx reactions and efficient soot oxidation mechanism.

2.6 In-cylinder Late Post Fuel Injections

During the last decade, several researchers suggested the importance of enhancing the CI combustion performance in terms of noise reduction, engine stress, power production and combustion efficiency. For this to happen, the design of a flexible fuel injection system that can

control the following factors: (1) start of the injection, (2) fuel quantity, (3) injection pressure and (4) injection shaping, becomes a necessity. In other words, the introduction of electronically controlled injectors instead of the traditional mechanical activation (i.e. the pump line nozzle system) was the key solution to meet all the above stated goals. As a result, “Common-rail” direct injection system was announced into the market. This technology offers a flexibility in the fuel injection system including the ability to control the timing, rate and pressure of the fuel injected, and most importantly permit multiple fuel injection strategies. Nowadays in the market, conventional common rail engines operate using a single pre-injection (pilot) fuel strategy followed by a main injection (Keeler, 2009). Pilot injections are usually applied at fewer CADs before the main injection to thermally condition the cylinder for this event, which helps in reducing the main-ignition delay and controls the premixed burning phase, thus reduce the rate of pressure rise during the process. This flexible calibration results in significant improvement in the engine vibrations, as well as noise and emission, without deterring the engine’s fuel consumption and combustion efficiency (Punov et al., 2017; Rajkumar, 2002). To keep our work consistent with the newest market approaches, the standard calibration of the engine work was performed using a pilot and main fuel injection events.

Post Fuel injection (PFI) refers to the addition of a short injection pulse after the main injection and usually presents no more than 20% of the total fuel injected. In case the post-fuel is injected with a dwell (i.e. duration between both simultaneous injections) of few crank angle degrees (CAD) after the main injection, the strategy is referred to as Close coupled PFI and if the PFI was applied at later stages of the combustion cycle, the strategy is referred to as “late PFI” (Faghani, 2015). If the dwell duration and PFI amount is properly optimised, a simultaneous reduction in PM, NOx, THC and CO could be achieved (O’Connor & Musculus,

2014). For better understanding of the different injection modes (pilot, main and post) presented in conventional common rail engines, the typical in-cylinder heat-release rate (HRR) profile resulted from each strategy is plotted in Figure 2.13.

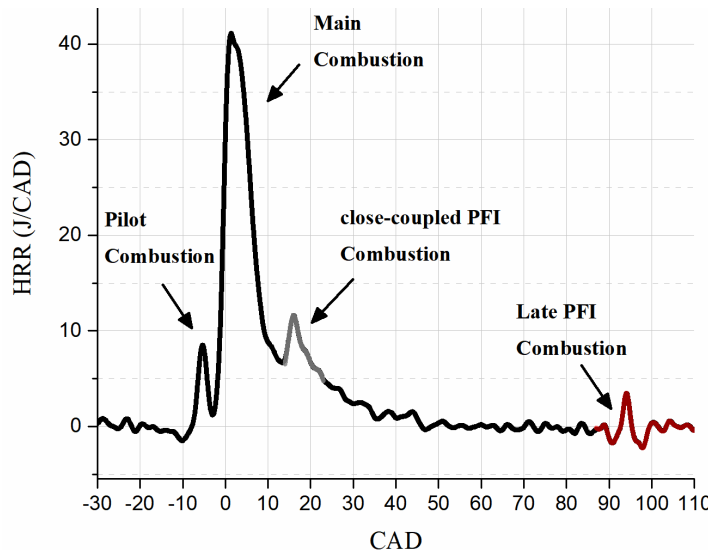


Figure 2.13: HRR produced from a common-rail engine operating with a pilot, main, close coupled and late post fuel injection strategy

2.6.1 Impact of PFI on the particulate matter emissions

The positive impact of applying in-cylinder PFIs to reduce diesel engine soot emissions has been demonstrated in several research works (Bobba et al., 2010; Desantes et al., 2007; O'Connor & Musculus, 2014). It is generally accepted that close coupled PFI strategies offer lower soot reduction capability compared to late PFI; besides, if the injection dwell is in intermediate stage (usually between 8 and 18 CAD after top dead centre (ATDC)), the resulting soot level may also increase from that of the baseline (i.e. no PFI strategy). A theoretical representation of the expected soot level with different main-post dwell timing (denoted as $\Delta\alpha$) compared to the no post case is presented in Figure 2.14.

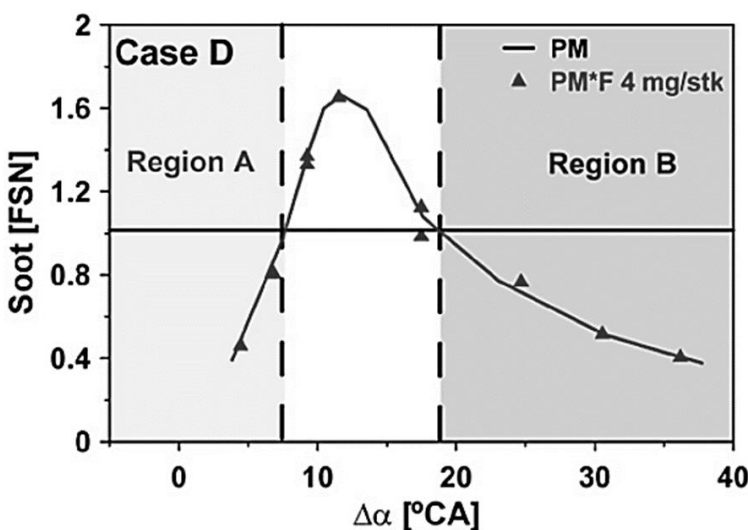


Figure 2.14: Expected soot level from different post injection strategies. The horizontal line present the equivalent soot FSN at no post condition, reproduced from (Arrègle et al., 2008)

Close coupled PFI strategies are usually expected to interact with the main injected mixture by increasing the turbulence of the main injected flow, in other terms, help in introducing newly fresh oxygen into the main mixture and reduce the local equivalence ratio. Consequently, soot inception is inhibited, and soot oxidation process is promoted throughout the combustion cycle. It is also suggested that the heat released from the post fuel combustion can significantly increase the in-cylinder local temperatures, which in turn help in oxidising the soot particulates that have been already produced from the main injection event. Both the availability of higher local temperatures and oxygen in the squish regions of the piston can also promote the oxidation of the soot imprisoned in this area (the squish) (O'Connor & Musculus, 2013).

In contrast to what have been reported earlier, Desantes et al. (2007) and Arregle et al. (2008) reported that when the PFI is applied at later stages of the combustion cycle, the soot reduction mechanism can differ to what have been reported above. The authors suggested that

the combustion of the late PFI does not interact with the combustion of the main mixture, regardless of the injection dwell – the “split flame” theory (Region B in Figure 2.14). They proposed that the combustion of the post-fuel injected is a completely or nearly soot-free mechanism and that the suppression shown in soot emissions is mainly produced from the shortened main-injection duration. The split flame theory suggests that when the main injection pulse is shortened, the available fuel-rich mixture in the spray tip, where soot is usually inceptioned, is not reloaded with more fuel when the injection is stopped and started over (i.e. PFI), thus suppressing the rate of soot formation from the main-injection pulse. This assumption is mainly based on the “fuel-replenishment” theory which suggests that with longer injection durations, more fuel is provided to the spray tip, establishing a more fuel-rich region that support the soot inception mechanism. In summary, late PFI was suggested to be a soot-free burning process and thus the soot reduction is only produced from the shortened main injection. Bobba et al. (2010) demonstrated in his study that late PFI (40 CAD ATDC) can effectively reduce soot emissions up to 60 % compared to long main injection, however, the fuel penalties were as high as 7%. It was also seen that late PFI can sharply increase the late-cycle temperatures of the soot imprisoned in the squish regions of the piston, yielding an efficient soot oxidation process even when PFI timing is as late as 67 CAD ATDC.

In summary, soot reduction with late PFI strategies is suggested to be the result of two different concepts, (i) the split flame theory (if main injection is shortened) and (ii) better soot oxidation in the squish area of the piston.

2.6.2 Impact of PFI on the gaseous emissions

As for the impact of PFI strategy on the engine-out emissions, a strong consensus concerning the impact of the post-injection timing and mass of the post-fuel introduced have

been reported in the literature. In case of close coupled PFI, it is expected that the in-cylinder temperature and pressure levels when the PFI is introduced are still enough to effectively combust the post-fuel injected and enhance the engine's thermo-dynamic efficiency. Hence, limited fuel penalty is usually reported with respect to the no-post mode and in some cases better fuel consumption is also seen. Furthermore, unburned hydrocarbons (UHC) and CO emissions will be reduced, while NOx tend to keep constant or slightly increase (Arrègle et al., 2008). Further retarding the PFI timing indicates that the post-fuel is injected into an environment where the pressure and temperature conditions are not enough to effectively combust the mixture. As a result, more incomplete combustion is expected, thus higher UHC and CO emissions are produced, and higher fuel penalties will be resulted. Also, the partial oxidation of the fuel indicates the possibility of in-cylinder H₂ production. This could also happen by steam reforming reactions of the post fuel injected due to the excess of water resulted from the combustion of the main fuel (Jeftić, Asad, et al., 2011).

Hydrocarbon speciation for late PFI strategies were carried out by several authors in the literature (Chen et al., 2014; Fayad et al., 2017; Jeftić et al., 2015; Storey et al., 2005). Storey et al. (2005) reported an increase in the level of light HCs, especially propene, when delaying the PFI timing from 78 to 100 CAD ATDC, while the heavy HCs remains flat throughout the timing sweep. However, another study launched by Jeftic et al. (2015) showed that retarding the PFI timing can increase the light HCs species for an injection dwell from 40 to 60 CAD ATDC, however, further retarding the injection results in significantly higher portion of UHC. Chen et al. (2014) reported that as from 70 CAD ATDC, PFI can dramatically increase the UHC level. Fayad et al. (2017) also showed that with 60 CAD ATDC, PFI was capable to fivefold

the UHC level but did not significantly increases the light HC species. Also, an increase of 10 °C was seen in the exhaust temperatures compared to the no-post mode.

2.7 Summary

Diesel soot particulates are carcinogenic compounds produced in the fuel-rich regions of the diesel combustion process. The physical and chemical structure of those particulates is reported to have a direct impact on its ability to combust in an oxidising environment (oxidative reactivity). Several theories and assumptions have been proposed in the literature to correlate these physio-chemical parameters to the assigned particulate's reactivity; however, the relationship is still quite complex and no clear agreement showing the sensitivity of each property is reported till date. Soot structural modifications do not only impact the oxidative/mutagenic properties of the soot but also influence the motion and contact (i.e. convective or diffusive flow) between the particulates within the diesel particulate filter. Understanding those properties is beneficial to design the new generation of aftertreatment devices. It is generally accepted that the combustion of oxygenated diesel blends results in more reactive soot particulates compared to conventional diesel fuelling. However, newly published researches suggested that the addition of oxygenated fuel compounds into conventional diesel fuel can also yield particulates with lower oxidative potential compared to that resulted from diesel combustion. Those new findings confirm the importance of testing the PM characteristics from different new-fuel generations to ensure that the advantageous role of those candidates in reducing the PM emissions is not negated by a worsened oxidative reactivity. Glycol ethers, especially TPGME is recognised for yielding near non-sooting combustion. Most of the studies focus on understanding the ignition mechanism of these compounds but none of them show the characteristics of the PM resulted from their combustion.

Concerning the NOx purification, the silver alumina ($\text{Ag}/\text{Al}_2\text{O}_3$) hydrocarbon-SCR (HC-SCR) is a metal-based catalyst that can convert NOx to N_2 through reactions with a variety of hydrocarbon-based fuels over a wide-temperature range window. However, in the low temperature regions, typically lower than 250 °C, the deposition of the soot particulates and heavy molecular weight species on the catalyst surface is faster than their oxidation, thus hindering the catalyst activity by coking and masking. H_2 is an active promoter that helps in increasing the catalyst de-NOx efficiency in the low temperature range and virtually withstand it through time. The literature indicates that late in-cylinder post fuel injection (PFI) strategies can simultaneously reduce soot emissions, while increasing the HCs level in the exhaust (i.e. regulate HC:NOx ratio in the exhaust) with the possibility of in-cylinder H_2 production and exhaust temperature increase. Combining these parameters together, late PFIs application present an interesting technique that has a good potential to enhance the HC-SCR de-NOx performance; however, the resultant fuel penalties remain a topic of interest to be evaluated for a realistic applicable solution.

Along with its known role as an efficient de-NOx selective catalyst, $\text{Ag}/\text{Al}_2\text{O}_3$ coating was also recognised as a promising catalyser that can promote the soot oxidation kinetics in a lean operating environment. In the presence of a diesel exhaust, especially NOx, $\text{Ag}/\text{Al}_2\text{O}_3$ can enhance the soot oxidation mechanism to start at 400 oC but cannot downgrade it to a more promising low temperature region (150 oC – 250 oC). This results from the nature of the silver particulates which shows to be inactive (cannot convert NO to NO₂) when the exhaust temperatures are lower than 400 oC (due to their deactivation by silver nitrate poisoning). In the absence of NO, it has been proved that O₂ flow can initiate the soot oxidation reactions at

a temperature as low as 150 oC. This is mainly attributed to the ability of silver to chemisorb several active oxygen species on its surface, thus acting as an oxidation catalyst.

In case the automotive industry wants to benefit from the full role of this catalyst, it should be applied to effectively combine both, selective de-NOx reduction and soot oxidation promotion. This implies that minute addition of H₂ gas will be required to achieve the low-temperature de-NOx function as highlighted in Section 2.4.1. Such kind of promoter (H₂) can effectively retard the surface nitrates poisoning, promote the reduction of Ag⁺ particulates into Ag⁰ and energise the catalyst surface with weekly chemisorbed oxygen species, factors which are speculated to enhance the soot oxidation behaviour in the low temperature region. For the author knowledge, no work has been carried out to check the H₂-assisted HC-SCR soot interaction mechanism. Recognising the impact of that aftertreatment unit becomes a necessity to understand if such technique can combine both, de-NOx reactions and efficient soot oxidation mechanism, despite of the limited residence time in the catalyst (flow-through substrates).

CHAPTER 3

TEST FACILITY AND METHODS

The equipment and data analysis methods implemented in this thesis work are presented in this Section. This will include the engine test rig, exhaust gas and particulate measurement analysers, TEM micrographs analysing methods along with the HC-SCR catalyst specifications and testing process.

3.1 Engine test rig

A water-cooled single cylinder naturally aspirated common-rail research diesel engine (four-stroke) was used to carry out the experiments. The engine is motored and loaded via an AC/DC ABB 75 kw motored dynamometer. The in-cylinder fuel injections can be split between pilot, main and post strategies. The fuel injection pressure can be also regulated in a range from 500 to 2000 bar. The main engine parameters are detailed in Table 3.1.

Table 3.1: Engine specification

Cylinder number	1
Charging type	Naturally aspirated
Connecting rod length	160 mm
Bore / Stroke	84 mm / 90 mm
Displacement volume	499 cc
Compression ratio	16:01
Engine speed	900 to 3000 rpm
IMEP	< 7 Bar
Injection system	Common-rail
Fuel pressure supply	500 to 2000 Bar
Injection events	Up to 3 separate injections

Prior running the engine, the water pump, water heater and oil pump were turned on for at least 2 hours till the oil temperature reach 50 °C. After that, the engine was started using the “warm-up parameters” listed in Table 3.2 and kept running for 20 min under this condition before changing the settings accordingly to meet the designated condition. Testing can be started once the coolant temperature reaches 90 °C and oil temperature stabilised at 70 ± 1 °C. Fuel temperature was always kept constant at 29 °C.

Table 3.2: warm-up engine parameters and the optimal condition to start the experimental test

Warm-up parameters				
Injection schedule	Pilot	Main	Post	
Injection timing	15 CAD BTDC	5 CAD BTDC	Not available	
Injection duration	0.15 ms	0.25 ms		
Engine speed	1000 rpm			
Fuel pressure	500 bars			
Optimal conditions to start the test				
Coolant temperature	90 ± 1 °C			
Oil temperature	70 ± 1 °C			
Fuel temperature	29 ± 1 °C			

The in-cylinder pressure was recorded using an AVL GH13P pressure sensor mounted in the top of the cylinder-head. The acquired signal is then amplified using an AVL FlexiFEM 2P2 Amplifier and inputted into an in-built LabVIEW program. To minimize the uncertainties resulting from cycle to cycle variation, an average of 200 cycles was accounted to represent the average pressure obtained from each operating condition. A digital-shaft encoder that produces 360 pulses/revolution was utilised to detect the crankshaft angle. A simple reaction model was designed to derive the HRR from the recorded pressure based on the relation provided by Heywood et al. (1988):

$$\frac{dQ}{d\theta} = \frac{\gamma}{\gamma-1} P \frac{dv}{d\theta} + \frac{1}{\gamma+1} V \frac{dp}{d\theta} \quad \text{Equation 3.1}$$

Where P is the instantaneous recorded pressure, θ is the instantaneous crankshaft position, $\frac{dQ}{d\theta}$ is the apparent HRR, γ is the heat capacity ratio and v is the instantaneous volume displaced.

γ is equal to $\frac{\text{Specific Heat in constant pressure } (C_p)}{\text{Specific Heat in constant volume } (C_v)}$ and it is actually interpolated from the obtained P-V relation.

3.2 Fuel specifications

In this thesis work, three fuels were examined, conventional ULSD, mixture of 20.90% TPGME and 79.1% ULSD, denoted as TP20 and a mixture of 20% DPGME and 80% ULSD, denoted as DP20. The resulted oxygen mass w.t.% of the blends is 6.5%.

A summary of the different fuel properties is shown in Table 3.3.

Table 3.3: Fuel physical properties of ULSD, TPGME, DPGME, TP20 and DP20 (source: (Hilden et al., 2001), unless stated else)

	Test method	ULSD	TPGME	DPGME	TP20	DP20
Formula	-	C ₁₄ H ₂₆ .1	C ₁₀ H ₂₂ O ₄	C ₇ H ₁₆ O ₃	-	-
Ash, wt.%	D-482	<0.01	-	-	<0.01	<0.01
Density (kg/m ³ at 20 °C)	D-1298	826.9	968 (Natarajan et al., 2001)	938 (Natarajan et al., 2001)	848.8	846.1
Fatty Acid Methyl Esters % vol.	EN14078 A	< 0.05	-	-	< 0.05	< 0.05
Cloud point	D-2500	-21			-20	-20
Cetane number	D-6890	43.4 (United, 2009)	80 (Burke et al., 2015)	43.9 (Yanowitz et al., 2014)	-	-
Heat of vaporization (kJ/kg)	-	243	357 (S. Park et al., 2016)	330 (Shell Chemicals, 2007)	-	-
Viscosity (cSt at 40 °C)	D-445	2.395	-	-	2.359	2.208
Flash point	D-93	71	>110 (Natarajan et al., 2001)	74 (Natarajan et al., 2001)	76	72
Lower Calorific Value (MJ/kg)	D-3338	43.11	28.1 (Frijters, 2012)	27.5 (Shell Chemicals, 2007)	39.55	39.58
Lubricity (SLBOCLE, g)	D-5001	3700	-	-	4100	2900
Sulphur (mg/Kg of fuel)	D-3120	< 10	-	-	< 10	< 10
10% distillation (°C)	D-86	208.6	-	-	207.8	191.8
20%		223.7	-	-	220.1	197.4
30%		239.9	-	-	231.3	207.2
40%		252.3	-	-	238.8	227.7
50%		260.3	-	-	244.8	251.5
60%		267.6	-	-	252.4	262.3
70%		276.1	-	-	262.9	270.7
80%		289.6	-	-	278.9	283.3
90%		319.2	-	-	308.5	313.5
95%		345.2	-	-	333.4	343.2
Fuel Boiling point		353.8	-	-	342.8	350.3
wt. % C	Calculated	86.47	58.22	56.73	80.55	80.5
wt. % H	Calculated	13.53	10.75	10.88	12.95	13
wt. % O	Calculated	0	31.03	32.39	6.5	6.5
Glycol ether volume (%)	Calculated	-	-	-	20.95	20.07

3.3 HC-SCR testing setup

The HC-SCR catalyst used in this thesis is a 2 wt.% Ag/Al₂O₃ coated monolith characterised with a high cell-density of 600 cell/in². The catalyst is 40 mm in diameter and 120 mm in length. The catalyst is supplied by Johnson Matthey Plc. (Figure 3.1).

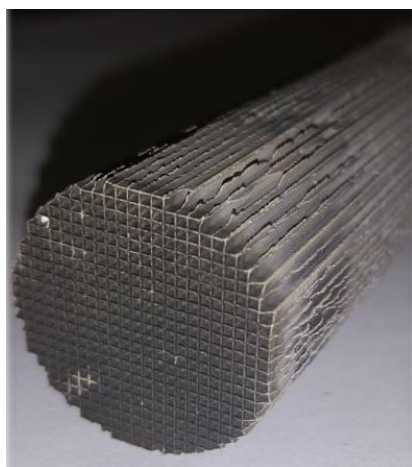


Figure 3.1: HC-SCR catalyst used in this thesis

The catalyst was placed inside a specially designed stainless-steel reactor and held vertically in a large tubular furnace to allow an accurate control of the exhaust flow temperature. The flow throughout the catalyst was regulated using an in-line suction pump in a way that a constant gas hourly space velocity (GHSV) of 35,000 h⁻¹ is achieved for all the testing conditions. This velocity was chosen as it is representative for the typical urban driving cycle's GHSV. Data was recorded 10 minutes after any modification in the engine operating parameters to make sure that the exhaust emissions had steady.

H₂ gas (99.99% purity) used in this analysis was supplied from BOC UK. H₂ line was connected to the exhaust using a one-way valve constraint to ensure that the gas is introduced to the system and not pushed back to the line by the opposing pressure of the exhaust flow. The resulted H₂ concentrations in the flow were regulated via a highly-accurate flowmeter and

monitored using the Gas Chromatography –Thermal Conductivity Detector analyser to ensure that the exact amount is introduced in each testing condition. A K-type thermocouple (range: 0-1250°C ± 2.2) was placed in the inlet of the reformer and positioned at 2 cm upstream the catalyst to ensure that the tested conditions are representative for that of the real exhaust flow.

A schematic representation of the HC-SCR testing setup and the soot collection point is presented in Figure 3.2.

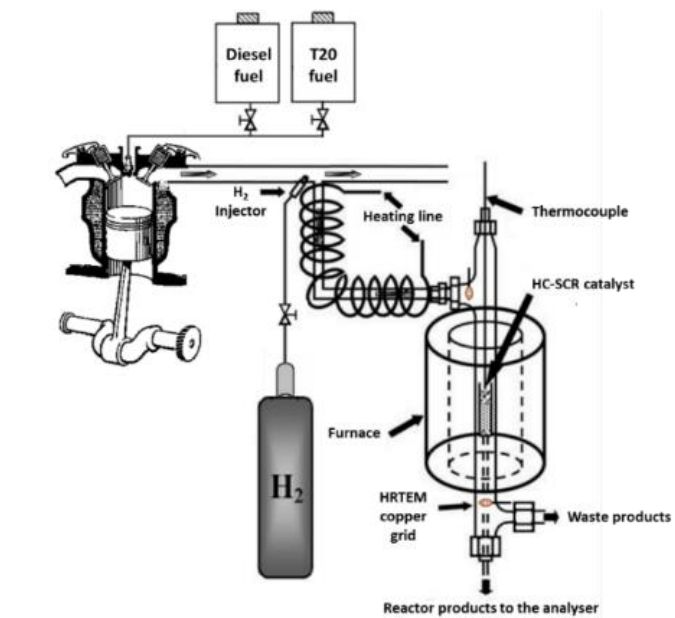


Figure 3.2: HC-SCR testing setup

3.4 Gas and particulate emission Analysers

3.4.1 Fourier Transform Infrared Spectroscopy (FTIR)

A 2030 MKS FTIR was employed to measure the exhaust gases concentration and a selection of hydrocarbons. The different compounds that can be tested with this equipment along with the lowest detection limit that can be recognised is detailed in Table 3.4.

Table 3.4: FTIR lowest detection limit for the different gaseous species

Species	Lowest detection limit
Tetrafluoromethane- CF4	40ppb
Nitric oxide- NO	3.6ppm
Silicon tetrafluoride- SiF4	0.15ppm
Sulphur dioxide- SO2	0.6ppm
Methane- CH4	0.6ppm
Ammonia- NH3	0.5ppm
Formaldehyde- H2CO	0.6ppm
Xylenes- C8H10	1.0ppm
Hydrogen chloride- HCl	1.5ppm
Carbon dioxide- CO2	0.2ppm
Hydrofluoric acid- HF	0.2ppm
Nitrogen trifluoride- NF3	0.5ppm
Nitrogen dioxide - NO2	0.4ppm
Carbon monoxide- CO	1.2ppm

Conceptually, FTIR operates based on the molecular infrared (IR) spectroscopy absorption concept. An IR spectrum travels through a gas mixture so that the incorporated molecules interact with that spectrum by absorbing light at specific wavelengths. Since each gas species has a unique fingerprint spectrum, FTIR is highly-effective method for gas analysis. However, the representative spectrum of medium and long chain HCs cause interferences in

the FTIR detector, thus the total concentration of those species was measured as a single exhaust gas group, so called “FTIR-Diesel”.

The exhaust gas samples were filtered to prevent any possible damage of the FTIR’s lens by soot particulates deposition. The gas sample was heated to 191 °C prior to introducing it to the analyser to prevent any possible condensation of the exhaust HCs and water in the sampling line.

3.4.2 Gas chromatography with a thermal conductivity detector (GC-TCD)

A Hewlett-Packard (series II) GC-TCD was utilized to monitor the H₂ concentrations in the exhaust stream and at the inlet of the reactor. To increase the sensitivity of the TCD towards H₂ detection, argon was used as a carrier gas since its thermal conductivity (0.024 W/m.K) is less similar to H₂ compared to that of other conventional carrier gases like Helium and Nitrogen. The sampled gas is injected into two separation tubes, known as “columns”, the first is Haysep Q (Length = 1 m, diameter = 1/8 in) and the second is Molesieve 5Å (Length = 2 m, diameter = 1/8 in). Prior testing any sample, the GC is calibrated using a gas mixture containing 5% H₂ and 95% N₂. The reference H₂ chromatogram is automatically generated using an in-built software that can plot and calculate the area of H₂ and nitrogen peaks detected by the equipment, as shown in Figure 3.3 (a). When measuring the actual samples, a new chromatogram is produced with different peak magnitudes at the same retention time (or slightly shifted) of that used for the calibration. This will allow the user to extrapolate the volumetric H₂ concentration out from the chromatograms of the calibration. An example of the method of extrapolation is detailed in Figure 3.3 (b).

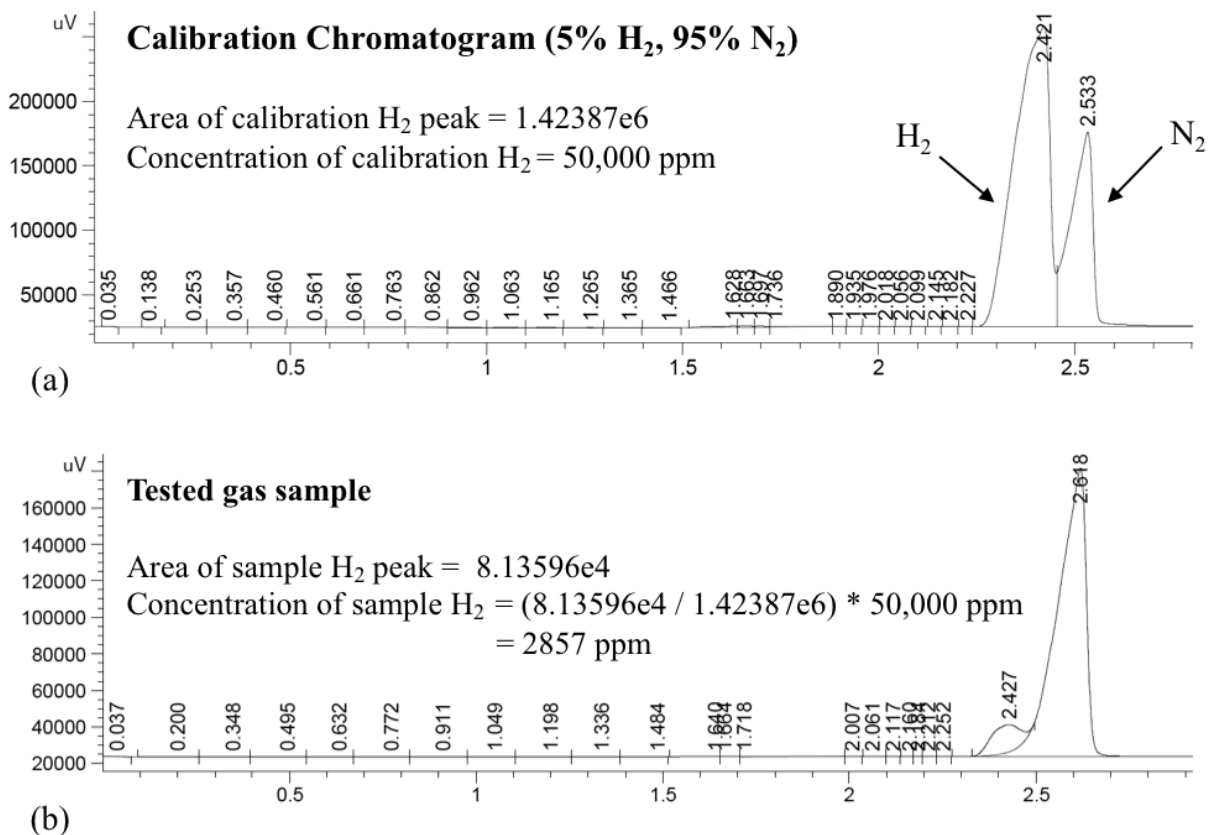


Figure 3.3: (a) GC-H₂ chromatogram of the calibration bottle and (b) Chromatogram of the sampled gas along with the method of calculation for the H₂ volumetric concentration

3.4.3 Scanning mobility particulate sizer (SMPS)

A TSI SMPS Aerosol Instruments that includes a 3081 Differential Mobility Analyzer (DMA), 3080 electrostatic classifier and a 3775 Condensation Particulate Counter (CPC) was utilized for testing the engine-out particulate size distribution. The sheath flow was set to 6 l/min and the sample flow to 0.6 l/min, which in turn allows the measurement of the particulates in the range of 10 to 406.8 nm. The sample diluting ratio (DR) was calibrated to 10-11 by the help of an ejector diluter to pre-condition the sample for the SMPS measurements. The DR was

continuously measured based on two different gases (NO and CO₂) concentration, as shown in

Equation 3.2

$$DR = \frac{NO_{raw\ exhaust} (ppm)}{NO_{diluted\ sample} (ppm)} = \frac{CO_2_{raw\ exhaust} (\%)}{CO_2_{diluted\ sample} (\%)} \quad \text{Equation 3.2}$$

3.5 Soot characterization analyzers

3.5.1 Thermo-gravimetric analysis (TGA)

TGA is an analytical method used to determine the VOF level in a soot sample and define its thermal stability by monitoring the sample weight variation when subjected to heat under different types of surrounding environments. The equipment used in the analysis (Perkin-Elmer) is presented in Figure 3.4.



Figure 3.4: TGA used in the research work

To achieve that, Tissue Quartz (TQ) filters with 47mm diameter, namely, TISSUEQTZ 2500 QAT-up, were used to gather the required soot samples for this analysis. Filters were pre-heated to 650 °C for a duration of 5 hours prior commencing the collection process. Thermal treatment ensures that the TQ filter will not have any chances to decompose (material loss) during any stage of the TGA program, especially in the nitrogen phase, which in turn can negatively influence the accuracy of the results. Afterwards, filters were fitted into an in-line holder and attached to a vacuum-assisted partial-exhaust line. The filters were loaded to a target mass of 3 mg by monitoring the soot deposition weight every 30 min using a precision balance model OHAUS PA114 with 0.01 mg readability.

Circular cuts of 5 mm in diameter were stamped out from the loaded TQ-filters using a sharp cutting tool and placed in the ceramic crucible of the TGA in a way that approximately 0.12 mg of PM is tested in each run, as advised in ref. (C. Wang et al., 2014). Soot was not extracted from the filters since it is earlier advised in reference (Bhardwaj et al., 2013) that this activity can alter the packing density of the particulates, which in turn will influence the original oxidative behaviour of the sample.

The TGA heating program implemented in this thesis work comprise two operating atmospheres, nitrogen phase and oxygen phase. Further clarification for the different heating steps (i.e. 1 to 5) and the purpose of each atmosphere is highlighted in Table 3.5.

Table 3.5: TGA heating program steps

Step	Description
1	Sample is heated from the normal room temperature (20-22 °C) to 400 °C with a rate of 10 °C/min using an inert atmosphere of N ₂ (40 ml/min)
2	Sample is kept isothermal for 30 minutes at 400 °C to ensure that all the VOF is devolatilised
3	Sample cooled-down from 400 °C to 200 °C with a rate of 10 °C/min
4	Nitrogen gas changed to oxygen rich environment (10% O ₂ , 90% N ₂) to start the carbon oxidation process. After changing the atmosphere, the sample is maintained isothermal at 200 °C for 10 min to stabilize the weight measurement fluctuations
5	Sample is heated with a rate of 3 °C/min using the oxygen rich atmosphere (40 ml/min) to reach 650 °C and kept isothermal for 20 min before cooling down the sample and finalising the test

The thermal characteristics of the collected PM were identified via two different methods:

(a) Soot activation energy denoted as “E_a” in the thesis body and calculated using the simplified Arrhenius-type relation presented in Equation 3.3
 and illustrated in Figure 3.5. E_a indicates the required energy to efficiently oxidise the soot, higher values indicate a lower oxidative potential.

$$\ln\left(-\frac{1}{m} \frac{dm}{dT}\right) = \frac{-E_a}{R} \left(\frac{1}{T}\right) + \ln(A_{PO_2}) \quad \text{Equation 3.3}$$

Where m is the instantaneous weight of the sample, T is the corresponding temperature in Kelvin, $\frac{dm}{dT}$ is the first derivative of the mass variation as a function of temperature, R is the universal gas constant (8.314 J/mol.K), and A_{PO_2} is the oxygen partial pressure. E_a is calculated by plotting $-\frac{1}{m} \frac{dm}{dT}$ as a function of $\frac{1}{T}$ as shown in Figure 3.5, which should result in a linear line that has $\frac{-E_a}{R}$ as a slope (Gogoi et al., 2015).

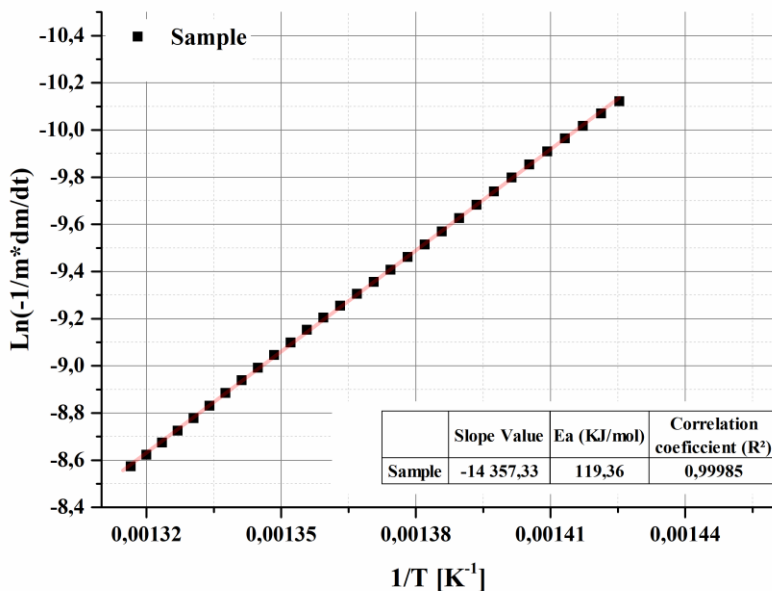


Figure 3.5: Representation for the E_a calculation method

(b) Soot ignition temperature which is technically recognised from the $\frac{dm}{dT}$ plot by assessing the position of the peak derivative over the temperature axis, as shown in Figure 3.6 (Man et al., 2015; Mühlbauer et al., 2016). The higher is the soot ignition temperature, the worse is the reactivity.

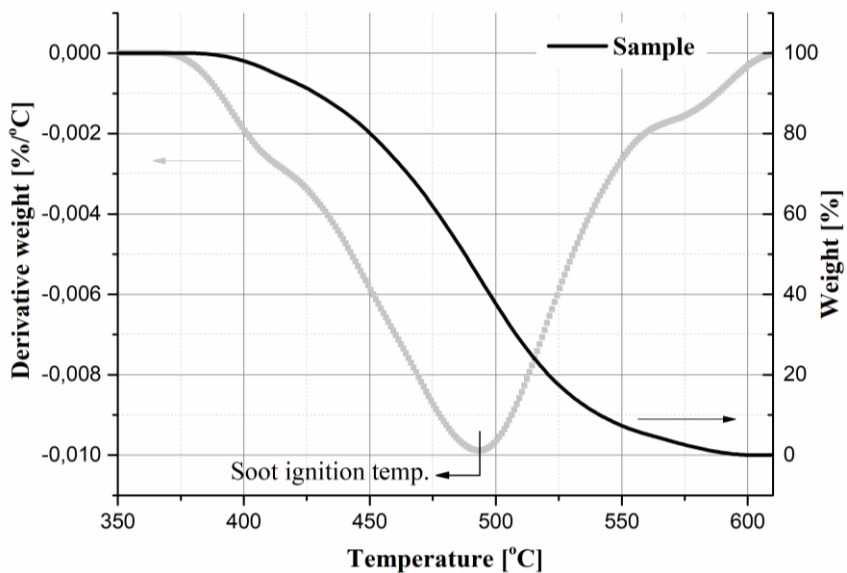


Figure 3.6: Representation for the soot ignition temperature calculation method

3.5.2 Scanning/Transmission electron microscope with energy dispersive x-ray spectroscopy

PM elemental composition was indicated by the help of a FEI TalosTM F200X S/TEM microscopy. The instrument is equipped with a super-X EDS that includes four silicon drift detectors and possess a compositional mapping capability of 10^5 spectra/second. Soot collected on the filters cannot be directly subjected to this testing method. Soot was extracted from the filters by dissolving it in an ethanol solution and then transferred to a TEM copper grid. Afterwards, the grids were heated in a TGA using a nitrogen flow to evaporate all the volatiles prior to the testing. Each grid was analysed in four different locations, making sure that we are testing agglomerates with different diameters to fairly determine the average elemental composition of each sample.

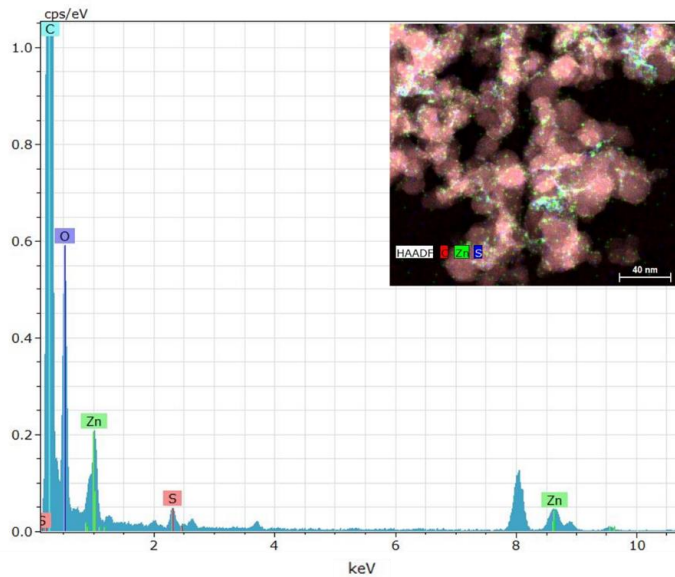


Figure 3.7: EDS micrograph showing the compositional element of the agglomerate

3.5.3 TEM and HRTEM analysis

When it comes to the soot structure, PM can be evaluated on two different scales, either by assessing the whole geometry of the aggregate (i.e. morphological analysis) or by inspecting the carbon layer ordering comprised in each primary particulate (i.e. nanostructure analysis).

The corresponding micrographs needed for the analysis were attained using the same TalosTM F200X S/TEM reported earlier in Section 3.5.2. This analyser can offer high-resolution micrographs with a precision up to 0.12 nm using an in-built Ceta 16MTM camera. To obtain the needed images, the camera operating voltage was set to 200 KV and the samples were examined under two different zooming scales of 100K and 500K, to capture the needed micrographs for the morphology and the nanostructure analysis, respectively.

3.5.3.1 Morphology analysis

To assess the particulates' morphology, several parameters should be defined from the S/TEM micrographs:

- primary particulate size (d_{p0})
- number of primary particulates within the aggregate (n_{p0})
- radius of gyration (R_g)
- the fractal dimension (D_f)

The accurate and exact evaluation of the primary particulate size is the crucial factor that will dictate the accuracy of the morphological analysis as all the other parameters (i.e. R_g , D_f and n_{p0}) are derived from it. The common methodology to evaluate d_{p0} is to manually calculate it from the micrographs. To do that, the background is first removed, and the image contrast is enhanced to ease the identification of the spherules and clearly recognise their boundaries. Afterwards, ImageJ software is used to fit a circular approximation over the primary particulates as presented in Figure 3.8.

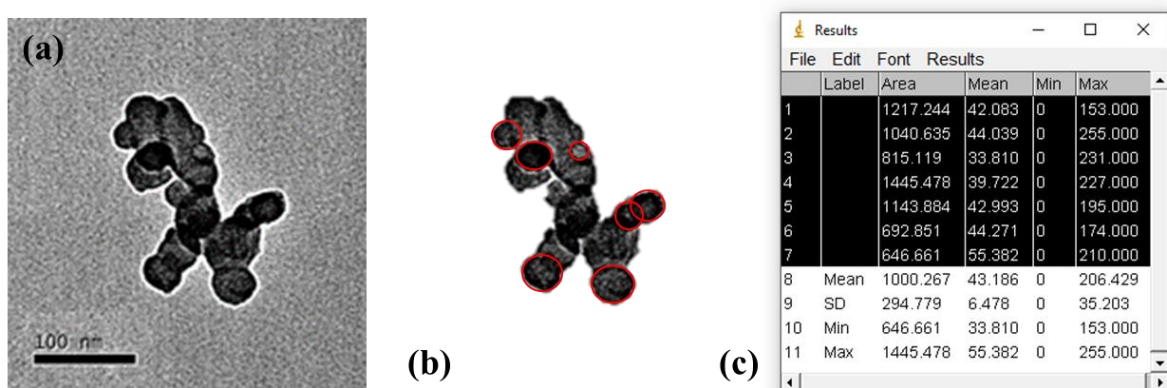


Figure 3.8: (a) Micrograph of an agglomerate, (b) Post processed micrograph: background removal and primary particulates fit by circular approximation using ImageJ, (c) Results

To increase the accuracy of this methodology, it is of importance to measure only the clearly recognised spherules and the size of the sample must be large enough. Technically speaking, around 350-400 primary particulates should be analysed for each sample by selecting around 30 particulates from different positions of the grid. d_{p0} should be fitted as a log-normal distribution.

n_{p0} is the number of the spherules (primary particulates) in an aggregate. This parameter is calculated by referring to

Equation 3.4

$$n_{p0} = \left(\frac{A_a}{A_p}\right)^\beta \quad \text{Equation 3.4}$$

Where:

A_a is the projected area of the aggregate

A_p is the area of the mean value of d_{p0} . A_p is calculated by assuming that the primary particulate is a circular entity, theoretically speaking, $A_p = \frac{\pi}{4} d_{p0}^2$

β is an exponential factor that represent the particulate overlap and assumed to be a constant equal to 1.09 as suggested by Lee et al. (2013)

R_g is calculated following the

Equation 3.5, as suggested in the following references (Filippov et al., 2000; Kondo et al., 2013; Lapuerta et al., 2006)

$$R_g = \sqrt{\frac{1}{m} \sum r_i^2} \quad \text{Equation 3.5}$$

Where:

m is the number of pixels that constitute the image of the analysed aggregate

r_i is the length (nm) that links the centroid of the aggregate with the centre of each pixel

As for D_f , the nature of the soot particulates, i.e. particulates overlapping and cluster anisotropy (Van Gulijk et al., 2004; Wentzel et al., 2003) increases the challenges to calculate this parameter and can result in misleading values. Several methodologies have been proposed in the literature to reduce these discrepancies, however, till date, the most acceptable method is defined as the power law relationship or the fractal equation. D_f can be calculated by referring to the gradient of the linear regression of $\ln(n_{p0})$ as a function of $\ln(\frac{R_g}{d_{p0}})$ (Equation 3.6).

$$\ln(n_{p0}) = \ln(K_f) + D_f * \ln\left(\frac{R_g}{d_{p0}}\right) \quad \text{Equation 3.6}$$

Where K_f is the pre-factor or structural coefficient (Wozniak et al., 2012). An illustration showing the method of calculation is presented in Figure 3.9.

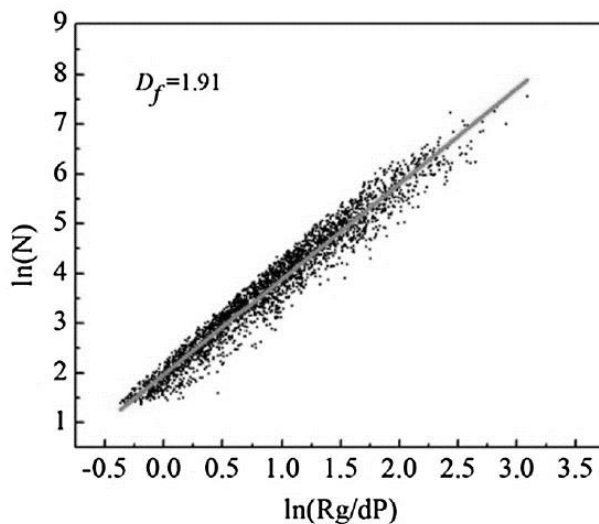


Figure 3.9: Calculation for the particulate fractal dimension

To calculate n_{p0} , R_g and D_f , the post processed micrographs used for the dp0 analysis are also analysed using an in-house MATLAB code that have been developed based on the equations reported above.

3.5.3.2 Nanostructure analysis

Concerning the particulates' nanostructure, as it was detailed in the literature body, it is of interest to identify:

- Separation distance between the carbon layers or interlayer spacing (d_{002})
- Basal plane length of the layer (L_a)
- Tortuosity of the layer (T_f)

To evaluate these parameters, the HRTEM images were post-processed using MATLAB based on the work of Yehliu et al. (2011). The processing method can be simplified as presented in the diagram below:

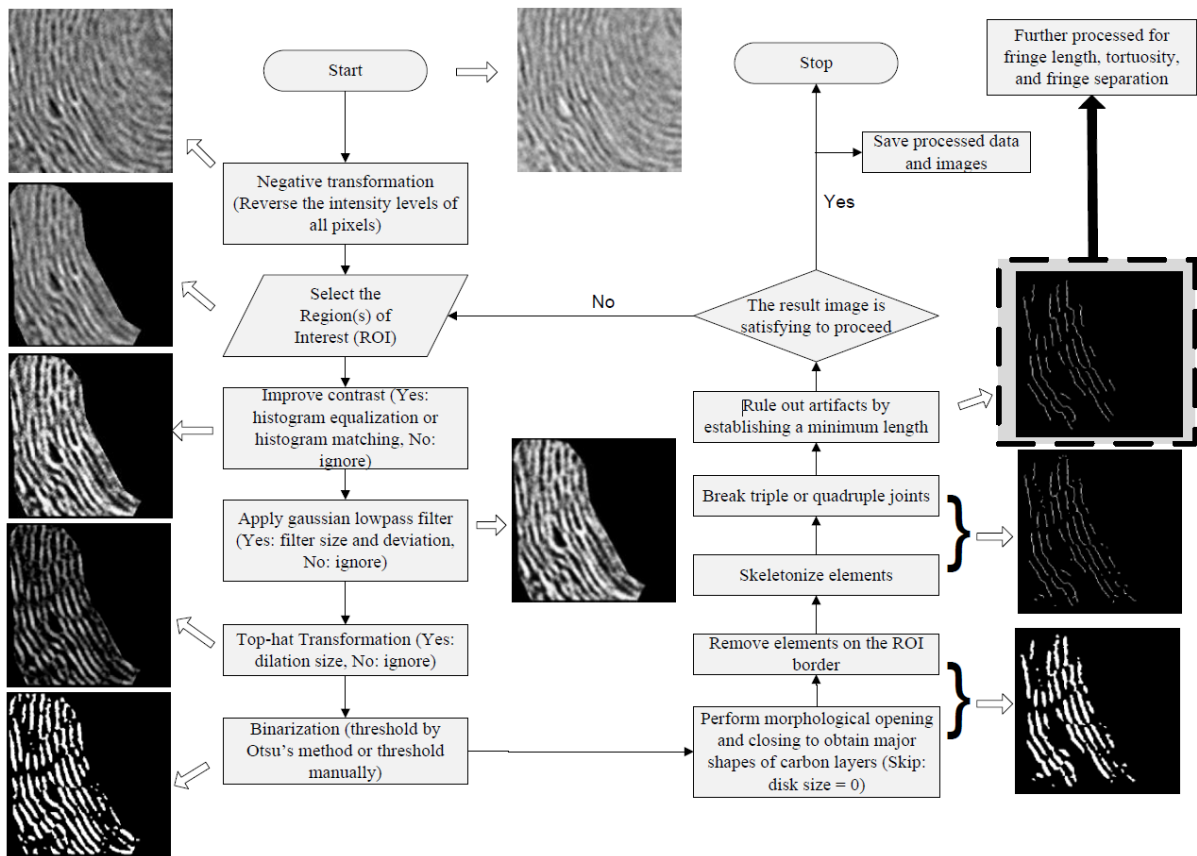


Figure 3.10: Image enhancement and post-processing methods implemented in the MATLAB coding, reproduced from (Yehliu et al., 2011)

Before starting the analysis method, it is of importance to clarify the process by which a HRTEM micrograph is obtained. The contrast of the micrographs (grayscale) is directly related to the interference of the electron beam with the carbon layers in the particulates. As a matter of fact, the carbon layers obstruct the passage of the electrons and results in a dark area at the detector. Consequently, the carbon layers appear like black lines in the micrographs.

Since the images are captured in a grayscale mode, the darker the pixels (i.e. the carbon layers), the lower the intensity, and vice versa. Therefore, negative transformation is applied to reverse the intensity level of all the pixels. Technically speaking, after applying this filter, the brighter fields, thus the more intense pixels, turns to be the carbon layer segments. This method

eases the application of the other transformations needed as the top-hat method and skeletonization.

Afterwards, a region of interest (ROI) is selected and the intensity of the pixels is increased to the highest scale possible by enhancing the contrast of the image (i.e. histogram equalization). This step is extremely important as it helps the user in differentiating the carbon segments from the background. By increasing the contrast, the noise level is also increased. Therefore, a low-pass filter is applied to reduce the effect of the high noise frequency.

The nature of the soot particulates, i.e. particulates overlapping, results in uneven illumination across the micrograph. Thereby, after applying the low-pass filter, the image is subjected to a top hat transformation (disk shape with radius of 5 pixel) to balance the irregular illumination.

The next step of the analysis consists of binarizing the image by selecting an appropriate threshold ($t = 0.133$) to extract the representative carbon layer-pixels from the background. In our analysis, the thresholding was based on Otsu's method (1979) and the representative function of this transformation can be presented as follows:

$$I_{binary}(x, y) = \left\{ \begin{array}{c|c} 1 & I_{input}(x, y) > t \\ 0 & I_{input}(x, y) < t \end{array} \right\}$$

Where,

$I_{input}(x, y)$ refers to the intensity of the processed pixel

If $I_{input}(x, y)$ is lower than the threshold, the pixel intensity is converted to 0 (black pixel) and if higher, it is converted to 1 (white pixel). After binarizing the ROI, morphological

opening and closing operation is applied to obtain the major shape of the carbon layer.

Afterwards, the layers are skeletonised based on the parallel thinning algorithm.

Figure 3.11 present a schematic of the resulted digitized image domain in the MATLAB coding.

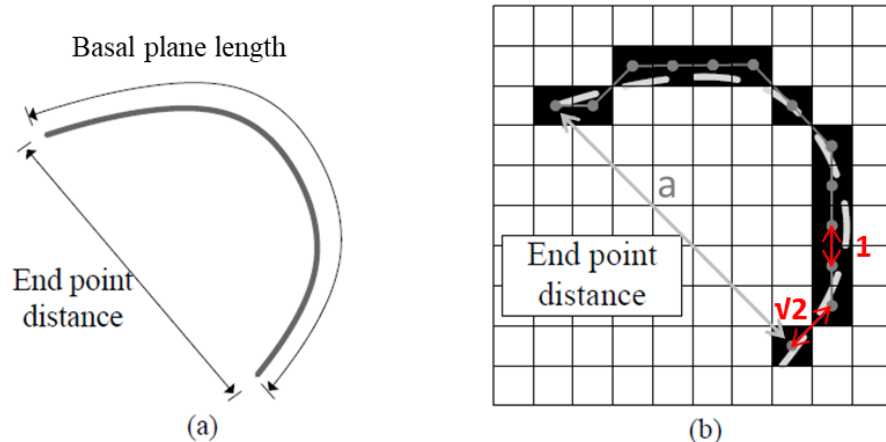


Figure 3.11: Calculation of L_a and T_f : (a) Carbon layer schematic in the continuous field, and (b) Binarized layer in the digitized field, reproduced from (Yehliu et al., 2011)

In a digitized domain, the basal plane length is calculated by summing the distance that links the center of each black pixel with the neighbouring black pixels. As presented in Figure 3.11 b, the distance between 2 adjacent pixels can be either 1 or $\sqrt{2}$ pixels. Based on the image resolution, the metric value of the pixel can be defined. The spatial resolution in this research work is 0.0235 nm/pixel for 500K magnification. To analyse the tortuosity, the distance between the two end nodes, defined as “a”, should be also calculated. T_f is then simply obtained following the equation below:

$$T_f = \frac{L_a}{a} \quad \text{Equation 3.7}$$

As for the interlayer spacing, as its name implies, it is the distance between two adjacent layers. To reduce the error in the calculation, the layers are manually selected for this operation. The closest distance separating two neighbouring layers is defined as the perpendicular distance that links the tangent-layer crosspoint with the adjacent layer (as shown in Figure 3.12 a). Although the carbon layers are usually not parallel, averaging the closest distances can highlight the interlayer spacing of the particulates.

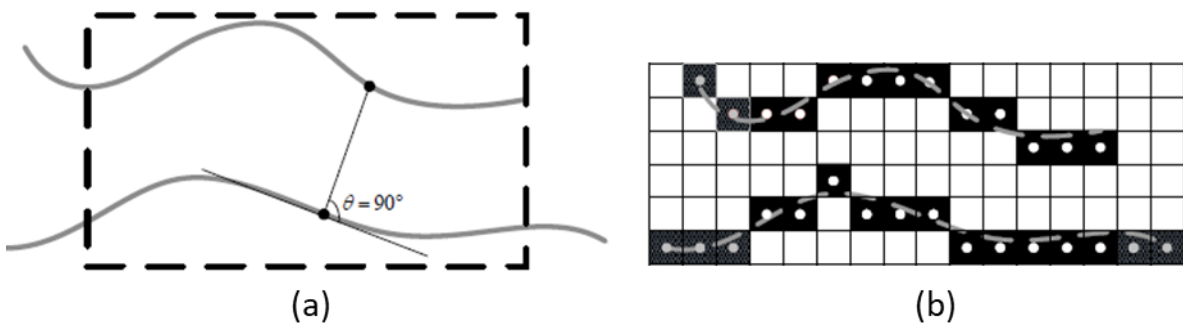


Figure 3.12: Calculation of d_{002} : (a) Carbon layer schematic in the continuous field, and (b) Binarized layer in the digitized field, reproduced from (Yehliu et al., 2011)

To calculate the nanostructure parameters, the post-processed micrographs are computed using another MATLAB coding that can generate the needed operations stated above. To ensure that the system is auto-calculating the parameters with a tolerable margin of error, a manual check for the results with respect to the MATLAB calculation have been made for each set of 5 micrographs.

3.5.4 Raman spectroscopy (RS)

The soot graphitic characteristics were determined using a Renishaw inVia Raman microscopy that comprise a research grade microscope with four objectives lens (5x, 20x, 50x and 100x) and a high-performance Raman spectrometer. Argon ion laser ($\lambda_0=532$ nm) with a

power source of 6.4 mW was used for the soot analysis to prevent any unwanted overheating which in turn can alter the nanostructure layout. The 50x lens was used to precisely guide the laser beam into the soot spots and then the spectra was recorded in the range of 800-2000 cm⁻¹. Analysis was made with an exposure duration of 20 seconds for each scan, targeting 15 accumulations for every tested sample to reduce the signal to noise ratio. To increase the reliability of the results, four distinct spots of each filter were examined.

The resulted spectrum was processed using Origin Pro 9.1 program. The data was firstly corrected with a linear-baseline, then de-convoluted to 4 Lorentzian bands, namely D1 ~ 1350, D3 ~ 1500, D4 ~ 1200 and G ~ 1590 cm⁻¹, as suggested by Sharma et al. (2016) and plotted accordingly in Figure 3.13. The corresponding indication of each spectra is discussed later in Section 4.3.5.

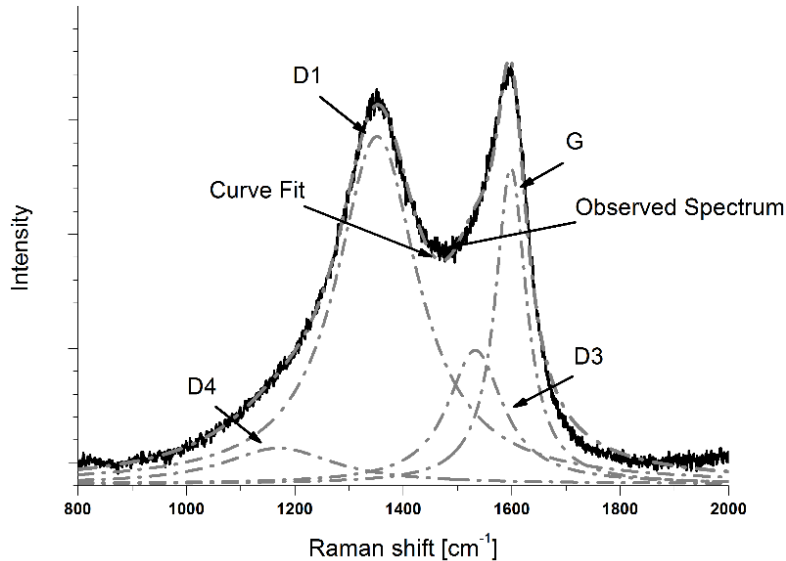


Figure 3.13: Example of a corrected and de-convoluted Raman spectra with the corresponding de-convoluted peaks

CHAPTER 4

FUEL-BORNE OXYGEN IMPACT ON PM STRUCTURE AND REACTIVITY IN MODERN DIESEL ENGINE

With the ability to synthesise propylene glycol ethers from the main by-products (glycerol) of biodiesel production process, the potential use of these oxygenates becomes a subject of interest. DPGME and TPGME were shown in the literature as viable oxygenates for mixing with diesel in terms of blend stability and PM reduction (Guo et al., 2016). Most of the studies (Burke et al., 2015; Dumitrescu et al., 2016; González et al., 2001; Mueller et al., 2003; Natarajan et al., 2001) focus on understanding the ignition mechanism of these compounds but none of them show the characteristics of the PM resulted from their combustion.

The key aim of this chapter is to study the extent for which DP20 and TP20 diesel blends can affect the engine performance, gaseous emissions and the PM tendency. A special attention was given to test the influence of the glycol ether compounds on the soot physio-chemical characteristics and its corresponding oxidative reactivity. Such findings will not only help in understanding the impact of these oxygenates on the particulate characteristics but also to clarify the gap presented in the literature regarding the correlation of each physio-chemical parameter with the oxidative potential of the particulate.

The soot analysis covered several areas, such as oxidative reactivity (TGA), elemental composition (EDS), morphology of the particulate (TEM), nanostructure of the primary particulates (HRTEM) and the corresponding graphitic order (Raman).

Tests were made under a steady state engine running condition of 1500 rpm speed, 4 Bar IMEP load condition and 600 Bar fuel injection pressure. Injections were split between a pilot-pulse at -15 CAD ATDC and a main-pulse at -8 CAD ATDC. This injection calibration (timing and fuel rail pressure) was set based on an engine optimisation that have been carried out to check the conditions on which the engine is more prone to produce soot particles. The main intention of this calibration is to ensure that the needed soot samples are collected with the least time possible. Main injection duration was updated accordingly in each fuelling condition to maintain the desired load condition; however, the rail pressure or injection timing remained constant.

A schematic representation of the soot collection and analysis methods are presented in Figure 4.1. A detailed explanation of the soot collection procedure was detailed earlier in Section 3.5.1.

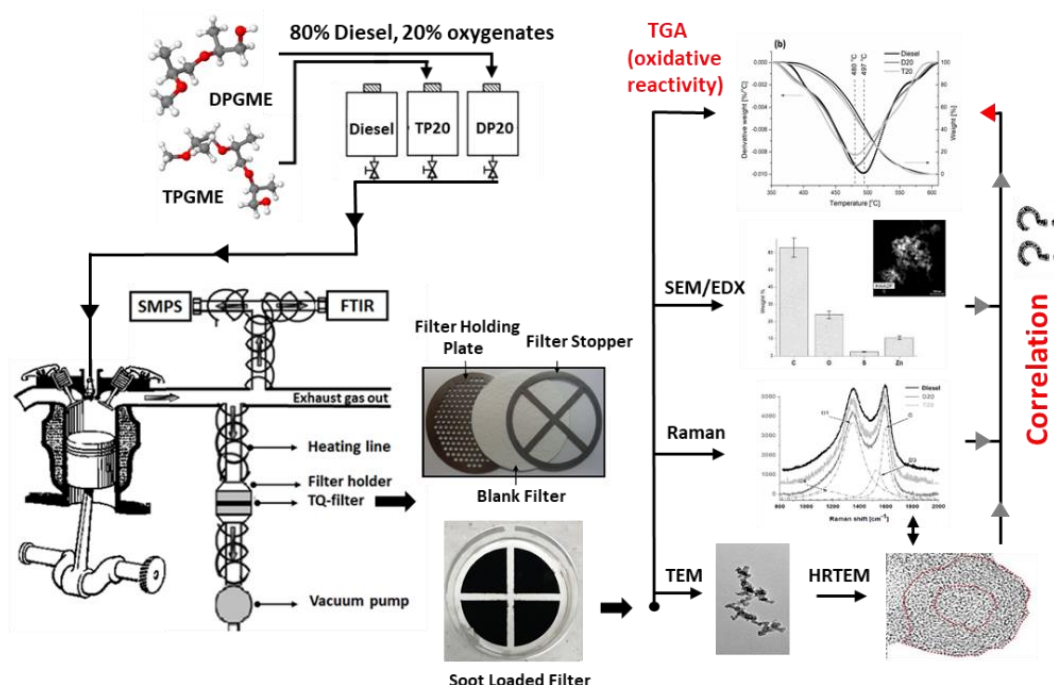


Figure 4.1: Schematic representation of the filter holder setup and location

4.1 Combustion performance and gas emission analysis

As detailed earlier in Table 3.3, both DP20 (39.58 MJ/kg) and TP20 (39.55 MJ/kg) present lower calorific value (LCV) with respect to the conventional diesel fuel (43.11 MJ/kg). Loss in heating value must be remunerated with higher fuel penalties to counter-balance the lower energy provided during the combustion cycles (Kousoulidou et al., 2010; Ren et al., 2008). Therefore, longer main injection durations were required to maintain the 4 bar IMEP load condition in case of DP20 and TP20. As indicated in Figure 4.2, engine's BSFC increase from 252.19 g/kWh (equivalent to 0.671 kg of diesel/hr) in case of diesel to 260.06 g/kWh (equivalent to 0.694 kg of TP20/hr) in case of TP20 and 260.44 g/kWh in case of DP20 (equivalent to 0.695 kg of DP20/hr).

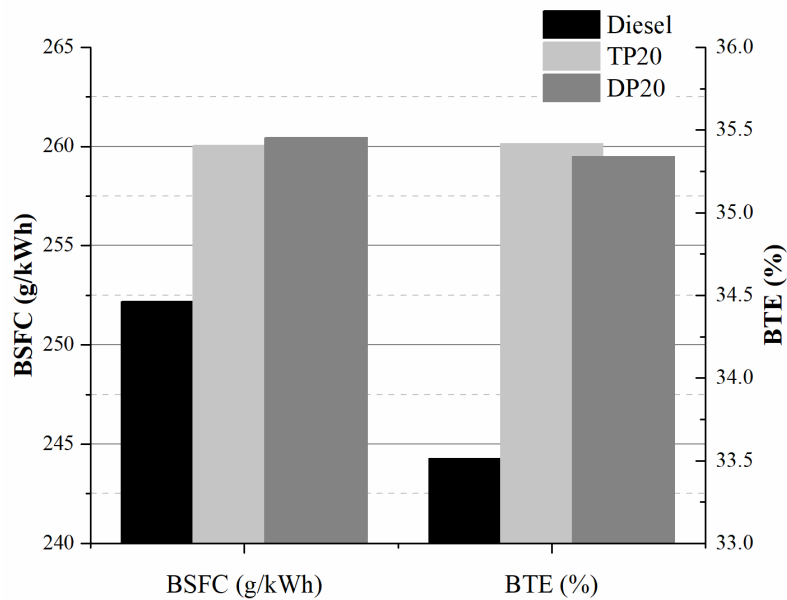


Figure 4.2: BSFC and BTE resulted from the combustion of diesel, DP20 and TP20

Concerning the CA50, the representative CAD on which 50% of the total heat is released, the value remains similar between the different fuel conditions (3 CAD ATDC). As for the combustion stability, referred to as Coefficient of Variance (COV), the value remained below 2% for all the fuel conditions, highlighting that the diesel-blends (DP20 and TP20) can result in the same stable combustion as the diesel.

However, to further evaluate the combustion efficiency, break thermal efficiency (BTE) was also calculated and plotted in Figure 4.2. It is seen that the slight increase in BSFC is compensated with an increase in the BTE, with 5.69% higher efficiency in case of TP20 and 5.44% in case of DP20. This is due to the more efficient combustion of these candidates, mainly resulting from the presence of the molecular oxygen that help in achieving more complete combustion.

Ignition delay (ID) in diesel engines is usually dependant on the fuel physical properties and chemical structure. This mechanism mainly comprises two different transitions, physical and chemical delays. The physical delay consist of three different steps: (a) droplets formation, depending on the fuel viscosity and surface tension (b) vaporization/atomization of the droplets, depending on the fuel specific heat, vapour pressure and heat of vaporisation and (c) fuel mixing with the air, depending on the fuel vapour diffusivity (Gill, 2012). Heating the fuel will help in breaking its weaker bonds to produce reactive radicals. The rate by which these radicals are generated is referred to as the “chemical delay” and it is basically influenced by the chemical structure of the fuel. However, in modern common rail diesel engines, the fuel physical properties are reported to have a limited impact on the ID which was seen to be solely dependent on the fuel cetane number (CN) (Lapuerta et al., 2008). Kidoguchi et al. (2000) reported that the higher is the CN, the shorter is the ID and as a result, the premixed combustion phase is

reduced which in turn results in lower in-cylinder peak pressures and HRR profiles along with longer combustion duration. This theory can summarise the combustion behaviour recorded with TP20 (Figure 4.3), as the CN of TPGME (CN 80) is higher than that of the diesel (CN 43.4). As for DP20 (DPGME CN 43.9), similar ID and combustion duration with slightly lower HRR peak is recorded compared to diesel as both fuels have comparable CN.

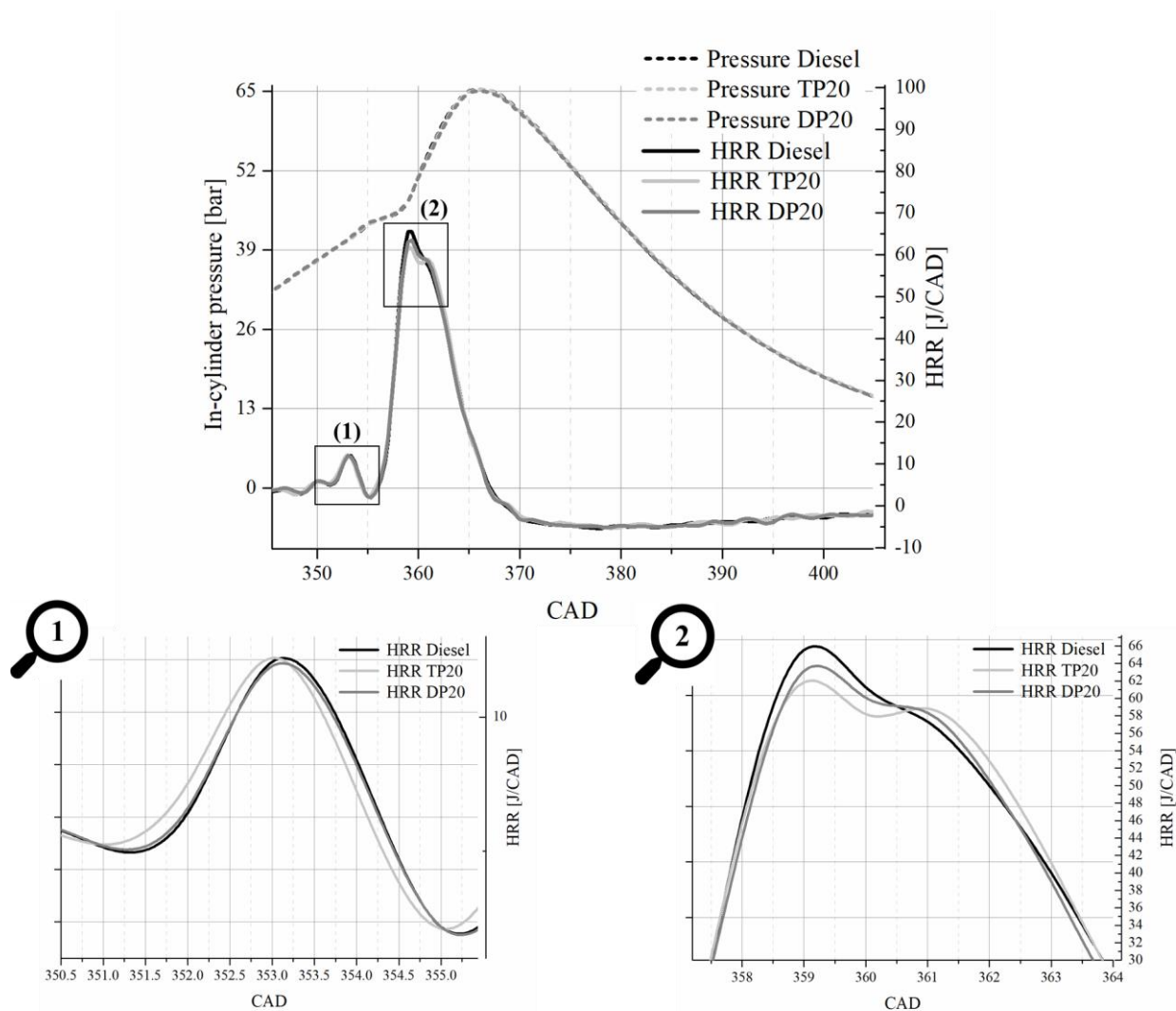


Figure 4.3: In-cylinder pressure and HRR resulted from the combustion of diesel, DP20 and TP20

The resulted gaseous emissions and exhaust gas temperatures produced from the different fuel blends is plotted in Figure 4.4.

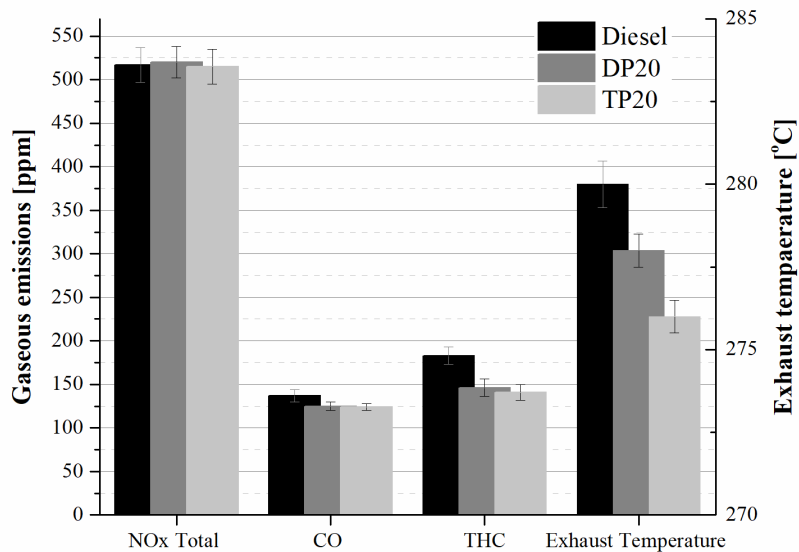


Figure 4.4: Gaseous emissions and exhaust temperature resulted from the combustion of diesel, DP20 and TP20

It is usually accepted that the combustion of oxygenated diesel blends increase the total engine out NOx emissions (Hoekman & Robbins, 2012). However, it is seen that in the case of DP20 and TP20, similar NOx level (falling within the error bar margin) is recorded compared to diesel. The most accepted NOx formation mechanism till this date is the “thermal NO” mechanism. The increased temperatures shown during the combustion helps in dissociating the O₂ into molecular oxygen (O), which helps in initiating the NOx development chain-reactions. As for the potential flame zone in which NO is produced, it is mainly located on the external boundaries of the diffusion flame. This is mainly due to the presence of (a) the needed high temperatures (~ 2700 K) to launch the thermal NO mechanism along with (b) enough amounts of oxygen since the outer side of the flame is considered as a lean region. The leaner the combustion, the higher the NO level (Gill, 2012; Heywood, 1988). The use of oxygenated fuels

is expected to yield more stoichiometric conditions compared to diesel during the premixed phase and as a result produce higher in-cylinder temperatures, which as explained above will increase the rate of NO formation. Also it is seen that along the flame lift-off length (i.e. the distance from the injector to the end of the flame during diffusion combustion), the greater availability of the molecular oxygen is reported to (a) increase the adiabatic flame temperature and (b) reduce the oxygen equivalence ratio (more lean) compared to diesel, thus result in higher local temperatures and NOx levels (Hoekman & Robbins, 2012). However, as seen from Figure 4.4, both TP20 and DP20 did not negatively impact the NOx level compared to diesel. It is likely that, since DP20 and TP20 blends present a higher latent heat of vaporisation (LHV) compared to diesel (Table 3.3), more energy is required to vaporise the A/F mixture. As a result the maximum flame temperature is reduced, which in turn decelerates the thermal NO formation and compensate the oxygenation impact discussed above (Lei et al., 2011).

HCs emissions are basically derived from the incomplete combustion of the A/F mixture, thus highly dependent on the in-cylinder oxygen availability. CO is also considered as a product of the non-complete combustion of the fuel when HCs are not fully oxidised into CO₂. It is seen that with DP20 and TP20 fuels, the total HCs and CO emissions are reduced. Oxygen-borne fuels reduce the mass of carbon fraction in the blend and also result in a more complete combustion (better oxidation of the HCs), which in turn help in reducing both HCs and CO emissions (Ren et al., 2008). The more efficient combustion suggested for DP20 and TP20 blends was approved earlier from the higher BTE level seen in Figure 4.2.

4.2 Particulate Matter tendency

The corresponding data for 4 repeated measurements of the distribution of the electrical mobility particulate diameter (d_{smps}) next to the total particulate number concentration (TPNC) and the agglomerates geometric mean diameter (GMD) are shown in Figure 4.5.

TPNC shows a reduction of 42% and 53%, and GMD has been reduced by 12.1% and 12.2% in case of DP20 and TP20 blends respectively. In general, oxygenated fuels are likely to yield more complete combustion compared to traditional diesel, even in the fuel-rich regions of the flame. This is mainly attributed to two phenomenon: (a) the extra amount of oxygen-borne species (O and OH) helps in oxidising the already formed soot precursors into combustion products instead of being transformed into aromatics and soot as explained earlier in Section 2.2 (Herreros et al., 2015; Mueller et al., 2003). (b) the molecular C-O moieties presented in the oxygenates structure are expected to survive the fuel-rich ignition phase by that suppressing the rate of soot formation (An et al., 2015; Westbrook et al., 2006). As a result lower level of particulate characterised with a smaller geometric mean diameter is expected from their combustion.

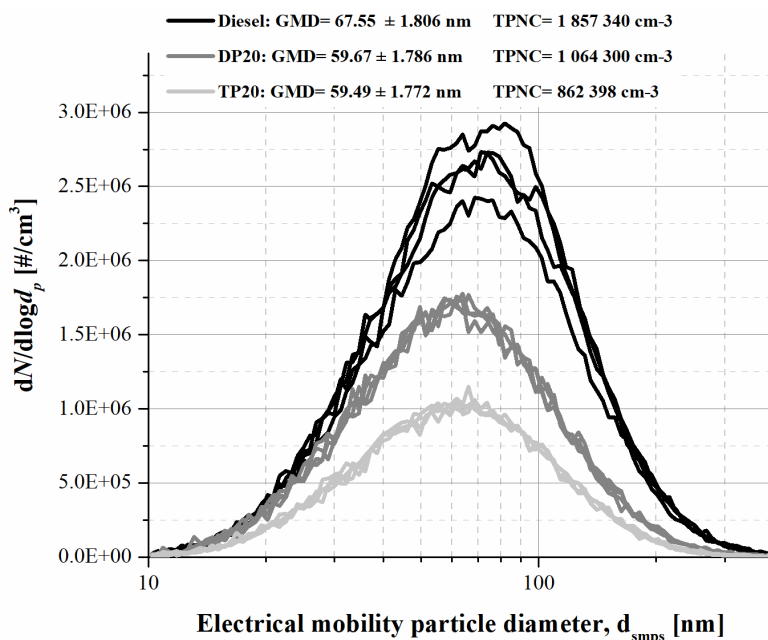


Figure 4.5: GMD, TPNC and d_{smps} distribution for the particulates produced from the combustion of diesel, DP20 and TP20

When it comes to TPGME, several researchers (Burke et al., 2015; Mueller et al., 2003; W. Park et al., 2017) suggested that along with the factors stated above, the atomic structure of this candidate presents an advantageous role in limiting the soot inception mechanism, as explained below. Figure 4.6 presents the position of the oxygen linkage and their type in the molecular chain of DPGME and TPGME fuels. It should be noted that a full representation of all the existing isomers of TPGME can be found in this reference (Burke et al., 2015).

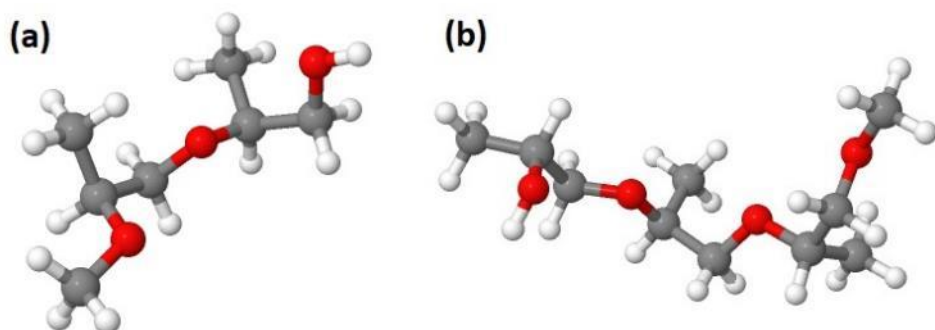


Figure 4.6: The corresponding structure of (a) DPGME, and (b) TPGME

TPGME presents a highly branched structure in which four oxygen moieties are evenly dispersed through the chain in a manner that three of them (i.e. the ether moieties) are linked to two carbon atoms and only one (i.e. alcohol) is linked to a single carbon atom. This effective configuration ensures that throughout the combustion process, TPGME is more likely to be decomposed into CO molecules rather than CO₂, hence eliminating the maximum portion of carbon elements from contributing to the pool of soot precursor species (Burke et al., 2015).

Despite that DPGME has the same chemical configuration as TPGME, lower soot reduction capability was shown in our test. This should be directly related to the fuel physical properties. It is widely accepted that the fuel atomisation process is directly related to the fuel boiling point and can have a direct impact on the soot emissions (Hellier et al., 2012; Hellier et al., 2017). Higher boiling temperatures indicates that higher energy is required to vaporize the fuel injected, thus, a poorer atomization will be resulted, which, consequently, will intensify the fuel-rich regions in the mixture and promote the soot formation process (Hellier et al., 2012; Hellier et al., 2017). As seen in Table 3.3, DP20 presents a higher boiling temperature compared to TP20 and as a result, it can be speculated that this physical property can be responsible for the difference recorded in our analysis.

4.3 Particulate characterisation

4.3.1 Soot oxidative reactivity

The PM loaded on the filters can be generally defined as a combination of three different compounds: (i) elemental carbon that constitute the base of the particulates, known as the soot fraction, (ii) soluble/volatile components which are adsorbed or condensed on the soot surface, (iii) ash deposits (C. Wang et al., 2014). Volatiles are mainly originated from the unburned fuel

hydrocarbons and engine lubricating oil. A detailed explanation of the soot composition was already detailed in Section 2.3.

The nitrogen phase testing in the TGA is an effective method to identify the volatile fraction in the PM, the air phase testing is helpful to evaluate the oxidative potential of the soot. It should be noted that the ash residuals cannot be adequately monitored in our samples since soot was tested without being removed from the TQ filters. As from this stage of the thesis, the PM produced from diesel, DP20 and TP20 combustion will be referred to as “ S_{Diesel} ”, “ S_{DP20} ” and “ S_{TP20} ” respectively.

Concerning the volatiles (Figure 4.7), it is seen that the soot chemical composition strongly depends on the parent fuel type, with S_{TP20} presenting the highest volatile fraction of 80.9%, followed by S_{DP20} and S_{Diesel} with 72.8% and 70.53%, respectively.

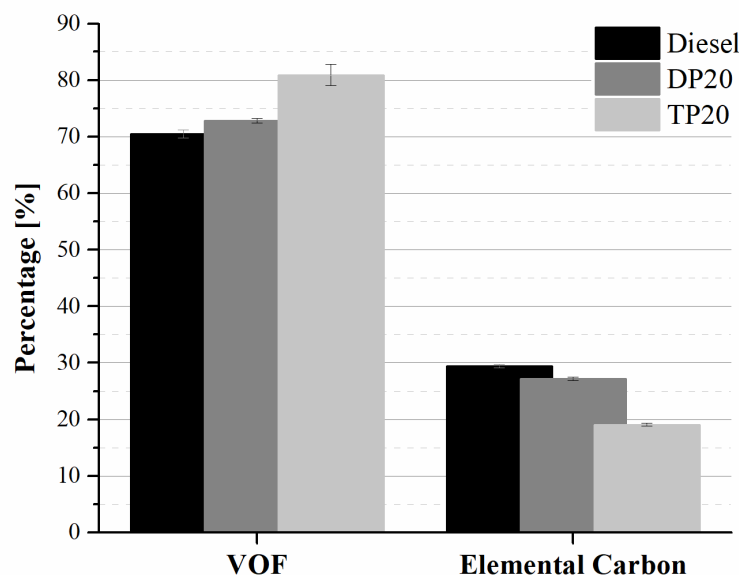


Figure 4.7: PM chemical distribution, elemental carbon and volatiles fraction

This increase in case of the oxygenates can be the result of several factors: (i) the lower exhaust temperatures favours the accumulation of the HCs on the soot surface, even though the

total HCs emissions were reduced compared to diesel (Wei et al., 2016). (ii) As seen from the SMPS results, lower PM level was produced from the combustion of DP20 and TP20. Consequently, the unburned HCs have fewer particulates to condense on, thus PM with higher fraction of volatiles is expected (Wei et al., 2016). Considering the resulted exhaust temperatures and engine-out PM levels, the combustion of the tested fuels can be ranked in the following order: TP20 < DP20 < Diesel, making a positive fit with the TGA results (volatile fraction) as clarified from the above bullets (i) and (ii).

Concerning the soot oxidation process, a representation of the soot weight loss and the rate of weight loss in function of temperature is plotted in Figure 4.8. S_{DP20} and S_{TP20} start oxidising at lower temperatures than S_{Diesel} but shows to end their oxidation in a similar range (~ 570 °C). Concerning the rate of oxidation, faster oxidation is recorded for both samples (S_{DP20} and S_{TP20}) along all the burn-off stages and a lower ignition temperature (475-480 °C) was seen compared to the diesel reference (500-510 °C).

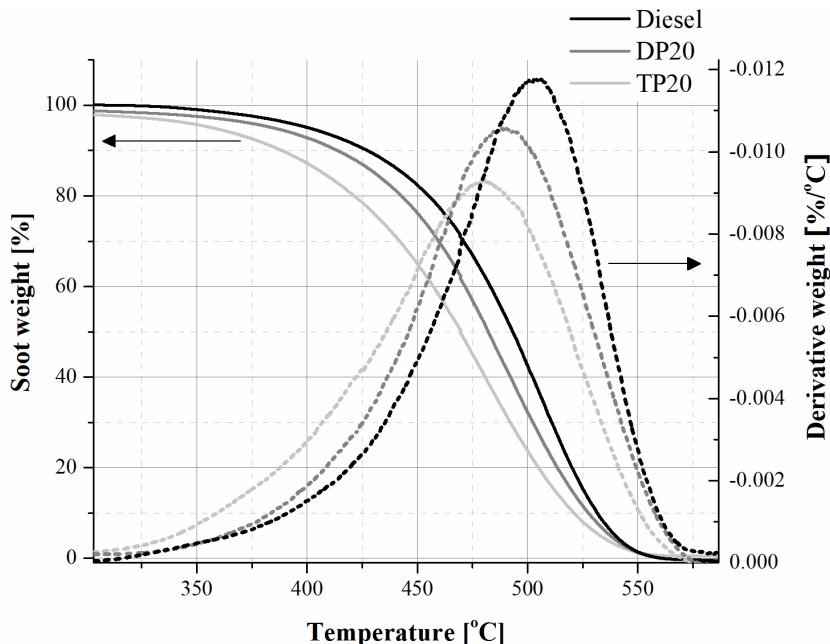


Figure 4.8: Soot weight loss and the corresponding rate of weight loss

To further confirm the ameliorated oxidative potential of S_{DP20} and S_{TP20}, the soot activation energy (Ea) was also calculated by applying the simplified Arrhenius-type model detailed earlier in Section 3.5.1 (Figure 4.9). To calculate Ea, the temperature range that results in the highest correlation coefficient of the linear fit of $-\frac{1}{m} \frac{dm}{dT}$ as a function of $\frac{1}{T}$ is used. Technically speaking, the soot weight-loss of 10% to 50% was considered for the calculation of Ea.

S_{TP20} proved to be the most reactive particulates with an Ea of 100 kJ/mol, followed by S_{DP20} and S_{Diesel} with 115.2 and 119.36 kJ/mol respectively. To understand the differences spotted in the particulate's oxidative behaviour, the correlation between the volatile fraction and the PM activation energy is plotted in Figure 4.9 (b).

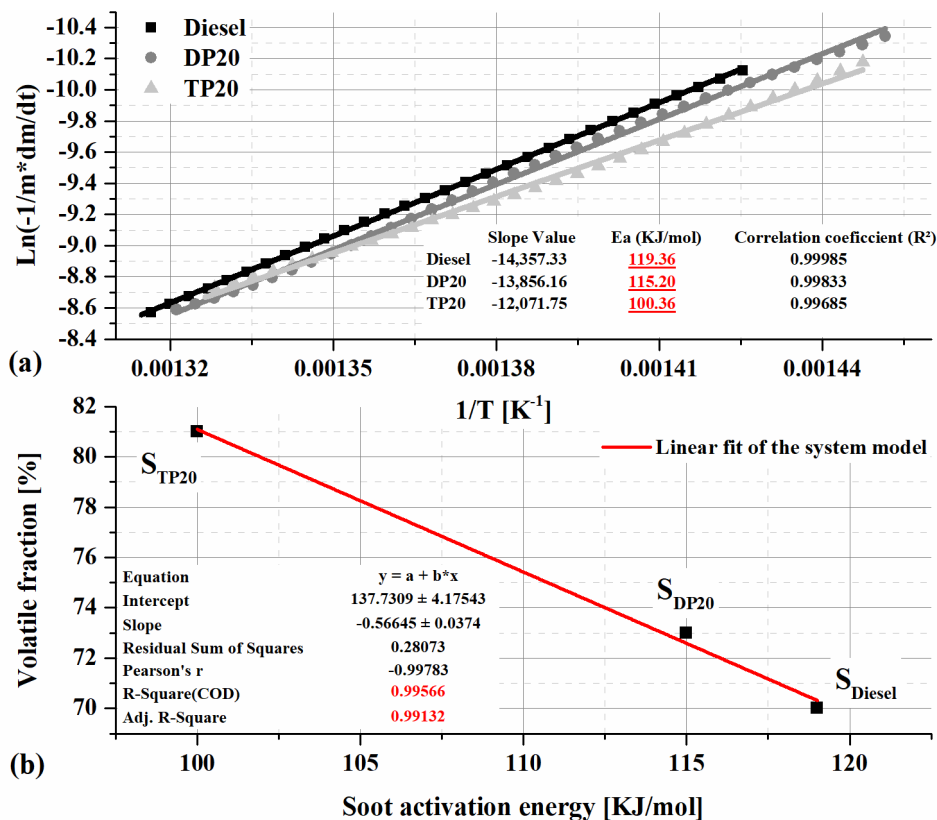


Figure 4.9: (a) Soot activation energy calculated following the Arrhenius-type model and (b) Correlation of volatile fraction with the soot activation energy

As shown in Figure 4.9, a linear fit is observed between these two factors, highlighting the dependency of the PM reactivity upon its volatile fraction. Even though the VOF was evaporated before starting the soot oxidation phase, the devolatilization of these species will lead to the opening of new micropores in the soot surface (increase the porosity). As a result, the area wherein the oxygen molecules can diffuse and react will become larger, which in turn will ease the oxidation process and increase its kinetics (Barrientos, 2014).

In the following sub-sections of this chapter, the soot elemental composition, morphological properties, nanostructure arrangement and graphitic structure are analysed to identify the relationship of each physio-chemical parameter with the recorded reactivity.

4.3.2 PM Elemental Composition

PM's elemental composition, oxygen as well catalytic active material (found in ash) is believed to have a direct influence on the soot oxidative reactivity (López Suárez et al., 2011; X. Wang et al., 2012). S/TEM-EDS technology has been employed in this research work to determine the oxygen, carbon and metallic compounds of the particulates collected on the TQ filters. However, the main drawback of this technique is that light elements (i.e. atomic number (Z) less than 11), such as H_2 ($Z=1$), cannot be quantified (Australian Micrpscopy and Microanalysis Research Faculty, 2014). The different elements detected in the analysis are plotted in Figure 4.10 and discussed in detail by assessing its relationship with the particulate's reactivity, if applied.

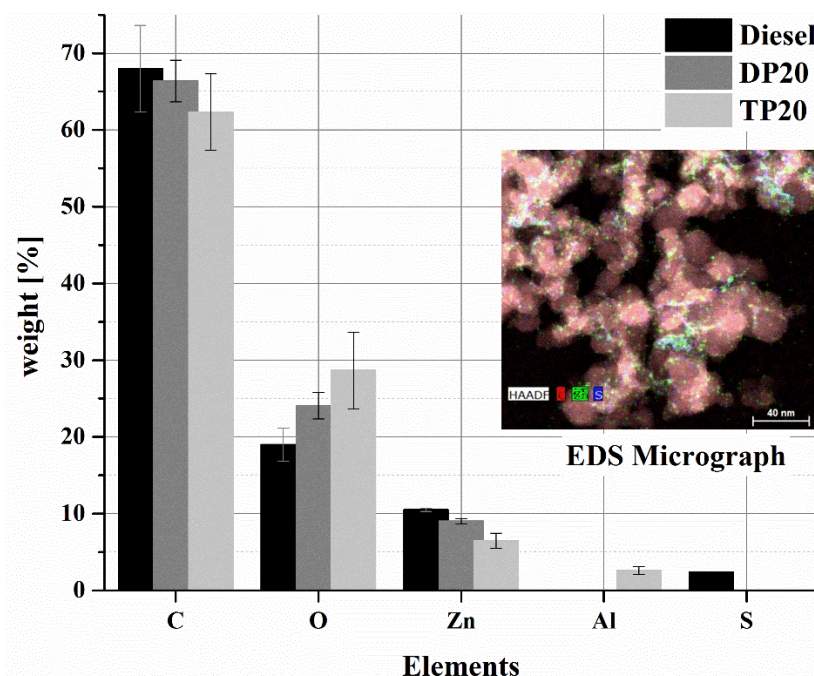


Figure 4.10: EDS analysis of the different tested samples

- **Carbon**

The average carbon content of the particulates shows a dependency upon the parent fuel type. It was seen that with the application of the oxygenated fuel, the carbon content decreased from 68% in case of ULSD to 65% in case of DP20 and 60% with TP20. As oxygenated fuels tend to further oxidise the soot particulates throughout the combustion process, not only the total engine-out soot emissions are reduced, but also the average carbon content of the individual particulates (Xi & Zhong, 2006). As a result, S_{DP20} and S_{TP20} presented lower carbon content compared to S_{diesel} . In addition, TP20 prove to be more effective than DP20 in reducing soot emissions, thus higher rates of soot oxidation can be expected, which in turn explain why S_{TP20} presents the lowest carbon content among all the tested samples. Those results were further verified in the TGA analysis where the solid carbon portion in S_{DP20} and S_{TP20} shows to be lower than that of the S_{diesel} .

- **Oxygen**

In the same way as the particulates carbon content, oxygen shows a strong dependence on the fuel type with TP20 showing the highest content (~30%) followed by DP20 (~25%) and Diesel (~19%) respectively. The higher portion of oxygen shown in case of S_{DP20} and S_{TP20} cannot be explained from the fact that the unburned fuel portion condensed on the soot is already oxygenated neither that the VOF portion is increased. The soot samples were devolatilized prior the EDS analysis, which in turn isolate the impact of the VOF on the composition. It can be then speculated that the presence of the molecular oxygen (i.e. ether and alcohol moieties) in DP20 and TP20 increase the level of the surface-bond oxygen functional groups in the soot produced from their combustion (J. Song et al., 2006).

EDS can be considered as a qualitative analysis more than being an accurate method to quantify the exact Carbon and Oxygen content in the particulates (Pettersson, 2013). Yet, it is usually used to determine the relative amount of oxygen with respect to carbon (O/C ratio) (Pettersson, 2013). The relationship between O/C ratio and the soot activation energy is plotted in Figure 4.11. Linear relation of a correlation ~ 92% is seen between the parameters. This positive relation indicates that the concentration of the surface oxygen functionalities has a direct impact on the soot oxidative behaviour. This could mainly result from the fact that surface oxygen functionalities can increase the reactivity of the edge plane by reducing the stability of the carbon layer (Barrientos, 2014; Radovic et al., 1983). For a detailed approach concerning the role of the oxygen moieties in enhancing the soot reactivity, the reader is referred to Section 2.4.2 in the literature body.

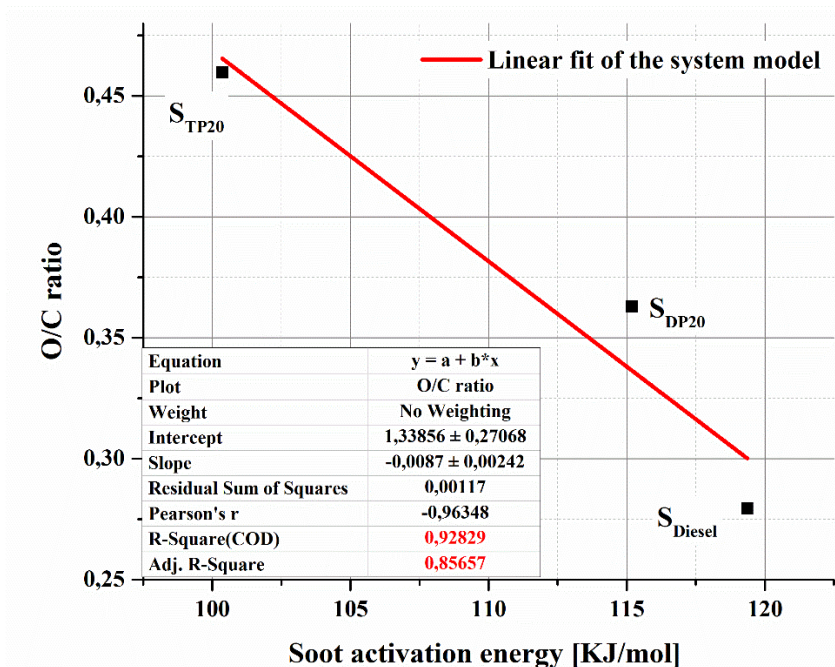


Figure 4.11: Correlation of the O/C ratio with the soot activation energy

- **Ash species**

EDS spectra indicates that aluminium and zinc are the sole constituents of the ash sediments in the tested samples. Previous work reported that zinc is a very active catalytic material that can significantly boost the soot oxidation kinetics whereas aluminium proves being less influential (López-Suárez et al., 2008; Moldanová et al., 2013). Such species are mainly produced from the engine wear and the different inorganic compounds contained in the lubrication oil and the operating fuel (Mühlbauer et al., 2016). S_{DP20} and S_{TP20} contains lower ash sediments (~8%) compared to the diesel reference (~12%), despite that the sample collection duration was longer in case of the oxygenates. The lower ash residues seen in case of S_{DP20} and S_{TP20} is expected to result from the chemical composition of the oxygenated hydrocarbons where no metals such as magnesium, copper, potassium, etc., can be found as it is the case in diesel or biodiesel fuels (López Suárez et al., 2011). Blending these oxygenated

HCs with diesel will dilute the concentration of the inorganics in the fuel and as a result soot with a lower ash level is produced from their combustion.

With regards to the DPF application, ash residuals present a severe problem for the filtration mechanism as regeneration cycles can combust the soot particulates, but their ash content will remain intact and deposit in the filter pores. This phenomenon will increase the backpressure resulted from the DPF which in turn will deteriorate the combustion efficiency and increase the fuel penalties (Sappok & Wong, 2010).

Concerning the soot reactivity, ash content did not present any catalytic influence on the soot oxidation process as it is suggested in the literature (Hansen et al., 2013; Johnson, 2015; Jung et al., 2003; Liati et al., 2012), since even with lower ash values, S_{DP20} and S_{TP20} remains more reactive than S_{diesel} .

- **Sulphur content**

Sulphur derived species were not detected neither in S_{DP20} or S_{TP20} samples, however, slight presence (~1.5%) was seen with S_{diesel} . It is believed that in the case of oxygenates, sulphur compounds are not fully eliminated; however, their concentration level was lower than the minimal detection limit of the equipment. Sulphur presence in the particulates is mainly derived from the sulphur bonded on the soot periphery. Blending DPGME and TPGME with diesel will not only dilute its inorganic species but also reduce the sulphur content, which can explain the results seen with our analysis.

4.3.3 Soot morphology

Multiple soot particulates (~30) were tested from each fuelling condition. Figure 4.12 displays the representative TEM micrographs (100 nm scale) of the different soot particulates

resulted from the combustion of diesel, DP20 and TP20. As it can be seen, diesel combustion results in more compact particulates compared to the other candidates where looser and stretched structure is generally spotted.

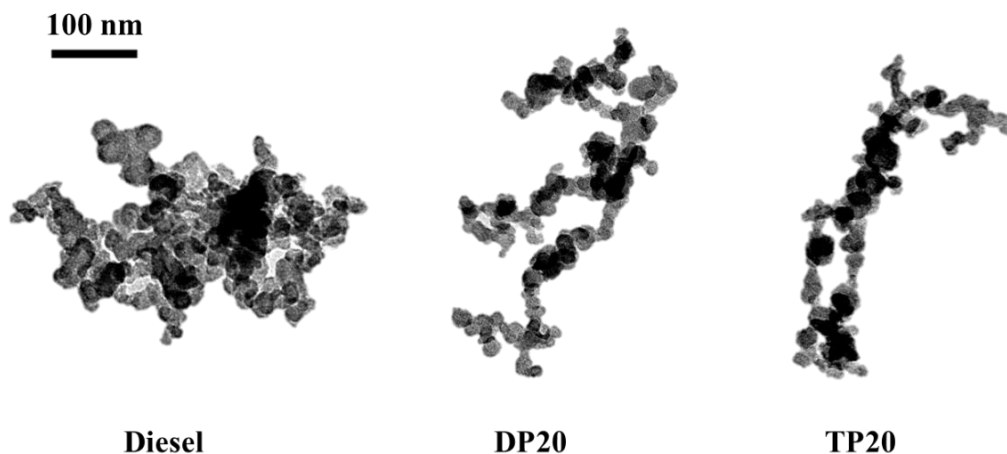


Figure 4.12: TEM micrographs for soot particulates produced from Diesel, DP20 and TP20.

Background was removed for better understanding of the morphology

To better understand the visual differences seen in the micrographs, the different soot morphological parameters such as fractal dimension (D_f), gyration radius (R_g) and number of primary particulates within the aggregate (n_{p0}) were analysed following the method proposed earlier in Section 3.5.3 and plotted accordingly in Figure 4.13. Primary particulate size (d_{p0}) was also analysed in this section by measuring around 350 particulates for each testing condition to plot a log-normal distribution that allows a fair comparison between the different fuelling types, as suggested in (Fayad et al., 2017).

In general, increasing the exhaust soot level (as in case of diesel) highlights the presence of higher chances of collision between the particulates and thus more chain-like aggregates (lower D_f) should be emitted (K. Park et al., 2004). However, in this study, despite that DP20 and TP20 combustion reduces the exhaust soot level, their particulates tend to be more chain-

like than the diesel case. Following these results, it can be speculated that both DP20 and TP20 combustion was extremely effective in oxidising the soot particulates up to a level that compensates the influence of the collision phenomenon and results in more fractal aggregates (Fayad et al., 2015; Fayad et al., 2017). This promoted oxidation mechanism is more pronounced when analysing n_{p0} , R_g and d_{p0} . It is seen that d_{p0} drop by 25% in case of DP20 and 17.8 % in case of TP20 compared to diesel. In turn, this reduction indicates that the oxygenated hydrocarbons combustion yield particulates with higher specific surface area (SSA). Technically speaking, the available area of contact between the oxygen molecules and the soot surface is increased, which in turn ease the oxidation mechanism and increase its kinetics. However, since S_{DP20} present smaller d_{p0} than S_{TP20} , thus higher SSA and in theory should be more reactive, it can be directly concluded that this parameter is not vital to dictate the oxidative behaviour of the particulates as reactivity of $S_{TP20} >$ reactivity of S_{DP20} .

In parallel, the number of primary particulates in the aggregates (n_{p0}) shows a remarkable drop from 29 in case of diesel to 20 and 19 in case of DP20 and TP20 respectively. Reducing both, d_{p0} and n_{p0} , results in smaller R_g in case of the oxygenated fuels (64 nm for DP20 and 65 nm for TP20) compared to that seen in the case of diesel (70 nm).

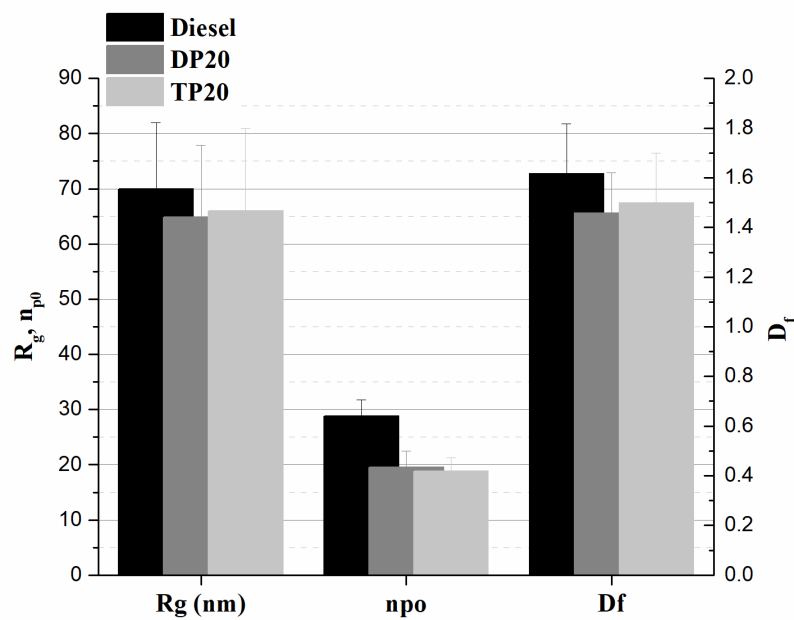


Figure 4.13: R_g , n_{p0} and D_f of the different particulates resulted from diesel, DP20 and TP20 combustion

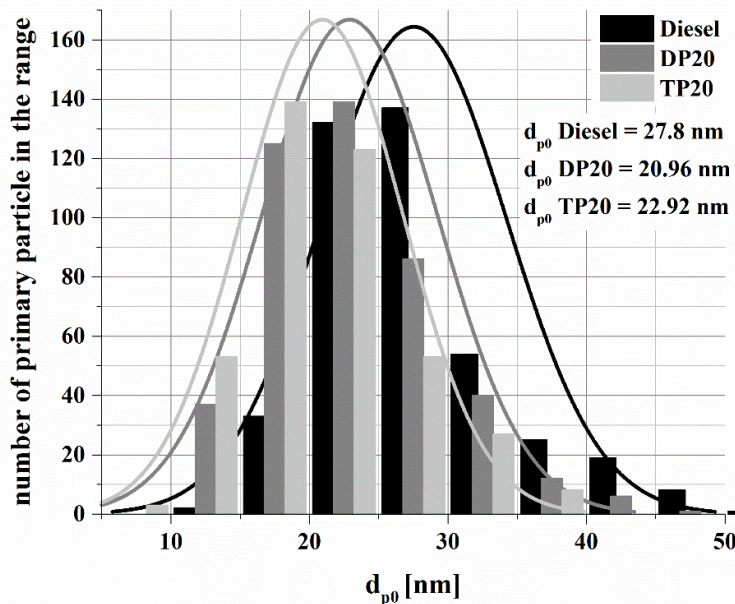


Figure 4.14: Primary particulate size distribution for the soot resulted from the combustion of the different fuel tested

4.3.4 Soot nanostructure

To further investigate the structure of the particulates, an HRTEM analysis was conducted to analyse the arrangement of the carbon layers comprised in the primary particulates. Figure 4.15 shows the original HRTEM micrograph for each testing condition along with the corresponding processed version using the in-house MATLAB coding discussed earlier in Section 3.5.3.

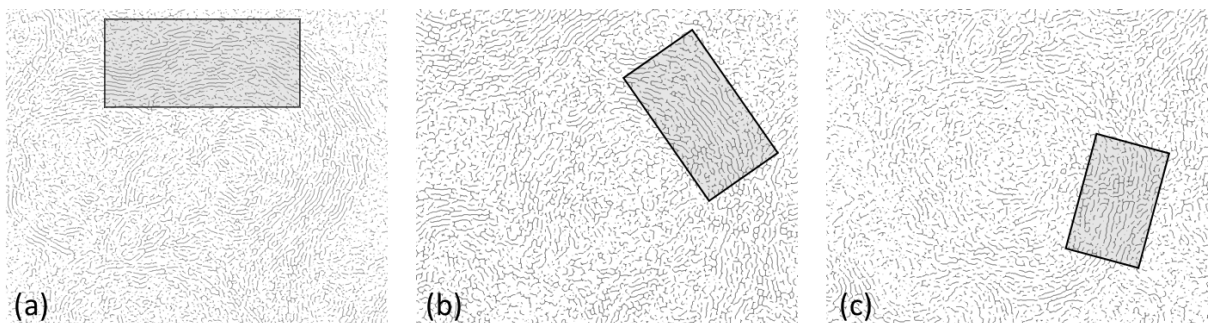


Figure 4.15: Post processed HRTEM micrograph showing the nanostructure of S_{diesel} , $S_{\text{DP}20}$ and $S_{\text{TP}20}$

All the tested samples show similar microstructural configuration consisting of a well-organised outer shell that surrounds a less structural nucleus in which the layers have no defined direction. Particulates' oxidative reactivity is mainly linked to the ratio of the carbon atoms in the edge sites with respect to these in the basal plane ($C_{\text{edge}}/C_{\text{basal}}$) (Ma et al., 2014; Marsh & Kuo, 1989; Randy L. Vander Wal & Tomasek, 2003). Increasing this ratio indicates that the particulates are more vulnerable towards oxidation as the edge carbon sites are more likely to react with oxygen compared to the basal sites (Ma et al., 2014; Marsh & Kuo, 1989; Randy L. Vander Wal & Tomasek, 2003). Further clarification was already detailed in Section 2.4.3. $C_{\text{edge}}/C_{\text{basal}}$ ratio can be evaluated by analysing the HRTEM micrographs and post-process it to

indicate the carbon layer length (L_a), separation distance between the layers (d_{002}) and their corresponding curvature (T_f).

L_a is mainly considered as the most representative factor for the C_{edge} / C_{basal} ratio with shorter layers highlighting the presence of a higher number of carbon atoms in the edge sites compared to the basal plane (Ma et al., 2014; Marsh & Kuo, 1989; Andrea Strzelec et al., 2017; Randy L. Vander Wal & Tomasek, 2003). Theoretically speaking, the shorter the L_a , the higher the reactivity (Ma et al., 2014; Marsh & Kuo, 1989; Andrea Strzelec et al., 2017; Randy L. Vander Wal & Tomasek, 2003). Figure 4.16 present the normal distribution of L_a for the different fuelling types.

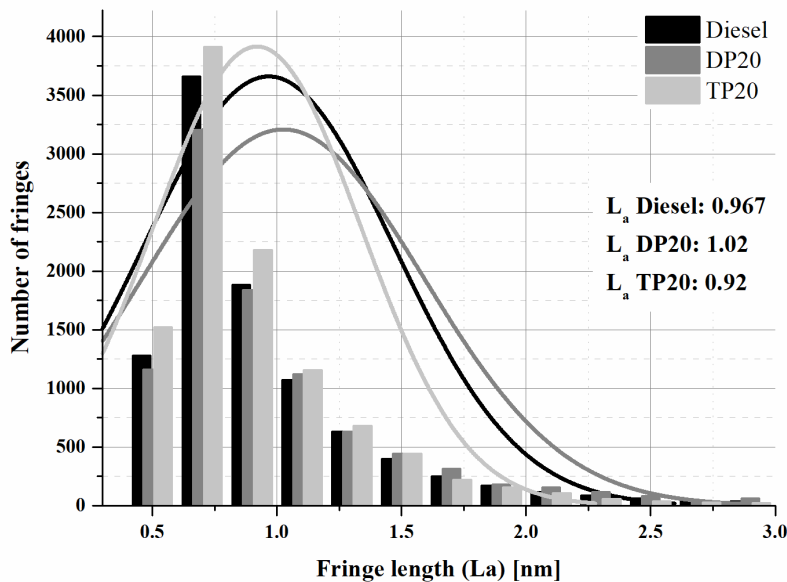


Figure 4.16: Normal distribution of the carbon layer's length in the primary particulates of diesel, DP20 and TP20 samples

It is seen that combustion of TP20 results in particulates with shorter L_a compared to diesel while DP20 tend to present slightly longer layers. This trend fits well with our TGA results when considering that S_{TP20} is more reactive than S_{DP20} ; however, since S_{DP20} and S_{TP20}

are both more reactive than diesel, a non-conclusive trend can be reported to link this factor with the overall oxidative potential of the particulates.

The layers' separation distance, d_{002} , was also plotted as a normal distribution in Figure 4.17.

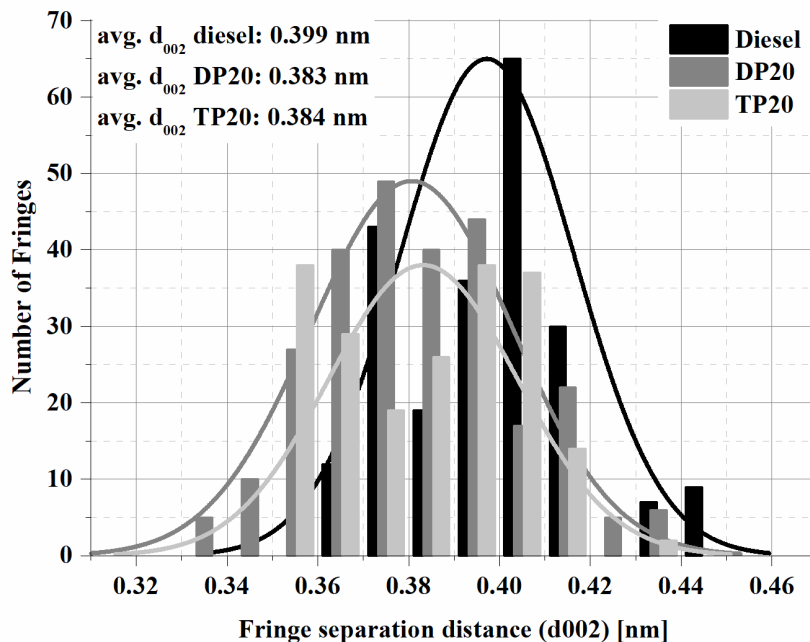


Figure 4.17: Normal distribution of the interlayer spacing of the primary particulates resulted from the combustion of diesel, DP20 and TP20

Generally, shorter d_{002} indicates a higher degree of graphitisation and thus lower oxidative potential could be expected (R. L. Vander Wal & Mueller, 2006). As explained earlier in Section 2.4.3, the particulate's graphitisation order mainly depends on the environment in which the particulates were incepted, usually higher in-cylinder temperature and pressure condition will result in more organised skeleton (Randy L. Vander Wal & Tomasek, 2004; Ye et al., 2014). Other research work suggest that the graphitisation degree is more influenced by the type of the fuel rather than by the in-cylinder condition (Lapuerta et al., 2012). In our

analysis, both S_{DP20} and S_{TP20} presents approximately the same interlayer spacing (0.384-0.385 nm) which is smaller than that of the diesel (0.399 nm). This more stable structure contradicts the better reactivity shown with the use of the oxygenated blends and approves that the initial interlayer spacing is not that influential in dictating the soot oxidative behaviour. Furthermore, DP20 and TP20 combustion is shown to reduce the exhaust temperature compared to diesel (Section 4.1), thus, it can be speculated that the in-cylinder thermal condition is also reduced – more disordered particulates should be expected. However, as highlighted above, the resulted particulates were more graphitised. Therefore, under these testing conditions, the nature and the chemistry of the fuel used (glycol ether) is more influential than the in-cylinder environment in term of dictating the soot graphitic structure.

The last nanostructure parameter inspected in this section is the tortuosity of the carbon layers (Figure 4.18).

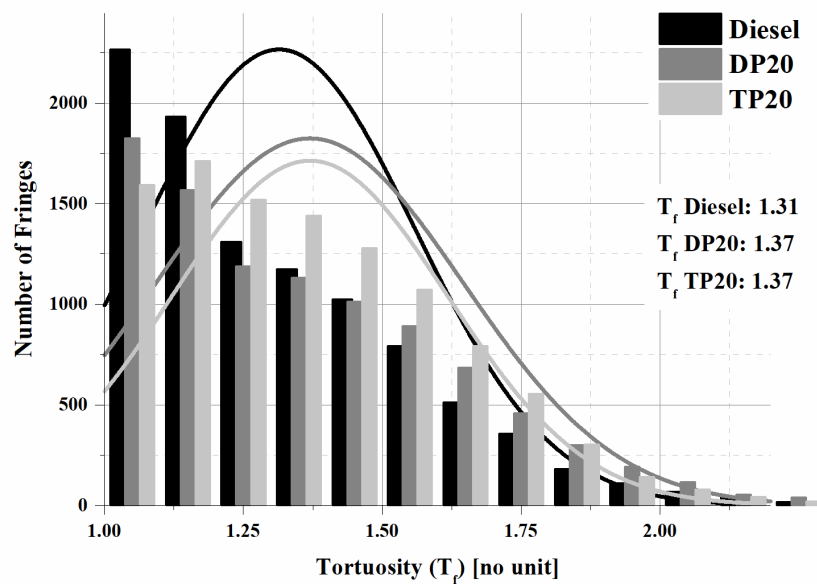


Figure 4.18: Normal distribution of the curvature of the carbon layers in the primary particulates resulted from the combustion of diesel, DP20 and TP20

There has been some debate in the literature concerning the importance of that factor in dictating the soot oxidative behaviour. Van Der Wal et al. (2003) and Abboud et al. (Barrientos, 2014) showed in their research work that the curvature of the carbon layers is more influential than the layers' length in ruling the global oxidative potential of the particulate. However, Ghiassi et al. (Ghiassi et al., 2014) reported that with n-butanol/n-dodecane mixtures, the soot reactivity was mainly ruled by the presence of short carbon segments which proves to be more reactive than the curved layer configuration. Carbon layers tend to present a curvy silhouette when there are imperfections in their 6-membraned rings, in other terms, when 5 or 7 membraned-rings are presented (Al-Qurashi & Boehman, 2008; Bogarra et al., 2017; Gaddam et al., 2016; Randy L. Vander Wal & Tomasek, 2004). The exact mechanism by which this configuration eases the oxidation reaction is detailed earlier in Section 2.4.3. S_{DP20} and S_{TP20} present higher tortuosity (1.37) compared to diesel (1.31) by that confirming the importance of this factor in determining the global reactivity of the particulates, as it is the only parameter that fully correlates with the induced oxidative behaviour of S_{DP20} and S_{TP20} . The reason for which the carbon layers tend to be more tortuous in case of DP20 and TP20 can be detailed as follows:

- (i) The reduction in the primary particulate size (Section 4.3.3) is an indication that the particulate's surface is more stretched, hence, more curved layers should be comprised in the outer shell (Lapuerta et al., 2012).
- (ii) The increase in the surface oxygen groups (approved in Section 4.3.2) can alter the final soot structure since the electron affinity of this moiety will increase the surface chemical activity and as a consequence alters its physical configuration to result in more curved layers (Morjan et al., 2004).

To clarify the correlation of each nonstructural parameter with the assigned reactivity, an evaluation between the test results versus the expected results (according to the literature review) is shown in Table 4.1. Positive correlation is denoted as a + sign and the negative correlation is denoted as a – sign.

Table 4.1: Correlation of the nanostructure with soot oxidative potential (theory versus tested results)

Diesel			DP20			TP20			
Ea (Kj/mol)	119.36			115.2			100.36		
	d002	Tf	La	d002	Tf	La	d002	Tf	La
Expected result (literature assumption)				> diesel value		< diesel value		> diesel value	
Results of the test	0.399	1.31	0.967	0.383	1.37	1.02	0.384	1.37	0.92
Correlation				-	+	-	-	+	+

In summary, curvature of the layers (T_f) is nominated as the most influential parameter dictating the oxidative behaviour of a particulate. In case the layers' tortuosity is increased compared to the “reference value” (i.e. values recorded in case of S_{diesel}), a better oxidative potential should be obtained no matter what initial graphitisation order is recorded (d002). However, if L_a is also larger than the reference value, as in case of S_{DP20} , the oxidative potential will be reduced but will always stay higher than that of the reference and vice versa. Therefore, the impact of the parameters on the soot oxidative behaviour can be arranged through the following order: $T_f > L_a > d_{002}$, with “>” defining a stronger and more influential effect.

4.3.5 Soot graphitisation order

To further approve the HRTEM analysis conducted earlier, the soot graphitic arrangement is further analysed by the aim of Raman Spectroscopy. Figure 4.19 presents the

corresponding spectra resulted from the analysis of the different soot samples. In general, the intensity, area and full width at half maximum (FWHM) of every recorded peak present valuable indication for the possible defects presented in the particulates' carbon layers (Lapuerta et al., 2012). G band represent the ideal graphitic structure and normally the intensity of this peak decrease when the number of defects in the structure increase. D1 indicates the disorder level presented in the edge sites position of the crystallite. Presence of defects breaks the symmetry in the crystalline graphite (6 membered rings), allowing the observation of the D1 mode. D3 band only indicates the non-graphitic content of the particulate, mainly arising from the molecular carbon in the soot (i.e. amorphous carbon). D4 band is only found in soot and char particulates and most likely correspond to polyene-like chains attached to the edges of the crystallites (Sharma et al., 2016).

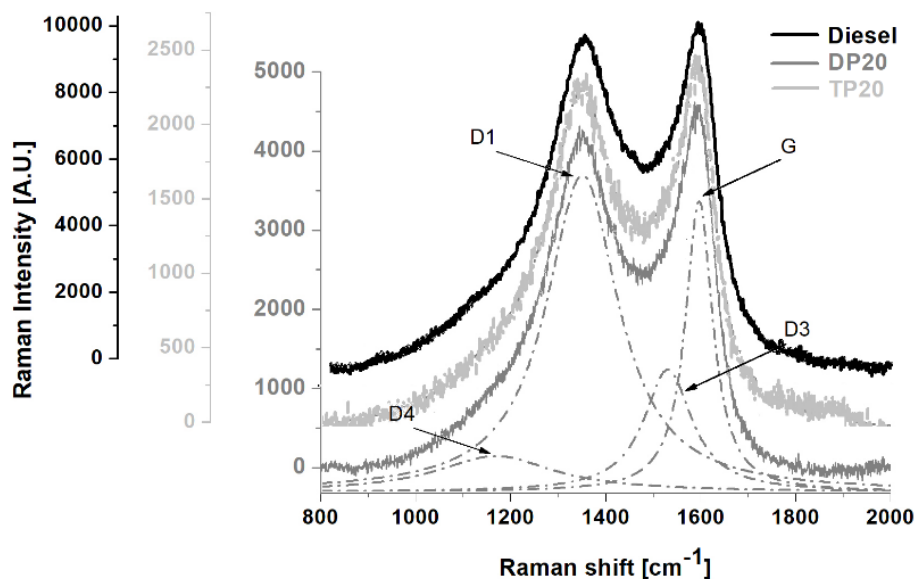


Figure 4.19: Raman spectra resulted from the analysis of the S_{diesel}, S_{DP20} and S_{TP20}

As seen in Figure 4.19, G and D1 are the most intense peaks recorded in this analysis, which is the typical configuration for the diesel soot structure. The ratio of the D/G spectra as

a function of area (A_{D1}/A_G , A_{D3}/A_G and A_{D4}/A_G) and intensity (I_{D1}/I_G , I_{D3}/I_G and I_{D4}/I_G) along with the FWHM of D1, D3 and D4 can define the disorder degree of the soot particulates. Particularly, A_{D1}/A_G and FWHM of D1 quantify the compactness of the edges sites and the size distribution of the crystallites (Ye et al., 2014). Seong et al. (2010) reported that these parameters can indicate the soot oxidative potential with higher ratios highlighting better reactivity and vice versa. As shown in Figure 4.20, S_{DP20} and S_{TP20} shows lower A_{D1}/A_G and FWHM D1 with respect to S_{Diesel} . Those findings further confirm the reduction shown along d₀₀₂ earlier in Section 4.3.4, confirming that the combustion of the oxygenated fuels result in more ordered soot particulates. However, these results did not follow the trend supported by Seong et al. (2010), where S_{DP20} and S_{TP20} displays lower A_{D1}/A_G ratio and FWHM D1 compared to S_{Diesel} , while their oxidative potential was kept higher. Although RS is a good method to analyse defects in the soot structure, it is extremely difficult to precisely nominate what type of disorder is influencing the reactivity (Ye et al., 2014).

Concerning D4, same as D1, a slight decrease was recorded, further confirming the higher graphitic order seen with the presence of the oxygenates. As for D3, no remarkable change was spotted between the different samples, highlighting that the particulates present similar amorphous content.

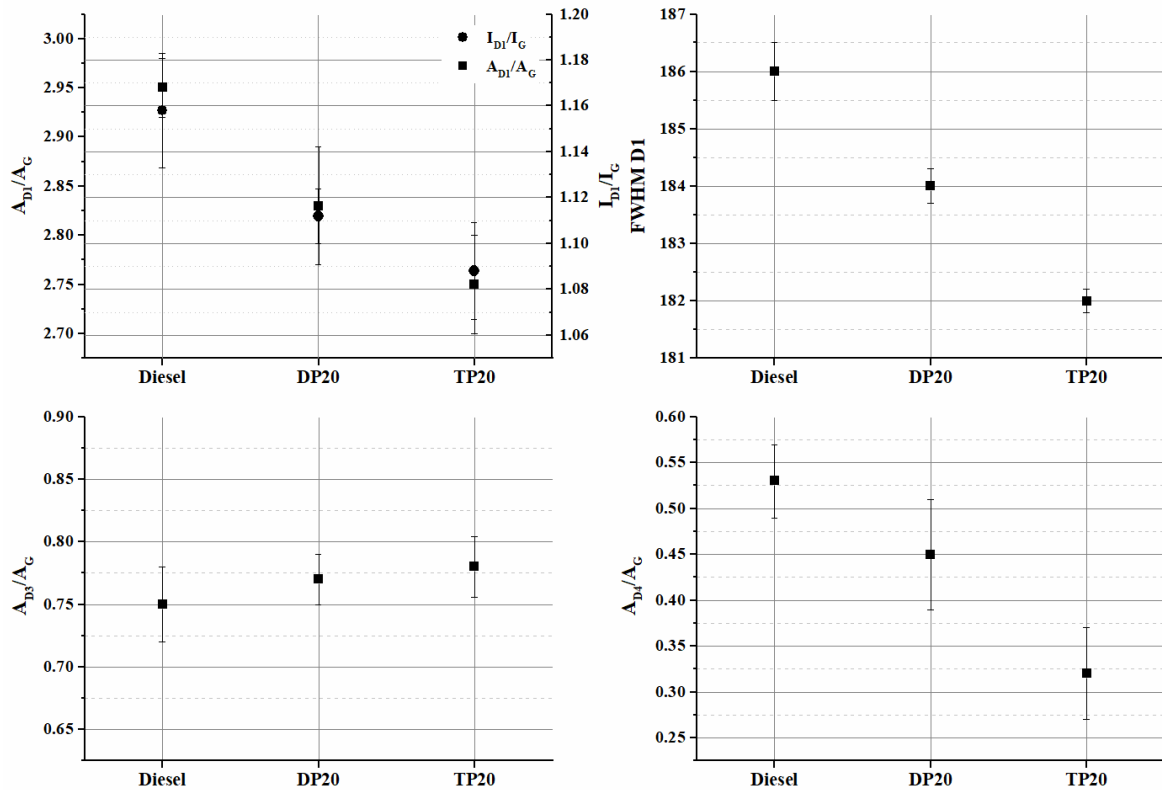


Figure 4.20: Intensity and area ratios results from the RS analysis for S_{Diesel} , S_{DP20} and S_{TP20}

4.4 Summary

The research work presented in this chapter investigates the influence of DPGME and TPGME diesel blends (~20% vol. replacement), namely DP20 and TP20 on the (i) engine behaviour, (ii) gaseous and PM emissions, (iii) soot oxidative reactivity and its (iv) different physio-chemical characteristics such as morphology, nanostructure and elemental composition. Special attention was given to relate the particulates' physio-chemical characteristics with the resulted reactivity.

Application of the oxygenated fuels (DP20 and TP20) slightly increases the engine BSFC, however, this negative impact was compensated with a higher BTE value. As for the PM

suppression, TP20 was more effective than DP20, mainly due to a lower boiling point temperature. Reformulating diesel with DPGME and TPGME compounds is considered advantageous as it permits a better engine calibration that allowed a lower NOx/PM trade-off line.

As for the particulate characteristics, significant changes were seen on the macro and micro scale of the soot. Particulates with higher oxidative reactivity were seen from the combustion of TP20 followed by DP20 and ULSD respectively. The particulates VOF and O/C ratio increases in the order of TP20>DP20>ULSD, making a perfect fit with the resulted reactivity. Ash precipitations and sulphur content of the aggregates were also suppressed, as glycol ethers can dilute the inorganic elements/sulphur in diesel fuel. On the macro scale (morphology), smaller aggregates that were restructured into a more chain-like shape were seen in the presence of the oxygenates. Furthermore, as the oxygenates tend to reduce the soot precursors formation and promote the oxidation reactions in the fuel-rich zone as well as in the post flame combustion, the number of the primary particulates comprised in the aggregates and their corresponding size were also reduced.

Quantitative analysis of the HRTEM images reveal that the initial graphene layers present no significant difference along their length (L_a) but show to be less flat (higher T_f) and arranged with a higher structural order (smaller d_{002}) compared to diesel. Interlayer spacing prove to be more fuel dependent rather than being influenced by the in-cylinder conditions. Raman analysis confirms the HRTEM findings and the unconventional higher graphitisation shown in case of the oxygenates was further verified, which contradicts with the higher oxidative reactivity recorded. The influence of the nanostructure parameters on the soot reactivity can be classified as follows: $T_f > L_a > d_{002}$.

CHAPTER 5

MANIPULATING DIESEL EXHAUST COMPOSITION THROUGH GLYCOL ETHER FUELLING AND POST INJECTION STRATEGIES FOR EFFICIENT HC-SCR PERFORMANCE

Studies suggest that the optimisation of HC:NOx ratio and concentration of HC in the exhaust can improve the Ag/Al₂O₃ HC-SCR de-NOx activity over a wide temperature range (Gu et al., 2015; Houel et al., 2007a; Theinnoi et al., 2010). Quality of HC species and injected fuels (light, heavy and oxygenated) in the active control of SCR are influential parameters as in one hand they can provide better initial deNOx activity but also can accelerate the catalyst deactivation. However, in the low temperature regions, typically lower than 250 °C, the deposition of the soot particulates and heavy molecular weight species on the catalyst surface is faster than their oxidation, thus hindering the catalyst activity by coking and masking. H₂ is an active promoter that helps in increasing the catalyst de-NOx efficiency in the low temperature range and virtually withstand it through time. Modern cleaner engines and new fuel generations are extremely beneficial in term of reducing the overall exhaust PM emissions, thus providing a new opportunity for the silver-based catalysts to operate more efficiently in real life applications. This is expected to reduce the needed amount of H₂ to fully activate the catalyst, which is critical in case exhaust fuel reforming will be used as a source for this gas.

The main objective of this study is to actively control the exhaust gas composition through the application of in-cylinder PFI strategies combined with the addition of minute concentration of H₂ (500, 1500 and 3000 ppm) to further enhance the Ag/Al₂O₃ HC-SCR

activity. The study was performed using a modern common rail diesel engine operating on ultra-low sulphur diesel and TP20 blend. As seen from chapter 4, TP20 can reduce the PM's concentration and increase their oxidative potential without introducing any extra NOx penalties, which is also seen as a promising parameter to further help the catalyst de-NOx functionality. The tests were carried for two different engine load conditions, 2 bar IMEP (low load) and 4 bar IMEP (medium load), representative for the low exhaust gas temperature of 180 and 290 °C, respectively. Also, the impact of the PFI technique on the morphology of the PM is addressed to understand the impact of this strategy on the soot formation pathway. A schematic representation of the general idea of this application and the different areas that this chapter is aiming to cover is presented in Figure 5.1.

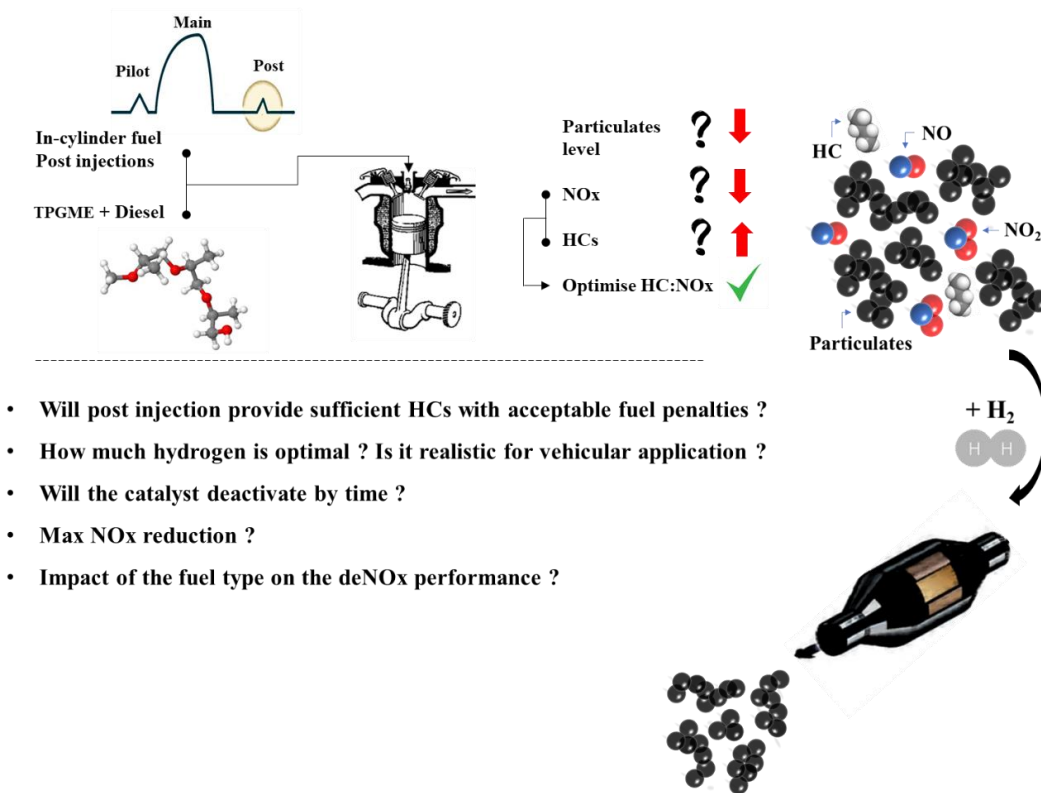


Figure 5.1: Schematic diagram presenting the main idea of the chapter and the related questions that this section is aiming to cover

5.1 Post injection optimisation

In the first section of this chapter, initial engine tests are presented on the ability of in-cylinder PFI strategies (i.e. injection timing) in controlling the exhaust HC:NOx ratio and composition (i.e. HC species, soot). General description of the pilot-main-post injections used in this research work is shown in Figure 5.2.

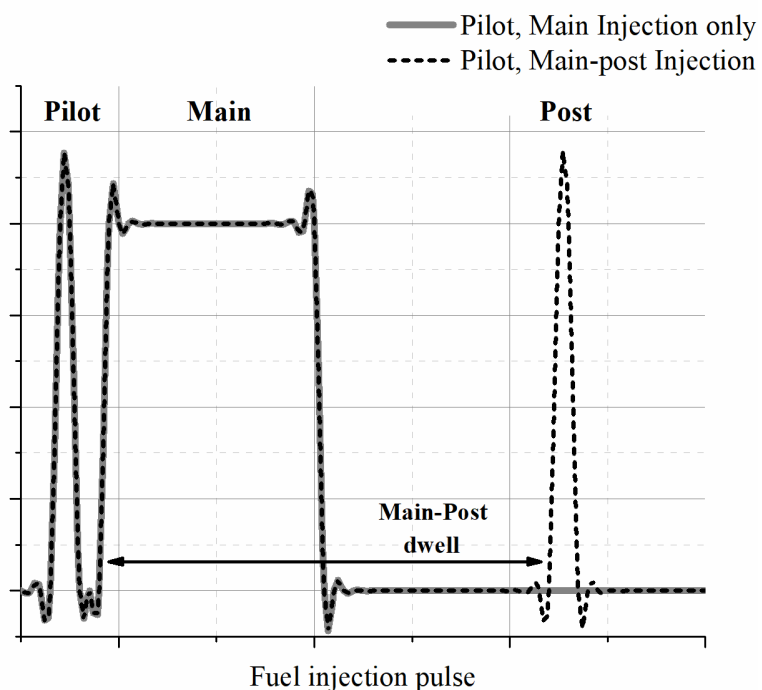


Figure 5.2: Schematic presentation of the pilot, main and post fuel injection pulses

The post injection duration was kept constant and set equal to the minimum duration needed to steadily operate the injector (0.04 ms). The impact of changing the post fuel quantity was not tested in this research work as the applicability of this technology is directly related to the resultant fuel penalties. Also increasing the post injection duration is disadvantageous since the late fuel injected tends to impinge on the cylinder walls and leak into the oil sump (Jeftić, Asad, et al., 2011). Instead, the main-PFI dwell was changed accordingly to manipulate the

exhaust gas composition with the least possible fuel penalties. Pilot and main injection timing and duration were kept constant during the tests to provide stable and repeatable background for the main-PFI dwell effect. Consequently, the changes to the exhaust gas conditions (temperature and composition) were attributed solely to the application of the PFI.

The active management of the exhaust gas was carried out under a steady engine speed of 1500 rpm and two baseline loads (e.g. produced from the pilot-main injection): 2 bar IMEP and 4 bar IMEP. The sections below will discuss in detail the impact of changing the PFI timing on (a) the combustion performance (HRR, brake thermal efficiency and brake specific fuel consumption), (b) gaseous emissions and (c) PM emissions.

5.1.1 Post injection impact on combustion performance and gaseous emissions

The influence of the different PFI strategies on the engine in-cylinder pressure and HRR resulting from the combustion of diesel fuel under 2 and 4 bar IMEP conditions are presented in Figure 5.3. Similar results were seen in the TP20 case and thus the results were not plotted to avoid duplication. As for the pilot-HRR and main-HRR peaks, no changes were seen between the different testing conditions as their injection parameters were not changed during the test. It should be also noted that during the expansion stroke, PFI application resulted in distinct post-HRR peaks which their magnitudes and ignition delays were directly correlated to the timing of the post. Retarding the PFI timing indicates that the post fuel is injected into a region where lower in-cylinder pressure and temperature is available, thus poorer chances are available to fully combust the fuel. As a result, longer period was needed to start the post-combustion reactions (i.e. longer post ignition delays) and lower post-HRR peaks were recorded. The CA50 for all the testing conditions did not vary and remains constant to 3 CAD ATDC. The time sweep of the PFI injection did not show any negative impact on the combustion COV (remains

< 2%). The only exceptional case where the PFI induced a slightly higher COV (2,6%) is at 50 CAD ATDC for the 2 Bar IMEP condition and 90 CAD ATDC for the 4 bar IMEP condition.

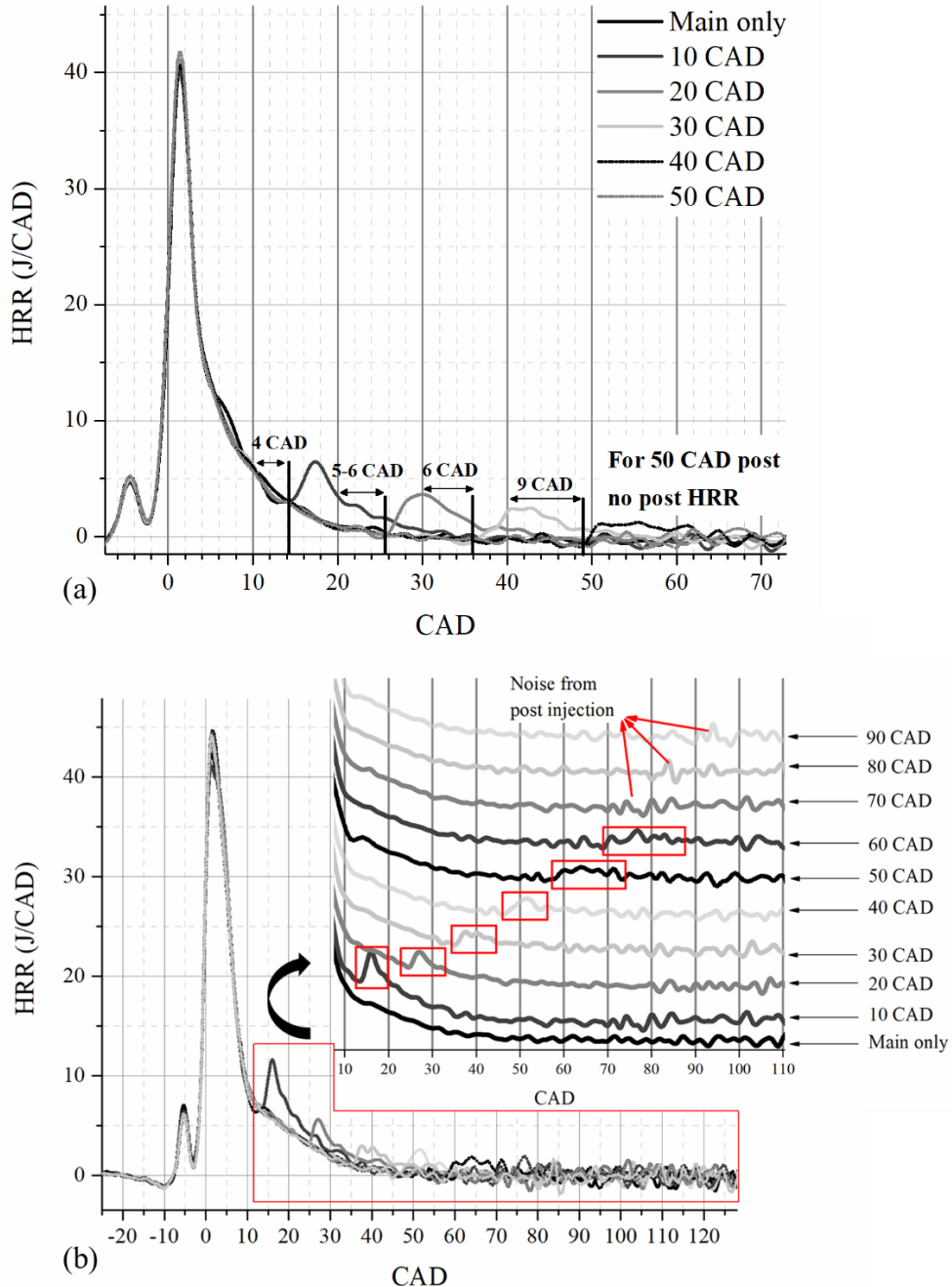


Figure 5.3: Impact of different PFI strategies on the combustion of diesel fuel under (a) 2 bar IMEP and (b) 4 bar IMEP

To further evaluate the applicability of this injection technique, the resulted brake specific fuel consumption (BSFC) and brake thermal efficiency (BTE) and exhaust temperatures are monitored for each fuelling and load condition and plotted accordingly in Figure 5.4. Gaseous emissions, such as THC along with the resulted HC:NOx ratios are also presented in Figure 5.5. The optimum configuration for the HC-SCR application will be the timing through which this technique will be able to produce the highest/most optimal HC:NOx ratio without significantly deterring the BSFC and BTE values.

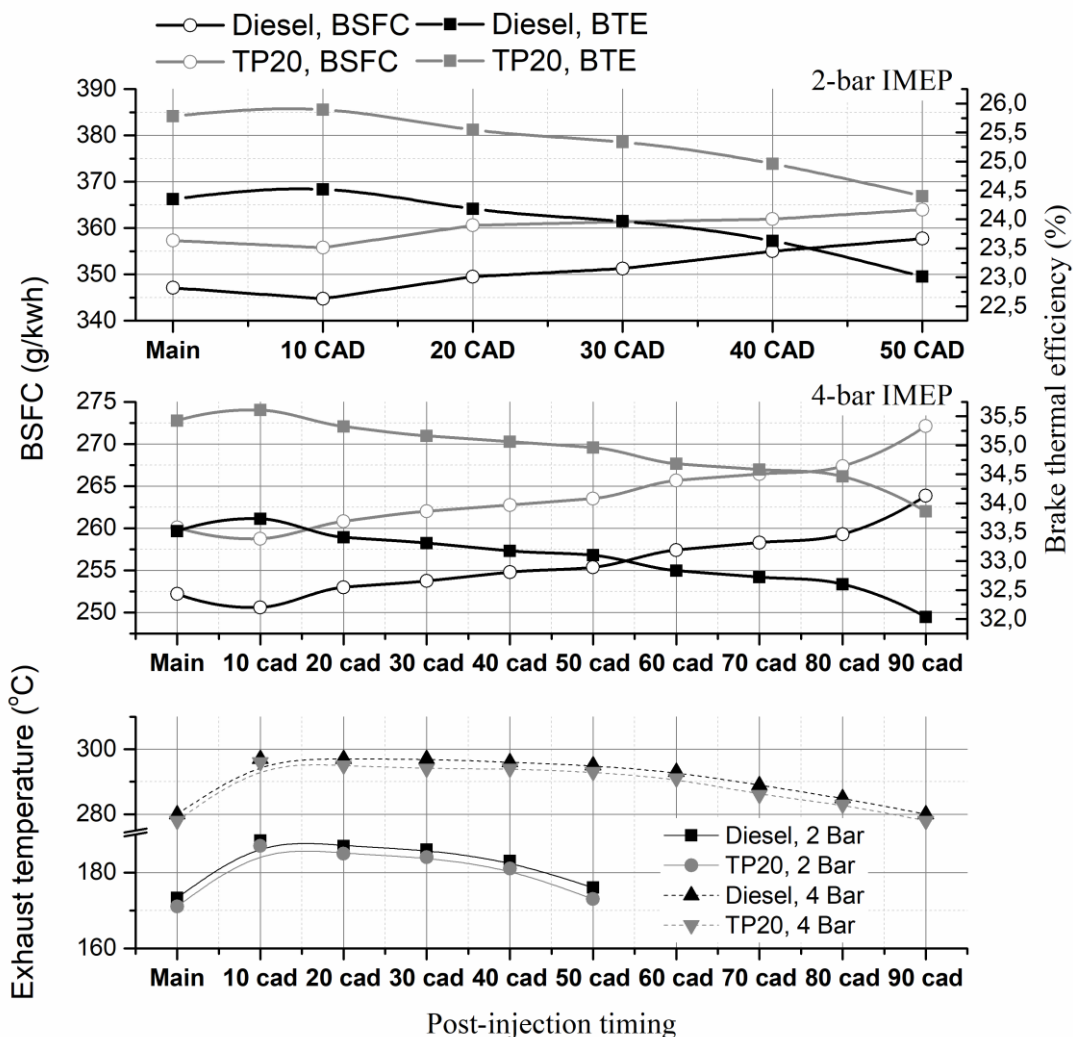


Figure 5.4: BSFC, BTE and exhaust temperature resulted from the different PFI strategies for diesel and TP20 under 2 bar IMEP and 4 bar IMEP conditions

Concerning the low-load case, applying the PFI at 10 CAD ATDC did not cost any extra fuel penalties for both fuelling and the total exhaust HCs were comparable to the single pilot-main injection case. Retarding the PFI gradually increases the engine's BSFC till reaching 40 CAD ATDC with an acceptable fuel penalty of maximum 1.2% and an effective HC:NOx ratio of 2.66 for the diesel case and 2.27 for TP20. However, further delay for the PFI (50 CAD ATDC) results in sharper increase in the BSFC (+1.95%) and deteriorate the thermal efficiency (-4.9%). This trend fits with the data provided in Figure 5.3 where no post-HRR peak is recorded for the 50 CAD PFI strategy, which indicates that the effective expansion ratio of the post-combustion is nearly eliminated. HC:NOx ratio of 4:1 can be achieved with the 50 CAD strategy compared to earlier injections, however, as the exhaust temperature at this load condition is limited to 180-190 °C, higher HC:NOx ratios are not needed for an optimised workability of the HC-SCR. In fact, higher ratios could be problematic for the catalyst de-NOx performance as the maximum tolerable HC:NOx ratio for this temperature condition is ranging from 1:1 to 2:1 (Houel et al., 2007a; Houel et al., 2007b). Thus, only the 30 and 40 CAD cases will be considered for the 2 bar IMEP HC-SCR testing in the upcoming section.

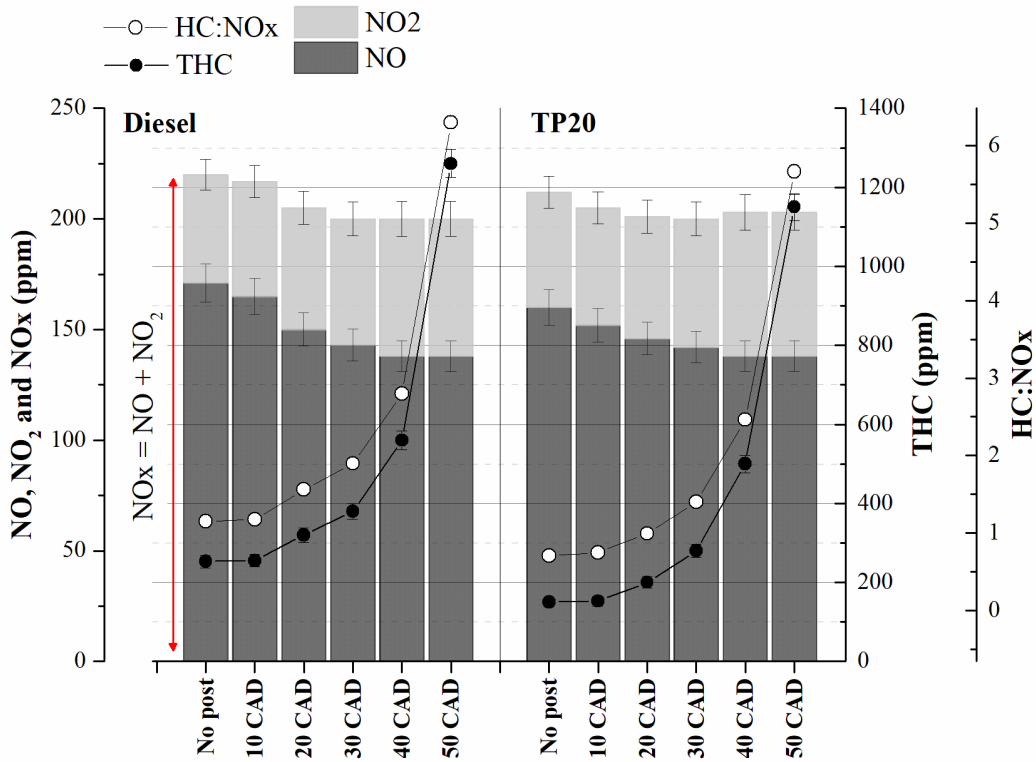


Figure 5.5: NO, NO₂, NOx, THC and the resultant HC:NOx ratio for the 2 bar IMEP testing

As for the 4 bar IMEP case, similar results are seen with the 10 CAD strategy, however, it can be also seen that further retarding the PFI was not that deterioristic as it was for the 2 bar IMEP case. This resulted mainly from the extra energy produced at higher load condition which substantially increase the local in-cylinder temperature and pressure conditions at later stages of the cycle. As a result, it was seen that the total HC level in the exhaust was kept similar to the no-post condition during the first 30 CAD sweep and start to increase with the 40 and 50 CAD strategies. However, the resulted HC:NOx ratios at those timings was marginal and did not exceed 0.4:1. Further retarding the PFI to 60, 70 and 80 CAD ATDC increases the HC level and results in an HC:NOx ratio of 2.1, 3.8, 4.2 and 1.5, 2.8, 3.8 for diesel and TP20 respectively, with a maximum fuel penalty of ~ 2.8% (Figure 5.4) when the PFI is applied at 80 CAD ATDC. However, further delaying the injection to 90 CAD ATDC results in a BSFC penalty of 4.5%

and reduce the engine thermal efficiency with 4.49% for both fuelling conditions (Figure 5.4). This accountable deterioration in the combustion performance is considered as a limitation for the real engine application and thus only the 60, 70 and 80 CAD cases will be considered for the HC-SCR testing.

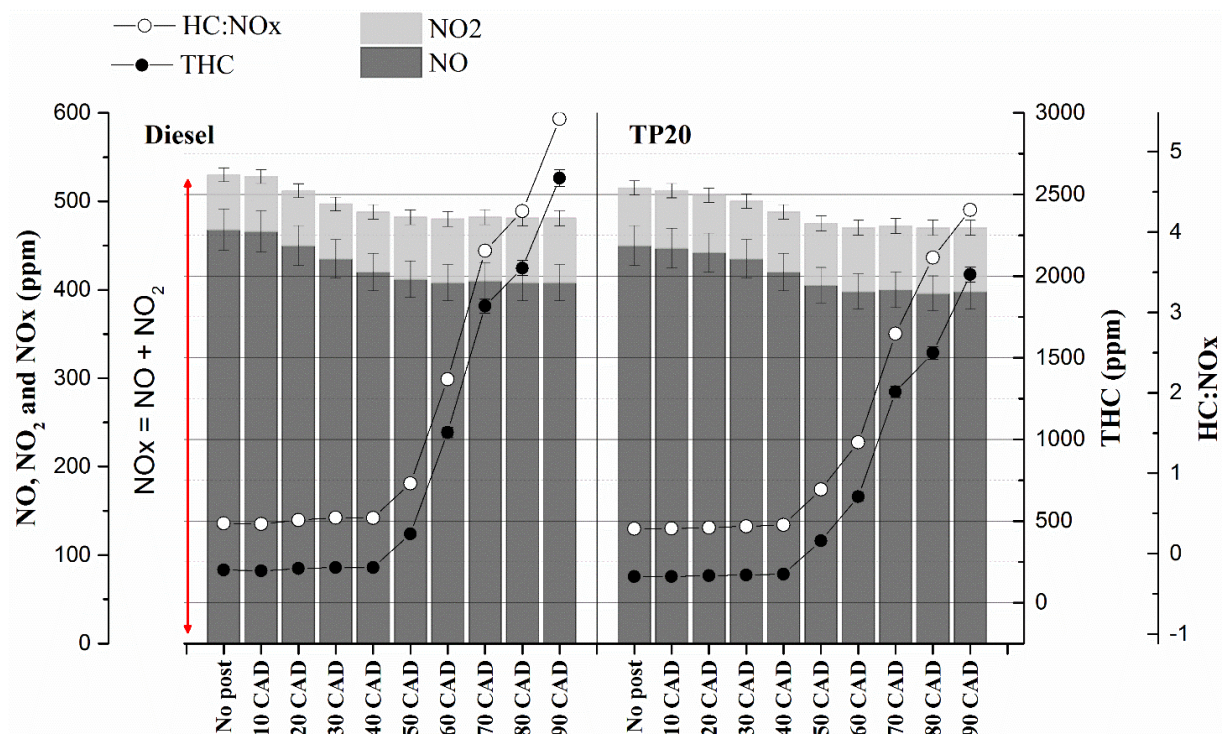


Figure 5.6: NO, NO₂, NO_x, THC and the resultant HC:Nox ratio for the 4 bar IMEP testing

It is of interest also to understand the impact of the PFI on the other gaseous emissions such as the NO_x mixture (i.e. NO and NO₂) and CO along with defining the different species included in the produced HC pool. Only the conditions nominated for further testing with the HC-SCR catalyst (30 and 40 CAD for 2 bar IMEP; 60, 70 and 80 CAD for the 4 bar IMEP) will be discussed in the section below:

- **NOx**

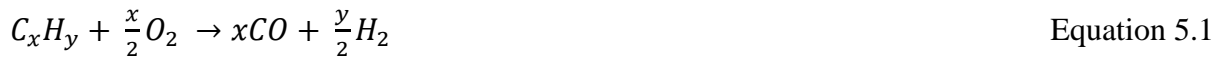
It is seen in Figure 5.5 and Figure 5.6 (note: the error bars are representative for the minimum and maximum value recorded due to engine fluctuations) that NOx level dropped by ~ 8% at the 2 bar IMEP testing and ~ 10% at the higher load condition when applying the PFI strategies. This is expected to result from the reaction of these species with the increased portion of hydrocarbons (radical HC) resulted from the post strategy which can possibly produce nitrated-hydrocarbon compounds (Fayad et al., 2017; Lyon & Cole, 1990). This explain why retarding the PFI result in further reduction in the NOx level. Also, it is seen that most of the NOx change is triggered from the NO recession, while NO₂ slightly increases with PFI, however, its increment was not sufficient to compensate the reduction seen along the NO. Late post combustion is expected to increase the hydro-peroxyl radicals (HO₂) which are keen to react with the NO and oxidise it to NO₂ (Lyon & Cole, 1990; Zheng et al., 2003).

In addition, it can be also seen that TP20 combustion did not increase the total NOx level compared to diesel under all the operating condition. This is mainly related to the higher latent heat of vaporisation of TP20, as detailed earlier in Section 4.1.

- **CO and H₂**

The resulted CO and H₂ emissions produced from the PFI application is presented in Figure 5.7 (note: the error bars are representative for the minimum and maximum value recorded due to engine fluctuations in case of CO – for H₂ it presents the standard deviation of 3 measurements). In the presence of the post application, it is seen that the resulted CO emissions have slightly increased during the 2 bar IMEP testing and approximately two-folded at the higher load condition, with similar trend between diesel and TP20. It is expected that at late stages of the expansion stroke, the local O₂ level is reduced since part of the oxygen has

been already consumed by the main-fuel combustion. As a result, a portion of the post-fuel injected could be partially oxidised into CO and H₂ instead of being fully combusted into CO₂ and H₂O compounds as it is suggested in the reaction below



In addition, Jeftic et al. (2011) also proposed that late fuel injection can yield H₂ by following the steam reforming path (i.e. reacting with the excess of H₂O resulted from the main combustion) as suggested in Equation 5.2.



To further approve this theory, GC-FID analysis was introduced to check if any H₂ production took place during the testing. As it can be seen from Figure 5.7, in the no-post mode around 35 ppm of H₂ is available at the 2 bar IMEP testing and this amount increased to 65 ppm when post injection is introduced. As for the 4 bar IMEP testing, the no-post mode produces around 30 ppm H₂ in the exhaust and with the introduction of the PFI the H₂ level substantially increased to 70-90 ppm, which seem to follow the CO trend spotted in each testing condition.

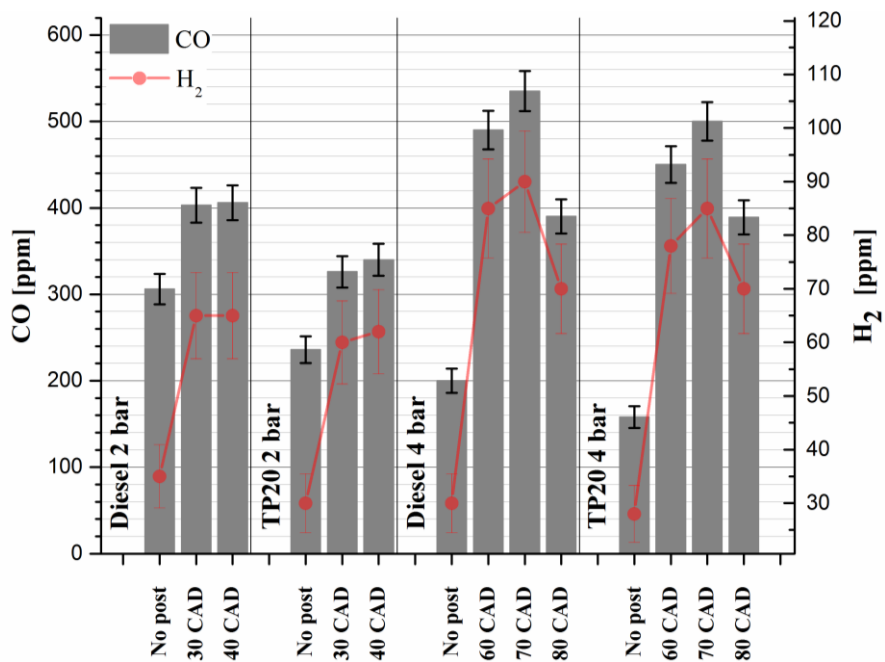


Figure 5.7: CO and H₂ emissions resulted from the post application

- **HC speciation**

Speciation of the different HC species presented in the pool of HCs produced from the PFI application is presented in Figure 5.8 (note: the error bars are representative for the minimum and maximum value recorded due to engine fluctuations). Concerning the 2 bar IMEP case, acetylene, ethane and methane emissions were limited to a maximum of 8-9 ppm, even when PFI application was introduced. However, formaldehyde, propylene and ethylene gradually increased while retarding the PFI to 30 and 40 CAD ATDC, yet, their concentrations did not exceed 27 ppm in the exhaust flow. Increasing the engine load to 4 bar IMEP results in a greater fraction of light HCs that shows to increase once moving from 60 CAD ATDC to later timings, indicating that the injected fuel is still undergoing combustion reactions at these late stages of the expansion cycle. However, these reactions cannot be seen from the pressure/HRR

curves as the piston is already at a late position and the effective expansion force resulted from the post-combustion is not expected to exert any noticeable power on the piston.

The medium and long chain hydrocarbon concentration in the exhaust, so called “FTIR-Diesel” and “FTIR-TP20” for Diesel and TP20 combustion respectively, is also plotted in Figure 5.8 . This range of HCs can be considered as representative for the unburned fuel HCs and the corresponding cracking products over the boiling range of the fuel (Storey et al., 2005). It is seen that most of the HCs emitted into the exhaust are constituted from unburned fuel portion and their level gradually increases when retarding the PFI timings, independently of the fuel type or load condition. At late stages of the expansion stroke, the injected fuel is more vulnerable to skip the combustion reactions since (a) the available in-cylinder temperature and pressure profiles are not enough to fully combust the fuel. (b) injecting the fuel at a relatively late position can also increase the in-cylinder wall wetting tendency, hence less fuel participated in the in-cylinder combustion (Jeftić, Asad, et al., 2011). (c) More retarded timing indicates that there is a shorter time for the fuel to undergo the combustion reactions before the opening of the exhaust valves, which also results in higher unburnt fuel portion in the exhaust.

Emissions of CO, light HC species and the unburned fuel portion in the exhaust were reduced when operating the engine with TP20 under all testing conditions. It is expected that the nature of the fuel, which is an oxygenated compound, reduce the carbon mass in the fuel (refer to Table 3.3, the calculated wt. % C in the fuel blends) which in turn limits the CO formation mechanism (An et al., 2015). Also, the presence of the molecular oxygen is also expected to result in more complete combustion, especially in the fuel rich regions, thus increase the HC oxidation rate and limit its presence in the exhaust (Ren et al., 2008).

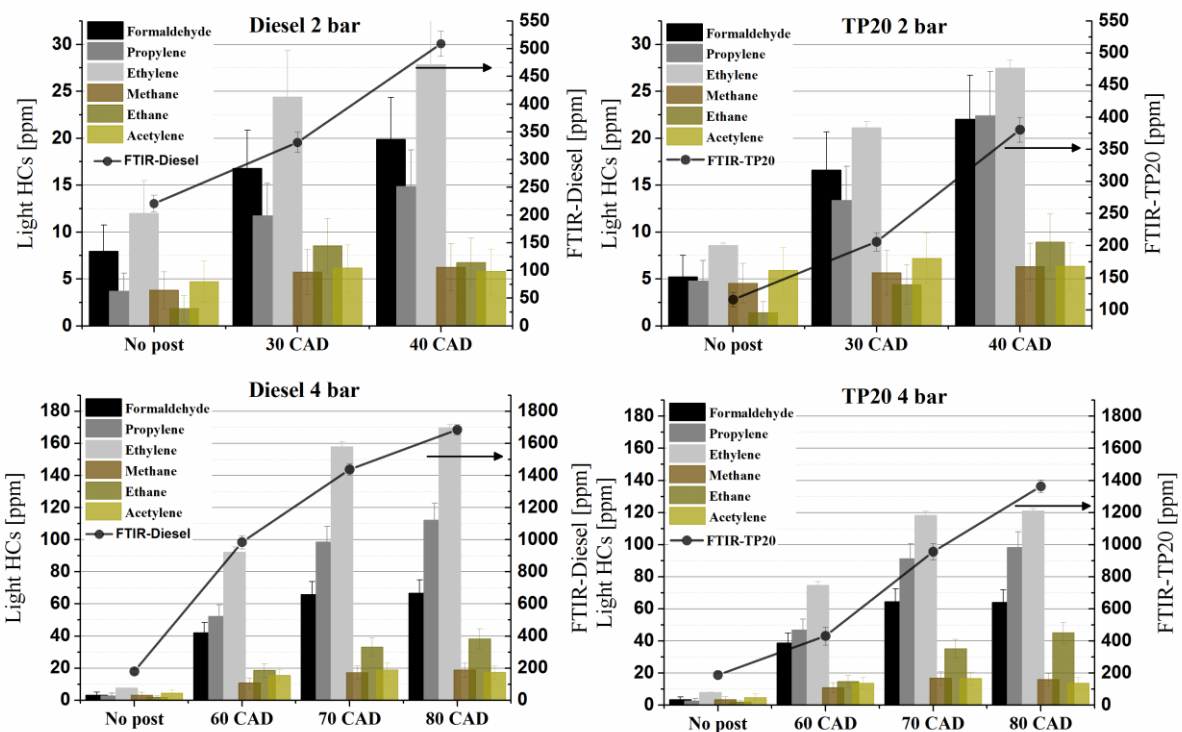


Figure 5.8: HC speciation for the different fuelling and operating conditions that will be tested with the HC-SCR

5.1.2 Post injection impact on PM emissions and morphology

The average of 3 repeated measurements presenting the TPNC and GMD of the particulates is shown in Figure 5.9. It is seen that TP20 lowers the level of particulates and reduce their GMD compared to diesel combustion. The detailed mechanism by which TP20 yields these changes was already discussed in Section 4.2.

Concerning the PFI application, reduction in the exhaust particulates' level was seen compared to the no-post mode with minor changes spotted between the different PFI time sweeps. Both fuels results in a reduction estimated to ~9 % at the 2 bar IMEP testing and ~11% at the 4 bar IMEP testing compared to the reference no-post condition. Also, the particulates'

average diameter tends to be smaller with the PFI application, however, the level of difference is considered not that significant laying within the margin of the error bars.

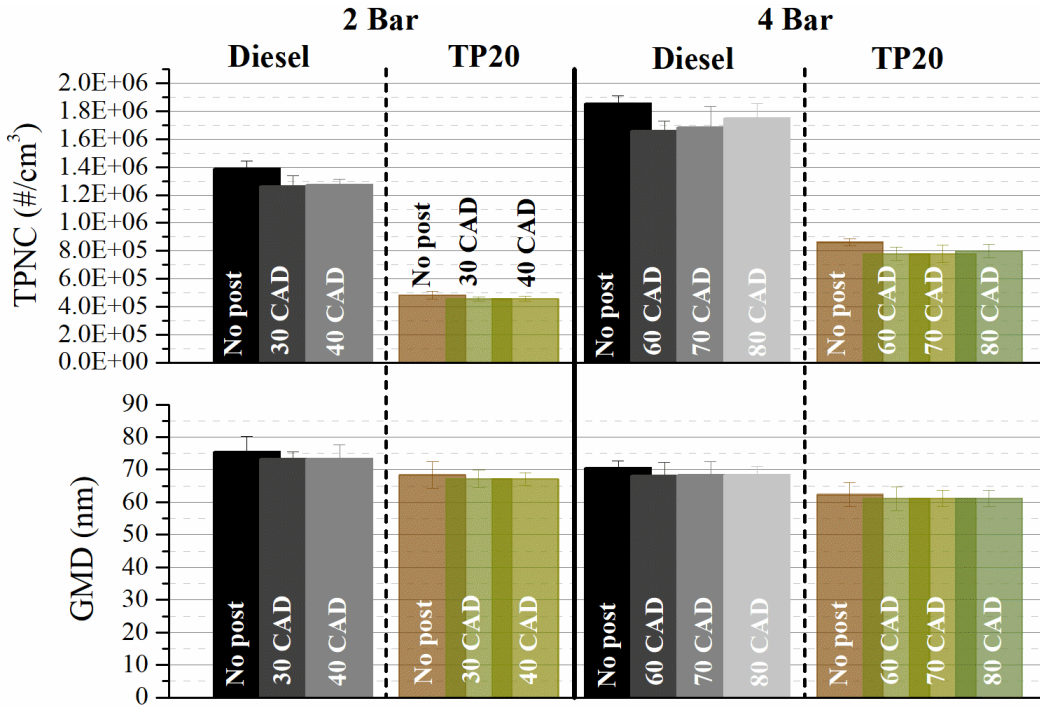


Figure 5.9: TPNC and GMD for the particulates produced from the combustion of diesel and TP20 under 2 bar IMEP and 4 bar IMEP with the most optimal PFI timings

To understand the exact role by which PFI is reducing the PM emissions, the soot morphological characteristics were also evaluated and presented in Figure 5.10. Since the SMPS results highlight the same trend of PM and GMD variation for all the PFI timings and load conditions, only the no-post injection mode and the 80 CAD PFI mode at 4 bar IMEP will be evaluated (for diesel and TP20).

PFI increases the corresponding D_f of the particulates compared to the no-post mode application. It is believed that since the PFI reduces the concentration of the PM, lower chances of collision are speculated between the aggregates (in the cylinder and in the tailpipe) and as a result, PM with more spherical silhouette (higher D_f) is expected. Concerning the fuel impact,

it is seen that despite the significantly lower level of PM emitted in case of TP20 (no-post and PFI mode), the D_f value is still lower than that seen with the diesel aggregates. This is mainly triggered by the extensive oxidation reactions generated from the presence of the molecular oxygen in the TP20 fuel which help in remodifying the soot silhouette into less organised configuration (lower D_f), even if fewer collision chances are presented.

In addition, it was seen that PFI also reduces the radius of gyration (R_g) and number of primary particulates (n_{p0}) of the incepted aggregates. However, the primary particulate size (d_{p0}) did not present any notable variation. The differences spotted in d_{p0} were considered statistically insignificant over the whole population of the tested particulates. To understand those differences, the following approach is proposed:

Arregle et al. (2008) reported that when the main-post dwell exceeds 20 CADs, the PFI combustion is considered as a soot-free ignition mechanism. Thus, in our case, it can be speculated that the extra PFI added to the combustion cycle did not produce any extra PM. Furthermore, introducing PFI at 80 CAD ATDC is incapable of increasing the turbulence of the main fuel/air mixture or replenishing it with fresh oxygen as the main combustion reactions at this timing are already quenched. In other words, at this delayed timing, PFI cannot alter the soot formation pathway but can still possibly help in its oxidation. Another import fact to be clarified is that at 80 CAD ATDC, most of the soot produced from the main combustion is considered mature and carbonised enough with a recognised structure. Thus, remarkably high in-cylinder temperatures are required to generate the oxidation reactions needed to impact the size of the primary particulates.

Following the (a) increase in the light HCs species seen in Figure 5.8 (i.e. indicating late combustion reactions) and (b) the slight increase in the exhaust temperature (Figure 5.4), it is confirmed that even at these late stages of the expansion stroke, the PFI application can still

produce some extra heat into the cylinder. Combining the reduction seen in the total PM level (SMPS) and the inconspicuous changes in d_{p0} , it can be then speculated that the heat generated from the PFI is mainly oxidising the non-mature part of the soot aggregates (i.e. mostly the nucleation mode), the part that has not experienced significant graphitisation during the combustion. Oxidation of the nucleation/non-mature particulates will limit the growth process (i.e. agglomeration) of the PM at the late stages of the expansion cycle/exhaust and help in reducing the final size of the aggregates (R_g). Following that process, the total PM level and to a lesser extent the GMD are reduced. However, the primary particulate size remains constant. Nucleation/non-mature particulates do not present a clear recognised shape in the TEM micrographs; thus, they are not accounted in the analysis of d_{p0} . For that reason, d_{p0} did not show any changes from the TEM analysis. However, the nucleation/non-mature particulates can still influence the rest of the morphological parameters (R_g , D_f and n_{p0}) as they are counted in the total projected area of the aggregates. Reader is referred to Section 3.5.3.1 for better understanding of the morphology analysis.

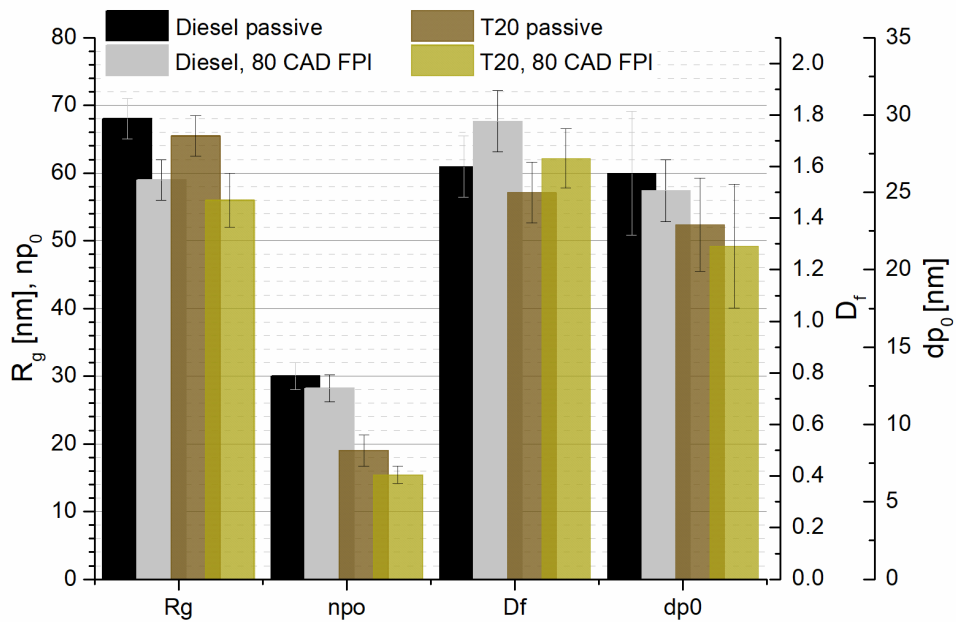


Figure 5.10: R_g , n_{p0} , D_f , and d_{p0} for diesel and TP20 combustion at 4 bar IMEP with and without 80 CAD ATDC PFI

5.2 HC-SCR de-NOx efficiency

The impact of the most promising injection configurations (nominated in Section 5.1) were tested accordingly in term of enhancing the overall HC-SCR de-NOx performance. H₂ gas was also added as an enhancer for the reactions to test the optimal concentrations needed for a real-life application.

5.2.1 2 bar IMEP testing

Figure 5.11 and Figure 5.12 show the variation of the different exhaust-gas emissions (NO, NO₂, NOx and THC) at the **2-bar load condition** before and after the HC-SCR catalyst, for diesel and TP20, respectively. The impact of the different PFI strategies and fuelling type with and without H₂ addition (500, 1500, 2500 and 4000 ppm) is investigated in the sections below:

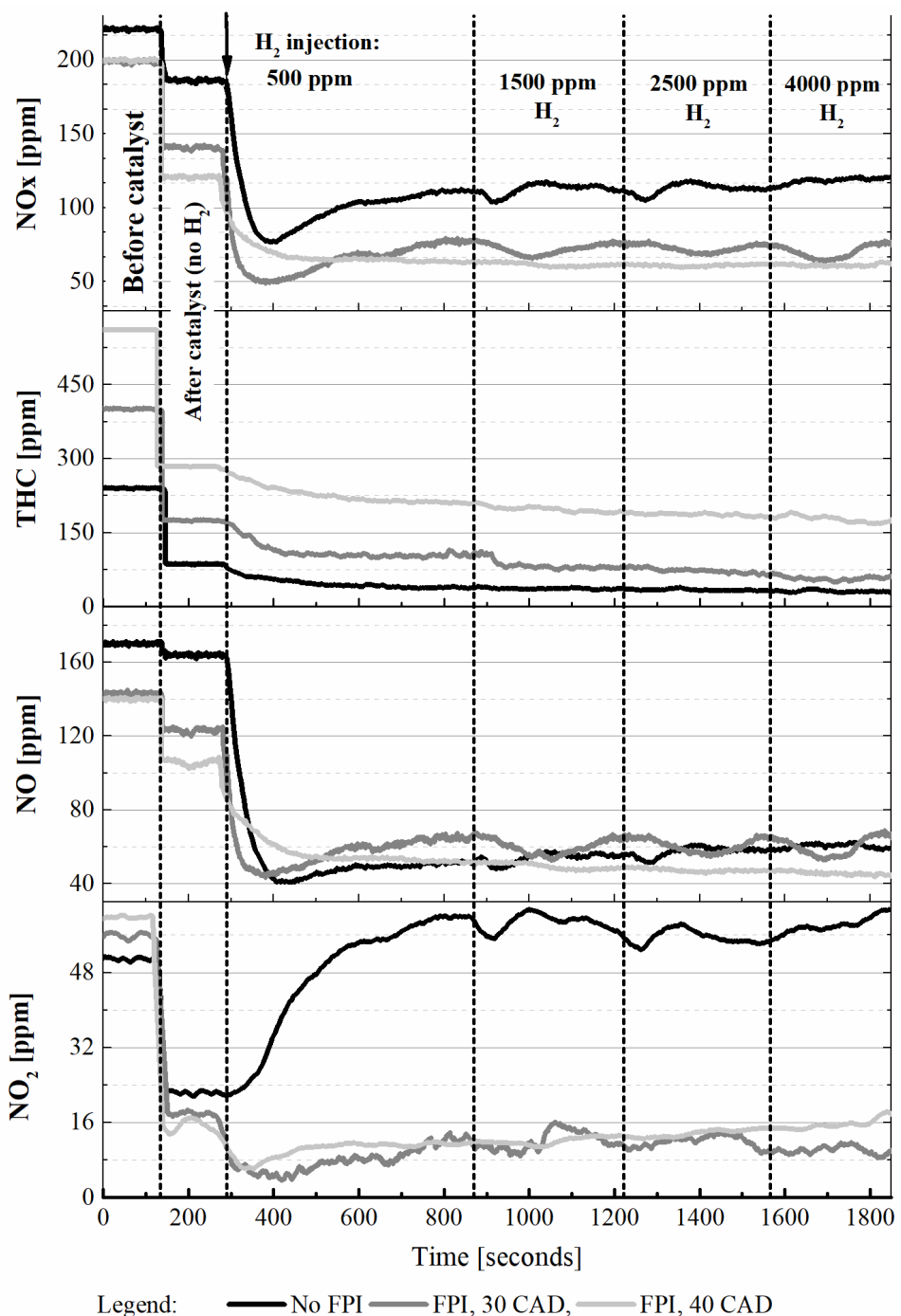


Figure 5.11: NO, NO₂, NOx and THC emissions before and after the HC-SCR with/without H₂ introduction at low-load testing for diesel combustion

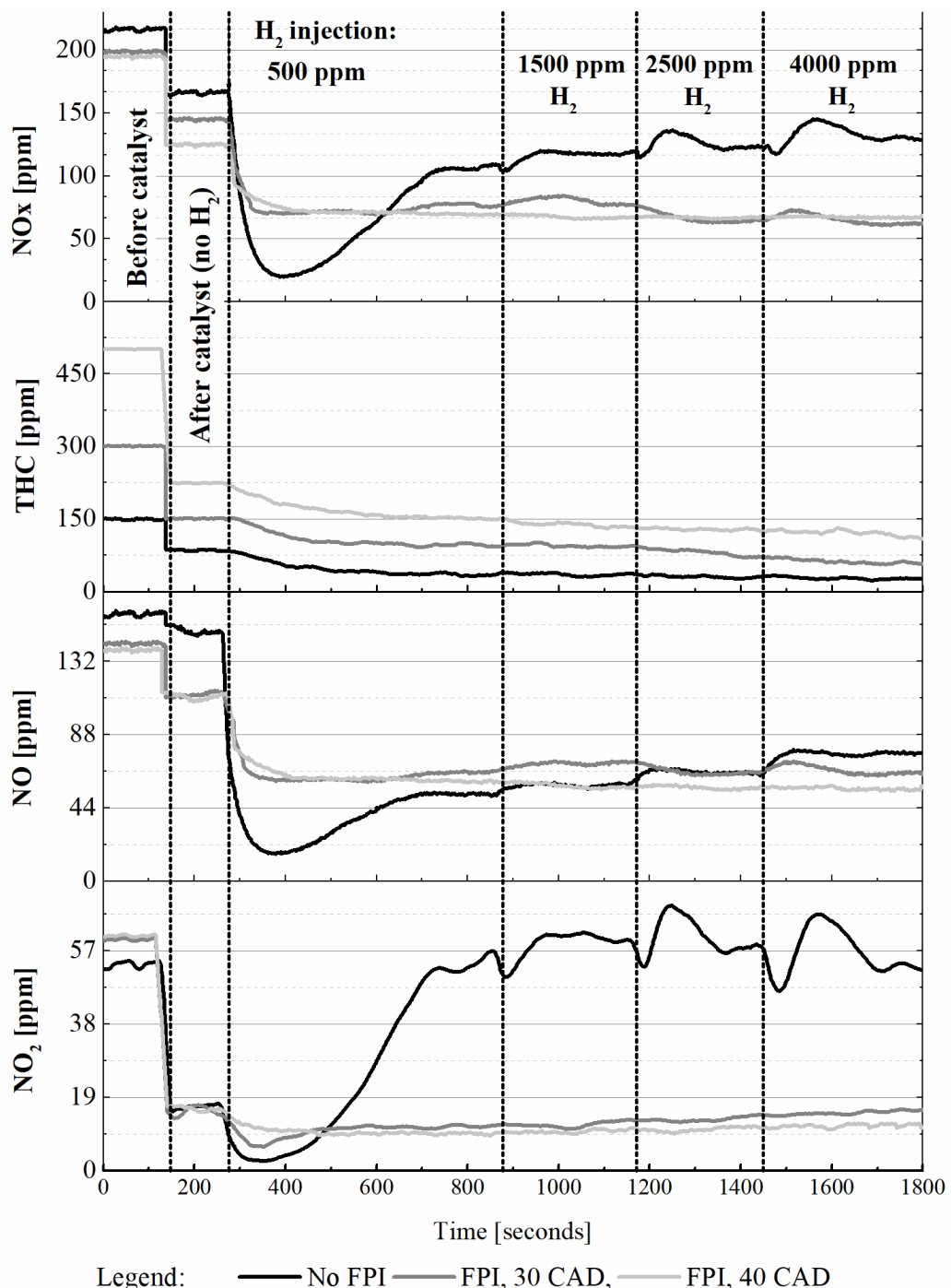


Figure 5.12: NO, NO₂, NOx and THC emissions before and after the HC-SCR with/without H₂ introduction at low-load testing for TP20 combustion

5.2.1.1 No-post mode

The activity of the HC-SCR catalyst in the no-post mode was very limited as only 16-22% NOx conversion was achieved when both diesel and TP20 fuels were used as reductants. This was highly expected since at this load condition, there is insufficient temperatures to help in activating the exhaust hydrocarbons into reactive agents (i.e. HCO) to participate in the catalytic conversion. It was seen that this conversion is directly attributed from the NO₂ portion in the exhaust, while NO did not present any noticeable conversion.

Introducing H₂ (500 ppm) to the exhaust feed considerably improves the SCR catalytic performance during the initial phase of the testing (first 5 minutes), where a NOx conversion of 63.3% (80 ppm residual) was recorded for diesel and 93% (15 ppm residual) for TP20. This is attributed to the role of H₂ in activating the molecular oxygen (O₂) or lower its activation energy to yield reactive-oxygen species such as O₂⁻ and HO₂ (Vassallo J. et al., 1995). The exact mechanism by which H₂ enhance the de-NOx catalytic activity is detailed in Section 2.5.1. The increased activity shown from the TP20 combustion will be further discussed in the Section 5.2.1.2.

Tracking the remaining HC emissions that survive the catalytic reactions, very low level can be detected downstream the catalyst, implying that no enough reductants were available to maintain the initial NOx conversion. Thus, the catalyst activity gradually decreased with time and stabilize at ~120-125 ppm (38-40% conversion), for both fuelling. In addition, the level of NO₂ gradually increased throughout the reaction stages (from 20 to 60 ppm) when H₂ was presented. Therefore, it can be speculated that after consuming the available HCs to launch the SCR reactions, the excess of H₂ surviving the reactions triggers the NO-NO₂ oxidation pathway.

To feed the catalyst with a fuel-rich exhaust feed, PFI application was introduced at 30 and 40 CAD ATDC (Section 5.2.1.2)

5.2.1.2 PFI mode

Application of PFI (without introducing H₂) drastically improves the catalyst de-NOx efficiency to 35% and 45% (for both fuels) at 30 and 40 CAD respectively. It is worthy to note that these de-NOx efficiencies are remarkably higher than what is expected from the literature (~20%) at these operating parameters (exhaust temp, 180 °C and HC:NOx ~ 2:1) (Houel et al., 2007b), where in-pipe diesel injection was used to regulate the exhaust HC:NOx ratio. This is mainly attributed to the minute concentration of H₂ produced from the PFI application as explained and shown earlier in Section 5.1.1.

The key role of H₂ in enhancing the HC-SCR activity is evident with the injection of no more than 500 ppm. NOx concentrations upstream the catalyst decreased and stayed in the range of 65-74 ppm (63–70%) for both fuelling (diesel and TP20) and strategies (30 and 40 CAD ATDC). No noticeable difference was seen between the two injection scenarios as the 30 CAD application delivers the needed optimal HC:NOx ratio (1:1) for this exhaust temperature condition, as suggested in the work of Houel et al. (2007b). In addition, no noticeable deactivation was seen during tests (roughly 25 minutes was tested for each operating parameter). The addition of higher amounts of H₂ (1500, 3000 and 4500 ppm) did not show any amelioration compared to the activity seen with only 500 ppm H₂, even when more HC:NOx ratios were presented (40 CAD ATDC). This could be mainly due to the fact that:

(a) HCs are sufficiently activated, and the catalyst reached its maximum performance under this exhaust temperature (180 °C). This implies that the reduction shown along the THC

when increasing the H₂ injection is correlated with direct oxidation of the former due to the local thermal effect of the H₂ gas (i.e. heat produced from the oxidation of H₂).

(b) limited rate of soot deposition in the catalyst and thus no additional amounts of H₂ were required to maintain the soot trapping-oxidation mechanism, as it is advised in the litterature (Theinnoi et al., 2010). The sustained catalytic activity confirms that with the use of modern common rail engines and cleaner fuel generation, the applicability of the HC-SCR catalyst is more pronounced as the level of exhaust particulates is significantly dropped compared to old engine technologies (Houel et al., 2007a; Houel et al., 2007b; Sitshebo, 2010; Theinnoi et al., 2010).

Furthermore, despite that combining the PFI application with TP20 combustion resulted in lower HC:NOx ratios compared to diesel, the catalyst de-NOx efficiency was similar between both fuelling. Along with the reduced soot level seen with the TP20 case, the reactivity of the fuel molecule (TPGME) also plays a significant role in terms of NOx reduction (K. I. Shimizu & Satsuma, 2006). Changing the oxygenate fuel structure significantly affect the Ag/Al₂O₃ de-NOx activity. Recent studies approved that in the absence of H₂, the reactivity of the different oxygenated group vary in the following order: “ethers > alcohols > aldehyde > ester > ketone”. However, when H₂ is introduced, the order of the functional group is changed in a way that “ethers > alcohols > ester > ketone > aldehyde” (Ken Ichi Shimizu, Tsuzuki, & Satsuma, 2007). The reactivity of the propylene glycol ethers molecules, such as TPGME ($\text{CH}_3\text{OC}_3\text{H}_6(\text{OC}_3\text{H}_6)_2\text{OH}$) is still not reported till date and the exact mechanism (i.e. the corresponding intermediates in the SCR reactions) by which these molecules reduce NOx emissions is still not discovered. However, due to the presence of both ether and alcohol moieties in the structure of this candidate, which shows to be the most reactive groups in

reference (Ken Ichi Shimizu, Tsuzuki, & Satsuma, 2007), it can be speculated that TPGME should be more reactive than the diesel molecules. Also, the physical properties of the incorporated oxygenate plays an important role in dictating its effectiveness:

- (a) TPGME have shorter chain-length and present a lower viscosity compared to the different hydrocarbons contained in the diesel fuel. This allow the TPGME molecule to diffuse more freely onto the catalyst surface which in turn offer a better access to the catalyst active sites (Herreros et al., 2014).
- (b) TPGME is also polar in nature and miscible in water as it includes OH radical in its structure. This is also another advantageous parameter compared to diesel as TPGME can effectively compete with water for being adsorbed onto the surface of the catalyst (Herreros et al., 2014).

5.2.2 4 bar IMEP testing

Figure 5.13 and Figure 5.14 illustrate the activity of the HC-SCR catalyst at the 4 bar IMEP condition with/without H₂ addition for diesel and TP20, respectively:

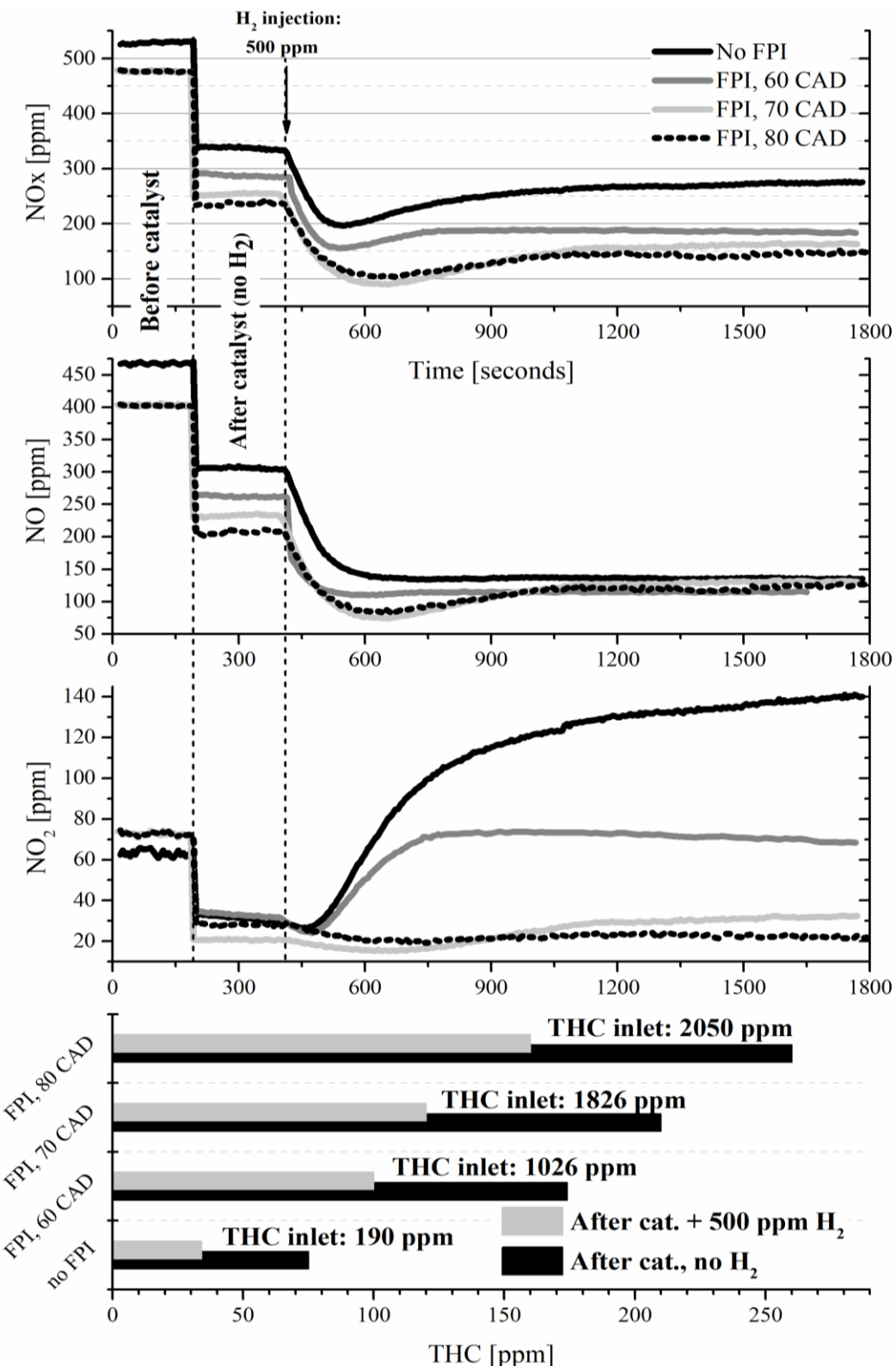


Figure 5.13: NO, NO₂, NOx and THC emissions upstream and downstream the catalyst with and without H₂ introduction at 4 bar IMEP for diesel combustion

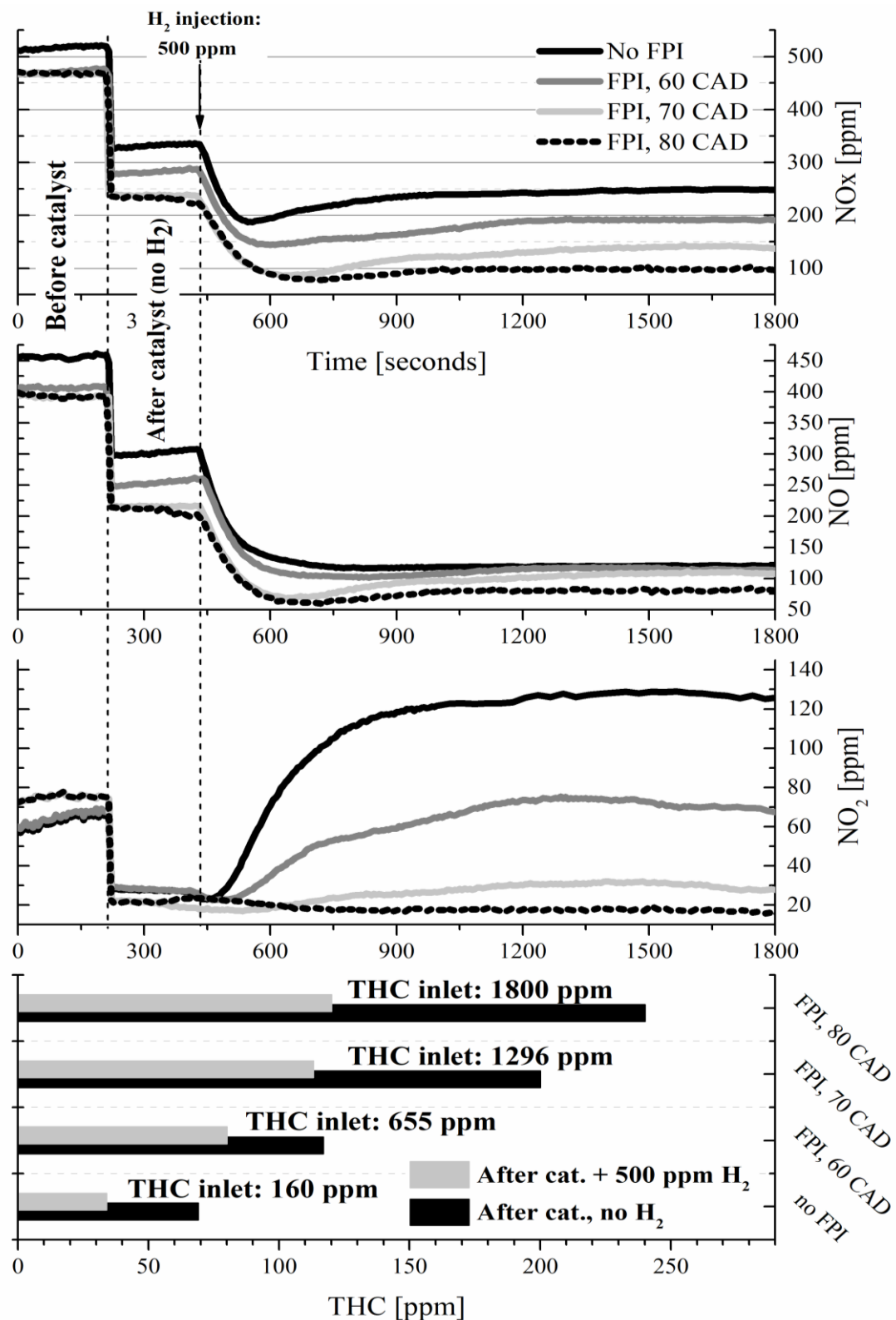


Figure 5.14: NO, NO₂, NOx and THC emissions upstream and downstream the catalyst with and without H₂ introduction at 4 bar IMEP for TP20 combustion

5.2.2.1 No-post mode

In the absence of H₂, the catalyst performance in the passive mode was improved for both fuels compared to the 2 bar IMEP results, reaching around 34% total NOx conversion for both fuelling. This was expected since the hydrocarbons can be activated more easily at this relatively higher temperature (~290 °C). Again, the addition of 500 ppm of H₂ enhances the de-NOx performance for both fuelling, with NOx concentrations dropping to 200 ppm (~ 61-62% conversion) at the early stages of the test. Nevertheless, the catalyst activity gradually deteriorated during the first minute of testing and the non-reacted NOx level increased from 200 ppm to 270 ppm (50.94 %) in case of diesel and from 200 ppm to 250 ppm (51.45%) in case of TP20. Following the insignificant THC level upstream the catalyst and the remarkable increase in the NO₂ emissions, it is evident that this lower de-NOx performance is not produced from any catalytic deactivation or surface poisoning by nitrates, it is mainly attributed to the low level of HCs in the exhaust. Same as in the 2 bar IMEP testing, the optimised PFI strategies suggested earlier in Section 5.1.1 were introduced to test the applicability of this strategy.

5.2.2.2 PFI mode

Retarding the PFI timing (increasing the HC:NOx ratio) increased the catalyst de-NOx ability for both fuelling with and without the introduction of H₂. Comparable efficiencies were recorded between both fuels in the absence of H₂, limited to a maximum of 58% conversion at 80 CAD FPI. Monitoring the NO₂ levels upstream the catalyst, it can be concluded that after introducing 500 ppm H₂, the 60 CAD PFI strategy (HC:NOx ~ 1.5 for TP20 and HC:NOx ~ 2.4 for Diesel) failed to supply the required HCs for this condition (e.g. NO₂ starts to increase). However, further retarding the injection to 70 and 80 CAD ATDC lead for enough reactants for

both fuelling. Significantly higher de-NOx conversion was shown with TP20 under all testing conditions, despite that lower HC:NOx ratios were produced compared to the diesel equivalent conditions (Figure 5.6). The best de-NOx performance was seen with the 80 CAD PFI application reaching 68.75 % (150 ppm) and 79 % (100 ppm) for diesel and TP20, respectively.

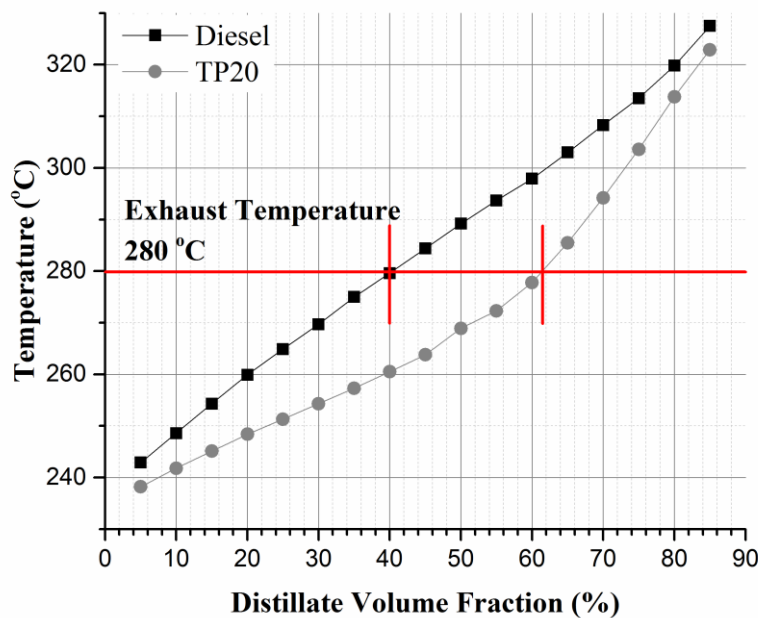


Figure 5.15: Diesel and TP20 distillation curves, reproduced from (B. L. Smith et al., 2008)

The possible explanations for that better activity was stated earlier in the 2 bar IMEP section, however, at this higher load condition (i.e. higher exhaust temperature), another possible reason could be clarified by referring to the fuel's distillation curves. As illustrated in Figure 5.15, at a representative exhaust temperature that corresponds to our testing condition (280 °C), around 40% of the hydrocarbons contained in the diesel fuel are expected to be in the vapour state. However, blending diesel with TPGME (TP20: 20.9% vol. replacement) increase this gaseous portion to 63% under the same temperature level. It is therefore suggested that in the case of TP20, greater portion of the reductants will undergo the de-NOx reactions in their gaseous state and thus better catalytic activity was seen compared to diesel.

To investigate the sensitivity of the H₂ addition, higher levels (2000 and 4000 ppm) were introduced into the catalyst in conjunction with the 80 CAD PFI event as it was seen that relatively higher amounts of HCs survived the SCR reactions compared to the 60 and 70 CAD applications (Figure 5.16).

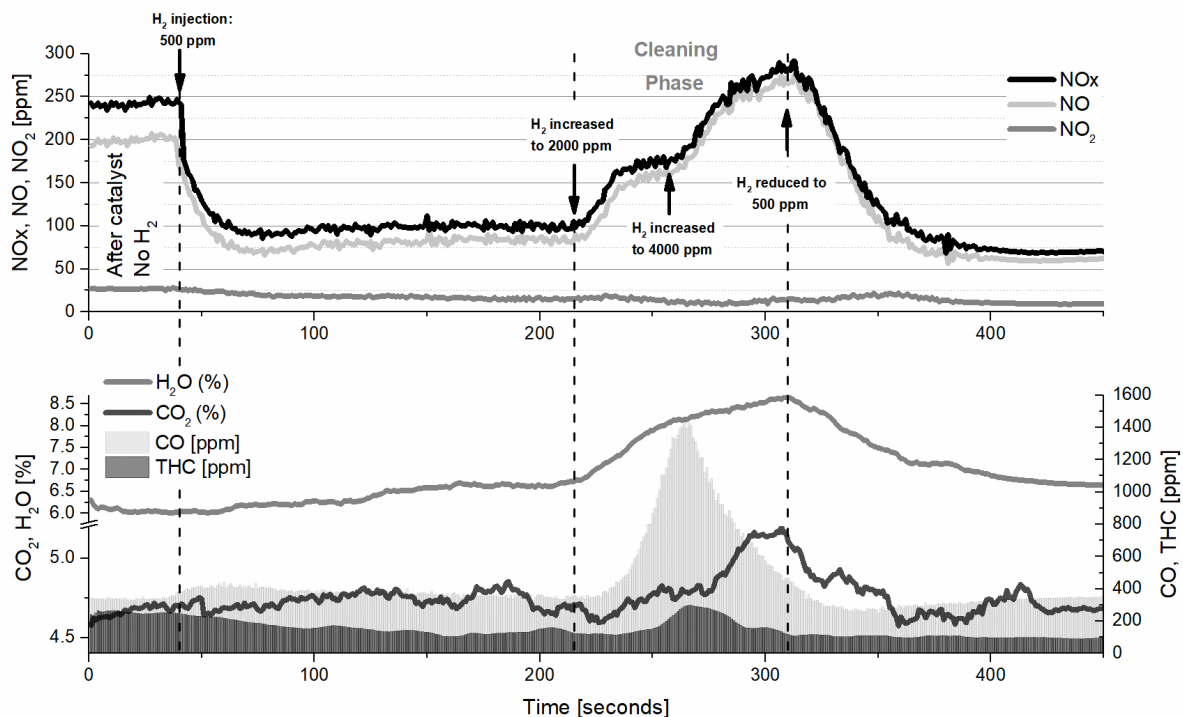


Figure 5.16: 2000 and 4000 ppm H₂ effect on the different gaseous emissions throughout the catalyst

Increasing the H₂ feeding level did not enhance the catalyst activity as it was expected. Oppositely, the de-NOx performance was drastically deteriorated and the total NOx emissions surviving the SCR reactions increased from 100 ppm to 170 ppm and 270 ppm when the H₂ level was increased from 500 ppm to 2000 ppm and 4000 ppm, respectively. This was majorly contributed from an increase in the NO emissions and not in the NO₂ as it is the case earlier when no enough HCs are presented. At this relatively higher temperature condition, higher

amounts of H₂ can lead to the oxidation of the exhaust HCs instead of its activation, which hinders the catalyst activity. This was clearly seen from the increased level in CO, CO₂ and H₂O emissions during that phase. Injecting 2000 ppm H₂ sharply increased the CO concentrations to 1400 ppm, indicating that part of the HCs is partially oxidised. Further increasing H₂ to 4000 ppm resulted in sharp increase in CO₂ and H₂O levels, while CO concentrations dropped back to its initial level, highlighting a complete oxidation mechanism of the exhaust HCs. Similar conversion trends were spotted between diesel and TP20 combustion and thus the impact of increasing the H₂ level is only shown for the TP20 case in Figure 5.16.

This increased level of CO and CO₂ emissions could also result from the oxidation of the soot trapped in the catalyst. To further investigate this theory, the H₂ level was set back to 500 ppm after subjecting the catalyst for an exhaust flow containing 4000 ppm H₂ for 5 minutes. It should be also noted that this H₂ sensitivity test was made at the last day of the experimental testing. The purpose of the test is to check the catalyst health after being subjected to all these extensive testing conditions, i.e. tests are always made in low temperature region and H₂ was not always supplied to the flow. As shown in Figure 5.16, reducing the H₂ level back to 500 ppm ameliorated the catalyst de-NOx activity, however no more than 10 ppm reduction was seen compared to what it used to be before this cleaning phase (from the original 100 ppm level to 90 ppm). This better activity seen confirm the role of H₂ in effectively oxidising the trapped soot particulates but most importantly, the limited increase in the total deNOx activity confirms that after all these extensive testing, the HC-SCR catalyst is still in a clean and non-deactivated state.

5.3 Catalyst sulphur tolerance

The SO₂ concentration in the exhaust was typically constant for all the testing conditions (fuel type, load condition and FPI timing) with a mean value of 0.6 ppm in the exhaust line, independent from the sampling position point (before or after the catalyst) (Figure 5.17). The readings in Figure 5.17 are only presenting the 4 bar IMEP load condition with PFI at 80 CAD ATDC using diesel as an operating fuel. Other testing conditions were not plotted to avoid duplication of the results. It should be also noted that 0.6 ppm is the lowest SO₂ detection limit that the FTIR gas emission analyser can recognise. In other words, those readings are more possible to be noise signal and the SO₂ level in the exhaust is expected to be even lower than 0.6 ppm. This minimal concentration of SO₂ resulted mainly from the nature of the base-fuel incorporated in our tests, namely, ultra-low sulphur diesel, which has less than 10 mg of sulphur in 1 kg, as specified by the supplier (Shell Global Solution) and detailed in Table 3.3.

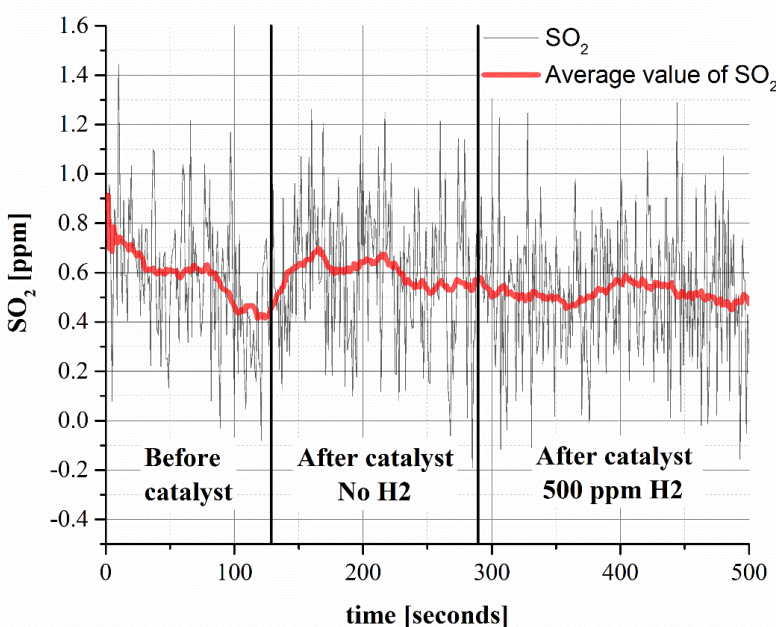


Figure 5.17: SO₂ concentrations before and after the catalyst with and without introduction of 500 ppm H₂

Shimizu et al. (2007) tested the SO₂-resistance of an Ag/Al₂O₃ HC-SCR by continuously feeding (6 to 48 hours) the catalyst with a representative flow of diesel exhaust gas saturated with different concentration of SO₂ (0, 5 and 50 ppm). The SO₂-resistance was mainly evaluated by recording the de-NOx activity of the catalyst with and without the presence of H₂. It was seen that in the presence of H₂ and under low temperature operating condition (250 °C), 50 ppm SO₂ deteriorated the catalyst de-NOx activity from 65% to 5% after 37 hours. However, with 5 ppm SO₂, only minor deactivation was seen during the same testing period.

Following the results of ref. (Ken Ichi Shimizu, Tsuzuki, & Satsuma, 2007), we did not find any importance to study the tolerance of the catalyst toward SO₂ deactivation for any of the testing conditions since as clarified earlier, the exhaust SO₂ level did not exceed 0.6 ppm. The catalyst is not expected to face any deactivation by sulphate deposition and as reported earlier in Section 5.2.2.2, the catalyst was found to be in normal activated state after all the tests.

5.4 Hydrocarbon activation in the HC-SCR

As indicated in Section 5.1.1, wide range of different HC species with different physical properties (i.e. chain length, boiling temperature, etc.) are generated into the exhaust stream with different PFI strategies. Quantitative analysis of the different HC reactants upstream and downstream the catalyst was carried-out to understand the reactivity of the individual species on the NOx conversion pathway. The below analysis is only considering the most optimal injection strategies that lead to the highest catalyst activity, i.e. 40 CAD FPI for the 2 bar IMEP condition and 80 CAD FPI for the 4 bar IMEP condition, with/without the presence of 500 ppm H₂. Concerning the light HCs, the same conversion trend was shown along both fuelling, thus only the emissions from the TP20 combustion was analysed and plotted in Figure 5.18.

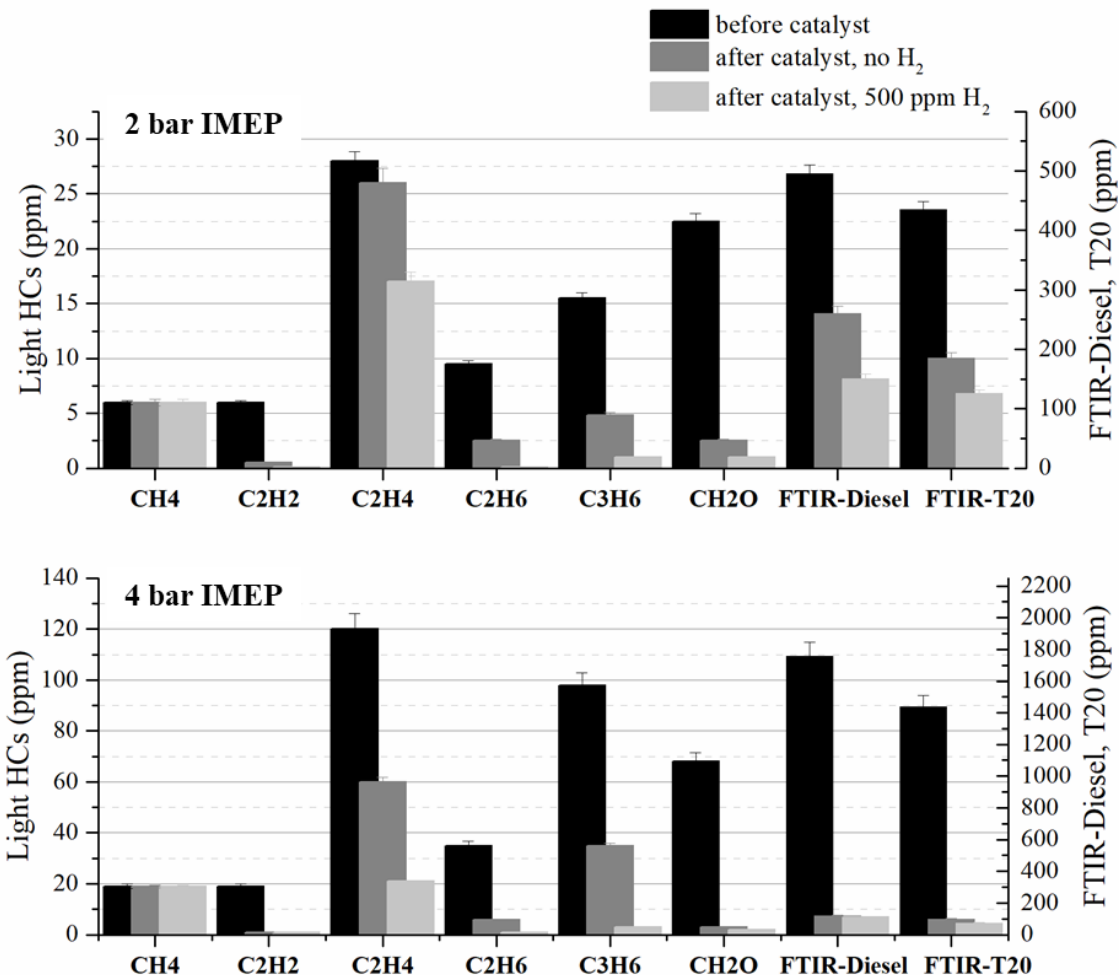


Figure 5.18: Light HCs and unburned fuel portion activity within the catalyst with/without 500 ppm H₂ addition

At 2 bar IMEP, acetylene (C₂H₂), ethane (C₂H₆) and propylene (C₃H₆) partially reacted in the catalyst in the absence of H₂ (90%, 75% and 70% respectively) and were fully reacted when H₂ was introduced. Ethylene (C₂H₄) remains intact when H₂ was not introduced and partly react (34.65%) in its presence. As for methane (CH₄), the case was different, HC-SCR fails in oxidising/activating this species even when H₂ was injected. It is generally accepted that short chain HCs (C<5) present a stable chemical structure and thus they require large dissociation energy to crack their chain for being activated, which is typically disadvantageous for the HC-

SCR application (Burch et al., 2002). However, Gu et al. (2015) reported that at low temperatures, short chain HCs can result in high conversion rates, since all the reductants are expected to participate in the HC-SCR mechanism in the gaseous phase due to their low boiling point. This could explain the good activation seen for the light HC species (except CH₄) at the low temperature condition (2 bar IMEP, 185 °C). The enhanced activation in the presence of H₂ was discussed earlier in Section 3.3.1.1. It appears that the stable structure of methane results in a very low reactivity that couldn't be prevented even if H₂ is added (Diehl et al., 2010). Increasing the engine load resulted in higher exhaust temperatures (280 °C) that enhances the HCs thermal cracking process and thus better activation was recorded for all the species. Nevertheless, these temperatures were not enough to activate the methane emissions. The increased amounts of formaldehyde (CH₂O) presented with retarded PFI timings are considered as a drawback for this technique due the harmful effect of that compound. However, it was seen that HC-SCR was able to fully activate this specie at low temperature condition without H₂ introduction.

To assess the fuelling effect, the activation of the unburned fuel portion from diesel and TP20 combustion (FTIR-Diesel and FTIR-TP20 respectively) were also plotted in Figure 5.18. At 2 bar IMEP testing, FTIR-TP20 shows better conversion than FTIR-Diesel, with 60% and 50% total conversion, in the absence of H₂ along with 79.54% and 70% in its presence respectively. As discussed earlier in Section 3.2, the reduced level of particulates in case of TP20 and the expected higher reactivity of the TPGME molecule could both clarify the enhanced activation of the FTIR-T20 compared to the FTIR-Diesel. At higher load conditions, no clear difference could be seen between both species, where similar reduction efficiency of 95 and 93% was recorded with and without H₂ introduction respectively. It should be noted that

at this exhaust temperature (285-295 °C), the catalyst reaction pathways cannot be fully distinguished from the residual HCs after the catalyst, since the exhaust species could be oxidised instead of being activated. However, the most important point is that most of the unburned fuel portion did not survive the catalytic reactions and the HC slip was limited to no more than 20-40 ppm.

In summary, the increased portion of light HCs seen with the PFI application did not present any drawback for the HC-SCR de-NOx mechanism. The unburned fuel portion along with the cracking products of the fuel (i.e. FTIR-Diesel and FTIR-TP20) prove to be the most important parameter dictating the catalyst activity, with TP20 proving itself as a promising agent able to launch and sustain the HC-SCR de-NOx reactions.

5.5 Summary

A novel approach in enhancing the low temperature de-NOx activity of an HC-SCR catalyst combined with small amounts of H₂ addition, using in-cylinder PFI strategies to control the exhaust HC:NOx ratio and exhaust gas composition (i.e. HC species, NO, NO₂ and soot) was presented. In addition, the impact of the PFI application on the soot morphology was evaluated.

Retarding the PFI timing from 10 CAD ATDC to 90 CAD ATDC lead to an increase in the exhaust THC concentrations (specially the unburned fuel portion after 50 CAD ATDC) and slightly reduced the exhaust's NOx emissions and particulates level for all the tested parameters. TP20 combustion significantly decreases the PM emissions without negatively affecting the NOx discharges. PFI proved itself as a feasible replacement for the in-line injection technique as a wide range of the HC:NOx ratios (1:1 to 4.5:1) could be optimised with

a maximum fuel penalty of 1.5% at the 2 bar IMEP testing and 2.8% for the 4 bar IMEP condition, with no more than 2% penalty in the engine brake thermal efficiency. Concerning the soot morphology, more circular and smaller particulates that comprise a lower number of primary particulates was seen in case of PFI. However, very limited changes were seen along the primary particulate size. A novel approach is suggested regarding this strategy: the heat generated from the PFI is mainly oxidising the non-mature part of the particulates, most probably the nucleation mode, and prevent it from aggregating over the bigger particulates, thus reducing both, the PM level and their corresponding geometric mean diameter.

Interestingly, even though the HC:NOx ratios of the combusted fuels with similar PFI timings followed the order diesel > TP20, the catalyst was able to achieve higher NOx conversion with the TP20 fuelling under all testing conditions. Increasing the H₂ addition in low temperature condition did not improve the NOx conversion, which was already significant with maximum NOx conversions of 63-70% achieved with diesel and TP20 fuels at 2 bar IMEP and 68.75% and 79% at 4 bar IMEP respectively, with no sign of catalyst deactivation. This could be possibly due to a low rate of soot deposition in the catalyst (i.e. due to the modern diesel engine, PFI application and oxygenated fuel combustion) and thus additional H₂ amounts were not necessary to maintain the balance between the trapping of the particulates and their oxidation, as it is advised in the litterature. As a consequence, concentration of 500 ppm of H₂ in the flow was considered sufficient to fully activate the catalyst with the use of modern common rail diesel engine, even without the application of oxygenated fuel combustion. Technically speaking, if the on-board reforming method will be used to supply the needed H₂, very limited fuel penalty should be expected (~1%).

A summary of the chapter findings is presented in Figure 5.19.

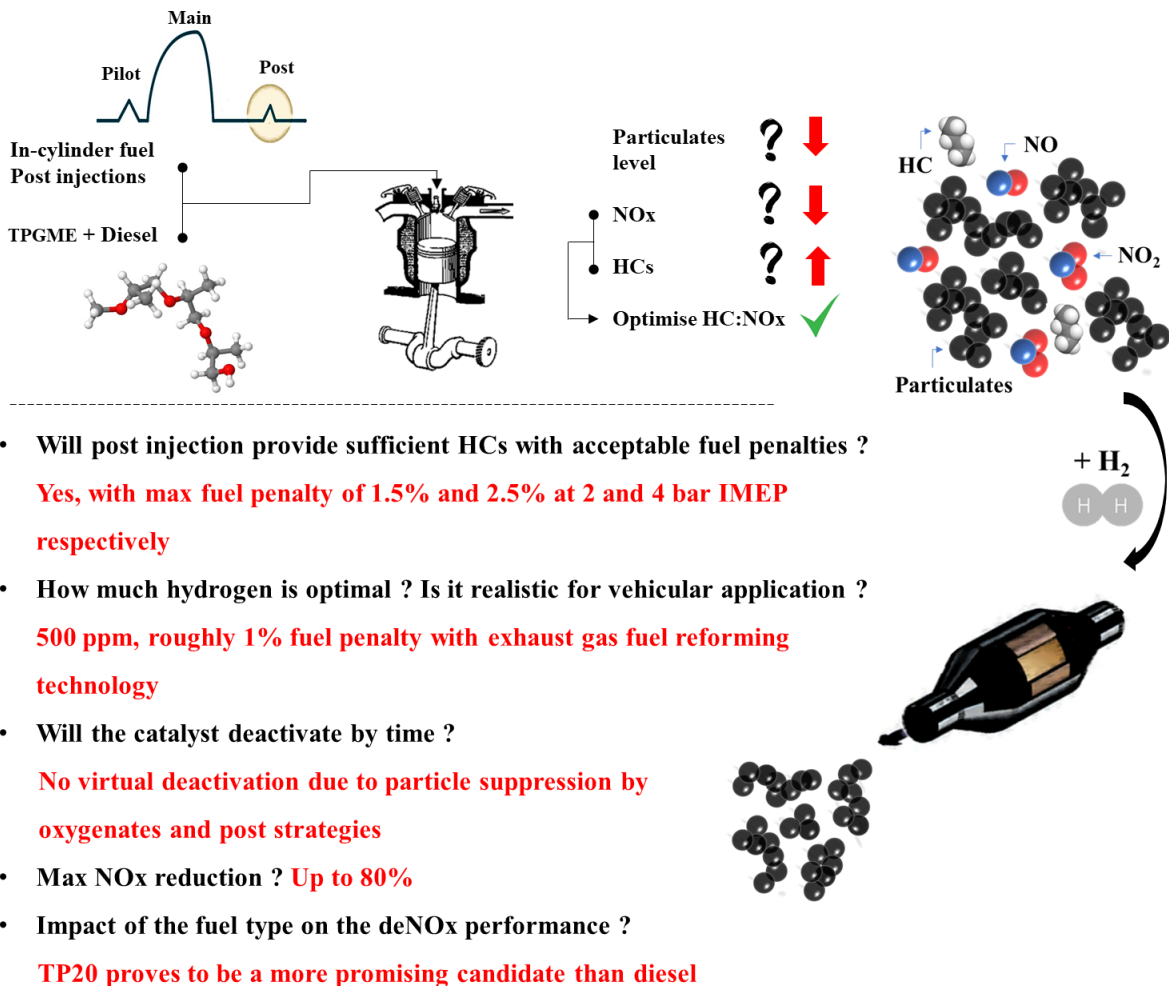


Figure 5.19: Summary of the HC-SCR findings with the application of post fuel injections and TP20 fuelling

CHAPTER 6

CATALYTICAL BREAKDOWN OF THE EXHAUST SOOT PARTICULATES BY THE USE OF SILVER BASED HC-SCR CATALYST

Silver based catalyst ($\text{Ag}/\text{Al}_2\text{O}_3$) can efficiently oxidise the PM particulates if enough residence time is provided throughout the catalyst (i.e. trapped particulate in the HC-SCR or $\text{Ag}/\text{Al}_2\text{O}_3$ coated DPF) (Aneggi et al., 2009; Corro et al., 2013; Gao et al., 2017; Ken Ichi Shimizu et al., 2010; Villani et al., 2005). As it is earlier reported in Chapter 5, the HC-SCR activity was sustained under all testing conditions with minor deactivation seen compared to the fresh catalyst activity. It is expected that the presence of H_2 in the exhaust helps in actively oxidising the soot particulates trapped within the catalyst during the live-operation of the system. Consequently, it becomes a subject of interest to understand if any oxidation reactions are launched over the particulates passing throughout the catalyst and not only those that have been trapped inside it. Such findings will help in predicting the most optimal design for the new generation of DPFs that have to be implemented with such novel de- NO_x technologies. Thus, after proving the ability of the HC-SCR system to operate effectively with post-injection strategies and new fuel generations, it is also important to understand if the catalyst will also aid the DPF regeneration process. To investigate this theory, the soot filtration efficiency of the catalyst and the possible morphological and nanostructure alterations imposed on the particulates once passing the catalyst in the presence and absence of H_2 are highlighted in this chapter. As TP20 can produce particulates which are more vulnerable for oxidation compared

to diesel, the study also covers the impact of the catalyst on the particulates produced from this oxygenated fuel.

A schematic representation of the main idea of the chapter and the related questions that this section is aiming to cover is presented in Figure 6.1.

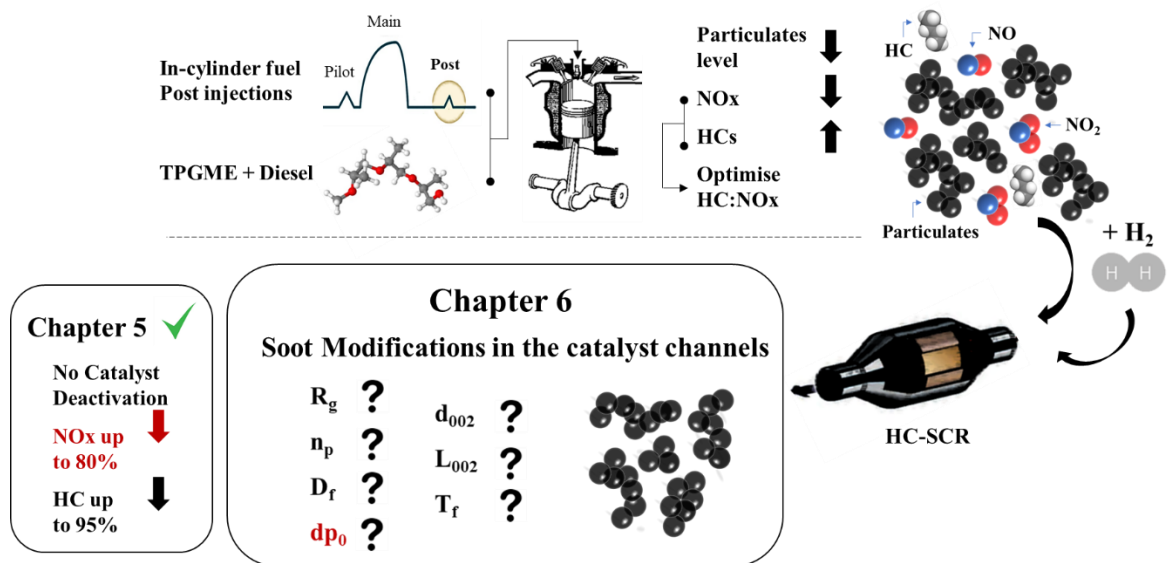


Figure 6.1: Schematic diagram presenting the chapter aims and the questions that will be covered in this research work

To better understand the impact of the catalyst on the structure of the particulates and to further investigate the role of H₂ in promoting the soot oxidation mechanism, exhaust soot aggregates were collected on TEM grids before and after the HC-SCR catalyst and characterised in terms of morphological and nanostructure alterations.

The catalyst filtration efficiency is also evaluated to build a basic understanding of the soot-catalyst surface interactions and evaluate the capability of this catalyst in filtering the PM from the exhaust.

To simplify the testing methodology, only the most optimal injection configuration that led for the highest HC-SCR de-NOx efficiency (in chapter 4) are investigated in the soot structural section. The testing plan is presented in Table 6.1:

Table 6.1: Testing parameters for the HC-SCR impact on the particulates

Fuel type	load (IMEP)	tested injection configuration	H ₂
Diesel	2-bar	40 CAD ATDC	0 ppm
			500 ppm
TP20	2-bar	40 CAD ATDC	0 ppm
			500 ppm
Diesel	4-bar	80 CAD ATDC	0 ppm
			500 ppm
TP20	4-bar	80 CAD ATDC	0 ppm
			500 ppm

As for the filtration efficiency (Section 6.1), identical results were seen with both fuel types, thus only the diesel case with the strategies reported in Table 6.1 is presented to avoid duplication.

6.1 Catalyst filtration efficiency

Particulate size distribution, GMD and TPNC recorded before and after the HC-SCR catalyst along with the resulted filtration efficiency when H₂ is present/absent are plotted in Figure 6.2 and Figure 6.3 for the 2 bar IMEP and 4 bar IMEP conditions respectively. It is seen that at the 2 bar IMEP testing, 80 to 90% of the nano-sized particulates with a d_{smps}<20 nm is filtered throughout the catalyst, with no remarkable differences seen when H₂ is added to the reactants. As for the particulates ranging from 20 nm to 380 nm, constant filtration capability of 20-30% was seen, independently from the particulate size. Concerning the GMD, it is seen that an increase of ~8% is seen with or without H₂ introduction. Combining all the above, it can be speculated that the particulates with d_{smps}<20 nm have been mostly trapped in the catalyst by diffusion mechanism and/or aggregated with bigger particulates due to an enhanced collision phenomenon throughout the catalyst channels.

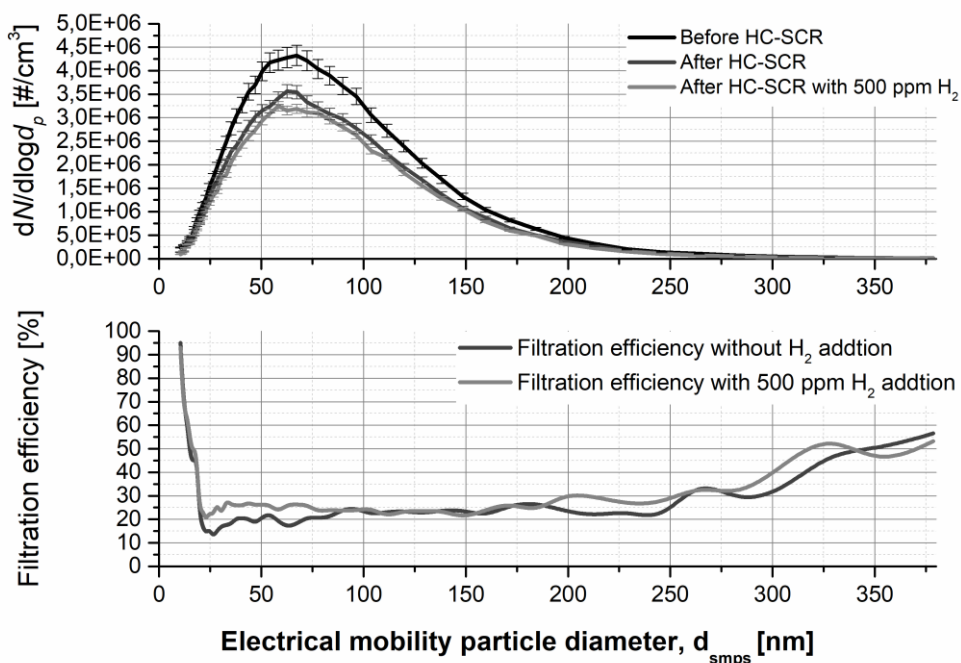


Figure 6.2: HC-SCR soot filtration efficiency at 2 bar IMEP for diesel combustion with and without the presence of 500 ppm H₂

Increasing the engine load did not present any remarkable difference when H₂ is not injected to the flow. Particulates with d_{smps} < 20 nm are mostly filtered and the rest of the range faces similar filtration of 30-40% (Figure 6.3). This small increase in the filtration efficiency compared to the 2 bar IMEP can be generated from the higher concentration of particulates passing throughout the catalyst and as a result better trapping capability could be seen due to the enhanced diffusion and collisions within the channels.

However, with the introduction of H₂, the filtration efficiency was slightly enhanced and most importantly the average GMD shows a small drop of 3%. Those results may be due to an enhanced oxidation mechanism launched over the soot flowing throughout the catalyst channels. To further approve these assumptions and have a clear hypothesis regarding the PM-catalyst surface synergies, morphological and nanostructure alteration of the particulates before and after the HC-SCR catalyst will be evaluated in detail in the following sections of the chapter.

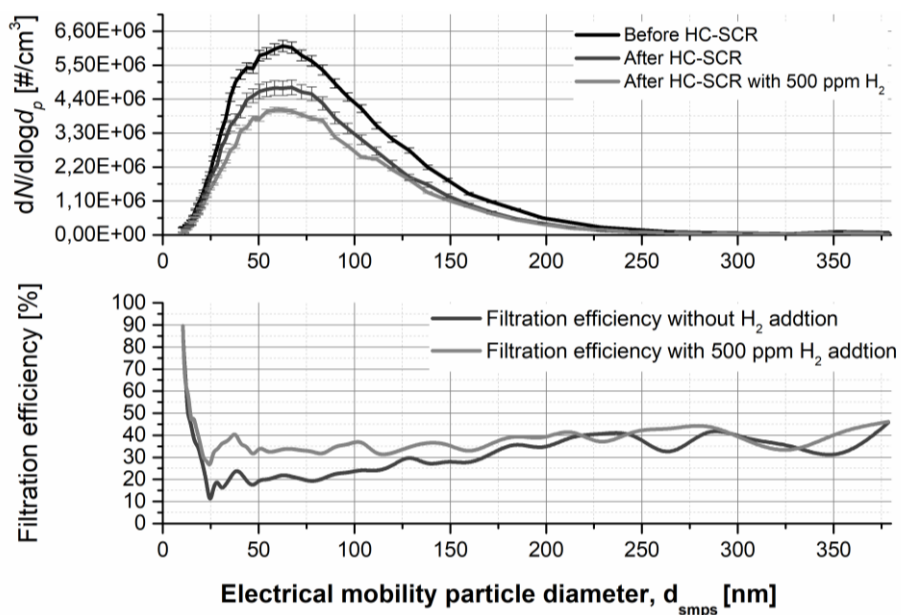


Figure 6.3: HC-SCR soot filtration efficiency at 4 bar IMEP for diesel combustion with and without the presence of 500 ppm H₂

6.2 Catalyst impact on morphology at 2 bar IMEP

The different soot morphological parameters including R_g , n_{p0} and D_f for the different testing conditions are plotted in Figure 6.4.

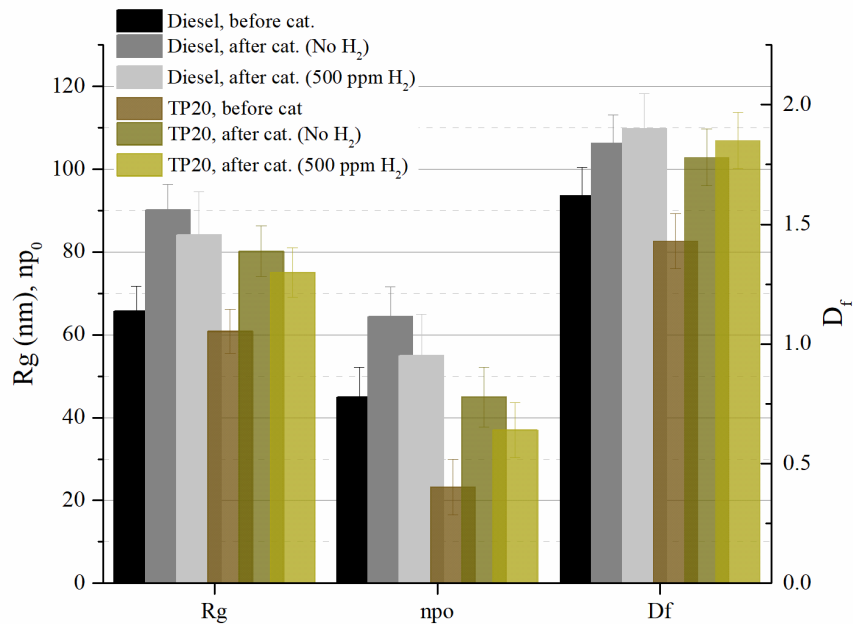


Figure 6.4: R_g , n_{p0} and D_f before and after the HC-SCR catalyst with/without H_2 addition at 2 bar IMEP condition

The normal distribution of the primary particulate's size (d_{p0}) is plotted in Figure 6.5. To generate a statistically significant analysis, ~ 30 aggregates were analysed for the morphological characterisation and ~ 350 primary particulates were measured to fit the log-normal distribution of d_{p0} .

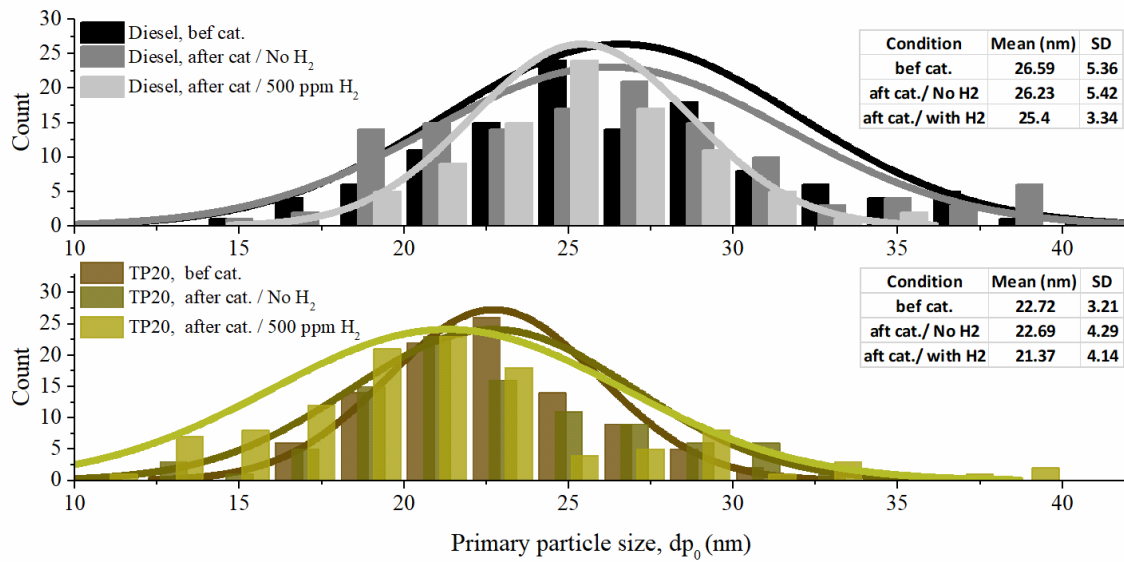


Figure 6.5: Primary particulate size distribution (d_{p0}) before and after the HC-SCR catalyst at 2 bar IMEP (a) Diesel, (b) T20

For better understanding of the different morphological alterations seen throughout the catalyst, the original TEM micrographs presenting each testing condition are also presented in Figure 6.6.

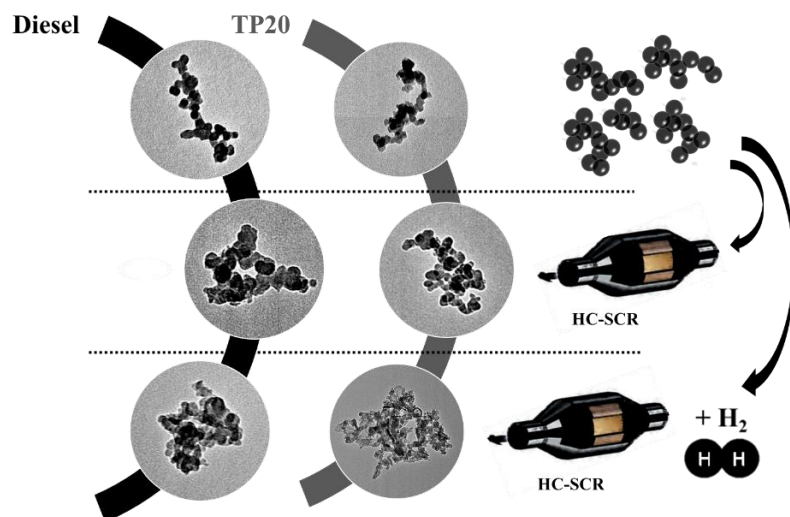


Figure 6.6: TEM micrograph for diesel and TP20 soot particulates before catalyst, after catalyst without H₂ addition and after cat with 500 ppm H₂ addition

It is seen that independently from the exhaust's H₂ level, aggregates with greater R_g and n_{p0} are seen after the catalyst for both, diesel and TP20 fuelling. Therefore, it can be concluded that only a limited portion of the particulates have been trapped inside the catalyst, as it was suggested earlier in reference (Fayad et al., 2015). Besides, it is expected that upon passing the catalyst channels, the soot particulates have faced higher chances of collision with the other neighbouring particulates and as a result more mature aggregates (i.e. by size) is spotted downstream the HC-SCR.

Furthermore, more spherical particulates were seen downstream the catalyst as suggested from the higher D_f values recorded in

Figure 6.4. This could be also the result of the enhanced collision process suggested earlier. Furthermore, the oxidation/activation of the HCs (exothermic reactions) throughout the catalyst along with the localised thermal effect of the H₂ are likely to increase the local and overall temperature of the catalyst. Higher catalyst temperatures can also help in thermally restructuring the soot shape into a more spherical entity, especially when H₂ is presented. Although it can be assumed that a worsened DPF trapping efficiency will result from the presence of more compact and spherical aggregates, the remarkable increase in the overall particulate's size (R_g) is expected to compensate their impact (Fayad et al., 2015). This assumption is mainly triggered from the fact the particulate's diffusion/convection pathway in a DPF (i.e. filtration mechanism) is mostly pronounced from the particulates' size and not their shape, as detailed earlier in Section 2.5.3.

Concerning d_{p0}, insignificant variations were spotted in the absence of H₂ for both fuelling conditions (Figure 6.5). However, in the presence of H₂, d_{p0} dropped by 2.7% in case of diesel and 3.6% in case of TP20. The only possible theory to clarify these results is that

despite the limited residence time of the particulates in the catalyst channels, soot oxidation reactions were launched once H₂ is injected. As for the increased reduction seen in case of TP20 with respect to diesel, it is expected to outcome from the enhanced oxidative potential of S_{TP20} (i.e. soot produced from the combustion of TP20) compared to that of S_{diesel}, as clarified earlier in Section 4.3.1.

These possible oxidation reactions are mostly generated from the increased level of NO₂ throughout the catalyst channels (i.e. transition on NO into NO₂ before being converted to N₂) since this oxidiser can launch the soot oxidation reactions in a temperature region as low as 200 °C (Ehrburger et al., 2002). This assumption was partially approved by Houel et al. (2007b) who reported that in low-temperature window (200 °C to 350 °C), H₂ addition will not only enhance the Ag/Al₂O₃ de-NOx activity but also withstand it. No virtual deactivation was recorded during the tests and that was mainly attributed to the oxidation of the already trapped soot via the excess of NO₂ emissions produced during H₂-SCR assisted cycle, as it was also advised by Breen et al. (2007).

The simplified reaction pathways presenting the NO₂-soot assisted oxidation mechanism are presented below:



Conversely, it is expected that O₂ should not assist the oxidation kinetics in this temperature window since higher temperature level (ranging in 500 to 700 °C) is needed. Furthermore, it is also confirmed in the literature that introducing H₂ gas in conjunction of an oxygen rich flow (as the diesel exhaust) can change the Ag particulate chemistry to act as an

oxidation catalytic agent. This is believed to result from the production of numerous sub-oxide elements (Kim et al., 2013) along with promoting the development of the active O₂⁻ ions that can also assist the soot oxidation process (Vassallo J. et al., 1995). Reader is referred to check Section 2.5.2 for a detailed review of the corresponding mechanism.

In summary, it can be concluded that despite the low catalyst temperature (180 °C), the increase in the local NO₂ emissions and surface oxygen functional species, with the presence of H₂, can partially oxidise the soot passing throughout the catalyst despite the very limited soot/catalyst residence time (flow-through substrate).

6.3 Catalyst impact on morphology at 4 bar IMEP

The different soot morphological parameters including R_g, n_{p0} and D_f for the different testing conditions are plotted in Figure 6.7.

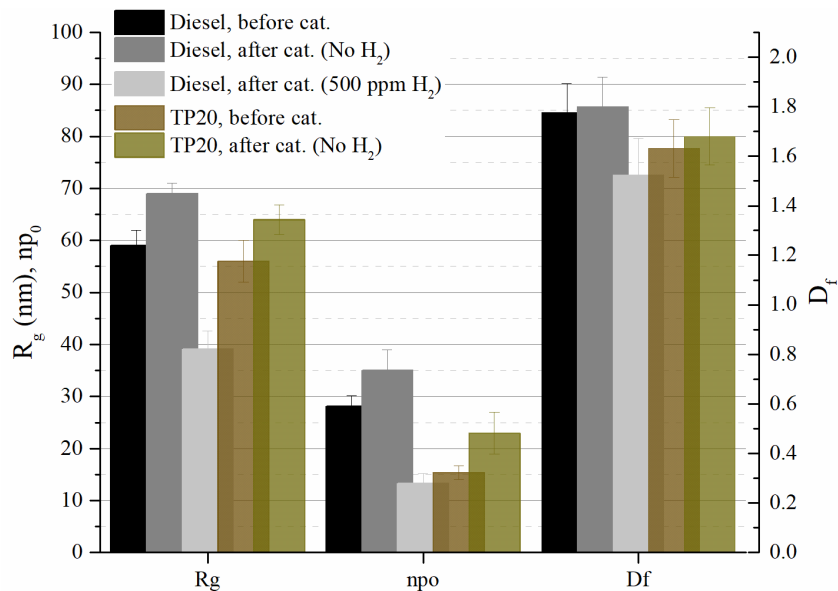


Figure 6.7: R_g, n_{p0} and D_f, before and after the HC-SCR catalyst with/without H₂ addition at 4 bar IMEP condition.

The normal distribution of the primary particulate's size (d_{p0}) is plotted in Figure 6.8

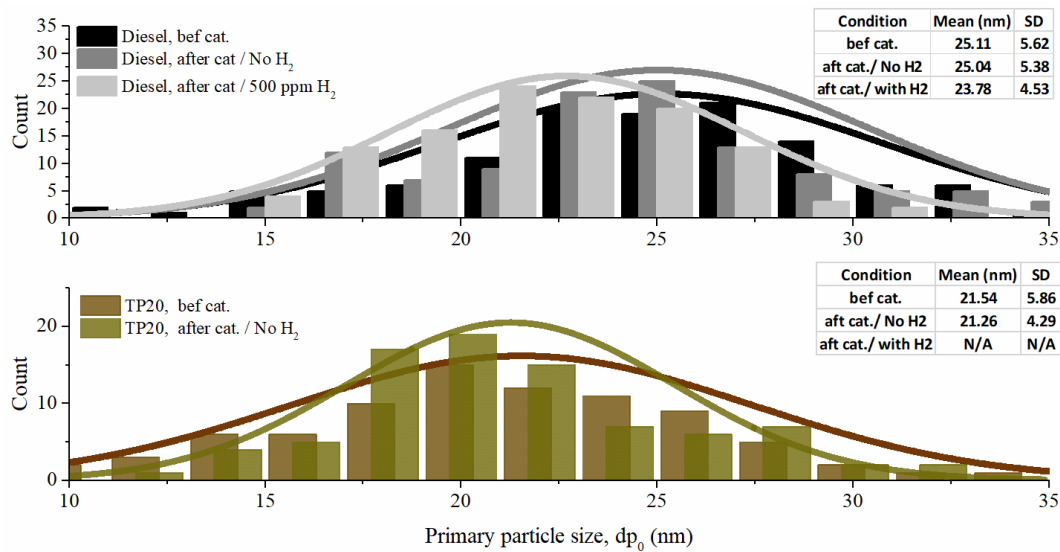


Figure 6.8: Primary particulate size distribution (d_{p_0}) before and after the HC-SCR catalyst at 4 bar IMEP

For better understanding of the different morphological alterations seen throughout the catalyst, the original TEM micrographs presenting each testing condition are also presented in Figure 6.9.

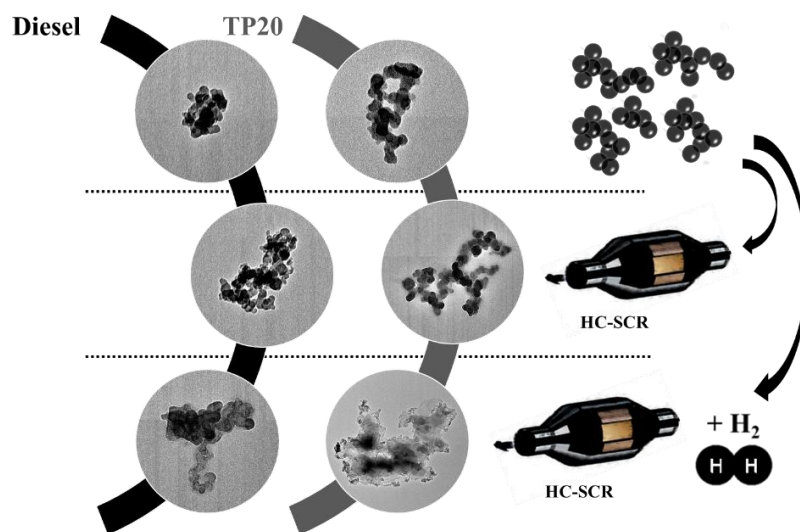


Figure 6.9: TEM micrograph for diesel and T20 particulates before catalyst, after cat without H_2 addition and after the catalyst with 500 ppm H_2 addition

Increasing the catalyst temperature to 280 °C (i.e. increasing the engine load) result in similar morphological changes to that seen with lower exhaust temperatures (~ 180 °C) when H₂ is not injected to the flow. It is seen that the particulates surviving the catalytic reactions present greater R_g, n_{p0} and D_f while d_{p0} kept constant for the diesel case with insignificant drop seen only for the TP20 case. As a result, it is expected that the particulates have survived an enhanced aggregation mechanism throughout the catalyst channels and no possible catalytic oxidation is presented, even though that the catalyst temperature is increased by 100 °C compared to the 2 bar IMEP test.

Introducing 500 ppm of H₂ activates the catalyst/soot synergies with significant modifications spotted compared to the 2 bar IMEP testing. As for diesel, a drop of 22% is seen for n_{p0}, 5.29% for d_{p0} and a total reduction of 10.16% for R_g. The significant reduction seen along d_{p0} confirms that with a little increase in the exhaust temperature, which is still representative of the low-temperature window, minute concentrations of H₂ can yield a powerful oxidation along the soot passing throughout the catalyst channels. It is expected that the NO₂-soot oxidation path is fully activated in this operating margin (~ 295 °C) and that the localised thermal impact of H₂ assisted with the promoted HC exothermic reactions (as HC level is increased in the exhaust compared to lower load testing) can also activate the O₂-soot oxidation pathway (Ehrburger et al., 2002; Theinnoi et al., 2012). As for R_g, the catalyst impact was more pronounced with more sever reduction seen along this parameter compared to d_{p0}. A hypothesis could be drawn regarding this trend and can be mainly identified with two different approaches (Lee & Zhu, 2004):

- (a) Breakdown of the aggregates throughout the catalyst channels

- (b) Reduction in the interstitial distances among the primary particulates constituting the aggregates

As n_{p0} also faces a noticeable drop downstream the catalyst, it is most probable that hypothesis (a) is the most dominant mechanism leading for this significant reduction in R_g . In addition, it is also speculated that the active oxygen species produced on the Ag particulates can also improve the soot/oxidisers contact and create electronic interaction between the surface of the catalyst and the soot particulates (thus promoting the breakdown phenomena).

Concerning the soot fractal like, particulates with more chain-like structure (~ 12% drop in D_f) is spotted downstream the catalyst. This configuration further indicates that hypothesis (b) is not valid for our analysis and highlight that a better DPF functionality can be expected with the application of the H₂-assisted HC-SCR catalyst to the exhaust flow. On the other hand, the increased local and global temperature of the catalyst is expected to thermally restructure the particulates into a more spherical entity (higher D_f), as seen in Section 6.1. However, this was not the case with this testing condition, which in turn signifies that the catalytic oxidation reactions were remarkably prevailing at this slightly higher exhaust temperature and were sufficiently energetic to dominate the thermal impact of the catalyst (i.e resulting in more spherical-like particulates).

The catalytic oxidation of the soot was not only seen through the reduction in their d_{p0} , but also through qualitative inspection for the TEM micrographs (Figure 6.9). It is seen that upstream the catalyst, the particulates collected present the standard graphitic configuration of a diesel soot, where the primary particulates are mostly spherical and quite distinct from the other spherules. However, downstream the catalyst, the primary particulates appear to have no definite borders and seem to be fused in each other, confirming the presence of a catalytic

oxidation. This blur appearance is mostly seen in case of TP20 where no statistically significant number of aggregates were detected on the TEM grids to produce a confident morphological analysis.

6.4 Catalyst impact on nanostructure

Since the soot morphological analysis highlights the presence of possible oxidation mechanism, it is of interest to check if any variation will be seen in the particulates' nanoscale arrangement. Such kind of information will be valuable to predict the reactivity of the aggregates surviving the catalytic reactions and can also give better insights to validate the oxidation reactions speculated from the reduction seen in d_{p0} .

Since no noticeable changes were seen with d_{p0} when H_2 is not introduced to the flow, the below analysis will account the impact of the catalyst only in presence of the H_2 . To simplify the results, Figure 6.10 summarise the resulted nanostructure parameters as a ratio of the values recorded upstream the catalyst compared to that seen downstream the catalyst (i.e. referred as post/pre in Figure 6.10).

Concerning the 2 bar IMEP testing, similar trend was seen between diesel and TP20: the catalyst helps in reducing the length of the carbon layers (-8.5% L_a for diesel and -13% L_a for TP20) and further twist their skeleton (+2.8% T_f for diesel and +1.5% T_f for TP20). However, inconspicuous variation ranging within the data-error bars is seen along the interlayer spacing ($d_{002 \text{ after cat}} / d_{002 \text{ before cat}} \sim 1$) for both fuelling. All the resulted parameters highlight a better oxidative reactivity for the particulates collected downstream the catalyst.

Concerning the 4 bar IMEP testing, only diesel particulate will be evaluated since as discussed earlier in Section 6.3, no statistically significant number of soot aggregates survived

the catalytic reactions in case of TP20. Starting with L_a , similar results are seen compared to the 2 bar IMEP condition while T_f show a further increase reaching 3.5%. However, d_{002} present a small drop of 1% compared to the pre-catalyst case, highlighting that more graphitic particulates are presented. It is expected that at this relatively higher exhaust temperature (~ 300 °C) the higher HC oxidation phenomena and increased NO₂-soot oxidation reactions can help in thermally restructuring the neighbouring carbon layers into more ordered series, resulting in slightly more graphitic configuration (Ma et al., 2014). However, accounting all the nanostructure parameters, it can be speculated that despite this shorter interlayer spacing, the particulates are expected to be more reactive since the layers' curvature have been increased by 3.5% and L_a reduced by 8.5%. Carbon layers curvature and length have been earlier proved to be more influential in dictating the particulate's reactivity compared to d_{002} , as reported in Section 4.3.4.

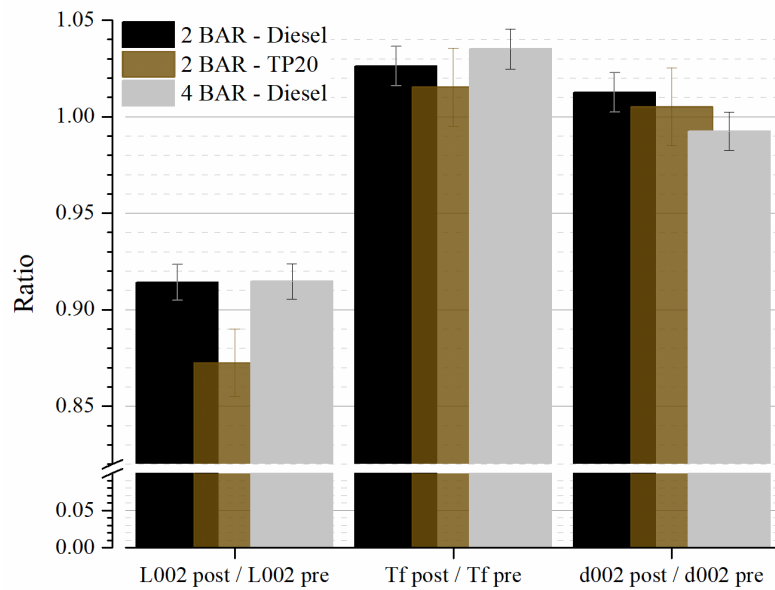


Figure 6.10: Nanostructure parameters ratios including L_a , T_f and d_{002}

Furthermore, to relate the nanostructure alterations to the possible soot/catalyst oxidation mechanism, the rate of soot burn-off in the catalyst will be calculated according to the difference in d_{p0} before and after the catalyst. Song et al. (2006) reported that during the first 40% stage of the soot burn off cycle, the oxidation reactions should follow the surface burning mode mechanism.

As a result, the following formula from reference (J. Song et al., 2006) can be used to assess the soot burn-off rate

$$\frac{dp \text{ post } SCR}{dp_0 \text{ pre } SCR} = (1 + z)^{1/3} \quad \text{Equation 6.3}$$

Where z is the burn-off rate.

The resulted rates are presented in Figure 6.11.

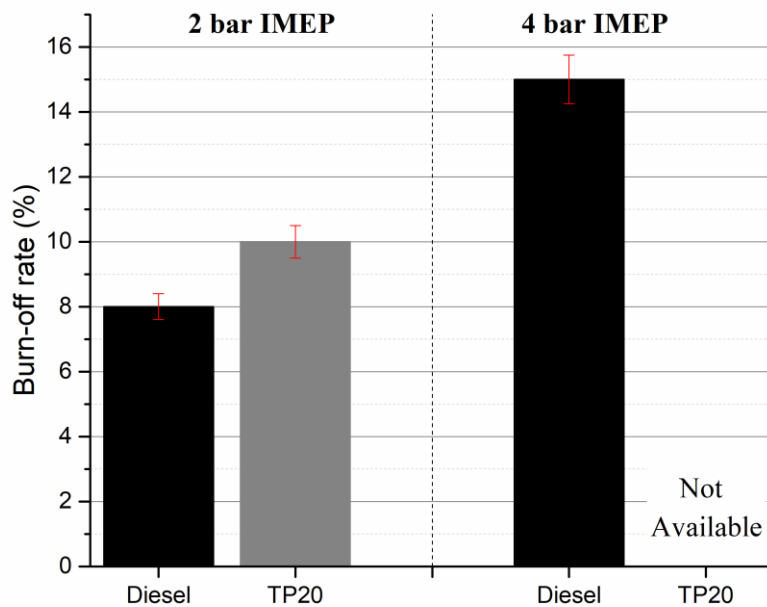


Figure 6.11: Soot burn-off rate for 2 bar IMEP and 4 bar IMEP conditions

As seen, at the 2 bar IMEP testing around 8 to 10% soot burn-off rate is expected and increases to 15% when increasing the load condition.

According to Song et al. (2006), Surface burning mode mechanism is generally defined as slow combustion reactions translated with a notable reduction in L_a and no more than 3% increase in the particulate graphitic ordering (using Raman analysis) during the first 20% burn-off phase. However, Ma et al. (2014) presented a more detailed approach concerning the above. The study covers the progress of the soot nanostructure alterations during the oxidation process of separate particulates collected upstream and downstream a DOC catalyst. Different trends were seen along L_a and d_{002} between both samples, thus no clear conclusion can be beneficial for our analysis, however, it was confirmed that T_f should increase by ~ 2% during the first 20% burn-off phase, independently from the soot collection point (downstream or upstream the DOC).

Summarising the findings of reference (J. Song et al., 2006) and (Ma et al., 2014), during the 20% burn-of phase, L_a is expected to decrease, while T_f is expected to slightly increase with moderate variation along d_{002} . Those findings positively correlate with the nanostructure variation shown in our analysis, thus confirming that these alterations are resulted from an enhanced oxidation mechanism in the catalyst channels.

6.5 Summary

The impact of an Ag/Al₂O₃ HC-SCR catalyst on the structure (morphology and nanostructure) and the filtration of the aggregates produced from the combustion of diesel and TP20 fuels was investigated in this part of the thesis. The catalyst role was evaluated upon three

main areas, the exhaust temperature (2 and 4 bar IMEP), fuel type and H₂ presence in the exhaust.

PM filtration efficiency was higher for small particulates and show to be constant for the bigger range of the aggregates (20-40% depending on the engine load). It was seen that independent from the fuel type or exhaust temperature condition, soot particulates tend to aggregate with the other neighbouring particulates when H₂ is not introduced to the flow. However, injecting 500 ppm of H₂ helps in significantly modifying the morphology of the particulates which seem to be more dependent on the exhaust temperature when H₂ is presented. At 2 bar IMEP (190 °C), particulates' aggregation remains the most dominant mechanism, however, it was seen that d_{p0} faces some reduction, highlighting the presence of oxidation reactions throughout the catalyst. Increasing the load condition to 4 bar IMEP, thus the exhaust temperature and the reactants in the catalyst, enhances the catalytical modification of the aggregates. It was seen that not only d_{p0} was reduced but also R_g and n_{p0}. Those alterations highlight that at this relatively higher exhaust temperature, soot particulates are not only oxidised, but they also tend to breakdown throughout the catalyst channels instead of being aggregated together.

The impact of the fuel nature was also seen in this study with higher rates of oxidation recorded with TP20 compared to diesel. The effect of the fuel was more pronounced when increasing the exhaust temperatures with better oxidation reactions seen in case of TP20. The aggregates were evaluated directly from the TEM micrographs instead of being morphologically analysed (i.e. post process in MATLAB) since the majority of the particulates were fused in each other (as hydrocarbon droplets) rather than being a solid soot aggregate.

In addition, following the nanostructure alteration detected downstream the HC-SCR, it was also expected that particulate with better oxidative potential can result from this application in the presence of H₂.

A summary of the catalyst role in the presence and absence of H₂ is presented in Figure 6.12.

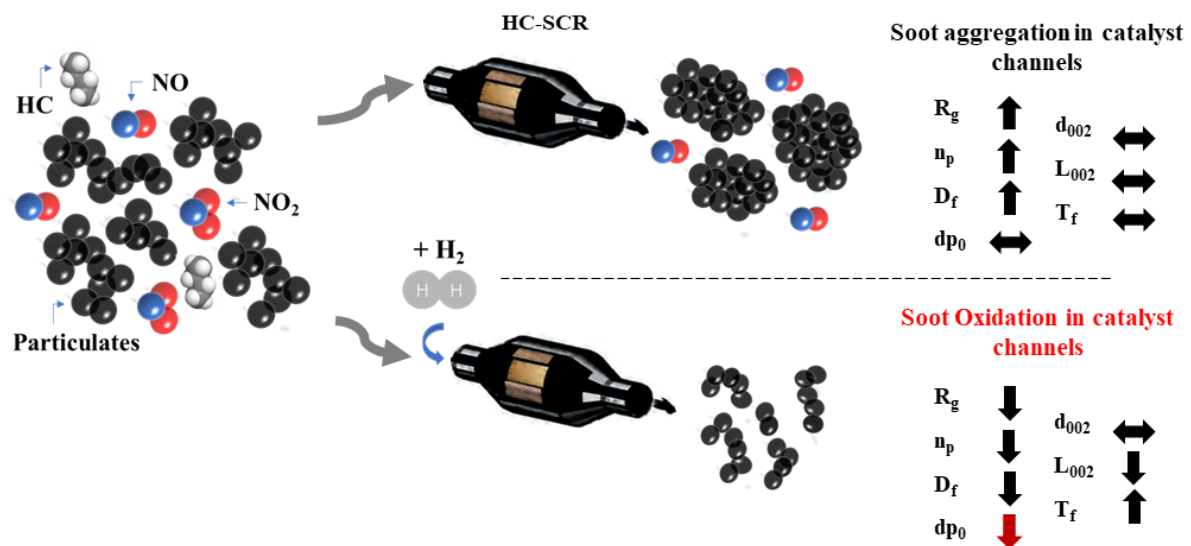


Figure 6.12: Summary of the chapter 6 findings

CHAPTER 7

CONCLUSIONS

7.1 Concluding Remarks

The main aim of this study is to understand how new fuel generations, namely, glycol ethers and late in-cylinder post fuel injections (PFI) can influence the diesel PM characteristics and alter the exhaust gas composition to ease the functionality of a non-commercial H₂-assisted Ag/Al₂O₃ HC-SCR catalyst. Following the remarkable de-NOx achieved when combining these technologies, it was also of interest to understand the impact of the catalyst itself on the soot characteristics to provide a full mapping regarding the soot destruction inside the cylinder and throughout the exhaust system, together.

Glycol ether diesel blends, especially DPGME and TPGME, are known for their capability in effectively reducing PM emissions; however, no study till date highlights their impact on the physical and chemical characteristics of the soot particulates. The tests were carried out using a modern common rail diesel engine operating with diesel, DP20 and TP20 blends respectively. It was seen that the use of these oxygenates can offer a better NOx/soot trade-off as both fuels kept the NOx emissions constant while significantly dropping the PM level, with TP20 being the most promising. Combustion stability did not show any negative impact when reformulating diesel with the oxygenated HCs (COV < 2%). DP20 and TP20 significantly alter the soot characteristics in a way that more chain-like aggregates with lower number of primary particles are emitted to the exhaust. Also, the average size of the primary

particle was also reduced. Concerning the soot chemical composition, it was seen that the portion of carbon and ash was reduced with the introduction of the oxygenates, however, the VOF and oxygen fraction was increased. It is expected that those alterations are the result of an enhanced oxidation mechanism caused by the oxygen functional groups presented in DP20 and TP20. As for the lower ash level, it is expected to result from the chemical composition of the oxygenated hydrocarbons where no metals such as magnesium, copper, potassium, etc., can be found as it is the case in diesel. Blending these oxygenated HCs with diesel will dilute the concentration of the inorganics in the fuel and as a result soot with a lower ash level is produced from their combustion. Concerning the soot oxidative reactivity, the oxygenated diesel blends reduce the soot ignition temperature with TP20 samples being the most reactive. The particulate's initial graphitic structure did not comply with the assigned reactivity, which was confirmed by referring to the interlayer spacing of the particulates and direct analysis via Raman Spectroscopy. Both, DP20 and TP20 results in more graphitic soot structure compared to diesel, highlighting that worsen oxidation should be seen, however, this was not the case. As for the carbon layer length, no clear conclusion could be made as the changes were marginal and did not follow any trend. Tortuosity of the carbon layers followed the reactivity trend where both DP20 and TP20 presented more tortuous layers compared to diesel. It is suggested that the increased portion of oxygen functional groups in the soot surface has altered the surface activity and resulted in more defected layers (5 and 7 membered rings). Also, the reduction in the primary particulate size is an indication that the particulate's surface is more stretched, hence, more curved layers should be comprised in the outer shell of the particulate. During the oxidation process, curvy layers weakens the C-C bonds and can be more easily stripped out from the outer surface of the particulate, hence improving the particulate's reactivity. Overall, along with reducing the PM discharges, reformulating diesel with glycol ethers, especially

TPGME, can also enhance the DPF functionality by allowing less severe regeneration (lower soot ignition temperature) along with increasing the filter lifetime span (lower ash precipitations).

Application of late PFI was tested under 2 bar IMEP (~ 190 °C exhaust temperature) and 4 bar IMEP (~ 290 °C) engine conditions, using ultra-low sulphur diesel and TP20 blend as operating fuels. PFI prove to efficiently regulate the exhaust HC:NOx ratio under various operating conditions, with limited fuel penalties ranging from 1 to 1.5% at 2 bar IMEP and a maximum of 2.8% at 4 bar IMEP. PM and NOx level were slightly dropped with these strategies along with a minute production of H₂ gas during the combustion. However, the H₂ production was limited to a maximum of 60 ppm. PFI application slightly reduces the PM level and alter the morphological characteristics of the particulates by increasing their fractal dimension, and simultaneously reducing their number of primary particulates, radius of gyration and to lesser extent, the primary particulate size. PFI combined with small H₂ injections (500 ppm) improved the HC-SCR de-NOx activity and withstand it (no activity deterioration with time) with maximum de-NOx efficiency reaching 68.75% in case of diesel and 79% in case of TP20. Further increase for the H₂ concentrations did not present any positive impact, highlighting that the catalyst is fully activated in the low temperature window. The catalyst shows to remain fully active under all testing condition. In summary, the engine fuel quality can influence the HC-SCR activity, with TPGME presenting a promising candidate. In-cylinder PFI strategies assisted with small H₂ amounts can be considered as an applicable approach to enhance and withstand the low-temperature AgAl₂O₃ de-NOx activity.

Apart of reducing the NOx discharges, HC-SCR also proves to alter the particulates structure and modifies their morphology, especially when H₂ is fed to the flow. In the absence

of hydrogen, the catalyst role does not seem to differ by varying the operating fuel type or exhaust temperature (i.e. load condition). Exhaust particulates always tend to aggregate within the catalyst channels to yield bigger and more compact entities downstream the catalyst. However, introducing H₂ significantly activate the catalyst and make it more dependable on the exhaust conditions. It was seen that at low temperature condition (190 °C), the catalyst can slightly oxidise the particulates (reduce dp₀) but the aggregation phenomena remain the dominant path. However, a slight increase in the exhaust temperature (290 °C), stops the aggregation mechanism and instead the particulates tend to be breakdown throughout the catalyst and survive more severe oxidation reaction. This phenomenon was further approved by direct inspection of the TEM micrographs where, downstream the catalyst, the soot primary particulates appear to have no definite borders and fuse in each other, confirming the presence of a severe catalytic oxidation. Based on the approach of Song et al. (2006), a maximum soot oxidation rate of 17% was calculated for the diesel case. As for the TP20 case, the calculation was not possible as no statistically significant number of aggregates were detected on the TEM grids, the majority of primary particulates had a blur appearance.

This thesis offers valuable information for the catalyst designers to understand the sensitivity of the soot particulates towards changing the parent fuel type, fuel injection strategies and alternative exhaust aftertreatment units. The series of the soot alterations and destruction expected from the moment when the soot is emitted to the exhaust until being trapped within the DPF was detailed in this thesis along with a novel approach to enhance the HC-SCR activity using in-cylinder fuel-injection modifications.

7.2 Future Work

- Since the 2D calculation of the fractal dimension (the study done in this research work) generally underestimate the 3D value, it is also important to recognise the aggregated skeletal aspect ratio in 3D. Such findings can help in further understanding the toxicology and behaviour/interaction of the aggregates with the aftertreatment system.
- Research into an integrated H₂ assisted Ag/Al₂O₃ SCRF (SCR coating over a porous DPF) is a necessary step to increase the competency of this deNOx system. Following the promising soot/catalyst synergies presented in this thesis work, H₂ assisted SCRF is expected to yield a continuous deNOx - regeneration (i.e. passive) trap system in the low-temperature window. Confirming this theory is vital to increase the reliability of the application.
- Testing the impact of the H₂ assisted Ag/Al₂O₃ coating on the partial-flow filter trapping efficiency. After approving that in the presence of H₂, the active sub oxygen species produced on the Ag particulates can improve the soot/oxidisers contact, this investigation becomes a topic of interest.
- H₂-assisted Ag/Al₂O₃ SCR should be considered for heavy duty applications where exhaust temperatures are typically maintained higher than 290 °C during the normal operation of the engine. With the new regulations imposed for the 2020 marine industry, the marine fuel sulphur level should be dropped to 0.1 wt.% (0.5% for emergency operation) instead of 3.5 wt.%. Consequently, the exhaust SO₂ level should be drastically reduced which will also allow the integration of the HC-SCR with the marine exhaust. In such applications, hydrogen supply is not problematic as it can be produced via several green strategies from renewable energy.

References

- Abboud, J., et al. (2017). **Impacts of oxygenated compounds concentration on sooting propensities and soot oxidative reactivity: application to diesel and biodiesel surrogates** Fuel 193: 241-253. <https://doi.org/10.1016/j.fuel.2016.12.034>
- Abboud, J., et al. (2018). **Impacts of ester's carbon chain length and concentration on sooting propensities and soot oxidative reactivity: application to diesel and biodiesel surrogates** Fuel 222: 586-598. <https://doi.org/10.1016/j.fuel.2018.02.103>
- Ahlstrom, A. F., & Odenbrand, C. U. I. (1989). **Combustion characteristics of soot deposits from diesel engines** Carbon 27(3): 475-483. [https://doi.org/10.1016/0008-6223\(89\)90080-8](https://doi.org/10.1016/0008-6223(89)90080-8)
- Al-Qurashi, K., & Boehman, A. L. (2008). **Impact of exhaust gas recirculation (EGR) on the oxidative reactivity of diesel engine soot** Combustion and Flame 155(4): 675-695. <https://doi.org/10.1016/j.combustflame.2008.06.002>
- Al-Qurashi, K., et al. (2011). **The deconvolution of the thermal, dilution, and chemical effects of exhaust gas recirculation (EGR) on the reactivity of engine and flame soot** Combustion and Flame 158(9): 1696-1704. <https://doi.org/10.1016/j.combustflame.2011.02.006>
- Amann, C. A., & Siegla, D. C. (1982). **Diesel Particles - What They Are and Why** Aerosol Science and Technology 1: 73-101. <https://doi.org/10.1080/02786828208958580>
- An, H., et al. (2015). **Modeling study of oxygenated fuels on diesel combustion: Effects of oxygen concentration, cetane number and C/H ratio** Energy Conversion and Management 90: 261-271. <https://doi.org/10.1016/j.enconman.2014.11.031>
- Aneggi, E., et al. (2009). **Soot combustion over silver-supported catalysts** Applied Catalysis B: Environmental 91: 489-498. <https://doi.org/10.1016/j.apcatb.2009.06.019>
- Arrègle, J., et al. (2008). **Insights on postinjection-associated soot emissions in direct injection diesel engines** Combustion and Flame 154: 448-461. <https://doi.org/10.1016/j.combustflame.2008.04.021>
- Australian Micrpscopy and Microanalysis Research Faculty, (2014) **Quantitative EDS X-ray microanalysis using SEM** [Online]. Available from <http://www.ammrf.org.au/myscope/analysis/eds/quantitative/>. [Accessed June 2018]

- Barrientos, E. J., (2014) **Impact of oxygenated fuels on sooting tendency and soot oxidative reactivity with application to biofuels.** (Doctoral dissertation, The Pennsylvania State University). Retrieved from https://etda.libraries.psu.edu/files/final_submissions/9482
- Bartok, W., & Sarofim, A. F. (1991). **Fossil fuel combustion: a source book:** Wiley. ISBN: 9780471847793
- Bethke, K. A., & Kung, H. H. (1997). **Supported Ag catalysts for the lean reduction of NO with C₃H₆** Journal of Catalysis 172: 93-102. <https://doi.org/10.1006/jcat.1997.1794>
- Bhardwaj, O. P., et al. (2013). **Impact of biomass-derived fuels on soot oxidation and DPF regeneration behavior** SAE International Journal of Fuels and Lubricants 6(2): 505-520. <https://doi.org/10.4271/2013-01-1551>
- Bhardwaj, O. P., et al. (2014). **Utilization of HVO fuel properties in a high efficiency combustion system: part 2: relationship of soot characteristics with its oxidation behavior in DPF** SAE International Journal of Fuels and Lubricants 7(3): 979-994. <https://doi.org/10.4271/2014-01-2846>
- Bobba, M., et al. (2010). **Effect of post injections on in-cylinder and exhaust soot for low-temperature combustion in a heavy-duty diesel engine** SAE Technical Paper No. 2010-01-0612. <https://doi.org/10.4271/2010-01-0612>
- Boehman, A. L., et al. (2005). **Impact of biodiesel blending on diesel soot and the regeneration of particulate filters** Energy & Fuels 19: 1857-1864. <https://doi.org/10.1021/ef0500585>
- Bogarra, M., et al. (2017). **Influence of on-board produced hydrogen and three way catalyst on soot nanostructure in gasoline direct injection engines** Carbon 120: 326-336. <https://doi.org/10.1016/j.carbon.2017.05.049>
- Bogdanchikova, N., et al. (2002). **On the nature of the silver phases of Ag/Al₂O₃ catalysts for reactions involving nitric oxide** Applied Catalysis B: Environmental 36: 287–297. [https://doi.org/10.1016/S0926-3373\(01\)00286-7](https://doi.org/10.1016/S0926-3373(01)00286-7)
- Bosch, R. (2005). **Diesel-engine management systems and components** (4th Edition): John Wiley & Sons Ltd. ISBN: 978-3-658-03981-3
- Breen, J., et al. (2007). **A fast transient kinetic study of the effect of H₂ on the selective catalytic reduction of NO_x with octane using isotopically labelled ¹⁵NO** Journal of Catalysis 246(1): 1-9. <https://doi.org/10.1016/j.jcat.2006.11.017>

- Brosius, R., et al. (2005). **Adsorption chemistry of NO_x on Ag/Al₂O₃ catalyst for selective catalytic reduction of NO_x using hydrocarbons** Journal of Catalysis 231(2): 344-353. <https://doi.org/10.1016/j.jcat.2005.01.034>
- Browning, R. G., & Curry, S. C. (1994). **Clinical toxicology of ethylene glycol monoalkyl ethers** Human & Experimental Toxicology 13: 325-335. <https://doi.org/10.1177/096032719401300508>
- Bueno-Lopez, A., et al. (2005). **Active oxygen from CeO₂ and its role in catalysed soot oxidation** Catalysis Letters 99(3-4): 203-205. <https://doi.org/10.1007/s10562-005-2120-x>
- Burch, R., et al. (2002). **A review of the selective reduction of NO_x with hydrocarbons under lean-burn conditions with non-zeolitic oxide and platinum group metal catalysts** Applied Catalysis B: Environmental 39: 283-303. [https://doi.org/10.1016/S0926-3373\(02\)00118-2](https://doi.org/10.1016/S0926-3373(02)00118-2)
- Burke, U., et al. (2015). **Experimental and kinetic modeling study of the shock tube ignition of a large oxygenated fuel: tri-propylene glycol mono-methyl ether** Combustion and Flame 162(7): 2916-2927. <https://doi.org/10.1016/j.combustflame.2015.03.012>
- Burtscher, H. (2005). **Physical characterization of particulate emissions from diesel engines: a review** Journal of Aerosol Science 36(7): 896-932. <https://doi.org/10.1016/j.jaerosci.2004.12.001>
- Chen, P., et al. (2014). **Experimental investigation of diesel and biodiesel post injections during active diesel particulate filter regenerations** Fuel 130: 286-295. <https://doi.org/10.1016/j.fuel.2014.04.046>
- Chiatti, G., et al. (2009). **Soot morphology effects on DPF performance** SAE paper No. 2009-01-1279. <https://doi.org/10.4271/2009-01-1279>
- Choi, M. Y., et al. (1994). **Simultaneous optical measurement of soot volume fraction and temperature in premixed flames** Combustion and Flame 99: 174-186. [https://doi.org/10.1016/0010-2180\(94\)90088-4](https://doi.org/10.1016/0010-2180(94)90088-4)
- Cordiner, S., et al. (2013). **Diesel Engine Biofuelling: Effects of Ash on the Behavior of the Diesel Particulate Filter** SAE paper No. 2013-24-0165. <https://doi.org/10.4271/2013-24-0165>

- Corro, G., et al. (2013). **Effect of Ag, Cu, and Au incorporation on the diesel soot oxidation behavior of SiO₂: role of metallic Ag** Topics in Catalysis 56(1-8): 467-472. <https://doi.org/10.1007/s11244-013-9998-0>
- CTS Corporation, (2019) **Basics of Diesel Particulate Filter (DPF) Operation** [Online]. Available from <https://www.ctscorp.com/products/sensors-2/rf-dpf-sensor/diesel-particulate-filter-dpf-knowledge-base/basics-dpf-operation/>. [Accessed 10th of May 2019]
- Curran, H. J., et al. (2001). **Detailed chemical kinetic modeling of diesel combustion with oxygenated fuels** SAE paper No. 2001-01-0653. <https://doi.org/10.4271/2001-01-0653>
- Daido, S., et al. (2000). **Analysis of soot accumulation inside diesel engines** Society of Automotive Engineers of Japan 21(3): 303-308. [https://doi.org/10.1016/S0389-4304\(00\)00048-5](https://doi.org/10.1016/S0389-4304(00)00048-5)
- Dec, J. E. (1997). **A conceptual model of DI diesel combustion based on laser-sheet imaging** SAE Technical Paper No. 970873. <https://doi.org/10.4271/970873>
- Dec, J. E. (1999). **Diesel combustion: an integrated view combining laser diagnostics, chemical kinetics, and empirical validation** SAE Technical Paper No. 1999-01-0509. <https://doi.org/10.4271/1999-01-0509>
- Desantes, J. M., et al. (2007). **A comprehensive study of diesel combustion and emissions with post-injection** SAE Technical Paper No. 2007-01-0915. <https://doi.org/10.4271/2007-01-0915>
- Diehl, F., et al. (2010). **Catalytic oxidation of heavy hydrocarbons over Pt/Al₂O₃. Influence of the structure of the molecule on its reactivity** Applied Catalysis B: Environmental 95(3-4): 217-227. <https://doi.org/10.1016/j.apcatb.2009.12.026>
- DieselNet, (2018) **EU: Cars and Light Trucks, Emission Standards** [Online]. Available from <https://www.dieselnet.com/standards/eu/ld.php>. [Accessed 26th of November 2018]
- Dulac, J., (2012) **Global transport outlook to 2050** [Online]. Available from https://www.iea.org/media/workshops/2013/egrdmobility/DULAC_23052013.pdf. [Accessed February 2017]
- Dumitrescu, C. E., et al. (2016). **Investigation of a tripropylene-glycol monomethyl ether and diesel blend for soot-free combustion in an optical direct-injection diesel**

engine Applied Thermal Engineering 101: 639-646.

<https://doi.org/10.1016/j.aplthermaleng.2015.12.068>

Ehrburger, P., et al. (2002). **Reactivity of soot with nitrogen oxides in exhaust stream** SAE Technical Paper No. 2002-01-1683. <https://doi.org/10.4271/2002-01-1683>

Ess, M. N., et al. (2016). **Reactivity and structure of soot generated at varying biofuel content and engine operating parameters** Combustion and Flame 163: 157-169. <https://doi.org/10.1016/j.combustflame.2015.09.016>

Faghani, E., (2015) **Effect of Injection Strategies on Particulate Matter Emissions From HPDI Natural-Gas Engines.** (Doctoral dissertation, The University of British Columbia). Retrieved from <https://open.library.ubc.ca/media/download/pdf/24/1.0220518/4/1243>

Fayad, M. A., et al. (2015). **Role of alternative fuels on particulate matter (PM) characteristics and influence of the diesel oxidation catalyst** Environmental Science & Technology 49(19): 11967-11973. <https://doi.org/10.1021/acs.est.5b02447>

Fayad, M. A., et al. (2017). **Manipulating modern diesel engine particulate emission characteristics through butanol fuel blending and fuel injection strategies for efficient diesel oxidation catalysts** Applied Energy 190: 490-500. <https://doi.org/10.1016/j.apenergy.2016.12.102>

Filippov, A. V., et al. (2000). **Fractal-like aggregates: relation between morphology and physical properties** Journal of Colloid and Interface Science 229(1): 261-273. <https://doi.org/10.1006/jcis.2000.7027>

Frenklach, M. (2002). **Reaction mechanism of soot formation in flame** Physical Chemistry Chemical Physics 4: 2028-2037. <https://doi.org/10.1039/b110045a>

Frenklach, M., & Wang, H. (1991). **Detailed Modeling of Soot Particle Nucleation and Growth** Symposium (International) on Combustion 23(1): 1559-1566. [https://doi.org/10.1016/S0082-0784\(06\)80426-1](https://doi.org/10.1016/S0082-0784(06)80426-1)

Frenklach, M., & Wang, H. (1994). **Detailed Mechanism and Modeling of Soot Particle Formation:** Springer Berlin Heidelberg. ISBN: 978-3-642-85167-4

Frenklach, M., & Warnatz, J. (1987). **Detailed Modeling of PAH Profiles in a Sooting Low-Pressure Acetylene Flame** Combustion Science and Technology 51(4-6): 265-283. <https://doi.org/10.1080/00102208708960325>

- Frijters, P. J. M., (2012) **Fuel composition impact on heavy duty diesel engine combustion & emissions.** (Doctoral dissertation, Eindhoven University of Technology). Retrieved from <https://doi.org/10.6100/IR735422>
- Gaddam, C. K., et al. (2016). **Quantification of nano-scale carbon structure by HRTEM and lattice fringe analysis** Pattern Recognition Letters 76: 90-97. <https://doi.org/10.1016/j.patrec.2015.08.028>
- Gao, Y., et al. (2017). **Aggregation and redispersion of silver species on alumina and sulphated alumina supports for soot oxidation** Catalysis Science & Technology 7(16): 3524-3530. <https://doi.org/10.1039/c7cy00831g>
- Ghiassi, H., et al. (2014). **Sooting behaviors of n-butanol and n-dodecane blends** Combustion and Flame 161(3): 671-679. <https://doi.org/10.1016/j.combustflame.2013.10.011>
- Gill, S. S., (2012) **Controlling diesel NOx & PM emissions using fuel components and enhanced aftertreatment techniques - developing the next generation emission control system.** (Doctoral dissertation, University of Birmingham). Retrieved from <https://etheses.bham.ac.uk/id/eprint/3643/1/Gill12PhD.pdf>
- Glassman, I. (1989). **Soot formation in combustion processes** Symposium (International) on Combustion 22(1): 295-311. [https://doi.org/10.1016/S0082-0784\(89\)80036-0](https://doi.org/10.1016/S0082-0784(89)80036-0)
- Glassman, I., & Yetter, R. A. (2008). **Combustion** (Vol. 4th edition): Academic Press. ISBN: 978-0-12-088573-2
- Gogoi, B., et al. (2015). **Effects of 2,5-dimethylfuran addition to diesel on soot nanostructures and reactivity** Fuel 159: 766-775. <https://doi.org/10.1016/j.fuel.2015.07.038>
- Gómez-Cuenca, F., et al. (2013). **The influence of propylene glycol ethers on base diesel properties and emissions from a diesel engine** Energy Conversion and Management 75: 741-747. <https://doi.org/10.1016/j.enconman.2013.07.012>
- González, M. A., et al. (2001). **Oxygenates screening for advanced petroleum-based diesel fuels part 2: The effect of oxygenate blending compounds on exhaust emission** SAE Technical Paper No. 2001-01-3632. <https://doi.org/10.4271/2001-01-3632>
- Gu, H., et al. (2015). **The effects of hydrogen on the efficiency of NOx reduction via hydrocarbon-selective catalytic reduction (HC-SCR) at low temperature using**

- various reductants** International Journal of Hydrogen Energy 40(30): 9602-9610.
<https://doi.org/10.1016/j.ijhydene.2015.05.070>
- Guo, H., et al. (2016). **Performances and emissions of new glycol ether blends in diesel fuel used as oxygenated fuel for diesel engines** Journal of Energy Engineering 142(1): 04015003. [https://doi.org/10.1061/\(asce\)ey.1943-7897.0000265](https://doi.org/10.1061/(asce)ey.1943-7897.0000265)
- Hansen, B. B., et al. (2013). **Performance of diesel particulate filter catalysts in the presence of biodiesel ash species** Fuel 106: 234-240. <https://doi.org/10.1016/j.fuel.2012.11.038>
- Haynes, B. S., & Wagner, H. G. G. (1981). **Soot Formation** Progress in Energy and Combustion Science 7(4): 229-273. [https://doi.org/10.1016/0360-1285\(81\)90001-0](https://doi.org/10.1016/0360-1285(81)90001-0)
- Hellier, P., et al. (2012). **The influence of fatty acid ester alcohol moiety molecular structure on diesel combustion and emissions** Energy & Fuels 26(3): 1912-1927. <https://doi.org/10.1021/ef2017545>
- Hellier, P., et al. (2017). **An overview of the effects of fuel molecular structure on the combustion and emissions characteristics of compression ignition engines** Journal of Automobile Engineering 232(1): 90-105. <https://doi.org/10.1177/0954407016687453>
- Herreros, J. M., et al. (2014). **Enhancing selective catalytic reduction of NOx with alternative reactants/promoters** Chemical Engineering Journal 252: 47-54. <https://doi.org/10.1016/j.cej.2014.04.095>
- Herreros, J. M., et al. (2015). **Extending the environmental benefits of ethanol-diesel blends through DGE incorporation** Applied Energy 146: 335-343. <https://doi.org/10.1016/j.apenergy.2015.02.075>
- Heywood, J. B. (1988). **Fundamentals of internal combustion engines**: McGraw-Hill. ISBN: 9788120346802
- Hilden, D. L., et al. (2001). **The emissions performance of oxygenated diesel fuels in a prototype DI diesel engine** SAE Technical Paper No. 2001-01-0650. <https://doi.org/10.4271/2001-01-0650>
- Hoekman, S. K., & Robbins, C. (2012). **Review of the effects of biodiesel on NOx emissions** Fuel Processing Technology 96: 237-249. <https://doi.org/10.1016/j.fuproc.2011.12.036>

- Houel, V., et al. (2007a). **Fuel effects on the activity of silver hydrocarbon-SCR catalysts** Applied Catalysis B: Environmental 73(1-2): 203-207. <https://doi.org/10.1016/j.apcatb.2006.12.005>
- Houel, V., et al. (2007b). **Promoting functions of H₂ in diesel-SCR over silver catalysts** Applied Catalysis B: Environmental 77(1-2): 29-34. <https://doi.org/10.1016/j.apcatb.2007.07.003>
- Ismail, S. A. A., & Ali, R. F. M. (2016). **Physico-chemical properties of biodiesel manufactured from waste frying oil using domestic adsorbents** Science and Technology of Advanced Materials 16(3). <https://doi.org/10.1088/1468-6996/16/3/034602>
- Jeftić, M., et al. (2011). **An analysis of the production of hydrogen and hydrocarbon species by diesel post injection combustion** ASME 2011 Internal Combustion Engine Division Fall Technical Conference. <https://doi.org/10.1115/ICEF2011-60135>
- Jeftić, M., et al. (2015). **Combustion and exhaust gas speciation analysis of diesel and butanol post injection** SAE Technical Paper No. 2015-01-0803. <https://doi.org/10.4271/2015-01-0803>
- Jeftić, M., et al. (2011). **Effects of postinjection application with late partially premixed combustion on power production and diesel exhaust gas conditioning** Journal of Combustion 2011: 1-9. <https://doi.org/10.1155/2011/891096>
- Johnson, T. V. (2015). **Review of vehicular emissions trends** SAE International Journal of Engines paper No. 2015-01-0993. <https://doi.org/10.4271/2015-01-0993>
- Jung, H., et al. (2003). **The influence of engine lubricating oil on diesel nanoparticle emissions and kinetics of oxidation** SAE Technical Paper No. 2003-01-3179. <https://doi.org/10.4271/2003-01-3179>
- Kandas, A. W., et al. (2005). **Soot surface area evolution during air oxidation as evaluated by small angle X-ray scattering and CO₂ adsorption** Carbon 43(2): 241-251. <https://doi.org/10.1016/j.carbon.2004.08.028>
- Keeler, B., (2009) **Constraints on the operation of a DI diesel engine in partially-premixed combustion mode.** (Doctoral dissertation, University of Nottingham). Retrieved from http://eprints.nottingham.ac.uk/10760/1/Final_Thesis.pdf

- Kidoguchi, Y., et al. (2000). **Effects of fuel cetane number and aromatics on combustion process and emissions of a direct-injection diesel engine** Journal of Society of Automotive Engineers 21: 469-475. [https://doi.org/10.1016/S0389-4304\(00\)00075-8](https://doi.org/10.1016/S0389-4304(00)00075-8)
- Kim, P. S., et al. (2013). **Effect of H₂ on deNO_x performance of HC-SCR over Ag/Al₂O₃: morphological, chemical, and kinetic changes** Journal of Catalysis 301: 65-76. <https://doi.org/10.1016/j.jcat.2013.01.026>
- Kondo, K., et al. (2013). **Uncertainty in sampling and TEM analysis of soot particles in diesel spray flame** SAE Technical Paper No. 2013-01-0908. <https://doi.org/10.4271/2013-01-0908>
- Konstandopoulos, A. G., & Kostoglou, M. (2004). **Microstructural aspects of soot oxidation in diesel particulate filters** SAE Technical Paper No. 2004-01-0693. <https://doi.org/10.4271/2004-01-0693>
- Konstandopoulos, A. G., et al. (2002). **Microstructural properties of soot deposits in diesel particulate traps** SAE Technical Paper No. 2002-01-1015. <https://doi.org/10.4271/2002-01-1015>
- Kousoulidou, M., et al. (2010). **Biodiesel blend effects on common-rail diesel combustion and emissions** Fuel 89(11): 3442-3449. <https://doi.org/10.1016/j.fuel.2010.06.034>
- Kumar, A. A. (2007). **Biofuels (alcohols and biodiesel) applications as fuels for internal combustion engines** Progress in Energy and Combustion Science 33(3): 233-271. <https://doi.org/10.1016/j.pecs.2006.08.003>
- Lapuerta, M., et al. (2008). **Effect of biodiesel fuels on diesel engine emissions** Progress in Energy and Combustion Science 34(2): 198-223. <https://doi.org/10.1016/j.pecs.2007.07.001>
- Lapuerta, M., et al. (2006). **A method to determine the fractal dimension of diesel soot agglomerates** Journal of Colloid and Interface Science 303(1): 149-158. <https://doi.org/10.1016/j.jcis.2006.07.066>
- Lapuerta, M., et al. (2007). **Effect of engine operating conditions on the size of primary particles composing diesel soot agglomerates** Journal of Aerosol Science 38(4): 455-466. <https://doi.org/10.1016/j.jaerosci.2007.02.001>

- Lapuerta, M., et al. (2012). **Effect of fuel on the soot nanostructure and consequences on loading and regeneration of diesel particulate filters** Combustion and Flame 159(2): 844-853. <https://doi.org/10.1016/j.combustflame.2011.09.003>
- Lee, D., et al. (2013). **Impact of SME blended fuel combustion on soot morphological characteristics in a diesel engine** International Journal of Automotive Technology 14(5): 757–762. <https://doi.org/10.1007/s12239-013-0083-2>
- Lee, K., et al. (2013). **Detailed morphological properties of nanoparticles from gasoline direct injection engine combustion of ethanol blends** SAE Technical Paper No. 2013-24-0185. <https://doi.org/10.4271/2013-24-0185>
- Lee, K. O., & Zhu, J. (2004). **Evolution in size and morphology of diesel particulates along the exhaust system** SAE Technical Paper No. 2004-01-1981. <https://doi.org/10.4271/2004-01-1981>
- Lee, K. O., & Zhu, J. (2005). **Effects of exhaust system components on particulate morphology in a light-duty diesel engine** SAE Technical Paper No. 2005-01-0184. <https://doi.org/10.4271/2005-01-0184>
- Lei, J., et al. (2011). **Performance and emission characteristics of diesel engine fueled with ethanol-diesel blends in different altitude regions** J. Biomed. Biotechnol. 2011: 417421. <https://doi.org/10.1155/2011/417421>
- Leidenberger, U., et al. (2012). **Experimental studies on the influence of diesel engine operating parameters on properties of emitted soot particles** Combustion Science and Technology 184(1): 1-15. <https://doi.org/10.1080/00102202.2011.611551>
- Liang, S., et al. (2011). **Synthesis of propylene glycol methyl ether catalyzed by MCM-41 Synthetic Communications** 41(6): 891-897. <https://doi.org/10.1080/00397911003707089>
- Liati, A., et al. (2013). **Variations in diesel soot reactivity along the exhaust after-treatment system, based on the morphology and nanostructure of primary soot particles** Combustion and Flame 160(3): 671-681. <https://doi.org/10.1016/j.combustflame.2012.10.024>
- Liati, A., et al. (2012). **Microscopic investigation of soot and ash particulate matter derived from biofuel and diesel: implications for the reactivity of soot** Journal of Nanoparticle Research 14(11). <https://doi.org/10.1007/s11051-012-1224-7>

- Lin, Y. C., et al. (2008). **Characterization of particle size distribution from diesel engines fueled with palm-biodiesel blends and paraffinic fuel blends** Atmospheric Environment 42(6): 1133-1143. <https://doi.org/10.1016/j.atmosenv.2007.10.046>
- Liu, D., et al. (2018). **Nanostructure and reactivity of carbon particles from co-pyrolysis of biodiesel surrogate methyl octanoate blended with n-butanol** Fullerenes, Nanotubes and Carbon Nanostructures 26(5): 278-290. <https://doi.org/10.1080/1536383x.2018.1436052>
- López-Suárez, F. E., et al. (2008). **Cu/Al₂O₃ catalysts for soot oxidation: Copper loading effect** Applied Catalysis B: Environmental 84: 651-658. <https://doi.org/10.1016/j.apcatb.2008.05.019>
- López Suárez, F. E., et al. (2011). **Study of the uncatalyzed and catalyzed combustion of diesel and biodiesel soot** Catalysis Today 176(1): 182-186. <https://doi.org/10.1016/j.cattod.2010.11.094>
- Lu, T., et al. (2012). **Size-resolved volatility, morphology, nanostructure, and oxidation characteristics of diesel particulate** Energy & Fuels 26(10): 6168-6176. <https://doi.org/10.1021/ef3010527>
- Lyon, R. K., & Cole, J. A. (1990). **A reexamination of the rapre NO_x process** Combustion and Flame 82: 435-443. [https://doi.org/10.1016/0010-2180\(90\)90013-H](https://doi.org/10.1016/0010-2180(90)90013-H)
- Ma, Z., et al. (2014). **Effects of diesel oxidation catalyst on nanostructure and reactivity of diesel soot** Energy & Fuels 28: 4376–4382. <https://doi.org/10.1021/ef500467a>
- Man, X. J., et al. (2015). **Effect of waste cooking oil biodiesel on the properties of particulate from a DI diesel engine** Aerosol Science and Technology 49(4): 199-209. <https://doi.org/10.1080/02786826.2015.1016214>
- Mansurov, Z. A. (2005). **Soot formation in combustion processes (review)** Combustion, Explosion, and Shock Waves 41(6): 727-744. <https://doi.org/0010-5082/05/4106-0727>
- Marsh, H., & Kuo, K. (1989). **Introduction to carbon science**: Butterworth-Heinemann. ISBN: 978-0-408-03837-9. <https://doi.org/10.1016/B978-0-408-03837-9.50009-9>
- Matti, M. M. (2007). **Chemical characterization of particulate emissions from diesel engines: A review** Journal of Aerosol Science 38(11): 1079-1118. <https://doi.org/10.1016/j.jaerosci.2007.08.001>

- Mccormick, R. L., et al. (1997). **Effect of several oxygenates on regulated emissions from heavy-duty diesel engines** Environmental Science & Technology 31(4): 1144-1150. <https://doi.org/10.1021/es9606438>
- Meakin P, D. B. a. M. G. (1989). **Collisions between point masses and fractal aggregates** Langmuir 5(2): 510-518. <https://doi.org/10.1021/la00086a038>
- Mendiara, T., et al. (2007). **Oxidation of acetylene soot: influence of oxygen concentration** Energy & Fuels 21: 3208-3215. <https://doi.org/10.1021/ef070182j>
- Meunier, F. C., et al. (1999). **Mechanistic aspects of the selective reduction of NO by propene over alumina and silver–alumina catalysts** Journal of Catalysis 187(2): 493-505. <https://doi.org/10.1006/jcat.1999.2622>
- Miller, J. A., & Kee, R. J. (1990). **Chemical kinetics and combustion modeling** Annual Review of Physical Chemistry 41: 345-387. <https://doi.org/10.1146/annurev.pc.41.100190.002021>
- Miller, J. A., & Melius, C. F. (1992). **Kinetic and thermodynamic issues in the formation of aromatic compounds in flames of aliphatic fuels** Combustion and Flame 91: 21-39. [https://doi.org/10.1016/0010-2180\(92\)90124-8](https://doi.org/10.1016/0010-2180(92)90124-8)
- Moldanova, J., et al. (2013). **Physical and chemical characterisation of PM emissions from two ships operating in European Emission Control Areas** Atmospheric Measurement Techniques 6(12): 3577-3596. <https://doi.org/10.5194/amt-6-3577-2013>
- Morjan, I., et al. (2004). **Gas composition in laser pyrolysis of hydrocarbon-based mixtures: influence on soot morphology** Carbon 42(7): 1269-1273. <https://doi.org/10.1016/j.carbon.2004.01.020>
- Mueller, C. J., et al. (2003). **Effects of oxygenates on soot processes in DI diesel engines: experiments and numerical simulations** SAE paper No. 2003-01-1791. <https://doi.org/10.4271/2003-01-1791>
- Mühlbauer, W., et al. (2016). **Correlations between physicochemical properties of emitted diesel particulate matter and its reactivity** Combustion and Flame 167: 39-51. <https://doi.org/10.1016/j.combustflame.2016.02.029>
- Müller, J. O., et al. (2006). **Diesel engine exhaust emission: oxidative behavior and microstructure of black smoke soot particulate** Environmental Science & Technology 40(4): 1231-1236. <https://doi.org/10.1021/es0512069>

- Natarajan, M., et al. (2001). **Oxygenates for advanced petroleum-based diesel fuels: Part 1. Screening and selection methodology for the oxygenates** SAE Technical Paper No. 2001-01-3631. <https://doi.org/10.4271/2001-01-3631>
- Niemi, S., et al. (2009). **HC-SCR catalyst for NOx reduction in an non-road diesel engine** SAE Technical Paper No. 2009-01-2880. <https://doi.org/10.4271/2009-01-2880>
- Nomanbhay, S., et al. (2018). **Sustainability of biodiesel production in Malaysia by production of bio-oil from crude glycerol using microwave pyrolysis: a review** Green Chemistry Letters and Reviews 11(2): 135-157. <https://doi.org/10.1080/17518253.2018.1444795>
- Nord, K. E., & Haupt, D. (2005). **Reducing the emission of particles from a diesel engine by adding an oxygenate to the fuel** Environmental Science & Technology 39(16): 6260-6265. <https://doi.org/10.1021/es048085h>
- O'Connor, J., & Musculus, M. (2013). **Post Injections for Soot Reduction in Diesel Engines: A Review of Current Understanding** SAE International Journal of Engines 6(1): 400-421. <https://doi.org/10.4271/2013-01-0917>
- O'Connor, J., & Musculus, M. (2014). **In-cylinder mechanisms of soot reduction by close-coupled post-injections as revealed by imaging of soot luminosity and planar laser-induced soot incandescence in a heavy-duty diesel engine** SAE International Journal of Engines 7(2): 673-693. <https://doi.org/10.4271/2014-01-1255>
- O'Connor, J., & Musculus, M. (2014). **Effect of load on close-coupled post-injection efficacy for soot reduction in an optical heavy-duty diesel research engine** Journal of Engineering for Gas Turbines and Power 136(10). <https://doi.org/10.1115/1.4027276>
- Omidvarborna, H., et al. (2014). **Characterization of particulate matter emitted from transit buses fueled with B20 in idle modes** Journal of Environmental Chemical Engineering 2(4): 2335-2342. <https://doi.org/10.1016/j.jece.2014.09.020>
- Omidvarborna, H., et al. (2015). **Recent studies on soot modeling for diesel combustion** Renewable and Sustainable Energy Reviews 48: 635-647. <https://doi.org/10.1016/j.rser.2015.04.019>
- Omidvarborna, H., et al. (2014). **Characterization and exhaust emission analysis of biodiesel at different temperatures and pressures: laboratory study** Journal of Hazardous,

Toxic, and Radioactive Waste 10(2): 4014-4030.
[https://doi.org/10.1061/\(ASCE\)HZ.2153-5515.0000237](https://doi.org/10.1061/(ASCE)HZ.2153-5515.0000237)

Otsu, N. (1979). **Threshold selection method from gray-level histograms** Ieee Transactions on Systems Man and Cybernetics 9(1): 62-66.

Park, K., et al. (2004). **Structural properties of diesel exhaust particles measured by transmission electron microscopy (TEM): relationships to particle Mass and mobility** Aerosol Science and Technology 38(9): 881-889.
<https://doi.org/10.1080/027868290505189>

Park, S., et al. (2016). **Development of a reduced tri-propylene glycol monomethyl ether-n-hexadecane-poly-aromatic hydrocarbon mechanism and its application for soot prediction** International Journal of Engine Research 17(9): 969-982.
<https://doi.org/10.1177/1468087416632367>

Park, W., et al. (2017). **The effect of oxygenated fuel properties on diesel spray combustion and soot formation** Combustion and Flame 180: 276-283.
<https://doi.org/10.1016/j.combustflame.2016.02.026>

Pettersson, H., (2013) **Chemical analysis for mapping of soot reactivity.** (Doctoral dissertation, KTH Kemiteknik). Retrieved from <https://www.diva-portal.org/smash/get/diva2:826709/FULLTEXT01.pdf>

Punov, P., et al. (2017). **Study on the combustion process in a modern diesel engine controlled by pre-injection strategy** IOP Conference Series: Materials Science and Engineering 252(1). <https://doi.org/10.1088/1757-899X/252/1/012090>

Radovic, L. R., et al. (1983). **Importance of carbon active sites in the gasification of coal chars** Fuel 62(7): 849-856. [https://doi.org/10.1016/0016-2361\(83\)90041-8](https://doi.org/10.1016/0016-2361(83)90041-8)

Raj, A., (2010) **Formation, growth and oxidation of soot: a numerical study.** (Doctoral dissertation, University of Cambridge). Retrieved from <https://doi.org/10.1016/j.combustflame.2009.01.005>

Rajkumar, M., (2002) **Heat Release Analysis and Modeling for a Common-Rail Diesel Engine.** (Master dissertation, University of Tennessee). Retrieved from http://trace.tennessee.edu/utk_gradthes/2144

Ren, Y., et al. (2008). **Combustion and emissions of a DI diesel engine fuelled with diesel-oxygenate blends** Fuel 87: 2691-2697. <https://doi.org/10.1016/j.fuel.2008.02.017>

- Richter, H., & Howard, J. B. (2000). **Formation of polycyclic aromatic hydrocarbons and their growth to soot—a review of chemical reaction pathways** Progress in Energy and Combustion Science 26: 565-608. [https://doi.org/10.1016/S0360-1285\(00\)00009-5](https://doi.org/10.1016/S0360-1285(00)00009-5)
- Rodrigues, A., et al. (2017). **Upgrading the Glycerol from Biodiesel Production as a Source of Energy Carriers and Chemicals—A Technological Review for Three Chemical Pathways** Energies 10(11): 1817. <https://doi.org/10.3390/en10111817>
- Rodríguez-Fernández, J., et al. (2016). **Effect of oxygenated and paraffinic alternative diesel fuels on soot reactivity and implications on DPF regeneration** Fuel 185: 460-467. <https://doi.org/10.1016/j.fuel.2016.08.016>
- Rodríguez-Fernández, J., et al. (2017). **Regeneration of diesel particulate filters: effect of renewable fuels** Renewable Energy 104: 30-39. <https://doi.org/10.1016/j.renene.2016.11.059>
- Roessler, D. M., et al. (1981). **Optical Properties and Morphology of Particulate Carbon: Variation with Air/Fuel Ratio**: Springer US. ISBN: 978-1-4757-6137-5
- Roth, P., & Gersum, S. V. (1993). **Turbulence and Molecular Processes in Combustion**: Elsevier Science. ISBN: 978-0-444-89757-2
- Salamanca, M., et al. (2012). **Influence of palm oil biodiesel on the chemical and morphological characteristics of particulate matter emitted by a diesel engine** Atmospheric Environment 62: 220-227. <https://doi.org/10.1016/j.atmosenv.2012.08.031>
- Santibáñez, C., et al. (2011). **Residual glycerol from biodiesel manufacturing, waste or potential source of bioenergy: a review** Chilean Journal of Agricultural Research 71(3): 469-475. <https://doi.org/10.4067/S0718-58392011000300019>
- Sappok, A., & Wong, V. (2010). **Ash effects on diesel particulate filter pressure drop sensitivity to soot and implications for regeneration frequency and DPF control** SAE International Journal of Engines paper No. 2010-01-0811. <https://doi.org/10.4271/2010-01-0811>
- Savic, N., et al. (2016). **Influence of biodiesel fuel composition on the morphology and microstructure of particles emitted from diesel engines** Carbon 104: 179-189. <https://doi.org/10.1016/j.carbon.2016.03.061>

- Seong, H. J., (2010) **Impact of oxygen enrichment on soot properties and soot oxidative reactivity.** (Doctoral dissertation, The Pennsylvania State University). Retrieved from https://etda.libraries.psu.edu/files/final_submissions/2279
- Setiabudi, A., et al. (2004). **CeO₂ catalysed soot oxidation** Applied Catalysis B: Environmental 51(1): 9-19. <https://doi.org/10.1016/j.apcatb.2004.01.005>
- Shah, S., (2011) **Experimental study and thermodynamical analysis of water injection in the intake manifold of an automotive diesel engine, for pollutant emission reduction.** (Doctoral dissertation, Ecole Centrale de Nantes). Retrieved from <https://hal.archives-ouvertes.fr/tel-01207643>
- Shandilya, K., & Kumar, A. (2013). **Particulate emissions from tailpipe during idling of public transit buses fueled with alternative fuels** Environmental Progress & Sustainable Energy 32(4): 1134-1142. <https://doi.org/10.1002/ep.11696>
- Sharma, V., et al. (2016). **Structure and chemistry of crankcase and exhaust soot extracted from diesel engines** Carbon 103: 327-338. <https://doi.org/10.1016/j.carbon.2016.03.024>
- Shell Chemicals, (2007) **Methyl dipropxitol specification sheet** [Online]. Available from http://webcache.googleusercontent.com/search?q=cache:I72Ijn_Y6n0J:www.alchemical.com/products.html%3Ffile%3Dtl_files/product_documents/MSDS/shell/glycol-ether-dpm-tech-07-01-01.pdf+&cd=2&hl=en&ct=clnk&gl=uk. [Accessed March 2018]
- Shimizu, K. I., et al. (2010). **Study of active sites and mechanism for soot oxidation by silver-loaded ceria catalyst** Applied Catalysis B: Environmental 96(1-2): 169-175. <https://doi.org/10.1016/j.apcatb.2010.02.016>
- Shimizu, K. I., & Satsuma, A. (2006). **Selective catalytic reduction of NO over supported silver catalysts-practical and mechanistic aspects** Physical Chemistry Chemical Physics 8(23): 2677-2695. <https://doi.org/10.1039/b601794k>
- Shimizu, K. I., & Satsuma, A. (2007). **Reaction mechanism of H₂-promoted selective catalytic reduction of NO with NH₃ over Ag/Al₂O₃** Journal of Physical Chemistry 111(5): 2259-2264. <https://doi.org/10.1021/jp0668100>

- Shimizu, K. I., et al. (2001). **Silver-alumina catalysts for selective reduction of NO by higher hydrocarbons: structure of active sites and reaction mechanism** Applied Catalysis B: Environmental 30: 151-162. [https://doi.org/10.1016/S0926-3373\(00\)00229-0](https://doi.org/10.1016/S0926-3373(00)00229-0)
- Shimizu, K. I., et al. (2007). **Reductive activation of O₂ with H₂-reduced silver clusters as a key step in the H₂-promoted selective catalytic reduction of NO with C₃H₈ over Ag/Al₂O₃** Journal of Physical Chemistry 111(2): 950-959. <https://doi.org/10.1021/jp066147f>
- Shimizu, K. I., et al. (2007). **Effects of hydrogen and oxygenated hydrocarbons on the activity and SO₂-tolerance of Ag/Al₂O₃ for selective reduction of NO** Applied Catalysis B: Environmental 71(1-2): 80-84. <https://doi.org/10.1016/j.apcatb.2006.08.009>
- Silva, G. P., et al. (2009). **Glycerol: a promising and abundant carbon source for industrial microbiology** Biotechnology Advances 27(1): 30-39. <https://doi.org/10.1016/j.biotechadv.2008.07.006>
- Silverman, D. T., et al. (2012). **The diesel exhaust in miners study: a nested case-control study of lung cancer and diesel exhaust** Journal of the National Cancer Institute 104(11): 855-868. <https://doi.org/10.1093/jnci/djs034>
- Sitshebo, S. W. T., (2010) **HC-SCR of NO_x emissions over Ag-Al₂O₃ catalysts using diesel fuel as a reductant.** (Doctoral dissertation, University of Birmingham). Retrieved from <http://etheses.bham.ac.uk/1338/1/Sitshebo11PhD.pdf>
- Smith, B. L., et al. (2008). **Composition-explicit distillation curves of diesel fuel with glycol ether and glycol ester oxygenates: fuel analysis metrology to enable decreased particulate emissions** Environmental Science & Technology 42: 7682–7689. <https://doi.org/10.1021/es800067c>
- Smith, D. M., & Chughtai, A. R. (1995). **Surface structure and reactivity of black carbon** Colloids and Surfaces A: Physicochemical and Engineering Aspects 105(1): 47-77. [https://doi.org/10.1016/0927-7757\(95\)03337-1](https://doi.org/10.1016/0927-7757(95)03337-1)
- Smith, O. I. (1981). **Fundamentals of soot formation in flames with application to diesel engine particulate emissions** Progress in Energy and Combustion Science 7(4): 275-291. [https://doi.org/10.1016/0360-1285\(81\)90002-2](https://doi.org/10.1016/0360-1285(81)90002-2)

- Song, H., (2003) **Diesel soot oxidation under controlled conditions.** (Doctoral dissertation, Brunel University). Retrieved from <http://bura.brunel.ac.uk/handle/2438/4814>
- Song, J., et al. (2006). **Examination of the oxidation behavior of biodiesel soot** Combustion and Flame 146(4): 589-604. <https://doi.org/10.1016/j.combustflame.2006.06.010>
- Soriano, J. A., et al. (2017). **Oxidation reactivity and nanostructural characterization of the soot coming from farnesane - a novel diesel fuel derived from sugar cane** Carbon 125: 516-529. <https://doi.org/10.1016/j.carbon.2017.09.090>
- Stanmore B. R., et al. (2001). **The oxidation of soot: a review of experiments, mechanisms and models** Carbon 39: 2247-2268. [https://doi.org/10.1016/S0008-6223\(01\)00109-9](https://doi.org/10.1016/S0008-6223(01)00109-9)
- Storey, J. M., et al., (2005) **Hydrocarbon species in the exhaust of diesel engines equipped with advanced emissions control devices** [Online]. Available from <https://crcao.org/reports/recentstudies2005/AVFL-10b-2%20Final%20Report%20January%2031%202005.pdf>. [Accessed July 2018]
- Strzelec, A., et al. (2010). **Diesel particulate oxidation Model : combined effects of volatiles and fixed carbon combustion** SAE Technical Paper No. 2010-01-2127. <https://doi.org/10.4271/2010-01-2127>
- Strzelec, A., et al. (2017). **Nanostructure and burning mode of light-duty diesel particulate with conventional diesel, biodiesel, and intermediate blends** International Journal of Engine Research 18(6). <https://doi.org/10.1177/1468087416674414>
- Sukjit, E., et al. (2013). **Finding synergies in fuels properties for the design of renewable fuels-hydroxylated biodiesel effects on butanol-diesel blends** Environmental Science & Technology 47(7): 3535-3542. <https://doi.org/10.1021/es400131j>
- Tassopoulos, M., et al. (1989). **Simulation of microstructure/mechanism relationships in particle deposition** American Institute of Chemical Engineers Journal 35(6): 967-980. <https://doi.org/10.1002/aic.690350610>
- The society of motor manufacturers and traders, (2018) **New Car CO2 Report 2018** [Online]. Available from <https://www.smmt.co.uk/wp-content/uploads/sites/2/SMMT-New-Car-Co2-Report-2018-artwork.pdf>. [Accessed
- Theinnoi, K., et al. (2012). **Diesel particulate filter regeneration strategies: Study of hydrogen addition on biodiesel fuelled engines** Energy & Fuels 26(2): 1192-1201. <https://doi.org/10.1021/ef201355b>

- fractal-like agglomerates** Journal of Aerosol Science 35(5): 633-655.
<https://doi.org/10.1016/j.jaerosci.2003.11.004>
- Vander Wal, R. L., & Mueller, C. J. (2006). **Initial investigation of effects of fuel oxygenation on nanostructure of soot from a direct-injection diesel engine** Energy & Fuels 20(6): 2364-2369. <https://doi.org/10.1021/ef060201+>
- Vander Wal, R. L., & Tomasek, A. J. (2003). **Soot oxidation: dependence upon initial nanostructure** Combustion and Flame 134(1-2): 1-9. [https://doi.org/10.1016/s0010-2180\(03\)00084-1](https://doi.org/10.1016/s0010-2180(03)00084-1)
- Vander Wal, R. L., & Tomasek, A. J. (2004). **Soot nanostructure: dependence upon synthesis conditions** Combustion and Flame 136(1-2): 129-140. <https://doi.org/10.1016/j.combustflame.2003.09.008>
- Vassallo J., et al. (1995). **On the role of gas-phase reactions in the mechanism of the selective reduction of NOx** Applied Catalysis B: Environmental 7: 65-78. [https://doi.org/10.1016/0926-3373\(95\)00032-1](https://doi.org/10.1016/0926-3373(95)00032-1)
- Villani, K., et al. (2005). **Catalytic carbon oxidation over Ag/Al₂O₃** Journal of Catalysis 236(1): 172-175. <https://doi.org/10.1016/j.jcat.2005.09.018>
- Viola, M. B. (2008). **HC-SCR catalyst performance in reducing NOx emissions from a diesel engine running transient test cycles** SAE Technical Paper No. 2008-01-2487. <https://doi.org/10.4271/2009-01-2775>
- Wagner, H. G. G. (1979). **Soot formation in combustion** Symposium (International) on Combustion 17(1): 3-19. [https://doi.org/10.1016/S0082-0784\(79\)80005-3](https://doi.org/10.1016/S0082-0784(79)80005-3)
- Walker, P. L., et al. (1966). **Chemistry and physics of carbon** (Vol. 2): Pergamon Press Ltd. ISBN: 9780824769918
- Wang, C., et al. (2014). **Fuel effect on particulate matter composition and soot oxidation in a direct-injection spark ignition (DISI) engine** Energy & Fuels 28(3): 2003-2012. <https://doi.org/10.1021/ef402234z>
- Wang, J., et al. (2009). **Oxygenated blend design and its effects on reducing diesel particulate emissions** Fuel 88(10): 2037-2045. <https://doi.org/10.1016/j.fuel.2009.02.045>
- Wang, L., et al. (2013). **Aliphatic C–H and oxygenated surface functional groups of diesel in-cylinder soot: Characterizations and impact on soot oxidation behavior**

Proceedings of the Combustion Institute 34(2): 3099-3106.
<https://doi.org/10.1016/j.proci.2012.07.052>

Wang, W., et al. (2013). **Ammonia as hydrogen carrier for transportation; investigation of the ammonia exhaust gas fuel reforming** International Journal of Hydrogen Energy 38(23): 9907-9917. <https://doi.org/10.1016/j.ijhydene.2013.05.144>

Wang, X., et al. (2012). **Identification of active oxygen species for soot combustion on LaMnO₃ perovskite** Catalysis Science & Technology 2(9): 1822. <https://doi.org/10.1039/c2cy20353g>

Wei, L., et al. (2016). **Influence of waste cooking oil biodiesel on the nanostructure and volatility of particles emitted by a direct-injection diesel engine** Aerosol Science and Technology 50(9): 893-905. <https://doi.org/10.1080/02786826.2016.1203390>

Wentzel, M., et al. (2003). **Transmission electron microscopical and aerosol dynamical characterization of soot aerosols** Journal of Aerosol Science 34(10): 1347-1370. [https://doi.org/10.1016/s0021-8502\(03\)00360-4](https://doi.org/10.1016/s0021-8502(03)00360-4)

Westbrook, C. K., et al. (2006). **Chemical kinetic modeling study of the effects of oxygenated hydrocarbons on soot emissions from diesel engines** Journal of Physical Chemistry 110: 6912-6922. <https://doi.org/10.1021/jp056362g>

Wozniak, M., et al. (2012). **Comparison of methods to derive morphological parameters of multi-fractal samples of particle aggregates from TEM images** Journal of Aerosol Science 47: 12-26. <https://doi.org/10.1016/j.jaerosci.2011.12.008>

Xi, J., & Zhong, B. J. (2006). **Soot in Diesel Combustion Systems** Chemical Engineering & Technology 29(6): 665-673. <https://doi.org/10.1002/ceat.200600016>

Xua, Z., et al. (2014). **Effects of injection timing on exhaust particle size and nanostructure on a diesel engine at different loads** Journal of Aerosol Science 76: 28-38. <https://doi.org/10.1016/j.jaerosci.2014.05.002>

Yanowitz, J., et al. (2014). **Compendium of experimental cetane numbers** National Renewable Energy Laboratory report No. SR-540-36805. <https://doi.org/10.2172/1150177>

Yazdani, S. S., & Gonzalez, R. (2007). **Anaerobic fermentation of glycerol: a path to economic viability for the biofuels industry** Current Opinion in Biotechnology 18(3): 213-219. <https://doi.org/10.1016/j.copbio.2007.05.002>

- Ye, P., et al. (2014). **Impact of rail pressure and biodiesel fueling on the particulate morphology and soot nanostructures from a common-rail turbocharged direct injection diesel engine** International Journal of Engine Research 17(2): 193-208. <https://doi.org/10.1177/1468087414564229>
- Yehliu, K., et al. (2012). **Impact of fuel formulation on the nanostructure and reactivity of diesel soot** Combustion and Flame 159(12): 3597-3606. <https://doi.org/10.1016/j.combustflame.2012.07.004>
- Yehliu, K., et al. (2011). **Development of an HRTEM image analysis method to quantify carbon nanostructure** Combustion and Flame 158(9): 1837-1851. <https://doi.org/10.1016/j.combustflame.2011.01.009>
- Yu, Z., et al. (2009). **A new route for the synthesis of propylene oxide from bio-glycerol derivated propylene glycol** Chemical Communications 26: 3934-3936. <https://doi.org/10.1039/b907530e>
- Zannis, T. C., et al. (2004). **Experimental investigation to specify the effect of oxygenated additive content and type on DI diesel engine performance and emissions** SAE Technical Paper No. 2004-01-0097. <https://doi.org/10.4271/2004-01-0097>
- Zhang, Z. H., & Balasubramanian, R. (2014). **Physicochemical and toxicological characteristics of particulate matter emitted from a non-road diesel engine: comparative evaluation of biodiesel-diesel and butanol-diesel blends** Journal of hazardous materials 264: 395-402. <https://doi.org/10.1016/j.jhazmat.2013.11.033>
- Zheng, J., et al. (2003). **Quantitative analysis of hydroperoxyl radical using flow injection analysis with chemiluminescence detection** Analytical Chemistry 75(17): 4696-4700. <https://doi.org/10.1021/ac034429v>